DEVELOPMENT OF A BIOLOGICALLY-RELEVANT PRECLINICAL RADIOTHERAPY DOSIMETRY PHANTOM

A thesis submitted to the University of Manchester for the degree of

Doctor of Philosophy

in the Faculty of Biology, Medicine and Health.

2021

Emma R Biglin

School of Medical Sciences, Division of Cancer Sciences

Contents

5

Final word count: 56525

6

List of figures

List of tables

Abbreviations

AAPM – American Association of Physicists in Medicine

ABS - Acrylonitrile Butadiene Styrene

AKT – Protein kinase B

ALR – ATP-Linked Respiration

ARRIVE - Animal Research: Reporting of *in vivo* Experiments

ATCC – American Type Culture Collection

ATM – Ataxia Telangiectasia Mutated

ATP - Adenosine Triphosphate

ATR - Ataxia Telangiectasia and Rad3-related Protein

BR – Basal Respiration

BSA – Bovine Serum Albumin

CAD – Computer Aided Design

CBCT – Cone Beam Computed Tomography

CHI3L1 - Chitinase-3-like Protein 1

CNS – Central Nervous System

^{60}Co – Cobalt 60

CT – Computed Tomography

CTV – Clinical Target Volume

DD – Dose Difference

dH_2O – Deionised Water

DLT – Dose Limiting Toxicity

DMEM - Dulbecco's Modified Eagle Medium

DMSO – Dimethyl Sulphoxide

DNA – Deoxyribonucleic Acid

DNA-PKcs – DNA Protein Kinase Complex

DSB – Double Strand Break

DTA – Distance-To-Agreement

EBRT – External Beam Radiotherapy

ECAR - Extracellular Acidification Rate

ECM – Extracellular Matrix

EDTA - Ethylenediaminetetraacetic Acid

EFS – Event-Free Survival

EGFR – Epidermal Growth Factor Receptor

EORTC – European Organisation for Research and Treatment of Cancer

EPID – Electronic Portal Imaging Device

ESTRO-ACROP - European Society for Radiotherapy & Oncology - Advisory Committee in Radiation Oncology Practice

FCCP - Carbonyl Cyanide-4-(trifluoromethoxy) phenylhydrazone

FBS – Fetal Bovine Serum

FDM – Fused Deposition Modelling

FGF – Fibroblast Growth Factor

GABRA1 - Gamma-Aminobutyric Acid Type A Receptor Subunit Alpha1

GBM – Glioblastoma Multiforme

GTV – Gross Tumour Volume

H2AX - H2A Histone Family Member X

HBS – HEPES-Buffered Saline

HGFR – Hepatocyte Growth Factor Receptor

HIF – Hypoxia-Inducible Factor

HR – Homologous Recombination

HU – Hounsfield Units

HVL – Half Value Layer

ICRU - International Commission on Radiation Units and Measurements

IDH - Isocitrate Dehydrogenase

IGRT – Image-Guided Radiotherapy

IMRT – Intensity Modulated Radiotherapy

IPEM - Institute of Physics and Engineering in Medicine

KV – Kilovoltage

KeV – Kiloelectron Volts

LET – Linear Energy Transfer

MBCF - Molecular Biology Core Facility

MGMT - O6-Methylguanine DNA Methyltransferase

MOSFETS – Metal Oxide Semiconductor Field Effect Transistors

MRC – Maximum Respiratory Capacity

MRE11 - Meiotic Recombination 11

MRN - MRE11-RAD50-NBS1 complex

MRI – Magnetic Resonance Imaging

MTD – Maximum Tolerated Dose

mTOR – Mammalian Target of Rapamycin

MV - Megavoltage

NADPH - Nicotinamide Adenine Dinucleotide Phosphate

NBS1 - Nijmegen Breakage Syndrome 1

NC3Rs - National Centre for the Replacement Refinement and Reduction of Animals in Research

NCIC - National Cancer Institute of Canada

NEFL – Neurofilament Light

NF1 – Neurofibromin 1

NF-κB - Nuclear Factor Kappa-Light-Chain-Enhancer of Activated B Cells

NHEJ – Non-Homologous End Joining

NIST – National Institute of Standards and Technology

NPL – National Physical Laboratory

OAR – Organs At Risk

OCR – Oxygen Consumption Rate

OCRB – Oglesby Cancer Research Centre

OLIG2 - Oligodendrocyte Transcription Factor

OS – Overall Survival

OSLD - Optically-Stimulated Luminescent Detectors

PBT – Proton Beam Therapy

PBRT – Partial Brain Radiotherapy

PBS – Phosphate-Buffered Saline

PDD – Percentage depth dose

PDGFR - Platelet-Derived Growth Factor Receptors

PE – Plating Efficiency

PET – Positron-Emitted Tomography

PFS – Progression-Free Survival

PI3K - Phosphoinositide 3-kinase

PLA – Polylactic acid

pRB – Retinoblastoma protein

PTEN - Phosphatase and Tensin Homolog

PTV – Planning Target Volume

PVA – Polyvinyl Alcohol

QA – Quality Assurance

QC – Quality Control

RC – Reserve Capacity

RGB – Red, Green, Blue

RNA – Ribonucleic Acid

ROS – Reactive Oxygen Species

RPA – Replication Protein A

RPMI - Roswell Park Memorial Institute

RT - Radiotherapy

RTK – Receptor Tyrosine Kinase

SABR – Stereotactic Ablative Radiotherapy

SARRP – Small Animal Radiation Research Platform

SC – Short Course

SF – Surviving Fraction

SLC12A5 - Solute Carrier Family 12 Member 5

SRB - Sulforhodamine B

SSB – Single Strand Break

SSD – Source-to-Surface Distance

STL – Stereolithography

SYT1 - Synaptotagmin 1

TEAE – Treatment-Emergent Adverse Effects

TCA - Trichloroacetic Acid

TCD - Trisodium Citrate Dehydrate

TEM – Tissue-Equivalent Material

TCGA – The Cancer Genome Atlas

TIFF - Tag Image File Format

TLDs - Thermoluminescent Detectors

TMZ – Temozolomide

TPS – Treatment Planning System

TTF – Tumour Treating Fields

ULA – Ultra-Low Attachment

VEGF - Vascular Endothelial Growth Factors

VMAT – Volumetric-Modulated Arc Therapy

WBRT – Whole Brain Radiotherapy

XLF – XRCC4-like Factor

XRCC4 - X-ray Repair Cross-Complementing Protein 4

53BP1 - p53-Binding Protein 1

Abstract

Small animal radiation research studies are a vital step in translational research. Recently, sophisticated small animal irradiators have been developed to combine treatment planning, image guidance and multi-angle delivery, to better mimic the techniques implemented in the clinic. However, these technological developments are hindered by a lack of dosimetry standards, without which puts into question the accuracy of dose measurements. Furthermore, the current generation of dosimetry phantoms consist of basic geometric shapes, lacking the capability to assess real world treatment plans and dose distribution delivered to the small animal.

Here, a tissue-equivalent murine phantom has been developed to represent the animal geometry and density to fully test the Small Animal Radiation Research Platform's (SARRPs) imaging, treatment planning and radiation delivery capabilities. Phantoms were constructed, using 3D printing, to capture 2D measurements of the dose distribution using Gafchromic EBT3 film. Furthermore, to assess the suitability of incorporating the phantom into existing quality assurance (QA) processes across centres, a multi-institute dosimetry audit was undertaken. Absolute dose and the 2D dose distribution, in static and arc beams, were assessed using alanine pellets and Gafchromic EBT3 film. All absolute dose measurements were within 10% of the planned dose. The arc irradiations had increased variability and measured lower than the static field, suggesting a geographical miss of the alanine pellet target. These results demonstrate the phantom is a suitable addition to pre-existing dosimetry assessments, but further work to implement QA protocols is required. To increase the biological relevance, specific pockets could be created within the phantom to hold biological material in the form of 3D cellular matrices.

Glioblastoma multiforme (GBM) is the most common primary brain tumour in adults with poor survival rates of ~5% at 5 years. The difficulty in improving clinical outcomes is mainly due to inter- and intra- cellular heterogeneity across tumours, restricting the identification of successful targeted treatments. A panel of five genetically heterogeneous cell lines were examined, assessing the radiosensitivity, DNA damage repair capacity, metabolic profile and migration. Variations in the radiation response were observed between cell lines, in each of the assays performed. The use of GBM spheroids provided a more realistic representation of a tumour geometry. Radiosensitivity, migration and invasion assays using these 3D models demonstrated differences between 2D and 3D cell culture. A second 3D model involved encapsulating GBM cells in a protective hydrogel.

Declaration

No portion of the work referred to in the thesis has been submitted in support of an application for another degree or qualification of this or any other university or other institute of learning.

Copyright

1. The author of this thesis (including any appendices and/or schedules to this thesis) owns certain copyright or related rights in it (the "Copyright") and she has given The University of Manchester certain rights to use such Copyright, including for administrative purposes.

2. Copies of this thesis, either in full or in extracts and whether in hard or electronic copy, may be made only in accordance with the Copyright, Designs and Patents Act 1988 (as amended) and regulations issued under it or, where appropriate, in accordance with licensing agreements which the University has from time to time. This page must form part of any such copies made.

3. The ownership of certain Copyright, patents, designs, trademarks and other intellectual property (the "Intellectual Property") and any reproductions of copyright works in the thesis, for example graphs and tables ("Reproductions"), which may be described in this thesis, may not be owned by the author and may be owned by third parties. Such Intellectual Property and Reproductions cannot and must not be made available for use without the prior written permission of the owner(s) of the relevant Intellectual Property and/or Reproductions.

4. Further information on the conditions under which disclosure, publication and commercialisation of this thesis, the Copyright and any Intellectual Property and/or Reproductions described in it may take place is available in the University IP Policy (see http://documents.manchester.ac.uk/DocuInfo.aspx?DocID=2442 0), in any relevant Thesis restriction declarations deposited in the University Library, The University Library's regulations (see http://www.library.manchester.ac.uk/about/regulations/) and in The University's policy on Presentation of Theses

Acknowledgements

First I would like to extend my sincere gratitude to my PhD supervisors: Prof Karen Kirkby, Dr Adam Aitkenhead, Dr Amy Chadwick, Dr Gareth Price, Prof Kaye Williams and Dr Alexander Oh. Their advice, guidance and support have been invaluable throughout this project and in my development to become an independent scientific researcher. I would like to offer a special thanks to Dr Elham Santina who provided much needed support and guidance in, and out of, the laboratory, particularly over the last 18 months. I would also like to acknowledge Dr Michael Merchant, my PhD advisor, for his support and advice.

I would also like to thank all my colleagues, past and present, in the PRECISE group for their support, encouragement and, most of all, friendship over the last 4 years.

I would like to thank the National Centre for the Replacement, Refinement and Reduction of Animals in Research (NC3Rs) for funding this project and to the regional programme managers Dr Kamar Ameen-Ali and Dr Joanna Stanley for their support and insightful comments.

Finally, a special thanks go to my family and fiancé Nik for their love and unwavering support during my studies.

Preface

This thesis is presented in the alternative format and comprises of a paper published in Radiation Oncology (Section 2, Chapter 1), a recently submitted manuscript to Scientific Reports (Section 2, Chapter 4) and result chapters in the format of papers (Section 2, Chapter 3, and Section 3, Chapters 3 and 4).

Section 2, Chapter 1 has been published as follows:

Biglin, E.R., Price, G.J., Chadwick, A.L. et al. Preclinical dosimetry: exploring the use of small animal phantoms. Radiat Oncol 14, 134 (2019). https://doi.org/10.1186/s13014-019-1343-8

Not included in this thesis is the publication of the following paper of which I helped draft and edit the manuscript but the main body of work was completed prior to the PhD project beginning:

Price, G.J., Biglin, E.R., Collins, S., et al. An open source heterogeneous 3D printed mouse phantom utilising a novel bone representative thermoplastic. Phys. Med. Biol. 65 (2020)

I obtained my B.Sc. degree in Human Biology from the University of Huddersfield in 2014 followed by the completion of a PgDip in Radiotherapy and Oncology in Practice from the Sheffield Hallam University and Castle Hill Hospital, Hull, qualifying as a Therapeutic Radiographer in 2017. Choosing research over a clinical career, I began my PhD at the University of Manchester in 2017.

Aims and outline

The aims of this thesis were to adapt an existing 3D printed phantom, developed by Price *et al.* (1)*,* to accurately capture measurements of X-ray radiation dose, with the end goal of being incorporated into routine quality assurance procedures, and to better integrate *in-vitro* experimentation with pre-clinical radiobiology to understand the contribution of real world dose distributions on tumour response.

To address these aims, the first part of this thesis describes the development of 3D printed zoomorphic murine phantoms to hold various detectors, and the assessment of the phantoms suitability in capturing radiation measurements, using Gafchromic EBT3 film, on the Small Animal Radiation Research Platform (SARRP). Further measurements were performed to validate the effects of the higher density material included in the model, mimicking the skeletal structure. Once the use of the phantom had been established on the SARRP, the next aim was to undertake a postal audit to investigate the current status of preclinical dosimetry on SARRPs across several UK small animal radiation research facilities. The phantom used to conduct these audit measurements consisted of Gafchromic EBT3 film and alanine pellet detectors, obtaining measurements of absolute dose and the 2D dose distribution across the target field, traceable to the National Physical Laboratory (NPL) UK reference.

This thesis also aimed to characterise the response to radiation across a panel of glioblastoma multiforme (GBM) cell lines and develop 3D GBM cellular models that could facilitate irradiation in the murine phantom, followed by harvesting for various experimental end points. Radiation responses were examined in the context of clonogenic survival, DNA damage and repair, mitochondrial metabolism, migration and invasion. Use of the phantom and biological material would identify concerns regarding dosimetric inaccuracy in radiobiology experiments whilst identifying potential avenues for research in the pathway to improve clinical outcomes, especially in the treatment of GBM.

In meeting these aims, a tissue-equivalent biologically-relevant radiation dosimetry phantom was developed that could be a suitable replacement for those mice used to measure the delivered radiation dose. The phantom, in combination with both radiation dosimeters and 3D cellular models, would compare the physical dose delivered and the biological radiation response at the micron scale. Uncertainties in delivered dose impact the validity of results and could create additional and unnecessary toxicity to the animal. Regular use of the phantom will refine animal

use by minimising these dose uncertainties and optimising the set up of experiments, further minimising toxicity from geographical misalignment of the target – especially important for multiple, fractionated regimes, and streamlines the experiment process, reducing the time the animal is subject to restrictive immobilisation or anaesthesia. Furthermore, this dose uncertainty contributes a major source of noise in experimental data, therefore regular use of the phantom for dosimetric assessment would increase the accuracy of delivered dose and potentially reduce the signal to noise ratio enough to reduce the sample sizes required to produce statistical power, especially in preclinical dose-response experiments as discussed by Ciecior *et al.* (2).

This thesis is presented in the alternative format, where each results chapter is presented in a format suitable for publication. Section 1 provides a general introduction to the topic. Section 2 discusses the first aims relating to the development and use of the dosimetry phantom, with Chapter 2.3 describing the commissioning of the SARRP used for all the phantom irradiations and the subsequent tests of several phantom models with Gafchromic EBT3 film. The commissioning of the SARRP provided a reference for all future phantom irradiations, with traceable dosimetry to the UK primary standard. Chapter 2.4 continues with the results from the UK multicentre dosimetry audit. Section 3 covers the biological experiments with Chapter 3.3 documenting the radiation response of several GBM cell lines in 2D culture. This established the radiosensitivity of each cell line to compare between 2D and 3D culture. Chapter 3.4 describes the development of 3D spheroid and hydrogel bead (microbead) models. The protective structure of the hydrogel microbead facilitates efficient transfer between tissue culture vessels for long term maintenance and analysis, which could also enable the irradiation of these 3D matrices within the dosimetry phantom. Section 4 discusses the overall conclusions as individual chapters, and in the context of the overall aims.

SECTION 1: INTRODUCTION

1.1. Cancer incidence

In the UK there are approximately 367000 new cases of cancer diagnosed each year (3). Earlier detection and longer life expectancies are increasing the populations of citizens living with cancer or those that have previously received treatment for the disease. This is predicted to pose an enormous burden to future healthcare and increase the demand for treatment (4,5). For people born after 1960, the lifetime risk of cancer is estimated to have exceeded 50%, and is predicted to continue to rise (4). To counteract these trends, Baumann *et al.* (5) suggest considerable investments into basic and translational research, scientific education, cancer prevention, early detection and treatments are required.

Approximately 12100 of these diagnosed cases are brain and central nervous system related (6). Glioblastoma multiforme (GBM), grade 4 astrocytomas, account for around 27% of all brain tumours (7), and is the focus of Section 3 of this thesis.

1.2. Cancer biology – The Hallmarks of Cancer

Normal cells are differentiated for a defined purpose, suit a specific microenvironment and have a limited life span. Disruption to the regulatory processes that sustain homeostasis create malignant cells with unlimited proliferative capacity, continuous growth cycles, resistance to cell death, undergo genomic adaptation to promote survival and have increased migration and invasion potential (8,9). Initially, Hanahan and Weinberg (8) defined cancer as a set of six principles that distinguish malignant and normal cells. A decade later they identified 4 more characteristic traits (10). These hallmarks are discussed below (Table 1.2.1), highlighting the genetic drivers relating to glioblastoma multiforme (GBM), discussed in more detail in Chapter 3.3.

Table 1.2.1. The hallmarks of cancer and radiobiology (10,11).

Hallmark	Summary	Link to radiobiology
Sustaining proliferative signalling	Deregulation of the controlled growth signals sustains unlimited proliferation.	Key evidence has demonstrated a correlation between increased RT time and accelerated repopulation of tumour cells.
Evading growth suppressors	The characteristic loss of tumour suppressor proteins, such as p53, in cancer cells disrupts the normal progression of the cell cycle and further promotes increased proliferation.	DNA labelling identified radiosensitivity differences in cell cycle phases and the use of sub-lethal doses of radiation promoted G1 and G2 phase arrest in some cell lines.
Avoiding immune destruction	Tumours avoid recognition or limit the damage imposed by immune cells.	Exposure to ionising radiation has shown many immunomodulatory effects. These include rapid lymphocyte death, vascular endothelial cell changes and immunostimulation. It is also suggested that the immune system is partly responsible for the "Abscopal Effect" where the effects of targeted RT are seen on distant metastasis.
Enabling replicative immortality	Cancer cells avoid senescence and apoptosis, therefore if they are undisturbed the cells will replicate indefinitely.	Clonogenic assays demonstrate radiation inhibits cellular replicative immortality indicated in survival curves.
Tumour-promoting inflammation	Inflammation may play a role in several of these cancer hall marks by supplying bioactive molecules that support growth, survival, angiogenesis, invasion, metastasis and activation of EMT. Inflammatory cells also have a mutagenic effect by releasing ROS.	Exposure to radiation can both promote and reduce inflammation, causing both beneficial anti-tumour effects and detrimental effects to the surrounding normal tissue. It is the oxidative burst of ROS that is suspected to be responsible for the bystander effect where non-irradiated neighbouring cells exhibit radiation damage.
Activating invasion and metastasis	Structural changes and EMT increase the efficiency of a cancer cells ability to invade surrounding tissue or migrate away from the solid tumour.	Clinical studies have shown ineffective treatment regimens could results in further invasion and metastasis. It is suggested that a metastatic phenotype is driven by the tumour microenvironment, presence of hypoxia and HIF-1 and deregulated signalling pathways – affected by radiation.
Inducing angiogenesis	To meet the demands for oxygen and nutrients to sustain the unlimited proliferation, cancer cells	Radiation-induced vascular cell death reduces the tumour burden, whilst stimulating blood vessel formation to reoxygenate

	flip the "angiogenic switch" to a permanent on position, driving the continued production of new blood vessels.	previously hypoxic areas of the tumour and therefore increasing the radiosensitivity. Numerous cytokines, including HIF-1, accumulates in tumours post-radiation exposure and attributes to the release of ROS and further reoxygenates the tumour.
Genome instability and mutation	Most of the discussed hallmarks rely on alterations to the genome of cancer cells.	DNA DSBs are critical to a cells response to ionising radiation, misrepair of these legions can cause cell death or the formation of chromosomal aberrations.
Resisting cell death	The most notable control of the apoptosis-inducing signalling pathways is p53 – mutations of this limit the induction of apoptosis in cancer cells allowing the cells to continue proliferating.	Radiation induces cell death by mitotic catastrophe, apoptosis, necrosis or autophagy, or may force the cells into a permanent senescent state. The exact mechanism of cell death is determined by a multitude of factors including cell type, radiation dose, quality and type, oxygen availability, DNA repair function and the cell cycle phase.
Deregulating cellular energetics	In addition to a constant stream of oxygen and nutrients to keep up with the excessive demand from sustained proliferation, cancer cells require a reprogrammed metabolism to fuel cell growth.	Radiation upregulates HIF-1, which in turn increases ATP metabolism.

ATP – Adenosine Triphosphate, DNA – Deoxyribonucleic acid, DSBs – Double strand break, EMT – epithelial-to-mesenchymal transition, HIF – Hypoxia-inducible factor, ROS – reactive oxygen species, RT – radiotherapy.

1.2.1. Sustained proliferative signalling.

Every normal cell requires a mitogenic growth signal to stimulate the active proliferative state, otherwise the cell will remain in a quiescent state. Many tumour-promoting oncogenes mimic normal growth signals to eliminate this dependence on exogenously-derived stimulation. Cancer cells may also acquire the ability to produce their own growth factors, obviating the need for signals originating from elsewhere. This liberation from controlled signalling interrupts the homeostatic mechanism and negative feedback loops operating to maintain normal tissue architecture, causing a rapid rate of tumour growth. A prominent tumour suppressor protein responsible for controlling the proliferative signalling circuitry is phosphatase

and tensin homolog (PTEN). By degrading phosphoinositide 3-kinase (PI3-K), PTEN terminates downstream proliferative signalling. Loss of function mutations in PTEN are a common occurrence in tumorigenesis. Furthermore, the overexpression of cell surface receptors responsible for growth signal transduction enables tumour cells to be hyper-responsive to signals which would not normally illicit a pro-growth response. Also, in extreme circumstances, structural alteration may occur which can induce ligand-independent proliferative signalling.

1.2.2. Evading growth suppressors.

Another mechanism by which normal cells maintain tissue homeostasis are growth inhibitory signals. These signals are responsible for blocking unnecessary proliferation by forcing cells into a temporary quiescent state or a permanent post-mitotic state. This is predominantly orchestrated by the proteins responsible for the cells transition through G1 phase of the cell cycle in response to stress, such as the retinoblastoma protein (pRb) and the tumour suppressor protein p53. Tumour cells also acquire the capability to avoid terminal differentiation, avoiding the post-mitotic endgame of cell division.

1.2.3. Evading cell death

Tumour formation relies on the rate of cell proliferation outweighing the rate of cell attrition. Apoptosis is carefully controlled programmed cell death, relying upon precisely controlled signalling cascades starting from cell surface receptors responding to abnormalities, including deoxyribonucleic acid (DNA) damage or hypoxia. Pro-apoptotic signals converge at the mitochondria, stimulating further pro-apoptotic proteins and caspases. p53 plays another significant role in the upregulation of pro-apoptotic stimuli. Mutation of the p53 gene, seen in >50% of cancers, is one mechanism by which tumour cells evade the induction of the apoptosis signalling cascade. Secondly, the abrogation of a death signal has been found to involve a decoy, non-signalling receptor antagonising the pro-death receptor. Another evasion of apoptosis mechanism employed by tumour cells involves the activation of the PI3K-protein kinase B (PI3-K/AKT) pathway, either by the loss of the PTEN protein, extracellular stimuli or intracellular signalling.

1.2.4. Limitless replicative potential

The acquired capability of a tumour to self-stimulate growth signals, ignore growth suppression signals and resist apoptosis should suffice in order to enable the uncontrollable proliferation to result in a solid tumour. However, it is only after a cells autonomous programme to limit multiplication is disrupted, that ensures limitless cell division to accomplish their tumorigenic agenda. Again, the proteins pRb and p53

are responsible for controlling the number of cell divisions until a senescent state is reached. Without these proteins, multiplying cells reach a crisis state followed by the occasional emergent of an immortalised variant. Most tumour cells propagated in *in vitro* cell culture are immortalised suggesting this phenotype is essential for malignant growth.

1.2.5. Sustained angiogenesis

To ensure constant access to oxygen and nutrients almost all cells are located approximately 100 μm from a capillary blood vessel, orchestrated by the carefully regulated process of angiogenesis during organ and tissue development. During tumour development, the ability to induce and sustain angiogenesis is vital for cell survival. Tumours activate the "angiogenic switch" by altering gene transcription to increase the expression of angiogenesis-initiating proteins vascular endothelial growth factors (VEGF) and fibroblast growth factors (FGF) and decrease expression of angiogenesis inhibitors – sometimes as a result of the loss of p53.

1.2.6. Tumour invasion and metastasis

Metastases, additional tumours produced from the primary mass at distant sites, are the main cause of mortality in cancer. The survival of this metastasis is reliant upon the five previously described hallmarks, with the addition of downregulation or loss of cell adhesion molecules, most notably E-cadherin, to allow cells to cleave from the primary tumour. Also important is the upregulation of matrix-degrading proteases, to facilitate invasion through the epithelium, stroma or blood vessels.

1.2.7. Genome instability and mutation

A large part of the acquisition of the previously described neoplastic characteristics rely on a series of modifications at the genomic level, allowing mutant genotypes to express a selective advantage and dominate the local environment. These alterations may be triggered by spontaneous mutations or epigenetic mechanisms, usually efficiently detected and resolved. However, once a malignant cell evades these surveillance systems, the rate of mutation is amplified by inheriting an increased sensitivity to mutagenic agents. p53 is once again responsible for overseeing these systems to ensure the surveillance and maintenance processes are uncompromised. These processes often involve eliminating mutagenic agents to prevent DNA damage or, when this is not possible, immediate detection of DNA damage and subsequent activation of repair.

1.2.8. Tumour-promoting inflammation

Most tumours contain regions of immune cells, initially believed to be a result of attempted eradication by the immune system. However, paradoxically the

involvement of the immune system has tumour-promoting effects, enabling the acquisition of hallmark phenotypes by supplying growth factors, survival factors, proangiogenic factors and extracellular matrix (ECM) -modifying enzymes. Moreover, inflammatory cells release mutagenic agents, in particular reactive oxygen species (ROS), accelerating the transition to malignancy.

1.2.9. Reprogramming energy metabolism

Energy production must be adjusted to meet the increased demand required to fuel uncontrolled cell proliferation and growth. Cancer cells show a preference for glycolysis over oxidative phosphorylation, even under aerobic conditions. Although a less efficient production of adenosine triphosphate (ATP), 2 vs 36 ATPs per glucose molecule from oxidative phosphorylation, the rate at which aerobic glycolysis occurs is 10-100 times faster making the overall ATP yield comparable (12). Activated oncogenes or loss of tumour suppressor genes (including PTEN and p53, further discussed in Chapter 3.3) have been linked to this preference for glycolysis, and the presence of hypoxia stimulates a pleiotropic response to continue the upregulation of glucose transporters and glycolytic enzymes.

1.2.10. Evading immune destruction

Both the innate and adaptive arms of the immune system are responsible for identifying and successfully eliminating malignant cells. The establishment of solid tumours must involve either avoidance of immune surveillance or restricted immunological killing.

1.3. Radiotherapy

Radiotherapy (RT) is a vital part of cancer treatment, recommended for 50% of cancer patients. It is the most successful and cost-effective non-surgical option, only accounting for 5% of the UK cancer budget (13).

The effects of radiation occur due to the physical energy deposition along defined tracks of ionisation and excitation interactions (14), causing direct and indirect damage to cells, discussed further in Section 1.3.1.2 and 3.1. Energy deposition can be characterised as either low or high linear energy transfer (LET). X-ray photons are deposited in a highly dispersed manner – low LET, displaying a broad distribution throughout the tissue due to scattering effects from interaction with surrounding matter and are not highly penetrating, with the maximum dose positioned close to the surface (14).

The success of RT relies on the accurate delivery of dose to the tumour volume (15). The relationship between dose and tumour control is a steep dose response curve, indicating higher doses delivered to a tumour will equate to improvements in clinical outcomes – the tumour control probability (TCP). The limiting factor of the total dose delivered is the tolerance of surrounding normal tissue – normal tissue complication probability (NTCP). This compromise between tumour control and normal tissue toxicity is known as the therapeutic ratio, Figure 1.3.1 (15). The aim of treatment delivery is to maximise the gap between the two curves with the addition of chemotherapeutics or other radiosensitising agents to reduce the dose required for clinically relevant responses, shifting the tumour curve to the left. Radioprotectors are used to prevent normal tissue toxicity, increasing the dose that is likely to induce adverse effects, therefore shifting the normal tissue curve towards the right (15). The Quantitative Analysis of Normal Tissue Effects in the Clinic (QUANTEC) review documents the relationship between irradiating normal tissue and clinical outcomes (16).
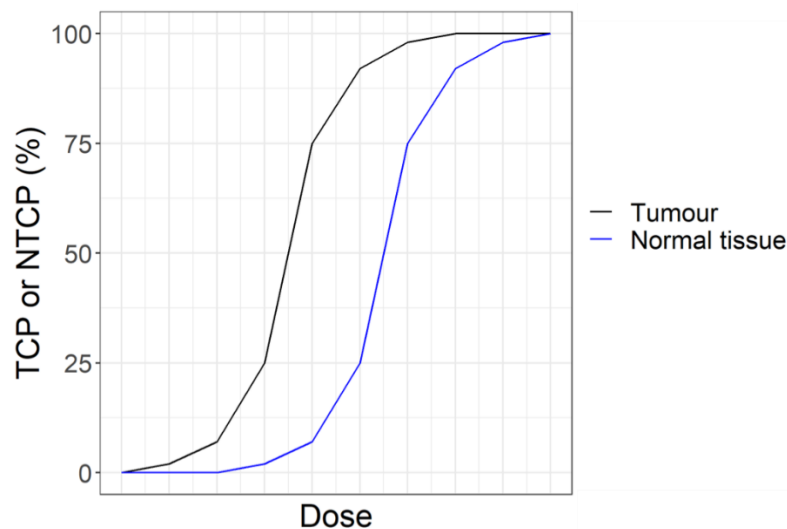
Figure 1.3.1. Diagrammatic plot of dose-response curves for a tumour and normal tissue.

The sigmoid curves depict arbitrary dose responses for tumour and normal tissues. The distance between the two curves represents the therapeutic ratio. This gap may be widened with the use of radiosensitisers, shifting the tumour curve to the left, and/or radioprotectors, shifting the normal tissue curve to the right.

Following diagnosis, a clinical oncologist will use computed tomography (CT) or magnetic resonance imaging (MRI) to outline the visible gross tumour volume

(GTV). To aid in the delineation of this GTV, some tumour sites (lung, oesophagus, cervix and head and neck) benefit from the addition of positron emitted tomography (PET) to these standard imaging modalities to accurately determine the extent of tumour distribution (17). To minimise the risk of not irradiating potential microscopic spread, an additional margin, clinical target volume (CTV), is added to the GTV. To account for any minor uncertainties in the planning and treatment delivery, including daily anatomical changes or differences in the daily positioning of the patient (set up errors), an additional planning target volume (PTV) is added to the CTV and GTV margins. The extent of these margins is tumour site dependent, accounting for the potential movement of the tumour and the proximity of critical organs at risk (OARs). For glioblastoma multiforme (GBM), the European Society for Radiotherapy & Oncology - Advisory Committee in Radiation Oncology Practice (ESTRO-ACROP), recommend a 2 cm CTV with an additional 3-5 mm PTV margin (18). These small margins rely heavily on effective immobilisation and regular image guidance, especially as techniques with a higher degree of precision and dose escalation are implemented (19).
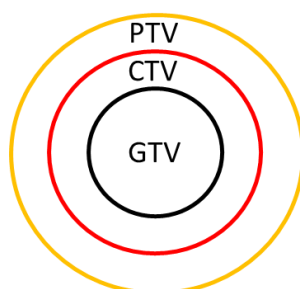
Figure 1.3.2. Diagrammatic representation of RT target volumes.
The gross tumour volume (GTV) delineates the visible tumour. An additional clinical target volume (CTV) accounts for any macroscopic spread. The planning target volume (PTV) ensures any daily anatomical or positioning changes do not affect the tumour coverage.

The advent of hybrid RT machines permits the use of daily X-ray, cone beam CT (CBCT), ultrasound or MRI images to confirm these target volumes and make minor adjustments to account for daily anatomical and positional changes prior to delivering the radiation – image-guided RT (IGRT) (5,20). Sophisticated IGRT minimises the risk of inadvertently irradiating normal tissue or missing the tumour target. Furthermore, technological advancements in external beam RT (EBRT)

increases the precision of the dose delivery to the irregular geometry of the tumour volume whilst minimising normal tissue exposure. Intensity-modulated RT (IMRT) adjusts the dose deposition intensity across the field to suit the irregular target geometry. Volumetric-modulated RT (VMAT) implements IMRT as the linear accelerator rotates around the patient, spreading out the dose deposition. Stereotactic ablative RT (SABR) allows the precise deposition of high radiation doses, in fewer treatment fractions, with a sharp dose fall-off minimising normal tissue toxicity (5). Internal RT can either be performed during surgery or as brachytherapy, allowing the positioning of a sealed radioactive source placed within or adjacent to the tumour (5).

Implementing RT in the treatment of cancer is a complex process requiring consideration of the principles of radiobiology, radiation safety, medical physics and dosimetry (discussed below) and multi-modality treatments (21).

1.3.1. Radiobiology

Damage to malignant cells disrupts the cells replicative ability, induces cell death and gradually reduces the tumour burden (22). The impact of radiotherapy (RT) treatment relies on the understanding of 5 radiobiological phenomena, referred to as the five R's (23,24):

- The capability of normal and tumour cells to **repair** DNA damage between fractions of radiation.
- Stages in the cell cycle have different inherent radiosensitivities with mitosis being the most radiosensitive and the synthesis phase being the most radioresistant. Multiple fractions of radiation will **redistribute** the population of cells through the sensitive phases and enable cell killing.
- Allowing **reoxygenation** of the tumour will enhance radiation-induced cell death by preventing repair of tumour cells – oxygen fixation hypothesis.
- The outcome of treatment varies depending on the **radiosensitivity** of the tumour. RT can be used in combination with radiosensitisers to improve outcomes.
- The capability of normal and tumour cells to **repopulate** between fractions of radiation.

Recently a 6th R, the **reactivation** of the immune system, has been proposed by Boustani *et al.* (22) based on the recent developments in immunotherapy.

1.3.1.1. Radiobiology and the hallmarks of cancer

Early radiobiological experiments established the effects of radiation on all aspects of the Hallmarks of Cancer as described by Hanahan and Weinberg (10), reviewed by Boss *et al.* (11) (Table 1.2.1). Key evidence has demonstrated a correlation between increased RT time and accelerated repopulation of tumour cells. This is stipulated to be a result of overexpression of epidermal growth factor receptors, to sustain proliferative signalling, seen on radioresistant tumours (25,26). DNA labelling identifies radiosensitivity differences in cell cycle phases and the use of sub-lethal doses of radiation promotes G1 and G2 phase arrest in some cell lines. p53 and ATM were later implicated as part of the control of this G1 phase arrest (27–29). Exposure to ionising radiation has shown many immunomodulatory effects. These include rapid lymphocyte death, vascular endothelial cell changes where in normal cells leukocytes have increased adhesive capacity, however with tumour cells leukocytes have reduced adhesive capacity and sub-lethal doses have shown immunostimulatory effects. It is also suggested that the activation of the immune system is partly responsible for the "Abscopal Effect" where the effects of targeted RT are seen on distant metastasis (30–32). Clonogenic assays demonstrate radiation inhibits cellular replicative immortality, indicated in survival curves (33). Exposure to radiation can both promote and reduce inflammation, causing both beneficial anti-tumour effects and detrimental effects to the surrounding normal tissue. Immune cells, predominantly macrophages, are a significant mediator of inflammation, increased by radiation, priming the release of reactive oxygen species (ROS) and other free radicals and the cytokine tumour necrosis factor. It is this oxidative burst of ROS that is suspected to be responsible for the bystander effect where non-irradiated neighbouring cells exhibit radiation damage (34–36). Clinical studies have shown ineffective treatment regimens could results in further invasion and metastasis. It is suggested that a metastatic phenotype is driven by the tumour microenvironment, presence of hypoxia and HIF-1 and deregulated signalling pathways. These effects are also elicited after exposure to radiation (37–42). It is well established that tumours can create their own vascular network to provide oxygen and nutrients. Radiation has stimulatory and death-inducing capacity with regards to vascular cells, both of which have beneficial effects. Vascular cell death reduces the tumour burden, whilst stimulating blood vessel formation to reoxygenate previously hypoxic areas of the tumour and therefore increasing the radiosensitivity. Numerous cytokines, including HIF-1, accumulates in tumours post-radiation exposure and attributes to the release of ROS and increased reoxygenation of the tumour (40,43). DNA double strand breaks (DSBs) are critical

to a cells response to ionising radiation, as discussed in Section 1.3.1.2. Misrepair of these legions can cause cell death or the formation of chromosomal aberrations (11). Radiation induces cell death by mitotic catastrophe, apoptosis, necrosis or autophagy, or may force the cells into a permanent senescent state. The exact mechanism of cell death is determined by a multitude of factors including cell type, radiation dose, quality and type, oxygen availability, DNA repair function and the cell cycle phase (44). Normal cells create energy as adenosine triphosphate (ATP) through oxidative phosphorylation, in which glucose is converted to pyruvate, then oxidised to form water and a high yield of ATP. Under low levels of oxygen very low level of ATP are generated by glycolysis when pyruvate is converted to lactate and ATP. However tumour cells prefer glycolysis, even when there is an abundance of oxygen present, creating an acidic microenvironment. The low yield of ATP from glycolysis means continuous activity must be sustained, this is driven by the crosstalk between HIF-1 and the proto-oncogene c-MYC, and the regulation of GLUT1 and GLUT3 glucose transporters. As previously mentioned HIF-1 is also upregulated after irradiation (11,45,46).

1.3.1.2. DNA damage and repair

The survival of a cell is dependent on maintaining genomic DNA stability. DNA damage from both exogenous and endogenous sources can compromise this stability (47). Without repair, DNA damage can cause cell death, chromosomal aberrations and mutation (48). When functioning normally, cells engage efficient surveillance systems, sophisticated DNA repair systems, cell cycle checkpoints and cell death pathways. Unsurprisingly these are often disrupted or deregulated in neoplastic cells, therefore promoting tumour progression (49).

In the context of cancer therapy, RT is used to cause DNA damage, creating both direct damage to the DNA molecules and indirect damage through the release of free radicals from water and organic molecules present in the cell. The majority of DNA damage is the result of the indirect action as free radicals are released from water which makes up 70% of the cell and other cellular organic molecules. The number of free radicals produced correlates with the amount of dose received (49). The presence of oxygen is vital for the chemical 'fixation' (made permanent) of this DNA damage, referred to as the "oxygen-fixation hypothesis" (50). Solid tumours with characteristically poor vasculature and inconsistent perfusion contain regions of low oxygen concentration (≤2% O_2), occurring approximately 100 µm from the nearest perfused blood vessel, correlating with treatment resistance for all modalities, summarised by Hammond *et al.* (51). This limited availability of oxygen

produces fewer free radicals, thereby reducing the indirect DNA damage capacity, and limiting the oxygen fixation capacity, making hypoxic cells 2.5-3 times more radioresistant than normoxic cells (50). Moreover, the biological response to hypoxia, due to action of hypoxia-inducible factor 1α (HIF-1α), alters the expression of genes involved in invasion and disruption of metabolism, vasodilation, apoptosis and autophagy (51).

In every cell exposed to 1 Gy of photon radiation around 10000 bases are damaged and 1000 single strand breaks (SSBs) and 40 DSBs occur (52). DSBs are defined as two SSBs occurring on opposing DNA strands, 10-20 base pairs apart. In response to DNA damage, protein sensors, including H2A Histone Family Member X (H2AX), the Mre11-RAD50-NBS1 (MRN) complex, Ku and p53 binding protein 1 (53BP1), trigger the DNA damage response (47). There are five major DNA repair pathways: base excision repair, nucleotide excision repair, mismatch repair, homologous recombination (HR) and non-homologous end joining (NHEJ). HR and NHEJ are the predominant repair pathway choices for DNA DSBs. NHEJ involves the ligation of the broken strands, initiated by the binding of the Ku protein to these ends, followed by the recruitment of the catalytic component of the DNA-dependent protein kinase complex (DNA-PKcs). The recruitment of DNA-PKcs activates kinase activity and regulates downstream signal transduction molecules for end-processing, whilst also stimulating recruitment of DNA ligase IV, XRCC4 and XLF/Cernunnos (9). NHEJ can occur at any point in the cell cycle, therefore is the most common repair pathway choice for DSBs. HR is more specific in both the cell cycle phase, only occurring in late S/G2 phases, and in the repair mechanism, by copying an intact DNA strand to complete the DSB (53). It begins with the resection of the broken DNA ends by CtIP/MRE11, regulated by 53BP1 and BRCA1 (9). These new resected single strands are quickly bound by replication protein A (RPA), subsequently followed by the involvement of RAD51 and BRCA2, replacing RPA and creating nucleoprotein filaments. The function of these filaments ultimately leads to the formation of a heteroduplex molecule and a Holliday junction from the pairing of displaced and broken strands. Repair of the DSB follows the synthesis of a new strand based on the undamaged strand (9). A summary of these DSB repair pathways is shown in Figure 1.3.3.
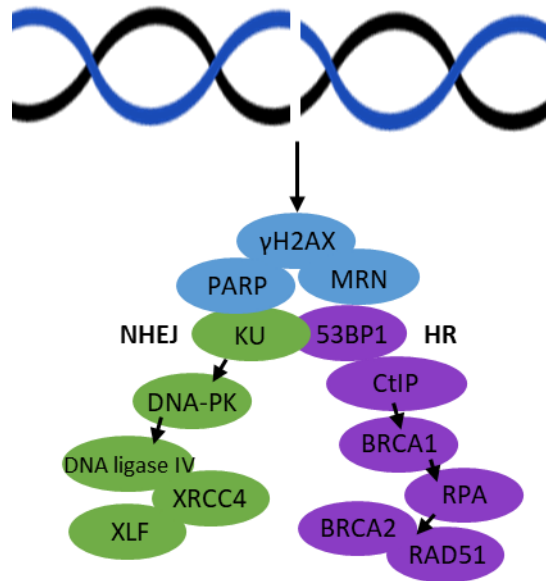
Figure 1.3.3. Diagrammatic representation of DNA double strand break repair. Following the recognition of a DNA double strand break (DSB) there are two main repair pathways, non-homologous end joining (NHEJ), the most common, and homologous recombination (HR).

1.3.2. Dosimetry

The benefits of accurate and precise RT techniques rely heavily on robust dosimetric quality assurance (QA) processes and quality control (QC) checks, verifying all aspects of the RT process (54). Accurate and safe treatment delivery is dependent on the consideration of both dosimetric and geometric uncertainties (55). As summarised by Palmer *et al.* (56), and documented in the Institute of Physics and Engineering in Medicine (IPEM) report 81 (57), there are 37 recommended routine QC checks relating to the dose output, radiation interlocks, machine function, collimation and alignment and reproducibility. The IPEM report 81 also recommends regular calibration of any equipment used to measure relative or absolute doses or dose rates against national primary standards. The Radiation Dosimetry Group within the National Physical Laboratory (NPL) is responsible for maintaining the UK's primary standards for EBRT, ensuring all NHS dosimetry equipment is calibrated against this primary standard (58). Any equipment used onsite should be directly calibrated against a portable secondary standard that is annually calibrated against the UK primary standard. Verification of the dose output is measured using an ionisation chamber and radiochromic film, providing a comparison between calculated and measured doses using absolute dose values

and gamma index maps. The gamma index provides an analysis of planned and measured doses in terms of the dose and the distance-to-agreement (DTA) differences, across the irradiated field (54). In general, treatment plans are tested by delivering the plan to a phantom holding radiochromic film and a gamma analysis is performed on the film data, applying tolerances of between 2%/2 mm to 4%/4 mm (55). Verification of the patient positioning is often performed with the aid of on-board imaging systems, including CBCT (54).

Dosimetry audits are a common tool for ensuring consistent dosimetry across sites, the purpose of which may be to assess general dosimetry, support clinical trials or to collect data for implementing advanced techniques (58). The use of audits in the preclinical setting is discussed in Section 2.4.

1.3.2.1. Biological dosimetry

Biological dosimetry makes use of biological samples to quantify radiation using biomarkers such as the protein γH2AX (59), a protein recruited in response to DNA double strand breaks. The inclusion of biological material within a dosimetry phantom holding radiation dosimeters permits the simultaneous measurement of absorbed dose with reference to physics and biology endpoints. The preferred choice for a biological dosimeter would be the inclusion of relevant biological material within a tissue equivalent phantom, simulating the heterogeneous tissue densities and the realistic dose delivery to the sample. These phantoms provide a valuable intermediate stage between reference dosimetric set ups and *in vivo* studies.

Improvements to dosimetry will decrease the uncertainty in the amount of dose delivered, a major source of noise in experimental data, which has the potential to decrease the sample sizes required to achieve statistically significant data. Furthermore, accurate measurements of delivered doses will reduce potential toxicity by eliminating accidental overdoses received by the animals.

SECTION 2: PRECLINICAL DOSIMETRY USING A 3D PRINTED MURINE PHANTOM

Summary

A literature review was performed to identify the gaps in preclinical radiation research that could be addressed using a 3D printed murine dosimetry phantom. Lacking dosimetry standards affects the accuracy, reproducibility and comparability of results so an accessible tool that accurately represent real world irradiations is necessary. The review also identified detectors regularly used in the radiation dosimetry community, such as Gafchromic EBT3 film, that would be suitable to incorporate into the phantom for quality assurance (QA) purposes. The review also discussed recent dosimetry phantom developments in this newly emerging field, enabling the consideration of any issues with these models when designing our phantom.

The methods section (Section 2.2) provides a general introduction to the material development for the tissue-equivalent models and the use of computer aided design to create custom phantoms. Several designs were 3D printed to hold film, thermoluminescent detectors and dosimetry gel. This demonstrated the capabilities of 3D printing to create such phantoms and, with the recent popularity of 3D printing, could facilitate wide dissemination of the phantom, promoting the phantom as a standardised dosimetry tool.

Chapter 2.3 documents the commissioning of the Small Animal Radiation Research Platform (SARRP) and the first radiation measurements using the murine phantom. Commissioning the SARRP established accurate dosimetry, traceable to the UK primary standard, for the subsequent phantom measurements, and for all other radiation experiments performed in this laboratory. The first end-to-end tests determined the suitability of the phantom and Gafchromic ETB3 film to capture measurements of radiation dose on the SARRP. The complete treatment planning and radiation delivery process was tested, from the use of the on-board cone beam CT for image guidance by identifying the internal skeleton structure, developing treatment plans on the resulting image and accurately delivering the dose, examined using a local gamma analysis to compare the treatment plan and film data. Several measurements were performed to examine the attenuation effects of the bone-equivalent material, targeting areas with a higher ratio of the bone to the

soft tissue material. The final optimisation experiments were performed to test the protocol for the proposed preclinical dosimetry audit.

The final chapter of this section discusses the results from the UK multi-institute SARRP dosimetry audit. 6 UK institutions actively undertaking *in vivo* radiation research were sent a questionnaire, to determine the current practices relating to QA of the SARRPs, and phantoms containing Gafchromic EBT3 film and alanine pellets. Users were instructed to follow their own standard operating procedure to separately deliver static and arc beams, to gauge the realistic radiation delivery of each SARRP. These audit measurements validated the suitability of the phantom to be incorporated as an additional tool into SARRP QA procedures across multiple institutions, by regular users of the SARRPs.

2.1. INTRODUCTION: PRE-CLINICAL DOSIMETRY: EXPLORING THE USE OF SMALL ANIMAL PHANTOMS

Summary

The introduction to Section 2 comprises of a literature review originally published in Radiation Oncology in 2019 (Vol. 14 (134)). The paper has been modified to include section, figure and table numbering, consistent with the rest of the thesis, and updated with relevant literature since it was published in 2019.

A gap in the literature was noticed surrounding the development of preclinical radiation dosimetry phantoms in the context of addressing the lack of standardised dosimetry quality assurance (QA) protocols on small animal radiation units. Therefore, we reviewed the current status of preclinical radiation dosimetry and the measures being undertaken to implement more robust QA practices including the development of dosimetry phantoms. Also reviewed is the recent technological developments in the production of clinically-relevant small animal radiation platforms that have image guidance, treatment planning and multi-angle/arc delivery capabilities.

This review identified areas within the preclinical radiation research field which could be improved with the use of the developed dosimetry phantom discussed in this thesis. Reference QA set ups are not representative of experimental procedures and currently used phantoms with basic geometries lack the relevant shape or heterogeneous density required to rigorously test the treatment planning system. Current zoomorphic phantoms under development lack the spatial resolution, tissue-equivalent density or are machined, hampering reproducibility and the creation of specific designs. Reviewing the commonly used detectors for small field dosimetry identified suitable dosimeters to be incorporated into our developed phantom – Gafchromic EBT3 film to capture the 2D dose distribution and alanine pellets for 1D measurements.

Author contributions

I performed the literature search, undertook the review and evidence synthesis and wrote the manuscript, which was reviewed by all authors.

PRE-CLINICAL DOSIMETRY: EXPLORING THE USE OF SMALL ANIMAL PHANTOMS

Emma R. Biglin[1]* , Gareth J. Price[1,2,] Amy L. Chadwick[1,2,] Adam H. Aitkenhead[1,2,] Kaye J. Williams[3] and Karen J. Kirkby[1,2]

[1]Division of Cancer Sciences, University of Manchester, Manchester Cancer Research Centre, 3rd floor Proton Beam Therapy Centre, Oak Road, Manchester M20 4BX, UK. [2]The Christie NHS Foundation Trust, Manchester, UK. [3]Division of Pharmacy and Optometry, University of Manchester, Manchester, UK.

*corresponding author

Abstract

Preclinical radiotherapy (RT) studies using small animals are an indispensable step in the pathway from *in vitro* experiments to clinical implementation. As RT techniques advance in the clinic, it is important that preclinical models evolve to keep in line with these developments. The use of orthotopic tumour sites, the development of tissue-equivalent mice phantoms and the recent introduction of image guided small animal radiation research platforms has enabled similar precision treatments to be delivered in the laboratory.

These technological developments, however, are hindered by a lack of corresponding dosimetry standards and poor reporting of methodologies. Without robust and well documented preclinical radiotherapy quality assurance processes, it is not possible to ensure the accuracy and repeatability of dose measurements between laboratories. As a consequence current RT-based pre-clinical models are at risk of becoming irrelevant.

In this review we explore current standardization initiatives, focusing in particular on recent developments in small animal radiation equipment, 3D printing technology to create customisable tissue-equivalent dosimetry phantoms and combining these phantoms with commonly used detectors.

2.1.1. Background

Radiation studies using mice span decades, creating a large database of results. Translational research requires a pre-clinical *in vivo* model to facilitate the shift from *in vitro* results into clinical applications (60). As radiotherapy (RT) clinical techniques evolve there is concern that data collected from mouse irradiation does not accurately represent the highly non-uniform focal or conformal dose distribution typically delivered to human patients (61). Poor reporting of methodologies - affecting the reproducibility of experiments - undoubtedly contributes to the problem. Draeger *et al.* (62) systematically reviewed the preclinical radiobiology research spanning 1997 – 2017, determining sufficient reporting in line with the guidance published by the National Institute of Standards and Technology (NIST) (63). Dosimetry and calibration procedures were the least reported parameters, with <16% papers documenting the equipment used, measurement geometry, medium used or protocol followed (62). However, the central issue has been the difference between human and small animal irradiation techniques. Human RT treatment machines have undergone huge technical development in recent decades and are now capable of delivering highly conformal dose distributions, yet many animal studies still utilise crude techniques targeting the whole body or using simple partial shielding (61,64). In an ideal scenario, mouse models would be used to map all aspects of human cancer treatment, multimodality combinations of surgery, chemotherapy, RT (using a range of doses and/or irradiation of a specific organ) and any new therapies as they develop. However, the lack of conformal irradiation units designed specifically for these mice models has hindered this goal (65).

Many studies have been initiated with the intent to find a method of animal irradiation that reflects precise human treatment, due to the high potential animal models have of progressing research and improving RT (reviewed in (63)). Small animal irradiation was first proposed in the early 1970s. Early modalities include using cesium-137 or cobalt-60 sources, kilovoltage (kV) X-ray units and clinical linear accelerators (60,61,64). The first example of a more clinically-familiar micro-irradiation unit was comprised of an iridium source, imaging system, motor controlled platform, and a collimator assembly with a computer to oversee the experiments (65). Refinements in small animal RT techniques have led to higher precision treatment, image-guided RT (IGRT), and dose escalation. However, the absence of dosimetry standards and poor reporting of dosimetry techniques in pre-clinical research is concerning as it limits the ability to compare and combine experimental cohorts between laboratories, and restricts reproducibility (63). The

causes of these issues are multifactorial and include a lack of awareness of the importance of rigorous radiation quality assurance amongst pre-clinical scientists leading to a paucity of dosimetric measurements, insufficient support from clinical physics and dosimetry colleagues, and inadequate equipment to undertake the task (67,68).

As new technologies and approaches advance clinical RT techniques, their laboratory equivalents have been neglected (69). Verhaegen *et al.* (64) hypothesise that the longer it takes for up to date pre-clinical RT to be developed the more likely it is that current radiobiological models become irrelevant. It is only recently that small animal irradiation units have begun to be developed to more closely mimic clinical equipment. It is now important that these advances are mirrored by the development of rigorous protocols and standardised equipment to modernise pre-clinical radiotherapy quality assurance. In clinical practice a series of standardised measurement phantoms and materials are commonly used, making it easy to compare and audit quality assurance (QA) techniques between centres. A similar approach would be valuable in the pre-clinical community. In this article we report current pre-clinical irradiation QA practice before reviewing the development of both small animal dosimetry phantoms, and the current state-of-the-art in small animal precision irradiation devices.

2.1.2. The Standardization of dosimetry

Dosimetry-related equipment and protocols in the clinical setting are well defined and regular QA and quality control (QC) is performed to ensure everything is working within defined tolerances (70). The importance of the precision of dosimeters is highlighted in the requirement of regular calibration to a national standard:

1. A primary standard is nationally maintained at a dedicated dosimetry laboratory.
2. This provides a calibration factor for a mobile secondary standard requiring re-calibration every 3 years.
3. This secondary standard is used within a hospital to calibrate dosimetry equipment annually (70).

There is no legal requirement for this protocol to be followed at a pre-clinical level. In addition to the uncertainty introduced by not having properly calibrated equipment, uncertainty in dose can reach high levels if the following factors are not reported: beam energy, dose rate, temperature and pressure (when using detectors such as

alanine pellets), fractionation regime, target volume and dosimeter depth (63). Preclinical radiobiological studies cover a wide range of samples and irradiation devices, resulting in a variety of experimental set ups significantly different to potential reference conditions (71). Despite continuous efforts to bring to light the issues surrounding preclinical dosimetry, first highlighted by Desrosiers *et al.* (63), a consensus on the exact protocol to maintain high dosimetry standards has yet to be reached. In recent years, several informative and comprehensive recommendations have been published (63,72,73) but none are implemented into standard practice. It then becomes the researcher's responsibility to ensure the production of high quality data, by accounting for factors that may impact any results, and enforce QA procedures in line with clinical practice (74). Implementing such recommendations and providing the relevant dosimetry equipment and expertise to perform any measurements mean it could take years to evaluate the impact of these guidelines. Enforcing dosimetry standards in pre-clinical radiobiology will increase confidence in scientific results and encourage wider multicentre studies by improving comparability and reproducibility.

2.1.2.1. Current methods of pre-clinical dose measurements

Mouse models are considered ideal investigative tools for research as they offer established genetic strains and produce efficient results translatable to humans (75). However, their heterogeneous density and intricate anatomy make both simulating and measuring delivered dose difficult (76). A way to minimise this uncertainty could be identifying the most contrasting densities - bone and lung - and measure the dose delivered to these targets (77). Another major source of uncertainty is the scattering processes, even when in reference to established protocols (78). The American Association of Physicists in Medicine (AAPM) Task Group-61 protocol is the reference outlining dose rate for energies up to 300 kV. This protocol is based on in–air measurements of the entrance surface dose of a water phantom, with tabulated backscatter correction factors. However, these scattering conditions are very different to those during pre-clinical irradiations with small heterogeneous targets with irregular surface geometry. Noblet *et al.* (78) investigated this difference and found that the lack of backscatter seen when using small, irregularly shaped targets (compared to a water phantom) causes a more rapid dose rate decrease. Without accounting for appropriate scatter conditions the measured dose will be an underestimate of that delivered.

2.1.2.1.1. Phantoms

Phantoms are used in radiation dosimetry (clinically and pre-clinically) to investigate and measure the effects of dose on an organ or tissue. They can be composed of water or more complex materials to closely resemble components of a body, in defined shapes and sizes (79). Inter-centre dosimetry audits are periodically undertaken in the clinical setting and, less commonly, at pre-clinical facilities, to assess accuracy in delivered dose. Phantoms containing dosimeters are distributed to participating centres with explicit experimental protocols and the resulting measurements compared (63,68). Pedersen *et al.* (68) sent 6 acrylic phantoms with space for 3 thermoluminescent detectors (TLDs) to 12 radiobiology institutions. Each institution was instructed to deliver 1 Gy to 3 of the phantoms and 4 Gy to the others. Taking accidental exposure into account, the results showed a substantial average difference between the delivered and intended dose, ranging from 0.9% to 42%. To get an accurate representation of the irradiation procedures at each institution limited instructions were provided with participants asked to follow their own irradiation protocol (68). Although this reduced the influence of bias, it is unclear how comparable the different centres' irradiation protocols were to the conditions under which the reference TLD irradiation procedure was completed. Further work might consider accounting for different baseline calibrations and could replace the cylindrical phantoms with a heterogeneous density phantom to show a more accurate demonstration of *in vivo* radiation dosimetry.

2.1.2.1.2. Detectors

Detectors are commonly used in conjunction with a phantom for dosimetry measurements. Dosimeter function depends on properties such as linearity (the relationship between the dosimeter reading and dosimetric quantity), dose rate, energy dependence (the effect of different energies on the measurements), spatial resolution (the clarity of the dose map) and, in particle therapy, the energy transferred per unit length of the track – linear energy transfer (80). A number of detectors have been well established in this field, summarised in Table 2.1.1.

Table 2.1.1 Summary of the detectors currently available (67).

Dosimeter type	Applications	Advantages	Disadvantages
Air-filled ionisation chambers	Machine commissioning Absolute dose calibration QA Uncertainty: 1%-5%	High precision and accuracy Wide variety of equipment available Parameter corrections well understood Dose rate independent Instant readout Waterproof models available	High voltage required Large volume of some models Fragile
Radiographic Film	Imaging Dosimetry Phantom measurements Uncertainty: 2%-5%	Superb 2D spatial resolution Measurement of planar dosimetry Dose rate independent Variety of film types Good measurement of radiation field size and flatness and symmetry	Requires darkroom Processing complex Results vary between film types and batches Dose calibration required Energy dependent Sensitive to visible light Not reusable Great care if used for dose calibration
Radiochromic Film	Imaging Dosimetry Phantom measurements Uncertainty: 1%-5%	Self-processing Insensitive to visible light Tissue-equivalent Energy independent Dose rate independent Superb 2D spatial resolution	Results vary between film types and batches Dose calibration required Not reusable Requires great care if used for dose calibration

		Measures planar dose Good measurement of field size and flatness and symmetry Easy to read	Requires stabilisation period after irradiation
TLDs	*In vivo* dosimetry Phantom measurements Comparisons between centres Uncertainty: 1.5%-5%	Small size-point dose measurements Multiple measurement points in single irradiation Various forms available Reusable after annealing	Time consuming calibration Delayed readout Elaborate care Signal erased during readout Results vary between same batch Light sensitive Signal lost over time
OSLDs	*In vivo* dosimetry Phantom measurements Multi-centre comparisons Uncertainty: 1.1%-3.7%	Small size Multiple measurement points in single irradiation Fast and multiple readouts Various forms available Dose rate independent	Sensitive to light Supralinear response at high doses Limited availability Not recommended for dose calibration Energy dependent
Silicon Diodes	*In vivo* dosimetry Small field dosimetry Detector arrays Relative dosimetry Uncertainty: 1.3%-3%	Moderate size Instant readout Better sensitivity than ion chambers No external voltage	Requires connecting cables Variability of calibration with temperature Directional dependence Special care for consistency

			Cannot be used for dose calibration
			Sensitivity changes with high doses
MOSFETs	*In vivo* dosimetry Small field dosimetry Detector arrays Uncertainty: 3%-5%	Small size (0.2 x 0.2 mm) Multiple measurements Instant readout Better sensitivity than ion chambers Little beam attenuation	Calibration required Energy dependent Temperature dependent Directional dependent Not to be used for dose calibration Limited lifespan High cost
Diamond Detectors	*In vivo* dosimetry Small field dosimetry Relative dosimetry Uncertainty: 1.3%-3%	Small size Tissue-equivalent High sensitivity Resistant to radiation damage Good spatial resolution Low energy dependence No current leakage	Voltage and cables required Requires pre-irradiation Variability among dosimeters Not recommended for calibration Hard to obtain
Alanine – Electron paramagnetic resonance	*In vivo* dosimetry Phantom measurements Multi-centre comparisons Uncertainty: 1.5%-4%	Tissue-equivalent Readout non destructive No fading	Readout requires special equipment
Gel dosimetry detectors	Measurements in complex geometries Multi-centre comparisons	Tissue-equivalent Gel acts as both phantom and dosimeter True 3D distribution	Complex preparation and evaluation Post-irradiation diffusion or ions and polymerisation

	Uncertainty: 5%-10%	Limited accuracy and reproducibility Not to be used for dose calibration

Key: QA – quality assurance, TLDs – thermoluminescent diodes, OSLD – optically-stimulated luminescent detectors, MOSFETS – metal oxide semiconductor field effect transistors.

2.1.3. Creating small animal dosimetry phantoms

The earliest examples of "mouse" phantoms included hollow cylinders containing liquid, mathematical representations based upon measuring the size and mass of a mouse, voxel-based approaches and cuboids with integrated detectors (76,81–83). Technological advances have allowed the current generation of phantoms to be developed with varying shapes or densities more recognisable as a small animal, and recent developments are incorporating more heterogeneous densities (75,76,84). Welch *et al.* (76) demonstrated the first construction of a phantom, based on cone beam CT (CBCT) data, with both the internal and external characteristics of a mouse. Individual slices were constructed of material mimicking soft tissues in both density and X-ray attenuation properties. Appropriate holes were then milled in these slices and filled with bone- (epoxy resin) or lung-equivalent material (urethane-based material with polystyrene microbeads) (76). The materials used to create this phantom are only available at 2 mm thickness, creating an uneven 'stepped' surface, limiting the resolution of the phantom and restricting the detail of smaller regions of heterogeneity. The milling process to create areas to be filled with different materials is also laborious, restricting production to institutions and companies who have the appropriate machinery, and if performed manually may impact reproducibility.

2.1.3.1. 3D Printing

In recent years 3D printing has been widely utilised in the manufacturing of radiotherapy phantoms. It is cost effective, efficient, capable of submillimetre accuracy, and can make use of a wide variety of materials (85). Fused deposition modelling (FDM) and stereolithography are the most commonly used techniques for 3D printing. FDM creates the model by melting a thermoplastic, most commonly acrylonitrile butadiene styrene and polylactic acid, and depositing it in layers. Stereolithography utilises photopolymer resin formed into layers using an ultraviolet

laser (85). FDM is the cheaper option for 3D printing but is less accurate than stereolithography, which may cause problems when creating small or irregular voids, or when printing intricate anatomy such as a mouse spine and ribs. Furthermore, the FDM process can unintentionally incorporate small air gaps between depositions potentially affecting reproducibility.

Price *et al.* (1) demonstrated the use of 3D printing to create unique and reproducible zoomorphic dosimetry phantoms to assess various aspects of the radiation pathway. Esplen *et al.* (86) incorporated three materials into their 3D printed murine phantom, representing the body, skeleton and lungs. Although this is a good example of a high quality and easily reproducible model, the materials used were not tissue-equivalent and therefore required further validation using Monte Carlo modelling to determine the differences between planned and delivered doses. Soultanidis *et al.* (87) fabricated a murine phantom using commercially available tissue-equivalent materials to include an alanine pellet detector, with the aim to allow traceable dose verification and to be used a tool for user training on the SARRP. The process of construction involved 3D printing (skeleton), computer numerical controlled milling (lungs) and injection moulding (body). Compared to 3D printing the complete model, these are laborious and time consuming processes and the positioning of the individual parts during the final casting process may affect the reproducibility. It also limits the capability to reproduce and edit the model by other institutions. Another phantom construction method that has been used is to 3D print the outside shell and important internal structures, such as the skeleton, and then fill the void with a tissue-equivalent liquid (84). With care this could reduce the risks of creating air gaps in the material, but may require non-anatomical support structures to correctly position the internal structures within the body surface shell, as well as requiring that the printed shell must be completely watertight.

2.1.3.2. Incorporation of dosimeters

A phantom constructed of slices allows the incorporation of interchangeable slices with an integrated detector, or can incorporate Gafchromic film between layers (75,76). Another way of incorporating space for dosimeters is to modify the model before 3D printing by using Boolean operations to create holes, print the model in segments to allow film to be sandwiched in different orientations, or print a hollow design to fill with a liquid detector (88,89). An advantage of 3D printing models is being able to design the hole to precisely fit the specific detector thereby reducing the geometric uncertainty and the risks of surrounding air gaps (90).

2.1.3.3. Tissue-equivalent phantoms

Categorising a material as "tissue-equivalent" suggests the composition has identical radiation characteristics and physical properties, when exposed to a defined energy range, as the tissue it represents. Developing phantoms that mimic both the material properties and anatomical shape of real mice permits the measurement of doses that account for the effects of both the beam attenuation and X-ray interaction processes that would occur during real experiments (67,91). When considering the materials being used for tissue equivalence it is also important to consider the conditions of the experiment to determine what properties to mimic (63).

To create tissue-equivalent materials (TEMs) it is common to combine a plastic, for stability, with an additional substance to produce the desired density and attenuation. For example, to create a soft tissue equivalent material Winslow *et al.* (92) mixed two parts urethane with one part calcium carbonate whilst a bone TEM was created using an epoxy resin blend with silicon dioxide and calcium carbonate. Another way of adapting density to suit a specific tissue type is the inclusion of particles in the mixture. This is commonly seen when creating lung-equivalent areas, for example, distributing polystyrene microbeads within a TEM to represent different amplitudes in the breathing cycle (76,92). The above material recipes were developed for diagnostic imaging (X-ray energy 80-120 kVp) and match the density, X-ray attenuation and energy absorption of soft tissue and bone well within this range. However, typical radiobiological irradiations use higher X-ray potentials (up to 300 kVp) (64). The use of 3D printing technology permits further modification of material properties by varying the way in which the printed materials are deposited - the modification of layer formation and infill density permits the creation of highly accurate and customisable tissue-equivalent models (85). Perks *et al.* (89) utilised this method to simulate lungs by purposely incorporating air gaps in the grid-structured print creating a model of 1/3 density. The next step could be creating multiple models with different grid structures to mimic different stages in the breathing cycle.

A state of the art dosimetry phantom would include all of the aforementioned properties. 3D printing using tissue-equivalent materials (for energies in the 10-300 kV range) creates a bespoke phantom suitable for imaging and radiation delivery QA. It is easily reproducible, can be combined with a range of detectors and is cost effective, allowing laboratories to manufacture and modify their own phantoms. Increased use of such phantoms could be encouraged by distributing a standard

phantom with QA equipment or by offering an open source computer aided design (CAD) file of the phantom. Reaching a consensus as a community and adopting a common phantom design and QA approach would be a big step towards improved reporting and experimental repeatability.

2.1.4. Small animal irradiation units

Questionable dosimetry, equipment cost, availability and the different relative biological effectiveness of kV compared to megavoltage (MV) energies led Parsons *et al.* (93) to investigate the use of a linear accelerator (linac) as a preclinical irradiator. Results showed accurate submillimetre targeting without substantial changes required to the linac to irradiate the significantly smaller targets. Koutsouvelis *et al.* (94) investigated the feasibility of using a standard linac for *in vivo* irradiations by 3D printing a section of bolus, to avoid the build-up effect, and a rat-like phantom, to evaluate the dosimetry using TLDs and Gafchromic EBT3 film. Using the bolus and phantom together optimised the dose distribution to within the 5% tolerance recommended. 3D printing the bolus, using an appropriate printing resolution, allows custom designs to ensure good bolus-skin contact for any animal (94). However, there are some challenges presented when using a linac for preclinical irradiations, the build-up region, wider penumbra and the characterisation of dose delivery to such small volumes is not part of the standard dose verification (94).

Since 2008 several small animal radiation systems have been developed (reviewed in (64), Table 2.1.2). Recent developments include increasing beam delivery to submillimetre accuracy, improving the dose delivered to within 5% of planned dose and increasing the number of treatment positions from the four cardinal angles. It is essential that the radiation techniques utilised by these machines mirror those used in radiotherapy on humans (Figure 2.1.1), including the ability to target small areas seen in stereotactic cranial irradiation and dose painting across the treatment field using a variable collimator (95,96). Small animal irradiation, compared to clinical machines, depends on a design that requires adaptation to: beam quality, radiation dose and dose rate, irradiation time, field size and source-to-surface distance (SSD) (63,67).

Table 2.1.2 Characteristics of the developed small animal irradiators (64)*.*

Model	Source	Imaging	Positioning	Additional
SARRP (Xstrahl Ltd)	X-ray, 5-225 keV	Amorphous Si flat panel detector for dual imaging system (CT) and planar X-ray	Robotically-controlled stage, 35 cm SSD, 4 degrees of freedom. Allows continuous radiation delivery either from rotating gantry or platform.	2 collimation systems: 1 for precision with smaller, conformal inserts, another for higher throughput with larger square field sizes.
X-Rad 225Cx (Precision X-Ray Inc.)	X-ray, 5-225 keV	Amorphous Si flat panel for single image or cone beam CT.	3D computer controlled stage with automated corrections	Selection of beam collimators providing 0.2 mm accuracy
Washington University	Iridium 192 (brachy-therapy)	N/A (fiducial markers)	Computer controlled stage, 4 gantry angles	Tungsten collimators 5-15 mm
Stanford University	X-ray, 70-120 keV (microCT scanner)	Designed for small animal imaging so 0.1 mm spatial resolution	Arc or fixed field	Brass iris collimators (0.1-6 cm field sizes
University of Texas Southwestern	X-ray 5-320 keV	Fixed panel	3D precision stage, cylinder for immobilisation	Cylindrical collimators 1-10 mm

Key: SARRP – Small Animal Radiation Research Platform, KeV – kiloelectron volts, CT – computed tomography, SSD – source-to-surface distance.

Small animal RT requires precise targeting, high resolution imaging capability and appropriate dose verification technology (64). Equipment should include an X-ray tube (10-320 kV), collimating device, generator and controls to set the beam energy, tube current and time. With small animal irradiation megavoltage beams may be too

high an energy which would lead to insufficient surface dose, increased lateral scatter and hotspots at depth (67).
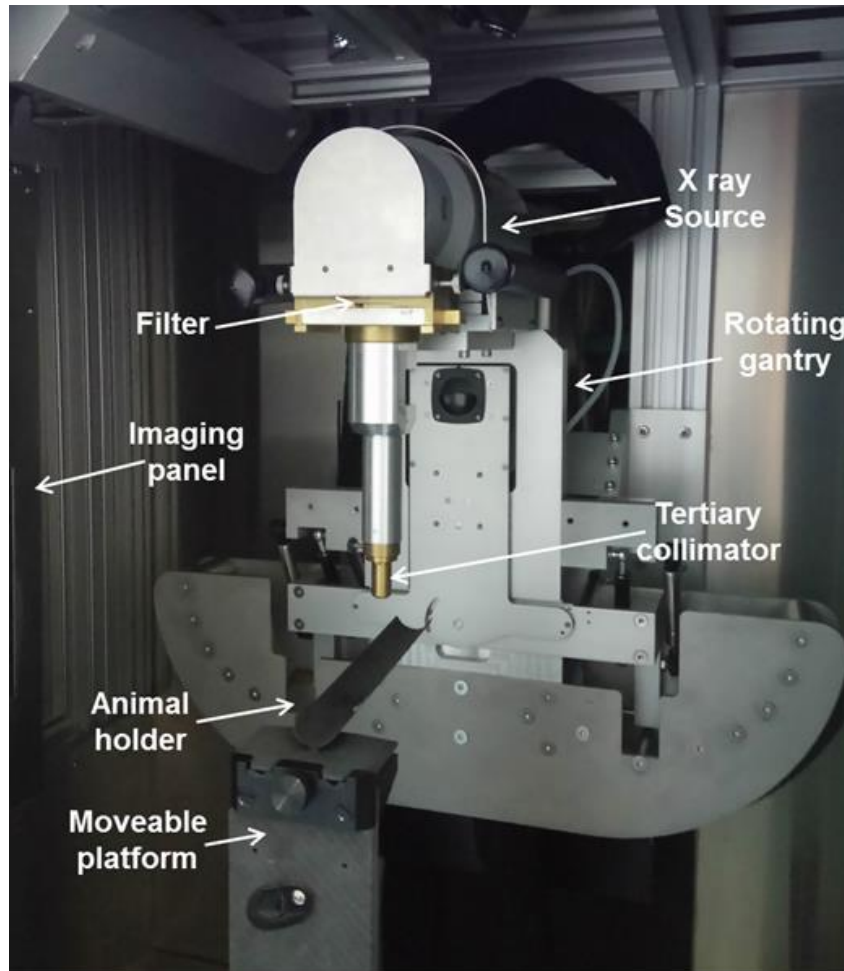
Figure 2.1.1. The Small Animal Radiation Research Platform (Xstrahl, Ltd).
With the aim of reflecting human radiotherapy, the Small Animal Radiation Research Platform (SARRP) has a rotating gantry, image guidance and moveable platform, all controlled through an accompanying treatment planning system.

2.1.4.1. Facilities

To achieve appropriate field sizes for small animals these machines should aim to achieve submillimetre field sizes, which introduces strict tolerances on the mechanical accuracy of the machine. For example the microRT device developed by Kiehl *et al.* (97) can produce conformal beams with an accuracy of ±0.2 mm. Once submillimetre field sizes are routinely implemented it may be necessary to introduce higher resolution detectors, such as diamond detectors, into the QA

procedures. The ability to accurately target the tumour, whilst sparing normal tissue, is the main goal of radiotherapy. One way to achieve optimal conformation is the use of a multi-leaf collimator that can create intricate shapes to best fit the tumour area. Until recently, small animal irradiators achieve this by the use of multiple fixed-shape collimators that are manually changed during the treatment. Cho *et al.* (96) developed a variable rectangular collimator suitable for use on the SARRP creating a dose painting effect using a series of rectangular geometries. The main limiting factor when using submillimetre field sizes is the reduction of dose rate meaning a suggested minimum of 20 cGy/min may not always be achievable. For example, at a depth of 6.15 cm, using a 0.5 mm diameter field size peak dose rates of 18.7 cGy/min and 10.9 cGy/min were achieved by Tryggestad *et al.* (98) at 34 cm and 38 cm SSD respectively, but all measurements at shallower depths achieved dose rates of above 20 cGy/min. Also reflecting current clinical practice, it should be possible to target the model from a variety of angles, or as a continuous arc treatment.

2.1.4.1.1. Target platform

For repeatable experiments, fractionated schedules and efficient use, small animal units have a motorised positioning stage that may be equipped differently for specific purposes using either individual restraining devices or removable carbon fibre animal beds (60). These platforms can move in the X, Y and Z directions and rotate 360˚ (99). An adapted couch with acrylic dividers can be used to facilitate multiple animals/phantoms, increasing throughput, improving immobilisation and facilitating positioning for thoracic, abdominal and brain irradiation (88). As with human RT, immobilisation devices have been developed to allow better targeted irradiation for more focused treatment such as stereotactic cranial irradiation (95). McCarroll *et al.* (100) created a 3D printed immobilisation device, specifically based on the CT scan of a mouse to reduce animal motion during irradiation and allow for accurate and reproducible positioning. However, this extension of the moveable platform must be rigidly attached to prevent additional motion when rotating the stage. Furthermore, the use of immobilisation devices will likely increase treatment time which is something that must be considered both from experimental throughput and animal welfare points of view, particularly where animals are anesthetised.

2.1.4.1.2. Imaging and tissue segmentation

Treatment plans have been numerically simulated on patients' CT scans for decades and image guidance is the standard of care in the clinic. Modern small animal irradiators now mimic this workflow (64). Schneider *et al.* (101) originally

proposed the method by which to derive the elemental composition of a material from its CT data. It uses the Jackson and Hawkes equation to relate CT number, physical density and atomic number from the CT images of known materials. Noblet *et al.* (78) proposed using this method of tissue segmentation as a means to calculate absorbed dose. They used Monte Carlo methods to calculate absorbed dose in 5 x 5 x 0.5 cm blocks of tissues simulated using data from International Commission on Radiation Units and Measurements (ICRU) reports 44 & 46, irradiation used a 5mm diameter circular beam at 225 kVp. Validation was performed using EBT3 Gafchromic film placed underneath cylinders of TEMs, also irradiated at 225 kVp. A gamma analysis performed to compare the dose measurements between the EBT3 film (reference) and Monte Carlo result. The authors conclude that this method shows satisfactory results at the energies used (78). Nevertheless, using CT numbers to distinguish between air, lung, muscle and bone, may not be as accurate as required causing incorrect segmentation and inaccurate dose measurements. Compared to clinical energies, Verhaegen *et al.* (99) suggests that at the lower energies (220 kV) differences of dose measurement could reach 40% if tissue segmentation is inaccurate but at 6 or 15 MV the same misalignment would lead to <10%.

For image guidance, micro-CT devices with smaller apertures and smaller X-ray tubes are available, working in the same way as standard CT scanners. Most small animal irradiators provide CBCT via a rotating turntable, a fixed source and amorphous Si flat-panel detector, whereby the mouse is rotated to create the desired image (64,67). Some models may have a second imaging system to acquire projection images to evaluate the movement of the stage and feasibility of the rotation for the CBCT or to confirm detector positioning (88,99).

2.1.4.1.3. Treatment planning system
As with clinical RT treatment plans defining beam directions, collimation, and dose are developed on CT images. The planning images are typically acquired using the irradiator's on-board CBCT system which may be used to distinguish internal structures or identify fiducial markers placed in tumours to allow precise targeting (64). CBCT imaging has intrinsically poorer image quality than diagnostic images. For this reason alternative modalities such as bioluminescence imaging, magnetic resonance imaging and standard CT can also be utilised in the treatment planning process (95).

Rutherford *et al.* (102) evaluated the capability of the SARRP to deliver clinically-relevant treatment plans with the primary objective of assessing organ at risk sparing. Four treatment plans were compared, a parallel opposed pair, a single beam, single plane arcs and couch rotation arcs. All plans provided acceptable tumour coverage with varying levels of dose outside the target region suggesting plan selection should be dictated by normal tissue toxicity and the end point of the study. The authors conclude by highlighting the limited collimation geometries currently available on the SARRP, restricting the conformity of treatment delivery (102).

However, there are further developments still required. Treatment planning system (TPS) commissioning is still problematic and rigorous validation using anatomically realistic phantoms should be undertaken as it is in the clinic. There is still more research needed on photon scatter at kV energies and when using narrow beams. Furthermore, some TPSs still rely on bulk density overrides from tissue segmentations that both increases dependence on their accuracy and masks the heterogeneity effects that will affect the actual dose delivered (72,103). Monte Carlo codes (FLUKA or GEANT4) are being incorporated into TPSs to try and improve upon dose modelling quality (103).

2.1.4.2. Quality assurance

As discussed in our introduction, lack of QA of irradiation facilities in radiobiology labs risks undermining much of the subject's foundation. One of the core principles of the scientific method is open reporting and repeatability of experiments. Without accurate knowledge of the doses delivered in experiments this principle is put at risk. The unique design of scaled down components in small animal units require specialised tools and methods for robust QA to ensure the dosimetry matches the clinically-relevant treatment delivery and treatment planning (104). There are many potential sources for error that may have a significant impact on dose accuracy, wrong external filter or tertiary collimator selection, misalignment of the beam and stage or animal motion so an accurate reading of delivered dose is of major importance to ensure reliability (105). Most common daily output measurements of the SARRP are completed with a solid water phantom and an ionisation chamber. However, unless multiple points are measured this does not provide information about the distribution of the beam. One phantom design currently recommended for the QA of the SARRP is the Mousefet phantom as designed by Ngwa *et al.* (104), which is particularly useful as it can be used for the verification of both the imaging and irradiation apparatus as it has an arrangement of metal oxide semiconductor

57

field effect transistors (MOSFET) detectors within the 3D phantom. However this is very reliant on accurate positioning when using small beams as it is easy to place a detector at the field edge by accident. TLDs and the electronic portal imaging device (EPID) on the SARRP have also been used for QA measurements (106,107). Scintillating fibre dosimeters allow direct-reading point measurements and have been used to assess surface dose of both phantoms and animals with good agreements between measured and prescribed dose (<4% and <9% respectively). One of the challenges with obtaining accurate and precise dosimetry measurements is the positioning and sizes of the detectors in beams smaller than 5 mm (105).

Phantoms can be designed to perform daily, monthly and annual QA (108). Examples include the ball bearing phantom to ensure accurate mechanical alignment, a quick procedure undertaken regularly, and the exhaustive beam quality tests using solid water slabs (60 x 60 x 5 mm), described below, using for commissioning and annual system checks of the SARRP platform. Whilst such approaches can be used to assure beam quality and systems' geometric accuracy, they cannot assure the quality of the delivered prescription – such assessments require end-to-end testing, often using anatomically realistic phantoms. Undertaking such testing is deterred by a lack of dosimetric expertise or restricted access to appropriate calibrated equipment. This problem can be partially addressed by the provision of equipment designed for the purpose, but will also require a greater investment in acquiring the necessary skills – either through appropriate training of laboratory staff, or through collaboration with medical physics departments where the skill base already exists.

2.1.4.3. Commissioning the Small Animal Radiation Research Platform
The commissioning of an irradiator should allow the characterisation of dosimetric properties such that the dose delivered is accurate within 5% (109). For the commissioning of the SARRP platform, Gafchromic EBT film, calibrated relative to an ion chamber at different exposures, is sandwiched between fifteen layers of solid water 5 mm thick at specified intervals (Figure 2.1.2) (98). The jig holding the solid water slabs in place has the ability to move along an axis to allow variable SSD measurements, between 32 and 38 cm (5 mm increments). This set up allows an accurate assessment of percentage depth dose (PDD) in addition to the flatness, symmetry and penumbra of the beam profile. Each brass collimator must be individually assessed using this set up (98). As discussed above, whilst this process ensures that the beam quality is within tolerance, it does not test for the myriad of other errors that can occur in the experimental workflow. It is vital that not only is

each step quality assured in its own right, but that the whole process is also tested end-to-end.
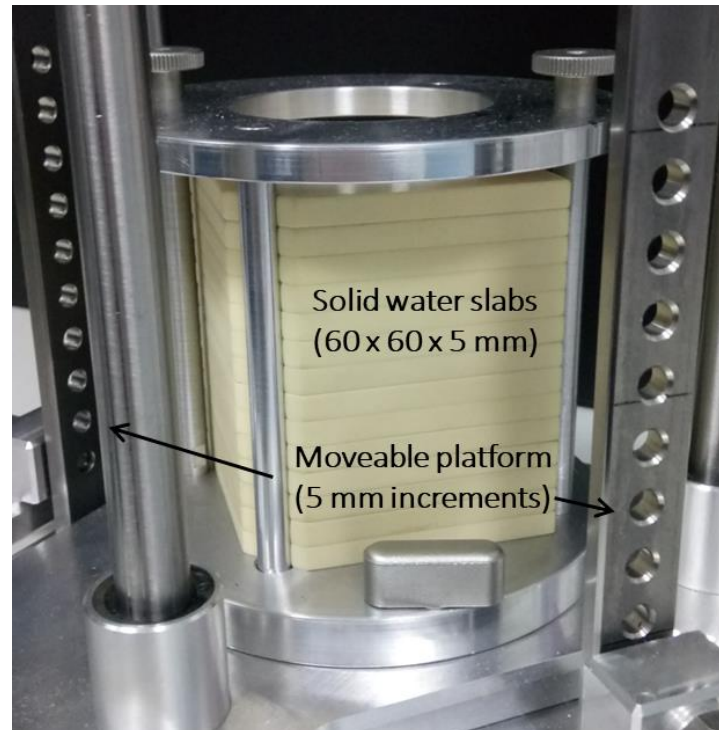
Figure 2.1.2. The Small Animal Radiation Research Platform (Xstrahl, Ltd) commissioning jig.

Solid water slabs 60 x 60 x 5 cm are arranged in a stack to create a phantom appropriate to incorporate layers of film at defined intervals to take measurements of dose to create a depth dose profile.

2.1.5. Conclusions

We have highlighted the potentially serious problems that the lack of rigorous quality assurance in pre-clinical radiation research can, and possibly has, caused. Not only is scientific quality at risk, we are ethically obliged to ensure that the data from each animal used in scientific research is fit for purpose and contributes to progress. Initiatives to address some of these problems have already been started, but there is still work to be done.

We have discussed developments in the QA of individual steps of the workflow in small animal irradiators. However, much of this work takes place at individual institutes with limited collaboration. There is a need for the whole international community to come to a consensus and adopt standardised QA protocols and

equipment. By combining biologically-relevant phantoms with the latest developments in detector technology it will be possible to conduct rigorous end-to-end tests from initial imaging and plan development, through image guidance, to treatment delivery. One of the first steps on the path to standardisation is to better understand the problem. We propose building on the work of Pedersen *et al.* (68) by undertaking audits using state-of-the-art phantom technology referenced to a national standard.

Developing rigorous QA protocols will drive quality, reducing dosimetric uncertainties, and, importantly, ensuring each animal used in experiment is contributing to scientific progress. Accurate treatment planning, precision targeting and arc irradiations will further close the gap between the techniques seen in the clinical and pre-clinical settings. The development of new therapies is reliant on pre-clinical experiments. However, only a third of animal research continues on to human randomised trials (110). If experiments do not reflect the clinical reality there is risk that results will not be translatable. By ensuring a close match between the pre-clinical and clinical radiation treatments this risk will be reduced (110). Increased used of precision irradiators, coupled with a concerted effort to adopt standardised QA procedures will be a large step in this direction.

Funding

2.2. Methods

2.2.1. Phantom material development

The development of the tissue-equivalent phantom used throughout this section is documented by Price *et al.* (1). To manufacture a zoomorphic phantom suitable for dosimetry applications the material composition must have radiation properties (mass and electron density) and physical characteristics identical to the tissue it is mimicking (91). The three fundamental tissues to mimic, due to their contrasting densities, are soft tissue, bone and lungs. In the first instance, voids were incorporated in the design in the place of lungs due to the similarity to the mass attenuation of air at medium X-ray energies. Acrylonitrile butadiene styrene (ABS) is a commonly used 3D printing plastic and has the appropriate physical density and mass attenuation to be a suitable soft tissue substitute. To create a bespoke 3D printing filament for the skeleton substitute doping powders can be added at an appropriate ratio to achieve the desired mass attenuation profile of bone, yet limited (<20%) such that the material is predominantly ABS remaining suitable for 3D printing. The end result was an ABS-CaTiO$_3$ blend with a <6.6% difference in mass attenuation compared to the ICRU report 44 standard (1).

2.2.2. Phantom designs

The phantom is based on a 20-25 g nude mouse imaged using the on board CBCT facilities of a SARRP. The image was segmented into the soft tissue, bone and lungs components using simple connected thresholding and exported as stereolithography (STL) files for modification and printing. Meshmixer (http://www.meshmixer.com) and Autodesk Netfabb (https://www.autodesk.co.uk/products/netfabb/overview) were used to create phantom designs to hold Gafchromic EBT3 film alone in various orientations (Chapter 2.3) or in combination with alanine pellets to complete a national dosimetry audit (Chapter 2.4).

Manufacturing phantoms using 3D printing permits the creation of models capable of assessing dose in 1D, 2D, or 3D, using an array of point detectors, such as thermoluminescent detectors (TLDs), film or dosimetry gel, respectively. For delicate TLDs it may be necessary to create a separate central slice to hold the 3 x 3 x 1 mm detectors in an array throughout the phantom model to facilitate the insertion and removal of the detectors. This was created by using the plane cut feature to slice the model into 3 sections with the central slice the same thickness

as the TLDs (1 mm). Boolean operations were then performed to remove portions of the central slice (centre of Figure 2.2.1) to create the voids to hold the detectors.
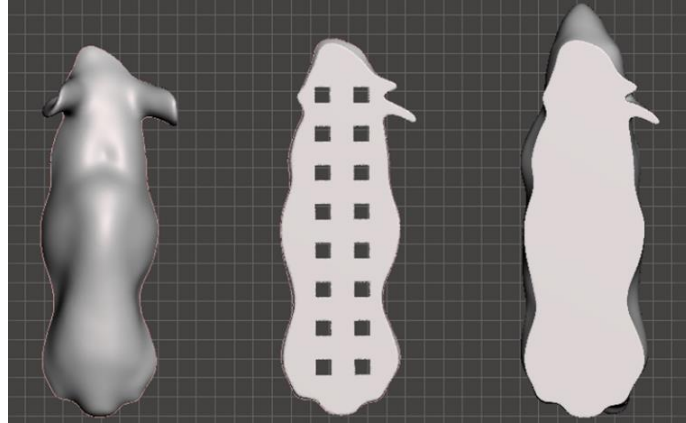
Figure 2.2.1. The phantom to hold an array of thermoluminescent detectors (TLDs). The mouse soft tissue STL file was imported into Meshmixer (Autodesk Inc.) and sliced into three sections, the central slice being the same depth as the 1 mm TLDs. A cuboid shape 3.2 x 3.2 x 2 mm was also created to represent the TLDs. All files were exported separately. The central slice and TLD replicate were then imported into Netfabb (Autodesk Inc.) and the cuboid subsequently removed from the slice using a Boolean operation to create 16 voids for the TLDs.

Radiochromic films are a well-established tool for radiation dosimetry, owing to favourable characteristics such as high spatial resolution, minimal energy dependence and almost tissue equivalence (111,112). Gafchromic EBT3 films present a symmetrical structure with an active layer sandwiched between layers of polyester. Upon exposure to ionising radiation, charged particles initialise polymerisation of di-acetylene monomers within this active layer causing a colour change to the film – optical density (112). Including film within a phantom provides a 2D dose distribution assessment across the target field. To ensure accurate positioning and to minimise air gaps between the phantom and the film it may be necessary to include pegs or slots within the phantom design (Figure 2.2.2).

a

b

c
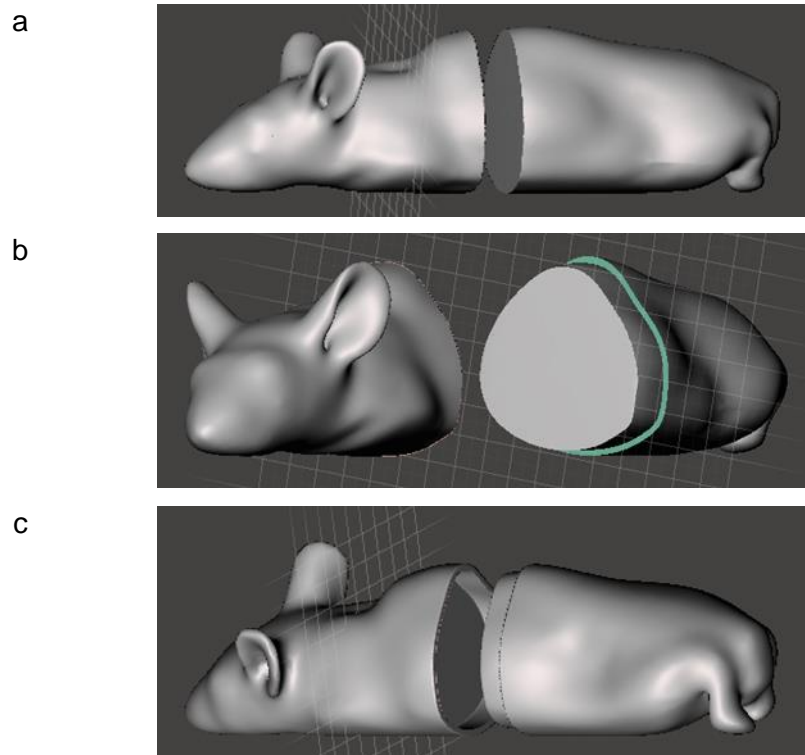
Figure 2.2.2. The phantom split down the axial plane in a slot design to hold film. To create a phantom to hold Gafchromic EBT3 film in the axial plane the STL file of the body is divide into 4 components: front, back and two central sections. a) Using the plane cut feature in Meshmixer, the phantom was split down the central axial plane creating the front and back of the phantom. b) A 5 mm section from the back of the phantom is cut and reduced by 1.5 mm in the x and y axis to create the inner section. c) This central section is duplicated, the size increased by 0.25 mm in the x and y axis and removed from the front half. Using a larger section ensures a smooth fit for the inner section.

The complex geometry and close proximity of the spine to the outer edge of the mouse makes it difficult to create a slot extending around the whole phantom, as depicted in Figure 2.2.2, in a sagittal or coronal model. To hold film in these planes it may be more appropriate to use pegs located away from the region of interest (Figure 2.2.3).

Figure 2.2.3. Sagittal and coronal plane cut models to hold film.
The complex geometry of the external body contour made it difficult to create a slot design to secure film in place therefore cylindrical pegs (3 mm diameter, 5 mm length) were added to the design. Slightly wider cylinders (3.25 mm diameter) were removed from the opposing side to account for any warping during printing that would prevent a smooth fit.

Polymer gel dosimetry captures a 3D representation of the dose distribution due to the polymerisation of the active substances within the gel by free radical generation after irradiation (113). The amount of polymerisation is directly proportional to the amount of local radiation dose. The degree of polymerization, and corresponding changes in the physical properties of the gel can then be detected using various imaging modalities (113). To accommodate gel within a phantom hollow models were created by using the hollow function in Meshmixer, with an offset of 2 mm to ensure the printed structure is complete to prevent the gel leaking. The new inner section was removed from the body, creating a hollow phantom (Figure 2.2.4a). To decant the gel into the phantom a cylinder (9 mm diameter) was added to the highest point of the hollow area and extended through the shell. A second cylinder (7 mm diameter) was removed from the centre of the first cylinder creating the opening (Figure 2.2.4b). To avoid collapsing during printing, a support structure was printed internally using dissolvable polyvinyl alcohol (PVA) plastic.

a

b
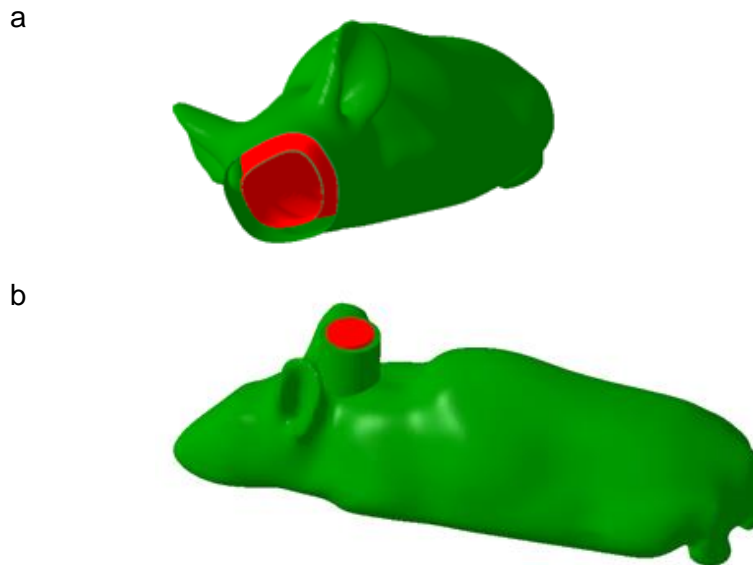
Figure 2.2.4. Hollow phantoms to hold dosimetry gel.

a) The body of the phantom was reduced by 2 mm and removed from the original body model. An offset of 2 mm ensures the shell is stable after printing to prevent the gel leaking out. b) To add the gel a cylinder was created above the brain – the region of interest. To create the insert, two cylinders (9 mm diameter and 10 mm length and 9 mm diameter and length) are placed through the mouse to reach the empty inner cavity. Using the Boolean tool the smaller cylinder is removed from the larger cylinder and the remaining cylinder attached to the phantom contour.

All prototype STL files were exported from Netfabb and converted into a gcode output, readable by the printer, using the Ultimaker Cura software (Ultimaker BV). The advantage of 3D printing a mouse phantom is there is little manual intervention required once the printing has begun. The solid models for film dosimetry took approximately 11 hours and the gel dosimetry hollow models were complete in around 2 hours. However, the hollow models required additional time after printing to dissolve the internal PVA support structure. The hollow models appear to have printed correctly from the outside but, if internal structure such as the skeleton are included, it may be useful to image these prior to use to assess the completed design. The models, or the shell of the hollow models, were printed with 100% infill density and 0.1 mm layer thickness using an Ultimaker 3 3D printer loaded with a Polylactic acid (PLA, RS Components Ltd.) filament.

2.3. RESULTS: VALIDATION OF A BESPOKE 3D PRINTED PRECLINICAL DOSIMETRY PHANTOM USING A SMALL ANIMAL RADIATION RESEARCH PLATFORM

Summary

This chapter describes the commissioning process performed on the Small Animal Radiation Research Platform (SARRP) in the Wolfson Molecular Imaging Centre at The University of Manchester. The commissioning procedure of an irradiator is usually performed upon installation and provides reference measurements to accurately set up the beam model within the treatment planning system (TPS). This SARRP was installed in 2014 so this procedure had previously been completed, but since then limited dosimetry quality assurance measurements had been performed so it was deemed necessary to repeat the commissioning to ensure accurate dosimetry, traceable to the national primary standard, for subsequent phantom measurements.

Following the commissioning of the SARRP, various phantoms were designed, based on the files made available by Price *et al.* (1), and printed to measure radiation dose using Gafchromic EBT3 film on this SARRP. Prior to each experiment, radiation output measurements were performed (Appendix 1, Figure A1.1) with a Farmer type ionisation chamber model TM300 10-10 (PTW Freiburg), calibrated against the secondary standard at The Christie NHS Foundation Trust, and the accuracy of the image guidance and TPS tested using a ball bearing phantom. Several measurements were performed to establish the use of the phantom on the SARRP, testing the image guidance, treatment planning, radiation delivery and subsequent local gamma analysis procedures, and to determine the attenuation effects of the heterogeneous density model. Measurements were also performed to test the protocol for a proposed multicentre dosimetry audit, including a more complex arc irradiation scenario.

Author contributions

As per the commissioning protocol, both A. Aitkenhead and I performed all the measurements for the SARRP commissioning, and the phantom validation. I scanned all the Gafchromic EBT3 films for the commissioning and phantom measurements and A. Aitkenhead generated the film calibration and the depth-dose curves, and performed the local gamma analyses.

VALIDATION OF A BESPOKE 3D PRINTED PRECLINICAL DOSIMETRY PHANTOM USING A SMALL ANIMAL RADIATION RESEARCH PLATFORM

Emma R. Biglin[1], Adam H. Aitkenhead[1,2], Gareth J. Price[1,3], Amy L. Chadwick[1,3], Kaye J. Williams[4], and Karen J. Kirkby[1,3]

[1]Division of Cancer Sciences, Faculty of Biology, Medicine and Health, University of Manchester, Manchester, UK. [2]Christie Medical Physics and Engineering. The Christie NHS Foundation Trust, Manchester, UK. [3]The Christie NHS Foundation Trust, Manchester, UK. [4]Division of Pharmacy and Optometry, Faculty of Biology, Medicine and Health, University of Manchester, Manchester, UK.

Abstract

Improvements in preclinical radiation research have been made to better mimic the equipment and techniques implemented in the clinic. The development of dedicated small animal radiation units facilitates such advances by combining treatment planning, image guidance and conformal delivery. One area significantly behind its clinical equivalent is standardised dosimetry quality assurance (QA) protocols, hampering the translatability of results into the development of clinical interventions. One potential solution is the addition of a zoomorphic phantom, holding appropriate detectors, to QA procedures. A fully commissioned Small Animal Radiation Research Platform (SARRP) was used to irradiate 3D printed murine phantoms, in combination with Gafchromic EBT3 film, in a series of static and arc irradiations. Differences between planned and delivered dose distributions, and the impact of a higher density bone-equivalent material were examined. The main difference between the film measurement and the planned dose distribution was around the field edges, a sharp dose gradient in the plan compared to a blurring effect seen on the film. These measurements demonstrate that film-based dosimetry using the presented phantom can be used to assess pre-clinical dose distributions. Expansion of this work could include the incorporation of point detectors to provide measurements of absolute dose.

2.3.1. Introduction

The use of mice models in research is well-established owing to their defined genetic strains, efficiency of breeding and housing, and relative physiologic similarity to humans (114,115). The development of small animal irradiators has extended the utility of small animal models to the field of radiation research, particularly over the last decade when clinically-relevant radiation platforms became commercially available. The Small Animal Radiation Research Platform (SARRP, Xstrahl, Walsall, UK, see Section 2.2, Figure 2.2.1) was designed to mimic clinical radiotherapy systems with on-board image guidance and treatment planning capabilities. With gantry and couch rotations of 360 degrees, high quality conformal radiotherapy plans can be delivered on such platforms to an accuracy of 0.2 mm and 5% of the dose prescribed (64). Due to the physical size of the target, irradiations are in the kilovoltage (kV) energy range, rather than the higher energy megavoltage X-rays used to treat humans, reducing the effect of insufficient surface dose, hotspots at depth and scatter, and permits the combination of both irradiation and imaging on the same platform (67). Cone beam computed tomography (CBCT) scans are captured on the SARRP platform allowing animals to be treated using an image-guided radiotherapy (IGRT) approach (64). The motorised stage allows accurate positioning and is equipped for various set ups requiring specific immobilisation. For efficiency, an adapted couch with acrylic dividers can be used to facilitate immobilisation and positioning in multiple subjects (88).

Concurrent to the development of these machines, there has been a focus on the lack of standardised dosimetry in small animal irradiation experiments (63). The lack of standards impacts the accuracy, reproducibility and overall quality of results produced because of questionable dosimetry. Stringent quality assurance (QA) protocols have been developed for clinical systems and should be adapted for use with small animal irradiators (70). Because of its unique design, it is important the SARRP has a detailed QA regime with specialised equipment. Most measurements of the radiation dose output are taken using an ionisation chamber within a solid water phantom, alongside specifically designed ball bearing phantoms used for the analysis of the imaging and targeting accuracy. Ngwa *et al.* (104) have developed a phantom using MOSFET (metal oxide semiconductor field effect transistor) detectors to analyse both the treatment delivery and imaging features simultaneously, increasing efficiency. The SARRP commissioning phantom (see Section 2.2, Figure 2.2.2) has been adapted by Jermoumi *et al.* (108), to include additional MOSFETs and optically-stimulated luminescent detectors (OSLDs) within

the slabs. Further advances in technology include the development of realistic dosimetry phantoms, moving from basic cylindrical shapes to more sophisticated geometries (76), facilitated by the increasing popularity of 3D printing (1,84,86,87,116). These devices facilitate end-to-end testing of the experimental pathway, including animal imaging, treatment planning system (TPS) calculations of dose and dose distribution in a complex and realistic 3D volume, and radiation delivery.

This chapter documents the commissioning of the SARRP and the optimisation of the heterogeneous mouse phantom developed by Price *et al.* (1), for use in preclinical dosimetry. This bespoke tissue-equivalent phantom was developed to standardise the imaging, treatment planning and radiation delivery QA processes of precision small animal radiotherapy platforms. In this report, multiple designs of the phantom were 3D printed to incorporate Gafchromic EBT3 film, capturing measurements of the 2D dose distribution to determine the suitability of the phantom to perform such measurements.

2.3.2. Methods

2.3.2.1. Radiation procedure

Unless otherwise stated, all irradiations were performed using a SARRP X-ray system with the source settings 220 kVp and 13 mA, with a broad focus field and a 0.15 mm Cu filter. The half value layer for this system is 0.67 mm Cu. To aid in the development of treatment plans, CBCT images were acquired, using source settings of 60 kVp, 0.8 mA and a 1 mm Al filter, with the gantry positioned at 90° while the motorised stage rotated the phantom 180°.

2.3.2.2. Commissioning of the SARRP

The commissioning procedure followed the protocol outlined by Tryggestad *et al.* (98). The SARRP dose output under reference conditions was measured using a Farmer-type ionisation chamber model TM300 10-10 (PTW Freiburg), calibrated with reference to the national primary standard. The American Association of Physicists in Medicine (AAPM) Task Group report 61 converts this reading into the dose output and the dose rate for this system, used to calculate the exposure times to generate a batch-specific Gafchromic EBT3 film (Vertec Scientific Ltd.) calibration curve. For full therapeutic commissioning, each available collimator requires depth dose characterisation over three separate source-to-surface distances (SSDs) to accurately set up the beam model within the Muriplan TPS.

2.3.2.2.1. Gafchromic EBT3 film calibration

The ionisation chamber described above was used to determine the SARRP dose output under reference conditions and to generate a calibration curve for the Gafchromic EBT3 film. X-ray radiation was delivered using the standard SARRP settings (outlined in Section 2.3.2.1) to an arrangement of solid water, creating a SSD of 33 cm, 2cm build up and 3 cm backscatter. The chamber was irradiated with a broad focal spot for 60 seconds, and the reading from the connected electrometer was converted to the SARRP dose rate using the formula depicted in the AAPM Task Group report 61 (80, Appendix 1, Table A1.1). This dose rate was used to calculate the timing exposures for which 18 films were separately irradiated at doses of 0, 40, 80, 120 160, 200, 250, 300, 350, 400, 450, 500, 550, 600, 650, 700, 800, 900 cGy, using the same solid water arrangement as the ionisation chamber measurement (Appendix 1, Table A1.2). This generates a calibration curve for this specific batch of film to convert optical density, a quantification of the film darkening, to dose (see below).

2.3.2.2.2. Depth dose measurements

The SARRP commissioning jig (see Section 2.2, Figure 2.2.2) provides a configuration of solid water slabs (60 x 60 x 5 mm each) to determine the depth-dose profiles for each of the tertiary collimators (Figure 2.3.1). Each collimator (10 x 10 mm, 5 x 5 mm, 3 x 3 mm, 3 x 9 mm and 1 mm and 0.5 mm diameter circles) was used to irradiate Gafchromic EBT3 film positioned at depths of 5, 10, 15, 20, 30, 40, 50 and 70 mm. These exact depths do not account for the additional thickness of the films (0.28 mm each) inserted between each layer. Each collimator was irradiated using three independent set ups to account for different SSDs (31, 34 and 38 cm). The standard irradiation settings, described above, were used to irradiate the films for 90 seconds. Irradiation using the 0.5 mm diameter circular collimator was repeated using settings: 480 seconds, 220 kVp, 3 mA, and a fine focus.

Figure 2.3.1. The standard tertiary collimators for use on the Small Animal Radiation Research Platform (SARRP).

The six standard brass tertiary collimators for use on the SARRP permit field sizes of 3 x 9 mm, 10 x 10 mm, 1 mm and 0.5 mm diameter circles, 3 x 3 mm and 5 x 5 mm (clockwise from top left).

2.3.2.3. Designing the phantoms to hold Gafchromic EBT3 film

The stereolithography (STL) files used to develop the phantoms described in this report can be found within Price *et al.* (1). To modify the phantom, computer aided design software Meshmixer (Autodesk Inc.) and Netfabb (Autodesk Inc.) was used.

To create phantoms to hold Gafchromic EBT3 film, the appropriate STL files: i) body, bones and lungs or ii) body and lungs, herein referred to as the heterogeneous and homogeneous density models respectively, were imported into Meshmixer. Using the "plane cut" feature, the model could be sliced in the desired location and orientation. To permit the simultaneous printing of each part, each segment was imported into Netfabb and joined using the Boolean operation tool to create the final design.

To secure the Gafchromic EBT3 film in a reproducible position, and to hold the two sections of each phantom together, the designs to create the phantom for the proposed preclinical dosimetry audit incorporated pegs. The pegs were created in Meshmixer, 5 mm in length and 3 mm in diameter and joined to the bottom section of the phantom in Netfabb. Three additional pegs 5 mm in length and 3.25 mm diameter were removed from the top half to form slightly larger holes, to ensure a smooth fit. To ensure the film was securely held around the pegs in these models,

and to aid in locating the irradiation field during analysis, the film was laser cut using the outline of the appropriate plane in the phantom exported from Netfabb.

2.3.2.4. Creating the phantoms using 3D printing

The final STL files were converted into a gcode output using the Ultimaker Cura software (Ultimaker BV). Cura allows the exact positioning on the 3D printer plate to be determined, confirmation of the materials in the 3D printer heads and sets the printing parameters. The phantoms were positioned on the printing plate so that the least amount of support material was required, the infill density used for all models was 100% and the layer thickness for printing was 0.1 mm.

An Ultimaker 3 (Ultimaker BV) fused deposition modelling 3D printer was used to print the phantoms. All homogeneous density phantoms were printed using Polylactic acid (PLA, RS Components Ltd.). The details for the exact composition and validation of the materials used to create the tissue-equivalent phantoms are described by Price *et al.* (1). The printing of these heterogeneous density phantoms used a dual extrusion print head to combine the commercially available acrylonitrile butadiene styrene (ABS, density of 1.07 g/cm^3) plastic for the soft tissue body, with ABS filament doped with $CaTiO_3$ (density of 1.27 g/cm^3) for the skeleton (1). All models substitute the lungs as an air gap incorporated into the design.

2.3.2.5. Phantom measurements

The mouse phantom, including Gafchromic EBT3 film, was imaged using the SARRP platform CBCT system and a treatment plan developed on the resulting image using the SARRP Muriplan TPS. As per the standard SARRP operating procedure, each component of the phantom (soft tissue, lung and bones) were segmented using pixel intensity thresholding and the standard bulk density overrides were applied. All measurements were performed with the standard SARRP imaging and irradiation settings, as noted above.

Figure 2.3.2 depicts the beam angles for the six phantom tests. The sequence of measurements involved testing the equipment and the Muriplan TPS with a homogeneous density phantom, then examining the higher density bone material by targeting the spine, brain and pelvis and, finally, a more complex arc beam arrangement with the intention of simulating the irradiation of one half of the mouse brain. The use of the phantoms split in the sagittal plane permits the beam delivery immediately following the acquisition of a CBCT without movement from the gantry which may cause a minor adjustment of the positioning of the phantom. The coronal phantom was implemented in the audit measurements to facilitate the delivery of an

arc beam across the brain. The 10 x 10 mm collimator was chosen to ensure coverage of both the soft tissue and bone equivalent densities within the same field. A 5 x 5 mm collimator was chosen for the arc delivery in line with similar *in vivo* experiments being performed in this laboratory.
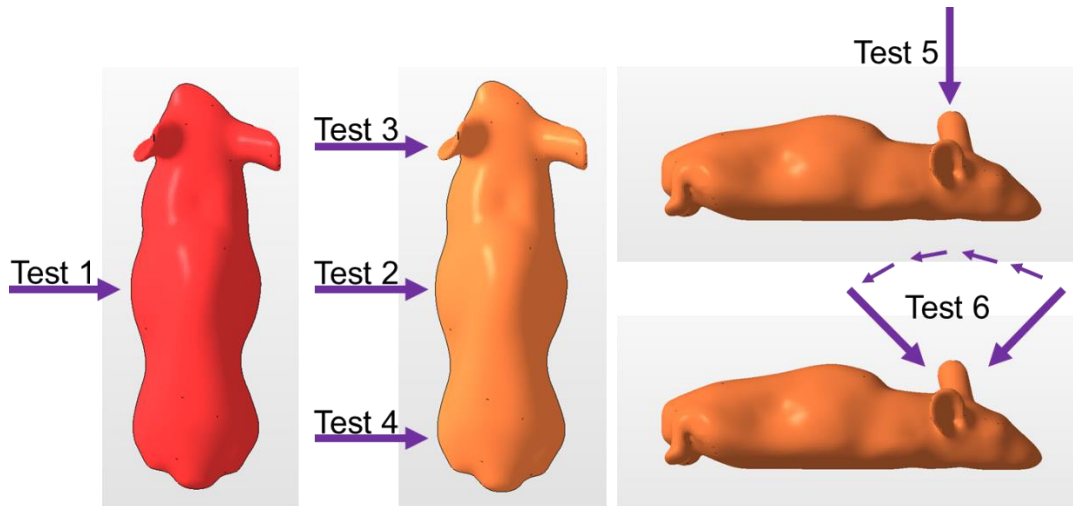
Figure 2.3.2. The beam arrangements for each of the six phantom measurements. The red mouse indicates the homogeneous density model, while the orange phantom represents the heterogeneous density model 3D printed with soft tissue and bone-equivalent materials. The purple arrows depict the beam angle for each of the six irradiations. The first test investigated the suitability of using the dosimetry phantom on the SARRP. Tests 2, 3, and 4 assessed the attenuation of the bone-equivalent material, irradiating through the spine, brain and pelvis. The final tests were to optimise the proposed audit procedure. All measurements were performed using a 10 x 10 mm collimator, with the exception of the arc irradiation which was 5 x 5 mm.

2.3.2.5.1. End-to-end test of the proposed phantom on the SARRP

To determine the suitability of the phantom for use as a dosimetry tool on the SARRP, an end–to-end test using the homogeneous density model was performed. This basic phantom, without the inclusion of tissue-equivalent materials, was chosen as this was a test of the set up, treatment planning, radiation delivery and film analysis processes and therefore the zoomorphic phantom was not required.

In this case, the phantom was split down the central sagittal plane, Gafchromic EBT3 film was taped in place and the external body contour marked on the film as a point of reference for later analysis. Following the acquisition of a CBCT, a treatment

plan delivered a 10 x 10 mm beam of 2 Gy X-rays to the isocentre, set in the film plane, with the gantry and bed angles set to 90° and 0° respectively. Approximately 40 hours later the film was scanned at 72 dpi resolution. This being the first use of the phantom, and a test of the irradiation and analysis procedures, a higher scanning resolution was unnecessary.

2.3.2.5.2. Validation of the heterogeneous densities within the phantom

To determine if the bone-equivalent material has any attenuation effects on the beam when using kilovoltage energy, three scenarios were assessed:

i.   Delivery of a 10 x 10 mm static beam to the spine, with the bed and gantry rotations set to 0° and 90° respectively. A perpendicular beam was used to plan a 6 Gy delivery to an isocentre defined at the film plane, transecting the spine. Approximately 24 hours later the film was scanned at 72, 150 and 300 dpi, to determine the optimal resolution to detect differences across the heterogeneous density.

ii.   Delivery of a 10 x 10 mm field through the brain region of the heterogeneous density phantom, as this contains a higher proportion of the bone-equivalent material. Gafchromic EBT3 dosimetry film was taped between the two halves of a phantom split down the sagittal plane. Using the acquired CBCT scan, Muriplan software was used to set the isocentre to the film plane in a region of the skull. With the bed angled at 0° and the gantry at 90°, 6 Gy was prescribed to the isocentre. The film was scanned more than 24 hours later. Following the results from the previous test this measurement was to detect any potential attenuation from the skull material, therefore a scanning resolution of 72 dpi was used as a higher resolution was unnecessary.

iii. Delivery of a 10 x 10 mm field targeting the pelvis region. Implementing the phantom split centrally along the sagittal plane, Gafchromic EBT3 film was secured with tape and marked with references to the external body contour. Following the acquisition of a CBCT scan, a treatment plan was developed on the resulting image using the Muriplan TPS. With the bed set to 0° rotation and the gantry at an angle of 90°, a 2 Gy delivery was planned to the isocentre defined at the film plane. This was delivered three times to increase the signal to noise ratio (a total dose of 6 Gy). 24 hours after irradiating, the film was scanned at 400 dpi resolution.

2.3.2.5.3. Optimisation of the proposed dosimetry audit procedure

To determine the suitability of the phantom as a standard dosimetry tool across multiple institutions, and the ease of which it could be adopted into practice, a national multicentre dosimetry audit was proposed (see Chapter 2.4 for results). To test the protocol for the proposed audit a heterogeneous density phantom, designed to hold both alanine pellet detectors and Gafchromic EBT3 film, was used. The phantom, split along the central coronal plane, contained a dummy alanine pellet in the brain cavity and laser cut film to cover the whole plane. The dummy pellet was included to ensure there were no air gaps underneath the film and was reused for all measurements. As per the Muriplan TPS, a CBCT image was obtained and the contours for the varying tissue densities were defined and applied (air: 0 - 8799, tissue: 8800 – 13499, bone: 13500 – 65535). For the first measurement, with the bed and gantry at 0°, a static beam collimated to 10 x 10 mm was delivered to the isocentre, set to the centre of the alanine pellet, and a dose of 12 Gy was prescribed. A second measurement was performed, using a 5 x 5 mm collimator, delivering 12 Gy to the centre of the pellet in an arc orientation, from -45° to 45° with the bed at 90°. More than 24 hours after the completion of these measurements, all films were scanned at 150 and 400 dpi in keeping with the proposed dosimetry audit protocol.

2.3.2.6. Gafchromic EBT3 film scanning and analysis

All films (commissioning and measurements) were scanned at least 24 hours after irradiation to allow for the post-irradiation polymerisation of the active layer within the film to stabilise (111). An Epson (Seiko Epson Corporation) 10000XL flatbed scanner in professional mode was used to scan the films without colour corrections, at a bit depth of 16-bits per colour channel (RGB) and a spatial resolution of between 72 and 600 dpi, depending on the experimental end point. Using a lower scanning resolution of 72 dpi has the advantage of a smaller file size and quicker scanning time, without compromising on image quality. A sharper resolution of 400 dpi provides a higher accuracy in dose distribution measurements, but the accuracy of the dose reading is consistent with lower resolutions (118). The scanner surface was wiped clean to avoid artefacts caused by dirt and a frame was used to ensure reliable positioning of the commissioning films, and to prevent Newton's rings artefacts (interference patterns from irregular air gaps between the film and the glass of the scanner bed).

During analysis a scanner-specific uniformity correction was applied to each pixel of the film scans to compensate for variations due scanner non-uniformity issues. The correction factor is dependent on the colour channel, the location of the pixel in relation to the centre of the scanner and the optical density. Using these factors, the correction map for the scanner bed was calculated by scanning films (of known doses) at all positions across the scanning plate.

The calibration curve was plotted based on the following equation:

(1) $\qquad Dose = A \times B^{O.D.} + C$

where A,B and C are the fit parameters and O.D. is the optical density (119).

The gamma index is a useful test in determining differences between planned and measured dose distributions, evaluating both dosimetric and geometric uncertainties (120,121). This tool assesses a combination of two criteria: the percentage dose difference and the distance-to-agreement (DTA), a measurement of distance between points in the dose distribution of the same dose (121). A score of ≤1 indicates the criteria acceptance region (green pixels), the gamma map then indicates the overestimated or underestimated planned doses in red or blue pixels, respectively (122). The gamma analyses were performed using in-house developed Matlab code within an Octave environment (123). The film measurements formed the reference dataset while the dose grids calculated in the planning system formed the evaluation dataset, following the convention described by Low *et al.* (124). The degree of interpolation applied to the evaluation dataset was dependent on the local dose gradient, such that the change in the dose per voxel after interpolation was limited to no greater than half the dose-difference criterion. A higher degree of interpolation can now be applied across steep dose gradients without the need for interpolation at shallow dose gradients (119). The reference data was normalised to the evaluation data, and therefore the gamma analysis was an evaluation of relative dose only. No standard gamma analysis criteria exists, therefore criteria were chosen based on clinical tolerances (119), ideal targeting accuracy (64) and the general consensus that the delivered dose should be in agreement with the planned dose to within a 5% tolerance (125). The choice of analysis criteria varied between measurements to highlight differences across the field, including any attenuation from the higher density bone-equivalent material.

2.3.3. Results

2.3.3.1. Film measurements from the commissioning of the SARRP

Upon installation of an irradiation unit, commissioning measurements are performed to set up the beam model within the TPS. The commissioning for this particular SARRP had previously been performed so the subsequent measurements described herein were used as a reference to provide traceable dosimetry for all future measurements using this machine.

Figure 2.3.3 plots the Gafchromic EBT3 film calibration taken during the commissioning of the SARRP. The calibration curve relates optical density for the red, green and blue colour channels to dose, and the remaining residual errors are shown on the right. The red and green colour channels showed little residual error (<5%) between planned and delivered doses across the dose range, whereas the blue colour channel was the least reliable, regularly exceeding 5% at doses less than 8 Gy, therefore was excluded from the subsequent film analyses.
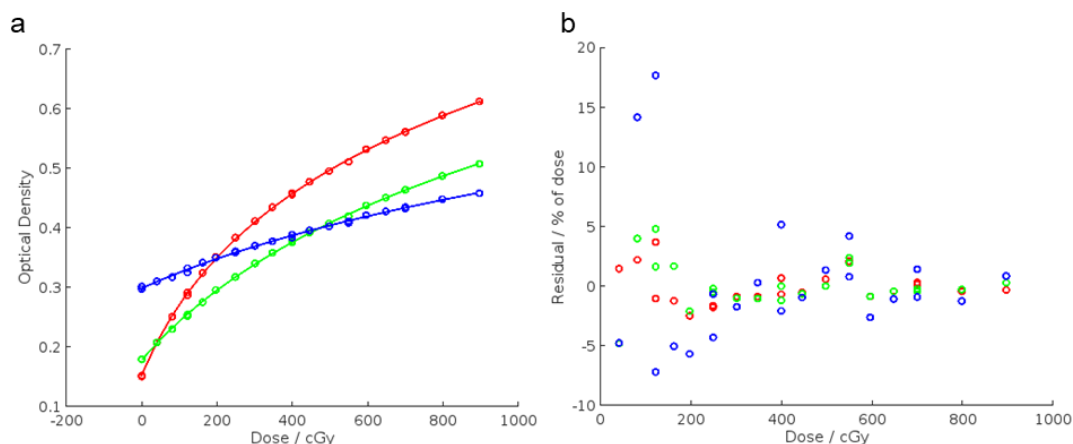
Figure 2.3.3. Film calibration data from the commissioning of the Small Animal Radiation Research Platform (SARRP).

The a) optical density and b) residual errors measured during the SARRP commissioning procedure are presented for the red, green, and blue colour channels, as a function of radiation dose.

The depth-dose profiles for the 10 x 10 mm, 5 x 5 mm, 3 x 3 mm, 3 x 9 mm and 1 mm and 0.5 mm diameter circle collimators, at 30, 34 and 38 cm SSDs, are presented in Figure 2.3.4. To ensure consistent and accurate dose measurements for all irradiations in our lab, all collimators were commissioned as discussed later

the 10 x 10 mm and 5 x 5 mm collimators were employed in the phantom measurements.
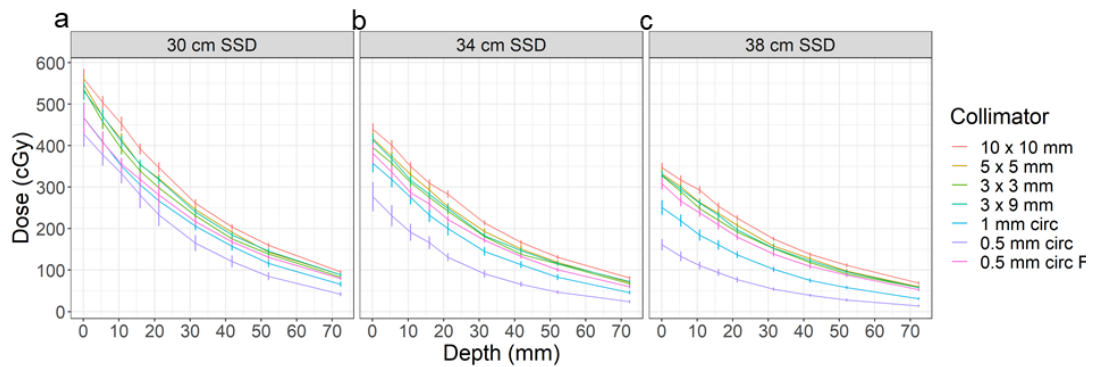
Figure 2.3.4. Depth dose curves for the standard brass collimators used on the Small Animal Radiation Research Platform (SARRP).

Gafchromic EBT3 film was sandwiched between blocks of solid water and separately irradiated at source-to-surface distances of a) 30, b) 34 and c) 38 cm. Each measurement was performed using the standard SARRP irradiation settings (220 kV, 13 mA) for 90 seconds, with the exception of the fine beam focus irradiation using the 0.5 mm circle collimator which was performed with 220 kV and 3 mA for 480 seconds. Data presented shows the median dose ± standard deviation of 78 pixels in the centre of the high dose region for each film measurement (n=1).

2.3.3.2. Development of the 3D printed dosimetry phantom

Table 2.3.2. 3D printed murine phantoms.

	Phantom characteristics	Optimisation	Use
	This phantom incorporated a slot design in the central axial plane to secure film in place. This was the first phantom designed and printed so was a test of the CAD software and 3D printing. The axial orientation was chosen as it was the easiest plane to create a slot design due to the phantom geometry.	To facilitate the printing of the slot, the phantom had to be printed from the slot and insert upwards which caused the ears and feet to warp slightly. This was not an issue here as these phantoms were not used for any experiments however for future designs the printing orientation was considered.	This was not used in any experiments due to the beam orientation to target the central axial slice not being suitable for any realistic experiments.
	Due to the curvature of the phantom, and the positioning of the spine, a slot design was unsuitable for the model split in the central sagittal plane so a hook was designed to secure the two sections together.	The hook failed to print due to the lack of space for supporting material. When creating intricate designs it was important to consider the print layout or supporting material and the ease at which this can be removed.	This was used in the first test experiment with the two sections secured with tape (Figure 2.3.6).

These phantoms were split in the central sagittal or coronal planes. Pegs were included as a simple alternative to hooks or slots as the external geometry and holes for the pegs could be laser cut into film. The coronal model incorporated the holes for the pegs into the top section to print with the flat edge on the printer.

An error when using the printing software meant these phantoms have an unknown infill density, <100%. It was important to ensure the pegs had a good fit as some of the pegs became damaged.

Due to the problem with the infill density these models were not used in any experiments.
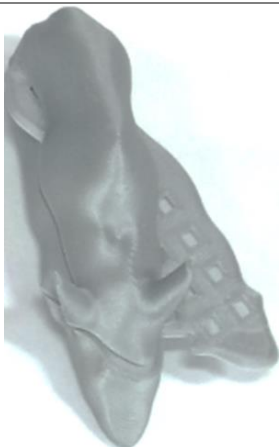
The small geometry of TLD detectors meant the use of a cavity would make it difficult to remove the detectors. To solve this a central slice was created with an array of voids for the TLDs. The purpose of this design was to demonstrate the capabilities of 3D printing to create sophisticated designs for a range of detectors.

This design could have been improved with the addition of pegs to secure the 3 parts together.

This design was not used for any experiments due to the availability of TLDs and the complex readout process.

Hollow phantoms were printed with or without a skeletal structure inside. A funnel was added for the purposes of decanting liquid into the model. These phantoms were printed to test the capabilities of 3D printing to create sealed designs that could be used for gel dosimetry.

One of the phantoms in which only the head was designed to be hollow failed to print the solid body which may have been an error when dividing the two segments to be made hollow and solid.

These phantoms were not used in any experiments due to the complex formulation of dosimetry gel and its limited use across other institutions.

This model is a development of the sliced model above with an additional cavity incorporated into the brain region to hold an alanine detector. A second version was printed with the alanine pellet cavity included in the pelvis region. Multiple phantoms were printed for use in a multicentre dosimetry audit.

Some of the alanine cavities had warped during printing. This meant the pellet extended out of the gap creating an air gap between the film and the phantom.

This phantom was used in the preclinical dosimetry audit described in Section 2.4.

Fused deposition modelling 3D printing was used to create phantoms designed to hold a variety of radiation dosimeters. All depicted models were printed with PLA and, with the exception of the hollow model, incorporated air gaps in the place of lungs. The original STL files can be found at: https://github.com/gpricechristie/mousePhantom. CAD – computer aided design, PLA – polylactic acid, TLD – thermoluminescent detector.

Various 3D printed phantoms are presented in Table 2.3.2. The main issue encountered was the printing of delicate features; the ears and feet depending on the orientation of the construction, some supporting material remained in the lungs and creating the cavities for the alanine detectors. For the tissue equivalent models (not shown), the distribution of the $CaTiO_3$ throughout the skeleton filament may not be evenly dispersed due to the manual manufacturing process (1) and the intricate rib cage, requiring a high resolution capacity printer, may affect the reproducibility of phantoms printed. Figure 2.3.5 demonstrates the contrasting densities of the phantom body and skeleton.

Figure 2.3.5. A CBCT scan of the 3D printed zoomorphic phantom.
A CBCT scan of the heterogeneous density model showing the varying density of the skeleton (white) in contrast to the soft tissue (grey). Not shown are the lungs.

2.3.3.3. Phantom validation

2.3.3.3.1. Establishing the use of the murine dosimetry phantom on the SARRP

Figure 2.3.6 presents the results from the first test using a homogenous density phantom, split down the sagittal plane. The first local gamma analysis test used criteria of 2%/2 mm which resulted in a pass rate of 99.9% (not shown). To further highlight any differences the gamma analysis pass criteria were reduced to 1%/1 mm criteria, shown on the far right of Figure 2.3.6. These criteria were chosen to be in line with clinical tolerances, however in reference to a small animal, 1-2 mm is a large margin for error so subsequent measurements were analysed with stricter criteria, down to 0.1 mm. In this case, the pass rate reduced to 93.9%, highlighted by the green pixels. In areas that failed the gamma index, the blue pixels identify the cold areas in which the film dose was less than the planned dose and the red shows where the film dose was higher than the planned dose. In this test the dose was normalised, therefore it is a representation of relative dose so only the beam profile could be compared. A good agreement is seen between the two distributions, the

gamma analysis highlighted the main difference at the edges of the field in a blurred dose gradient in the measurement compared to the sharp dose fall off in the plan.
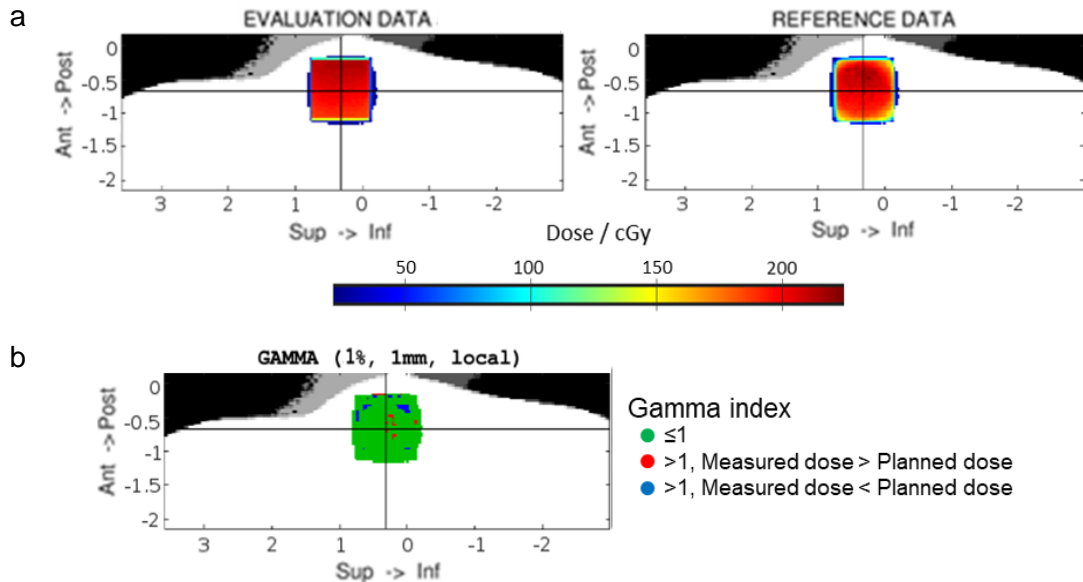
Figure 2.3.6. End-to-end test of the SARRP using the murine phantom with Gafchromic EBT3 film.
a) A 10 x 10 mm field set to the isocentre in the central film plane was delivered to a homogeneous density phantom split in the midline sagittal plane. The first two images show the dose information from the Muriplan treatment plan (left, evaluation data set) and the dose measured by the Gafchromic EBT3 film (right, reference data set). b) The difference between the planned and measured dose distribution was compared using a local gamma analysis, comparing the amount of dose deposited and the distance-to-agreement across the field. Using criteria of 1%/1 mm the green pixels highlight areas which satisfy this criteria and the red and blue pixels indicate the areas which failed, indicating higher (red) and lower doses (blue) measured in the film than modelled in the plan.

2.3.3.3.2. Assessment of the bone-equivalent material

Static 10 x 10 mm fields through the spine, skull and pelvis regions were chosen to assess the attenuation effects of the higher density bone-mimicking material due to the higher volume of the skeleton present in these areas (3%, 7% and 6% in a 10 x 10 mm volume across the sagittal phantom, respectively).

The plan layout and subsequent Gafchromic EBT3 film measurement, when delivering a 10 x 10 mm beam through the spine, are depicted in Figure 2.3.7a.

Local gamma analysis criteria of 2%/0.5 mm (83.7% pass rate) was implemented to detect differences across the field, in line with the small field sizes and suitable tolerances for small animals. Differences between the planned and delivered dose distributions were detected across the edge of the field, as seen with the homogeneous density phantom, and across the bone (Figure 2.3.7b). This additional difference shows the TPS predicting a high dose along the spine, highlighted by the spikes in the 1D beam profiles in Figure 2.3.7b, not depicted in the film measurement. This could be due to the resolution of the planning system being insufficient to detect the 0.28 mm thick film, and consequently this film plane was modelled as a continuation of the higher density material. To correct this, a manual Hounsfield unit (HU) override would need to be applied to input the correct CT number in the film plane as discussed later.

In this instance, the film was cut in a rectangular geometry and taped in place. In the absence of any external markings on the film, the location of the film plane in reference to the plan could not be determine during analysis and as a result, was manually aligned with the higher dose region. This prevented the assessment of the positional accuracy of the TPS.
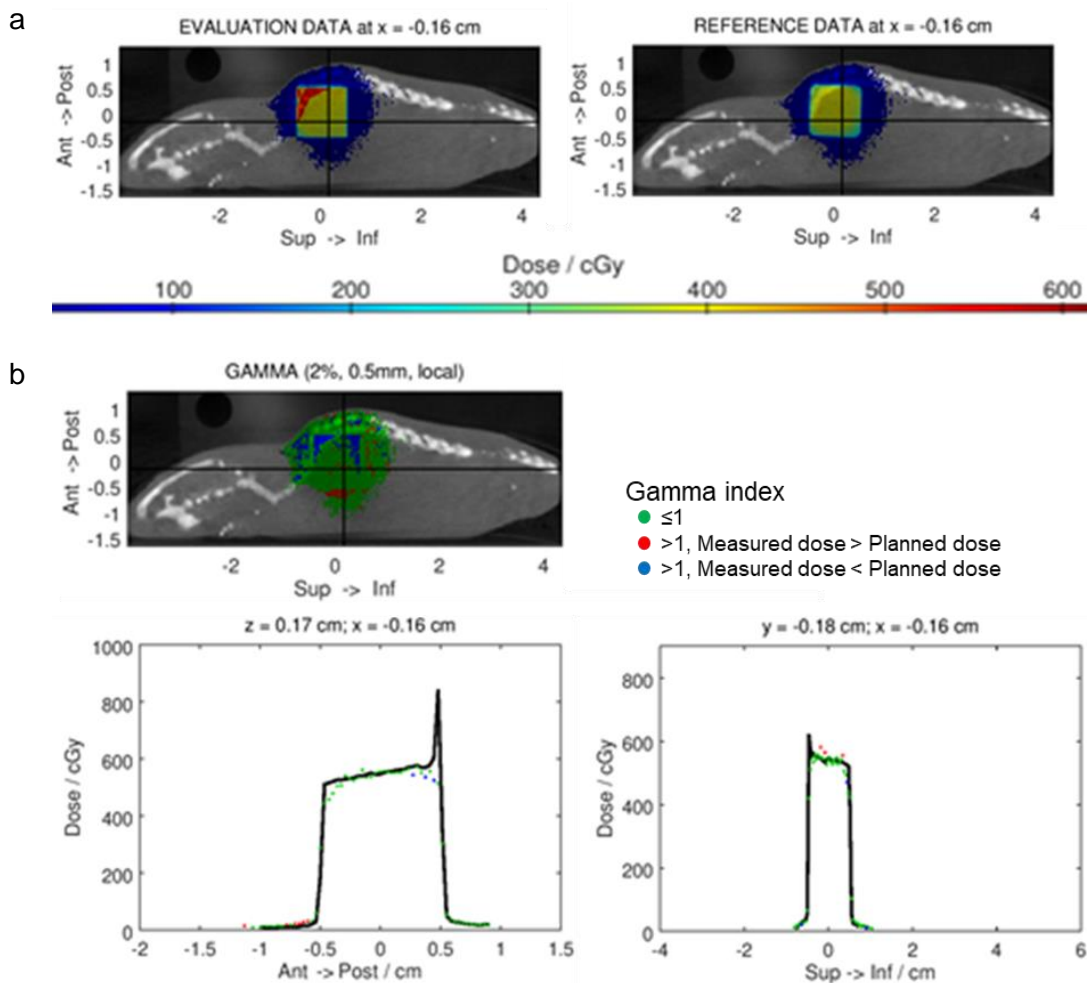
Figure 2.3.7. First irradiation of the heterogeneous density murine phantom.

A 10 x 10 mm field was planned through the spine region using the heterogeneous density phantom split down the sagittal plane, holding Gafchromic EBT3 film inside. The bed and gantry were positioned at 0° and 90°, respectively, to target the isocentre positioned in the film plane. a) The left image shows the Muriplan TPS planned dose distribution and the right image shows the resulting dose captured by the film. b) To compare the planned and delivered doses, local gamma analysis with criteria of 2%/0.5 mm was used, the 2D and 1D profiles are shown. The green pixels highlight areas which satisfied the criteria – 83.7%, the red pixels highlight areas were the dose measured was higher than planned and the blue pixels indicate the opposite.

Other issues raised in the following measurement were the importance of accurate set up and minimising air gaps when using film for dosimetry. Alone, these problems can be solved by either shifting the planned dose by a single pixel to correct the artefact produced by the air or by rotating the TPS image and interpolating the missing dose. However, to do both prevents a direct comparison between planned and delivered doses. The air gap and phantom rotation are clearly seen in Figure 2.3.8a, and causes a large artefact across the calculated dose, depicted as a low dose region in the Muriplan TPS (Figure 2.3.8b, left). When compared to the film measurement, the gamma analysis results at 2%/0.5 mm show the artefact had little effect, possibly due to the analysis of the TPS dose grid in 3D, while the artefact in the TPS dose grid is only a single-pixel wide (Figure 2.3.8c). However, the 1D profile highlights the density anomaly across the field. Overall, this artefact makes it difficult to determine if the higher density bone material attenuates the beam enough to cause a measurable dose difference at the location of the film.
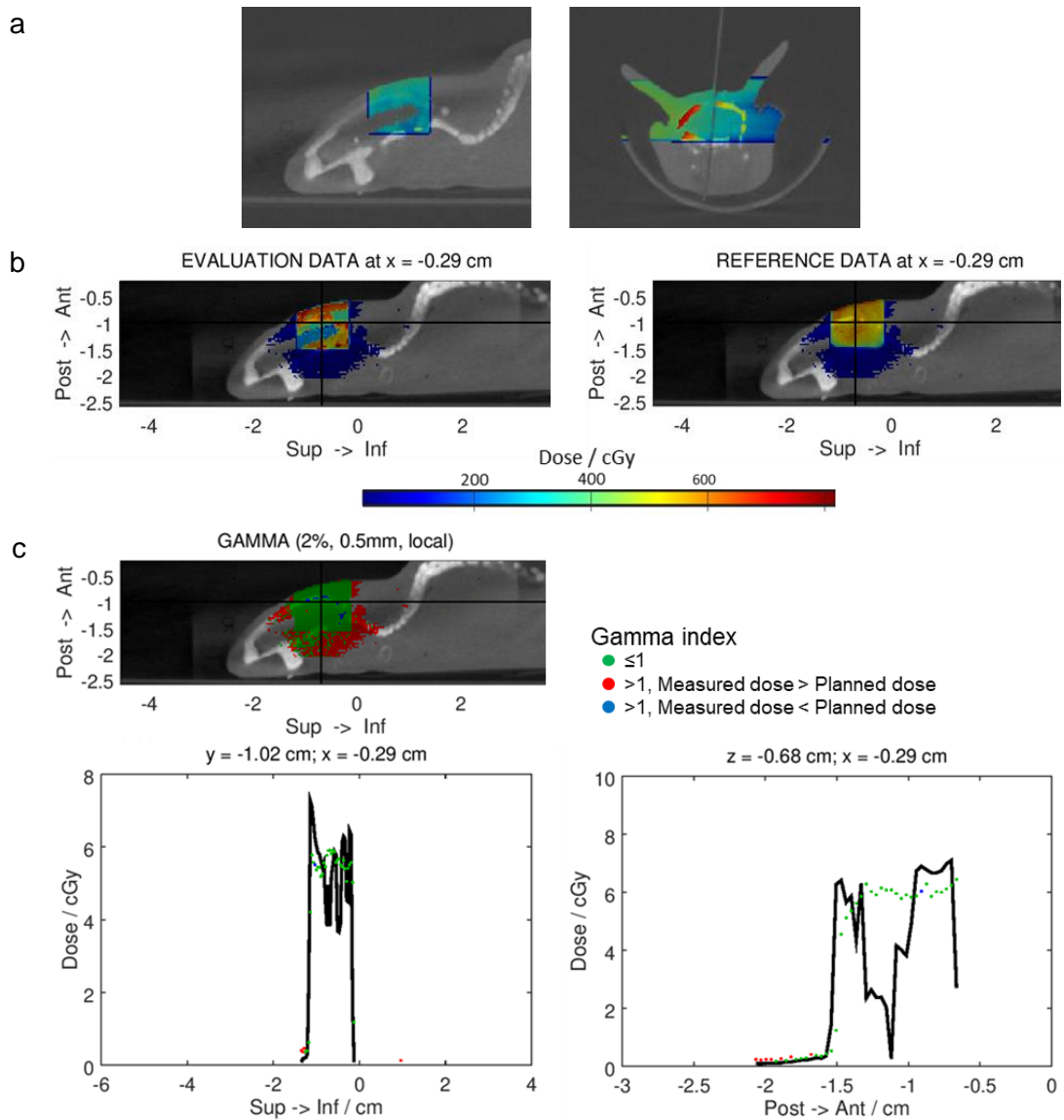
Figure 2.3.8. Gafchromic EBT3 film measurement to assess the bone-equivalent material in the brain region of the phantom.

A 10 x 10 mm field was planned through the brain region of a heterogeneous density phantom to deliver a beam to Gafchromic EBT3 film, located in the sagittal plane. a) The misaligned set up of the phantom included a slight rotation and the inclusion of an air gap adjacent to the film, hampering the analysis. b) The planned (evaluation) and measured (reference) dose distributions. c) To evaluate the higher density areas a gamma analysis comparing the dose delivered and the distance-to-agreement, with a 2%/0.5 mm tolerance, was performed across the 2D plane and as 1D profiles (black lines). The green areas and dots across the profiles highlights areas within tolerance. The blue colour shows area where the dose to the film was lower than depicted in the plan and the red highlights pixels of higher dose than was planned.

Figure 2.3.9 depicts the results of a 10 x 10 mm static beam delivered to the pelvis, with the isocentre in the midline sagittal plane of the phantom. The pass rates for the multiple local gamma analyses performed are presented in Table 2.3.1. The manual HU override to correct for the TPS misidentifying the Gafchromic EBT3 film plane to contain the higher density bone-equivalent material, as first identified in Figure 2.3.7, was applied and the set up ensured there was no rotation of the phantom and minimal air gaps present between the film and the phantom. The principal difference between the calculated and film measured dose distributions, as shown in the intensity profiles, is a blurring across the skeleton and at the field edge.
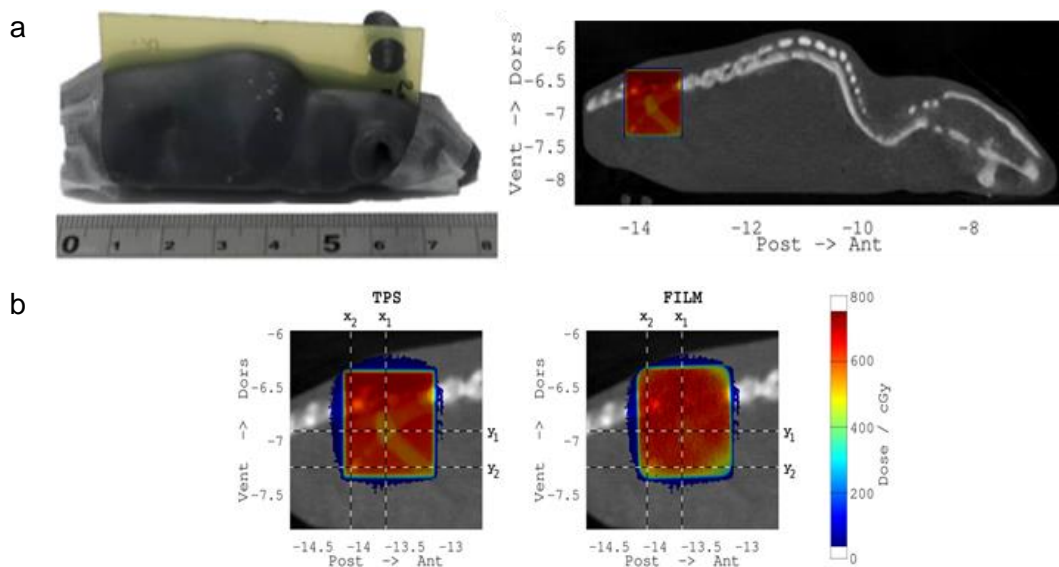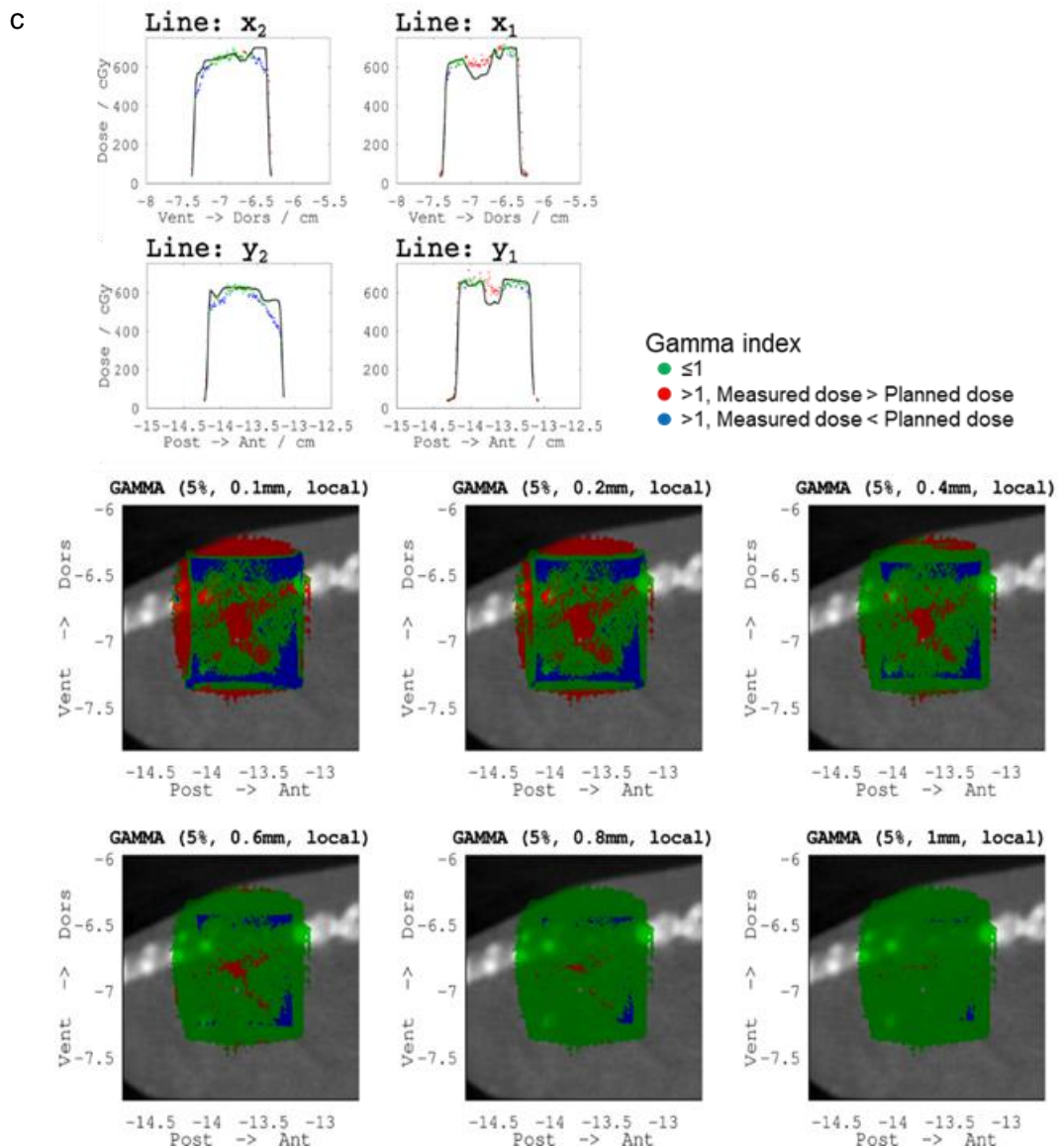
Figure 2.3.9. Further investigation of the impact of the higher density skeletal material. a) The mouse phantom was 3D printed in two halves, split centrally along the sagittal plane, to accommodate Gafchromic EBT3 film. A simple static 90° beam using a 10 x 10 mm collimator was planned through the pelvis to an isocentre in the film plane. b) The planned (left) and measured (right) dose distributions. c) corresponding 1D intensity profiles at the indicated positions (dashed lines on b) and local gamma analysis comparing the planned and delivered doses using pass criteria of 5%/0.1-1 mm. Green dots indicates areas which passed the gamma analysis and blue and red areas highlight where measured dose was lower or higher than the planned dose, respectively.

Table 2.3.2. Local gamma analyses results from the phantom irradiation targeted at the pelvis

Local gamma analyses dose difference and DTA criteria	Percentage of pixels passing the gamma analyses criteria
5%/0.1 mm	57%
5%/0.2 mm	65.1%
5%/0.4 mm	81.6%
5%/0.6 mm	92.1%
5%/0.8 mm	97.1%
5%/1 mm	99.9%

2.3.3.3.3. End-to-end test of the audit procedure

Figures 2.3.10 and 2.3.11 show the test irradiations in preparation for a national preclinical multi-centre dosimetry audit. Irradiating through the skull in the coronal orientation, which contains a high proportion of the higher density material (13% in the 10 x 10 mm beam path from the phantom surface to the film), led to a high dose artefact in the film plane (Figures 2.3.10a and 2.3.11a) identified most prominently by the 1D profiles. The TPS recognises this as a hot spot of absorbed dose, however as the film is a homogenous density it is hypothesised to be the result of the resolution of the TPS misidentifying the bone in this plane. To correct this manual adjustments to the HU numbers of the film were applied by identifying the abnormally high HU values in the film plane and setting these values to match the normal HU value for film. This adjusted image was imported into Muriplan and the dose recalculated, shown in Figures 2.3.10b and 2.3.11b. The local gamma analyses for a range of criteria are presented in Figures 2.3.10c and 2.3.11c and the pass rates are presented in Table 2.3.2 for both the static and arc beams.

a

EVALUATION DATA at z = -0.12 cm   REFERENCE DATA at z = -0.12 cm

Dose / cGy

GAMMA (4%, 0.2mm, local)
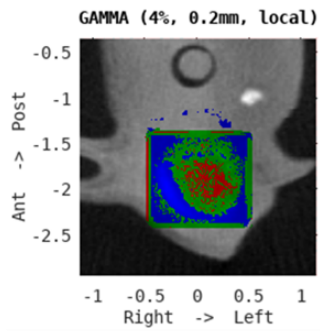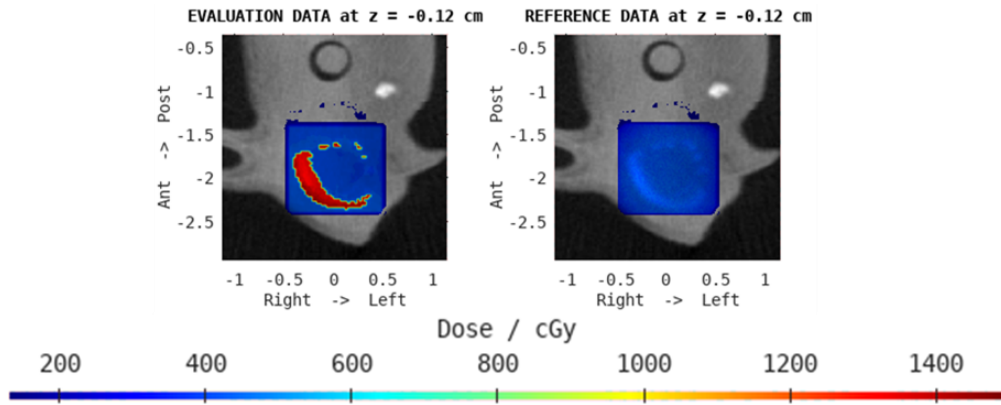
Gamma index
● ≤1
● >1, Measured dose > Planned dose
● >1, Measured dose < Planned dose

x = -1.83 cm; z = -0.12 cm   y = 0.00 cm; z = -0.12 cm

b

EVALUATION DATA at z = -0.12 cm   REFERENCE DATA at z = -0.12 cm

Dose / cGy
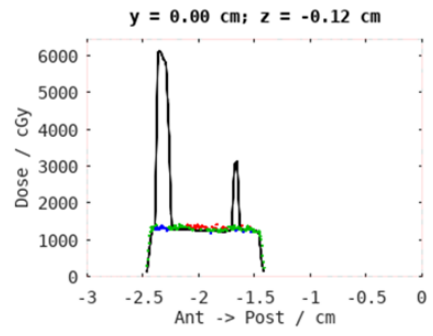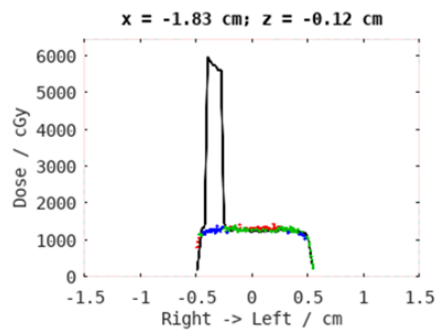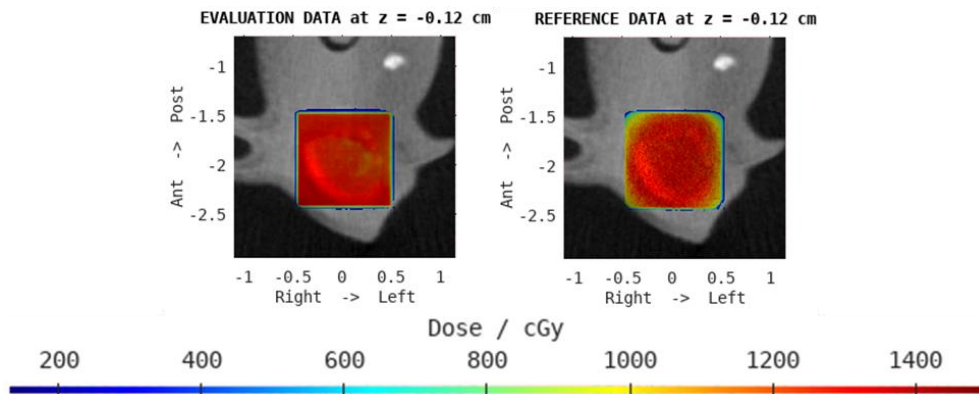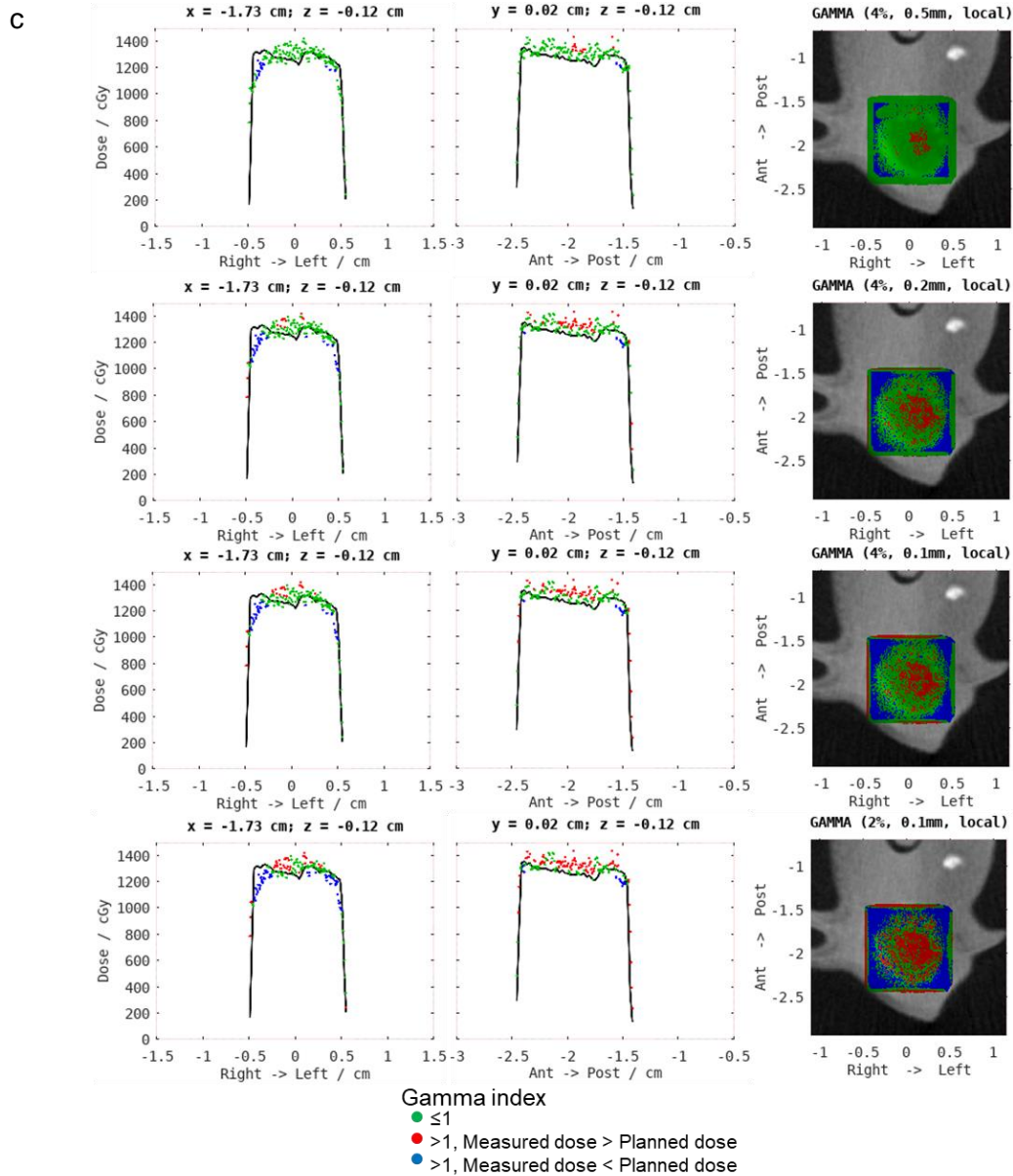
Figure 2.3.10. An illustrative use case of the presented phantom for a multi-centre audit. a) Using a heterogeneous density murine phantom split down the coronal plane, Gafchromic EBT3 film was secured using pegs and a static 10 x 10 mm beam was planned to the isocentre in the film plane. The top images present the planned and measured dose distribution and the bottom images show a representative local gamma analysis. The 1D profiles identify a higher dose region recognised by the treatment planning system situated within the film plane. b) The Hounsfield units were manually corrected in the CBCT image in the film slice and the corrected TPS image and film measurement is presented. Panel c displays various comparisons, using a local gamma analysis, of the planned and measured doses in both 1D and 2D orientations. Green pixels show good dose and distance agreements between the two images, red and blue pixels highlight hot and cold spots in the film (reference) compared to the plan (evaluation).

Figure 2.3.11. Gafchromic EBT3 film measurements of an arc delivery.
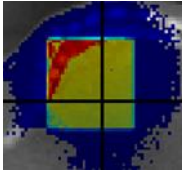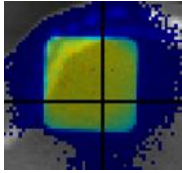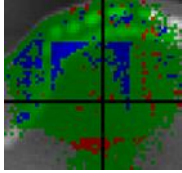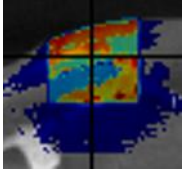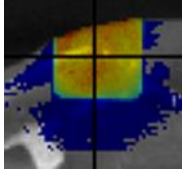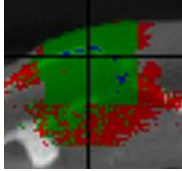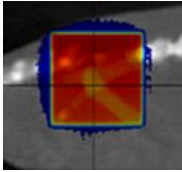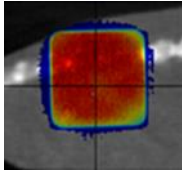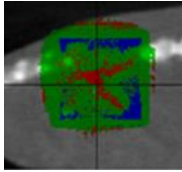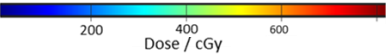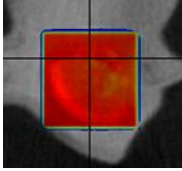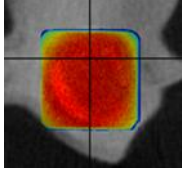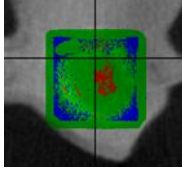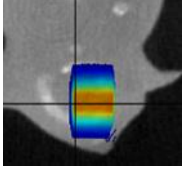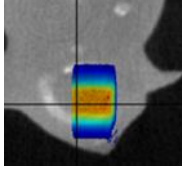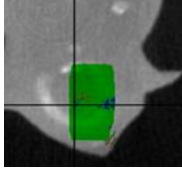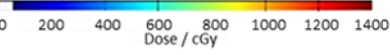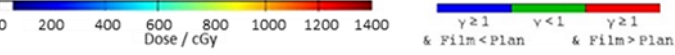
a) Using a heterogeneous density murine phantom and Gafchromic EBT3 film sandwiched in the central coronal plane, a 5 x 5 mm beam, arc plan was planned to the isocentre set in the film plane. The bed was angled at 90° such that an arc from -45° to 45° would cover the brain area. The top images present the planned and measured dose distributions and the gamma analysis is presented underneath. b) The Hounsfield units were manually corrected in the CBCT image slice to correct the area of high dose in the film and the corrected TPS plan and film measurement is presented. Panel c displays various comparisons, using a local gamma analysis, of the planned and measured doses in both 1D and 2D orientations. Green pixels show good dose and distance agreements between the two images, red and blue pixels highlight hot and cold spots in the film compared to the plan, respectively.

95

Table 2.3.3. Local gamma analyses results from the audit test for both the static and arc fields.

Local gamma analyses dose difference and DTA criteria	Percentage of pixels passing the gamma analyses criteria for the static 10 x 10 mm field	Percentage of pixels passing the gamma analyses criteria for the arc 5 x 5 mm field
2%/0.1 mm	36.6%	41.3%
4%/0.1 mm	54.8%	48.3%
4%0.2 mm	61.4%	66.9%
4%/0.5 mm	86.4%	98.9%

Table 2.3.4 provides a comparison across all Gafchromic EBT3 film measurements using the tissue equivalent density phantom. A gamma analysis criteria of 2%/0.5 mm was chosen as a suitable tolerance for preclinical dosimetry in line with clinical dose tolerance (2%) and realistic small animal margins (0.5 mm).

Table 2.3.4. Summary of the gamma analyses for all phantom measurements

Plan summary	Dose (Plan)	Dose (Film)	Local Gamma analysis 2%/0.5 mm	Local gamma analysis pass rate
10 x 10 mm field Gantry 90° 6 Gy Spine				83.7%
10 x 10 mm field Gantry 90° 6 Gy Brain				N/A due to air gap and film rotation
10 x 10 mm field Gantry 90° 6 Gy Pelvis				76.4%
10 x 10 mm field Gantry 0° 12 Gy Brain				80.9%
5 x 5 mm field Gantry 0° 12 Gy Brain				97.2%

2.3.4. Discussion

Commissioning an irradiator characterises the mechanical and dosimetric properties to permit the computation of dose within a 5% tolerance to the actual dose delivered (109). This process usually takes place when the irradiator is first installed, however to ensure confidence in the measurements performed in this study it was recommissioned at the beginning of the project. Furthermore, a report by Chen *et al.* (126) found large calibration errors caused by incorrect procedures and omission of required correction factors by the vendor upon installation. QA procedures are an extension of this commissioning process with daily, monthly and annual tests of the imaging, dosimetry and TPS components (63).

The zoomorphic mouse phantom described in this report is an improvement over currently used dosimetry phantoms by incorporating an accurate representation of the heterogeneous densities within a real animal (Figure 2.3.5). The ease of manufacturing, efficient production and increasing availability of 3D printing facilities promotes mass uptake of this tool worldwide. The phantoms can be reusable, are cheap to make, can accommodate additional custom equipment and are easily set up on a small animal irradiator. The most significant problem with 3D printing this model is mainly a limitation of technology available; either in the capability of printing multiple materials in one model, or the size of the printing nozzle to include the intricacies of the skeleton, especially if considering the inclusion of more soft tissue subtypes such as adipose or muscle. It may not be possible for other institutions to manufacture the bespoke $CaTiO_3$-doped ABS for the bone equivalent material and so for the proposed multicentre dosimetry audit homogeneous PLA-based phantoms were printed and distributed (Section 2.4.).

The blurred nature of the high gradient regions suggest a potential penumbra effect which, although sharp at kV energies, can still be significant in very small fields and have a greater effect on the uncertainty at the field edge when employing these small collimators (127). This is important to consider when using the smaller collimators for which the blurred edges will make up a higher proportion of the irradiated field. These illustrative use cases show the potential of using realistic phantom anatomies to enable real world dose distributions, rather than simple point measurements, to be used for radiobiology experiment QA. The attenuation effects of the bone-equivalent material was most pronounced trough the pelvis, as demonstrated in Figure 2.3.9. However, the uncertainties associated with film measurements, planning system bulk density overrides and dose calculation algorithm, amongst other factors, mean further investigation is required before the dose discrepancies can be meaningfully determined. Minimising such uncertainties within a multicentre dosimetry audit to assess delivered doses is important and it may be more suitable to utilise a homogeneous density model to avoid any tissue segmentation differences between centres.

In the clinic, advances such as arc therapy, better image guidance using 3D volumetric and 4D dynamic volumetric images and more precise planning techniques allows more conformal treatment and consequently, the ability to target the tumour with smaller margins and dose escalation without compromising normal tissue. In combination with this zoomorphic phantom, the improvements in technology at the pre-clinical level, with the development of the SARRP, improves

the translational impact of small animal research. These more sophisticated units, with the ability to achieve more conformal dose delivery, require more stringent QA procedures. The use of realistic geometry and tissue-equivalent densities create a more representative phantom of the murine anatomy and provides a better test of the predicted dose distributions from the TPS.

The major restraint in pre-clinical radiation research is the lack of dosimetry standardisation. Without robust dosimetry the value of any results are compromised, any time effort and expenditure are wasted and the justification for the use of animals cannot be made. Regular use of a zoomorphic mouse phantom in QA procedures will reduce the numbers of animals required to counteract the uncertainties associated with dose – representative of a major source of noise in experimental data (2). Sample size calculation studies in dose response trials suggest a reduction in animals of up to 60%, based on excluding very high doses for which tumour control is assumed (>90% tumour control probability) or very low doses where tumour control is not likely. However, these assumptions can only be made if trustworthy dose-response curves are made (2). Further use of such phantom can refine the use of animals in research by optimising experiment set ups akin to phase 0 trials, consequently minimising experiment time and toxicity to the animal.

2.3.5. Conclusion

This report describes the initial work undertaken to develop a set of reference standards for the robust QA of pre-clinical radiotherapy experiments in the modern era of high precision irradiation units. Over the last decade the advances in technology in and out of the laboratory has encouraged the development of a machine that can reflect all aspects of a clinical treatment: from CBCT image-guided treatment planning to arc delivery. Without strict protocols, well defined QA procedures and a maintained standard, the body of pre-clinical radiation research is undermined. The 3D printed phantoms described in this report are suitable for multiple uses including 2D and 3D measurements of dose whilst accurately representing the effects of varying densities. They are compatible with the SARRP, support all stages of experiments and are therefore the ideal tool to facilitate the translation of pre-clinical research into useable results.

Acknowledgements

2.4. RESULTS: A PRECLINICAL RADIOTHERAPY DOSIMETRY AUDIT USING A REALISTIC 3D PRINTED MURINE PHANTOM

Summary

This chapter has been recently submitted to Scientific Reports for consideration as part of their collection "Improving reproducibility in animal research", and is currently under review. The paper included here has been modified to include consistent section and figure numbering. The main focus of this study was the completion of a dosimetry audit of 6 UK centres, actively involved in preclinical radiation research, using a version of the Price *et al.* (1) phantom designed to include alanine pellet detectors and Gafchromic EBT3 film.

As discussed extensively in Chapter 2.1, there is a pressing need to address the currently lacking dosimetry quality assurance (QA) standards in preclinical radiation research. Chapter 2.2 described the capabilities of 3D printing phantoms of unique designs, to incorporate detectors capable of measuring dose in 1, 2 or 3 dimensions. Chapter 2.3 demonstrated a suitable use for the developed phantom to address this issue, implementing Gafchromic EBT3 film to evaluate delivered doses and the dose distribution. Various designs allowed tests of multiple target areas, using different angles of beam delivery and implementation of both static and arc beams. To validate the use of the phantom as an additional tool for preclinical dosimetric assessment, a dosimetry audit of several UK-based institutions was undertaken. The aim of the audit was to investigate the current status of preclinical dosimetry. Previous preclinical dosimetry audits implemented only point detectors or used basic cylindrical phantoms to assess differences between planned and delivered doses, predominantly using simple, static beam arrangements (68,74). The combination of Gafchromic EBT3 film and alanine pellets used in this study provided measurements of absolute dose and the dose distribution across the target area. The inclusion of static and arc deliveries provided a realistic representation of the use of the Small Animal Radiation Research Platforms across sites.

This audit demonstrates the potential for routine adoption of the phantom in QA procedures across multiple centres. The realistic phantom geometry will provide an accurate representation of the dose delivered to a laboratory animal, increasing

confidence in the dosimetry. Regular auditing, in addition to routine QA practice, validate the treatment planning and radiation delivery in the context of the wider community, facilitating the production of comparable and reproducible data.

Author contributions

All authors discussed the audit procedure. I designed the phantom, collated the data and wrote the manuscript. K. Williams provided relevant contacts and expertise to complete the measurements. A. Aitkenhead analysed the film data and edited the manuscript. G. Price reviewed the manuscript. A. Chadwick and E. Santina and K. Kirkby provided day to day supervision. All authors approved the final manuscript.

A PRECLINICAL RADIOTHERAPY DOSIMETRY AUDIT USING A REALISTIC 3D PRINTED MURINE PHANTOM

Emma R. Biglin[1]*, Adam H. Aitkenhead[1,2], Gareth J. Price[1,3], Amy L. Chadwick[1,3], Elham Santina[1,3], Kaye J. Williams[4], and Karen J. Kirkby[1,3]

[1]Division of Cancer Sciences, Faculty of Biology, Medicine and Health, University of Manchester, Manchester, UK. [2]Christie Medical Physics and Engineering, The Christie NHS Foundation Trust, Manchester, UK. [3]The Christie NHS Foundation Trust, Manchester, UK. [4]Division of Pharmacy and Optometry, Faculty of Biology, Medicine and Health, University of Manchester, Manchester, UK.

*corresponding author

Abstract

There is concern that preclinical radiation research lacks robust dosimetry procedures that provide traceability to a primary standard. Without this, ensuring accuracy and reproducibility between studies is challenging. Using a 3D printed murine phantom we undertook a dosimetry audit of Xstrahl Small Animal Radiation Research Platforms installed at 6 UK centres. 3D printing of the phantom facilitated the combined use of Gafchromic EBT3 film and alanine pellets to measure both the dose distribution and absolute dose delivered, respectively. Two phantom irradiation scenarios were developed: [i] a 10 x 10 mm static field and [ii] a 5 x 5 mm 90° arc. For the static fields, the mean percentage difference in absolute dose between the plan and alanine measurements was 3.9% (-2.3% to 10%), and for the arc fields -1.4% (-14% to 7.4%). Arc fields had increased variability and more pronounced under-dosing, suggesting an increased geographical miss of the target as the alanine pellet and irradiation field were the same width, highlighting the importance of accurate targeting. Film-measured dose distributions mainly differed from those planned around the field edges in regions of steep dose gradients in the treatment plan. The audit demonstrates that further work on preclinical radiotherapy quality assurance processes is merited.

2.4.1. Introduction

The late 2000s saw the first application of sophisticated small animal irradiation platforms to deliver clinically representative treatment designs and implement image guidance, albeit on a much smaller scale (125,128). Since then, as these machines became more widespread and regularly implemented, considerable technological advances have been made in the imaging, planning and delivery of preclinical irradiation, to keep up with the fast-paced advances of their clinical counterparts (129). Despite recent improvement, preclinical irradiation workflows still do not mirror the standardised and rigorous dosimetry quality assurance (QA) checks and national auditing procedures of clinical radiation (63,67,68,71,106). There are numerous different approaches employed by the small animal radiation platform community in terms of the tests are required, who should undertake these and at what frequency.

The lack of guidance and implementation of reporting vital radiation parameters hinders reproducibility and is one of the contributing factors to a paucity in dosimetry standardisation (62,72). Other *in vivo* research areas rely on the ARRIVE guidelines (Animal Research: Reporting of *in vivo* Experiments), as set out by the NC3Rs (National Centre for the Replacement Refinement and Reduction of Animals in Research), documenting the parameters that should be reported to facilitate accurate reproducibility (130). However, at present these do not include factors relating to radiation research.

Ableitinger *et al.* (131) recommend that if multiple institutions partake in collaborative studies then a dosimetry audit across the sites should be mandatory to ensure sufficient dosimetric accuracy, thereby increasing confidence in the comparability and reproducibility of the results. In this study, we used a postal audit to investigate dosimetric conformance of UK small animal precision irradiation facilities. Physical agreement of both a single beam and arc therapy treatment is measured using a realistic murine phantom containing Gafchromic EBT3 film (Vertec Scientific Ltd. Reading, UK) and alanine pellet detectors (National Physical Laboratory (NPL), Middlesex, UK). We additionally surveyed participating institutes to ascertain the equipment and techniques currently supported by departments, quality control processes in use, and also attitudes to the need for quality control in pre-clinical radiation experiments.

2.4.2. Methods

2.4.2.1. Questionnaire

Prior to the audit, information regarding the equipment in use, the techniques implemented and the QA procedures in place at 7 centres across the UK which actively undertake *in vivo* radiation research using an Xstrahl (Walsall, UK) Small Animal Radiation Research Platform (SARRP) was gathered via a questionnaire. There are currently 8 centres in the UK that use a SARRP for *in vivo* radiation research. The questionnaire also invited participants to give their opinion, through open-ended questions, on the necessity of dosimetry audits and defined protocols, the level of acceptable dose tolerances, QA responsibilities and required reporting parameters in publications to improve the currently poor reproducibility of research (72).

2.4.2.2. Phantom design and printing

The phantom used in this audit was previously described by Price *et al.* (1) and a link to the open source files can be found within. In short, to create the phantom the cone beam computed tomography (CBCT) scan of a nude mouse was segmented into three parts (body, bones and lungs) then transformed into stereolithographic files suitable for import into Meshmixer (Autodesk, Inc.) and Netfabb (Autodesk, Inc.) computer-aided design software. In this study, the phantom (body and lungs) was split on the central coronal plane to accommodate Gafchromic EBT3 film, and a cylindrical cavity 6 mm in diameter and 2.5 mm in height was incorporated in the ventral half of the phantom, in the brain region, to contain an alanine detector. The split in the central coronal plane permits the delivery of an arc beam. Three pegs (5 mm length, 3 mm diameter) were included in the design to hold the film in place (Figure 2.4.1). A second phantom but with the pellet cavity located in the pelvis region was also designed.
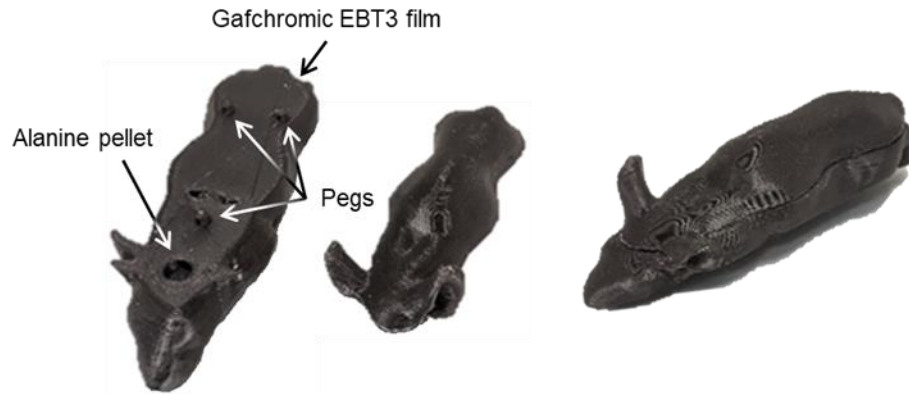
Figure 2.4.1. The 3D printed murine dosimetry phantom.

An Ultimaker 3 fused deposition modelling printer was used to create bespoke phantoms capable of securing Gafchromic EBT3 film over an alanine pellet to capture an absolute dose measurement and dose distribution with reference to a national primary standard. The assembled phantom is shown on the right. A second version of the same phantom was printed with the alanine pellet cavity situated in the pelvis region.

This design allowed simultaneous irradiation of the film and alanine detectors to allow a direct comparison between measurements. The plans were designed so that the beam was incident on the dorsal surface of the phantom, passing through the film and then through the alanine pellet located directly beneath the film. Gafchromic EBT3 film is thin (<0.3 mm) and relatively water/tissue-equivalent, so is unlikely to perturb the dose distribution downstream of the film. Furthermore, to avoid any risk of the bulkier alanine pellets perturbing the dose to the film, the alanine pellets were located beneath the film. The use of a realistic murine phantom over a simple cylindrical geometry allows a representative test of the treatment pathway, from phantom positioning, image guided treatment planning and treatment delivery. The homogeneous density phantom, without bone-equivalent skeletal material, was used to minimise interference on the dose calculations from any differences in segmentation between centres. The use of a tissue-equivalent phantom incorporating a bone-equivalent material may be more appropriate in imaging QA procedures or more stringent tests of the dose delivered when the use of such phantom has been established in standard dosimetry practice.

The phantom design was then imported into the Ultimaker Cura software package (132), where the 3D printing parameters were set and the gcode required to print the mouse model produced. All phantoms were printed by an Ultimaker 3 (Ultimaker BV,

Utrecht, Netherlands) fused deposition modelling 3D printer, which was loaded with a polylactic acid (RS Components Ltd.) filament for the body, printing with 100% infill density. The lungs were incorporated into the model as air cavities.

2.4.2.3. Audit procedure

The audit workflow (Figure 2.4.2) simulated the procedure of a typical *in vivo* experiment: CBCT acquisition, treatment planning and beam delivery. Two murine phantoms were delivered to each of the six SARRP institutions that completed the questionnaire, herein referred to as S1-S6. For logistical reasons the 7th centre was unable to participate in the audit measurements.
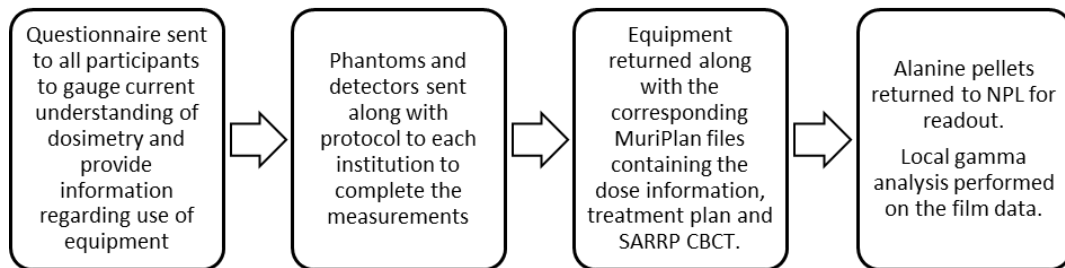
Figure 2.4.2. Workflow of the audit.

For the end-to-end audit, 2 scenarios were assessed:

i) Delivery of a simple static field to the pelvis using a 10 x 10 mm square collimator, with the bed and gantry at 0°.

ii) Delivery of a more complex 90° arc field to the brain using a 5 x 5 mm square collimator. The bed and gantry angles were 90° and -45° to 45° respectively, to create an arc in the sagittal plane intended to be representative of techniques designed to spare one hemisphere of the brain.

The plan layouts are illustrated in Figure 2.4.3. For both scenarios the prescribed dose of X-rays was 12 Gy to the centre of the alanine detector, and the source settings were 220 kVp and 13 mA. Each scenario was planned and delivered twice, with new alanine and film, to obtain repeat measurements. The prescribed dose of 12 Gy was chosen to suit the sensitivity range of the alanine dosimeters.
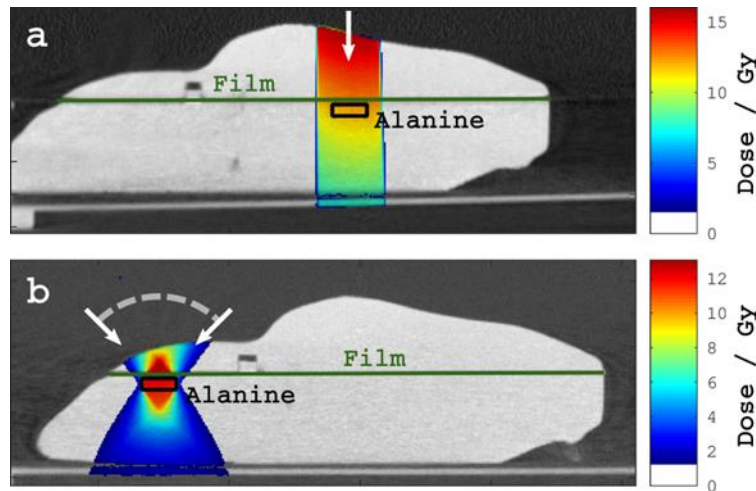
Figure 2.4.3: Illustration of the plan designs for the dosimetry audit.
a) The simple irradiation of the pelvis using a static 10 x 10 mm static field, and
b) The more complex irradiation of the brain using a 90° arc in the sagittal plane
and a 5 x 5 mm collimator. The arrows indicate the beam directions.

Each centre was provided with a protocol documenting the procedure and equipment handling instructions (Appendix 1.2, Table A1.3), four pre-labelled laser cut films and alanine pellets and spares. To assemble the phantom the alanine was placed into the cavity to minimise air gaps between the film and the phantom. For the SARRP irradiations, participants were instructed to follow their standard operating procedure to acquire a CBCT of the phantom with the alanine and film in place and develop a treatment plan on the resulting image using the SARRP Muriplan treatment planning system (TPS). As per standard SARRP operating procedure, soft tissue and lung were segmented using pixel intensity thresholding and the standard bulk density overrides were applied.

2.4.2.4. Alanine dosimetry

The alanine detectors were purchased from the alanine dosimeter reference service at the NPL to measure absolute dose (133). The detectors were 5 mm in diameter and 2.3 mm in height.

After use, the alanine pellets were returned to NPL for readout. The dose reported is traceable to the primary standard for ^{60}Co beam quality and therefore a correction factor is required when used with low and medium energy X-rays due to an energy dependence (74). This correction factor is based on each SARRP's half-value layer (HVL), the thickness of a material (most often aluminium or copper) required to attenuate the intensity of radiation by half (134). The HVL value was provided by

each institution, either from the manufacturer or previous QA procedures. The process of applying these corrections factors was as documented by Silvestre Patallo *et al.* (74). Measurements of absolute dose were compared to the median planned dose to the pellet volume and the percentage difference was calculated.

2.4.2.5. Gafchromic EBT3 film dosimetry

A set of calibration films was irradiated using a 300 kV source at the NPL to allow a calibration curve to be generated for the batch of Gafchromic EBT3 film used in the audit. Delivered doses were validated by ionisation chamber measurements, calibrated with reference to the UK primary standard 300 kV free air chamber. Irradiations were delivered using a beam quality of 0.5 mm Cu HVL, source-to-surface (SSD) distance of 75 cm, with solid-water (WT1) slabs arranged to provide 2 cm build up and 20 cm backscatter. 5 x 4 cm sections of film were irradiated at doses of 0, 1, 2, 3, 4, 5, 6, 9, 12 and 15 Gy to create the calibration reference.

All films (calibration and measurements) were scanned using an Epson 10000XL flatbed scanner in transmission RGB mode, colour corrections disabled, at a spatial resolution of 400 dpi and a bit depth of 16-bits per colour channel. A minimum time between irradiation and scanning of 24 hours was left to allow the polymerisation of the active layer within the film to stabilise (112,135). Scanned images were stored in TIFF format. All images acquired using the Epson 10000XL scanner were pre-processed prior to use to correct for scanner non-uniformity issues. The correction factor at each pixel of a scanned image is dependent on three things: [i] the colour channel; [ii] the position of the pixel on the scanner bed (in terms of the distance from the central axis of the scanner); [iii] the darkness of the film at that point. A correction map was previously created using a series of films, uniformly irradiated at doses from 0-25 Gy, and scanned at all positions across the scanner bed. This allowed a correction map to be created as a function of colour channel, position and optical density.

The calibration curve was parametrised using an equation of the form shown in equation (1), as described by Aitkenhead *et al.* (119).

(1) $$Dose = A \times B^{O.D.} + C$$

where A, B, C are the fit parameters and O.D. represents the optical density. Figure 2.4.4 shows the calibration film, and the fits and residuals for each colour channel.

To fit the exact geometry of the 3D printed design, sheets of Gafchromic EBT3 film were laser cut to form the outline of the phantom and accommodate the pegs. To

create the exact dimensions for the laser cutting, Netfabb was used to convert the model into slices and the slice corresponding to the film location was exported as a DXF file, compatible with the laser cutting software. The asymmetric geometry of the film aided both the fitting of the film into the phantom in the correct orientation, and locating the position of the film in the treatment plan during its analysis.
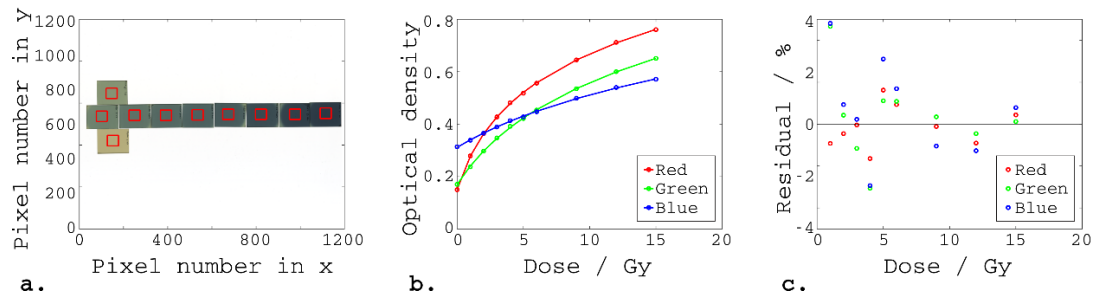
Figure 2.4.4: Calibration of the Gafchromic EBT3 film.

a) The calibration films. For each film, the median optical density within the region-of-interest marked by the red box was used for creation of the calibration curves. b) The calibration curves, relating optical density and dose for each colour channel. The circles represent the median measured optical densities, and the lines represent the fits of the form: Dose = A x B^{O.D.} + C. c) The residuals for each colour channel.

Film measurements of the delivered dose were compared to that calculated by the TPS using gamma analysis (121). Analysis was performed within an Octave environment (123) using in-house software which has previously been clinically commissioned for other applications (119,136,137). For each centre, following the terminology used by Low *et al.* (124), the film data formed the reference dataset while the planned dose grid formed the evaluation dataset. The software performed a full 3D gamma analysis, calculating the gamma index for each pixel in the 2D reference image by minimising the dose difference (DD) and distance-to-agreement (DTA) within the 3D evaluation image.

The film analysis procedure was designed to allow separate evaluation of [i] the positional agreement between the planned and delivered dose, [ii] the absolute dose delivered and [iii] the shape of the dose distribution:

For each film, the outline geometry and 3 holes corresponding to the pegs shown in Figure 2.4.1 were used to geometrically locate the film within the phantom. The

position of the film was then manually adjusted by applying small offsets to best match the field edges to the planned dose distribution. The positional offset applied was recorded as the residual shift.

The reference (film) data was normalised to the evaluation (plan) data prior to the gamma analysis in order to assess differences in the dose distribution shape without results being dominated by any difference in absolute dose. Normalisation factors were calculated for all pixels in the film within the 90% isodose region (relative to the prescribed dose of 12 Gy) for the corresponding point in the planned dose grid. The median of these factors was taken as the overall normalisation factor for that film.

The shape of the dose distribution was evaluated by performing gamma analyses for a range of DD criteria from 2% to 7%, and a DTA criterion of 0.3 mm. Dose differences were evaluated relative to the local dose. All pixels in the film corresponding to a dose >4% of the prescribed dose (12 Gy) were evaluated within the analysis.

2.4.3. Results

2.4.3.1. Questionnaire feedback

A summary of the questionnaire results can be found in Appendix 1, Table A1.4. All institutions agreed that audits and defined dosimetry protocols are important. Most participants suggested that a dose tolerance of within 5% was an acceptable dose agreement and one centre proposed that <15% would be satisfactory. Variations between centres arose with the questions pertaining to QA tests. Using various ionisation chambers these were either completed every 6 months (in two centres by the manufacturer), every 2 months, whenever the machine was used or daily. The calibration of three of these farmer-type ionisation chambers could be traced to the national primary standard and another two centres' chambers were calibrated by the chamber manufacturer (PTW-Freiburg GmbH). Output checks were performed either annually, bi-annually, monthly or bi-monthly and calibrated at least every 2 years.

With regards to reporting parameters, each institution gave different suggestions:

- dose, dose rate, irradiation protocol, geometry, collimation commissioning, tube current, filtration and the dose received by 90% of the target (D90),

- the dose delivered and the distribution over the target area,

- filters, set up, energy, mAs, dosimetry equipment, field size, beam quality,

- dose, isocentre, isolines, organ at risk sparing and

- device used, gating, dose delivered, fractionation, image guidance, irradiation technique, field size, SSD, backscatter, couch, D95, HVL, voltage, filtration, dosimetry protocol (air or water), output measurements, depth, backscatter, target medium, dosimetry system, calibration conditions, dose rate.

Although there were large variations in reporting information all participants agreed that more informed reporting would lead to better reproducibility of research. Two centres chose not to answer.

2.4.3.2. Alanine dosimetry

As described by Silvestre Patallo *et al.* (74) the HVL thickness of the individual irradiators can be used to correct the energy dependence of the alanine detectors. The HVL values reported for all sites ranged from 0.65 mm Cu to 0.85 mm Cu for the SARRPs corresponding to energy dependence factors of 0.79 to 0.81, respectively (Appendix Table A1.5).

The static beam measurement, in which the 10 x 10 mm square field covered the whole alanine pellet in the plan (5 mm diameter), was used as an accurate determinant of the absolute dose. The results, after applying the energy dependence correction factors, are presented in Figure 2.4.5. All institutions achieved an absolute dose difference of <10%, while 4/6 centres were within ±5%. The overall mean difference between planned and delivered doses was 3.9%.

Irradiation of the phantom using the more complex beam configuration of an arc (Figure 2.4.5) resulted in lower dose values than the static beam, principally due to the 5 x 5 mm field being the same width as the pellet diameter so a slight geographical miss of the target would result in underdosing of the alanine pellet. All but 1 measurement achieved <10% deviation from the planned dose, with a mean difference of -1.4%.
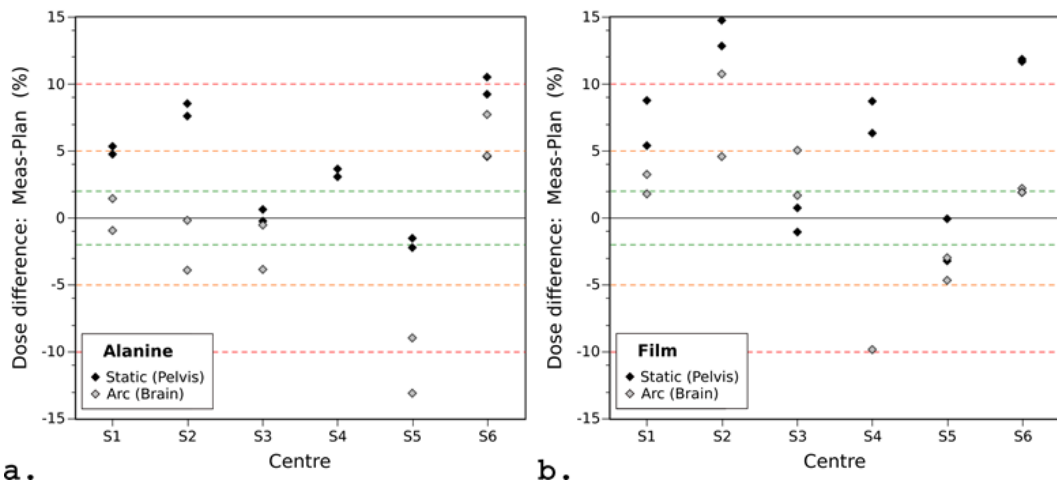
Figure 2.4.5. Percentage difference between planned and measured doses on the Small Animal Radiation Research Platforms for the a) alanine and b) film measurements.

A positive value indicates the measured dose was greater than the planned dose. The dashed green, orange and red lines indicate 2%, 5% and 10% differences from the prescribed dose, respectively.

The targeting accuracy of both techniques was also highlighted by the spread of the data from each individual centre. Dose differences ranged between 2.4-4.6% in the arc delivery compared to 0.5-1.2% when using the static beam.

2.4.3.3. Gafchromic EBT3 film dosimetry

The residual shifts required to match the film position to the plan were consistent across all centres, with an average residual of 0.68 ± 0.35 mm (mean ± standard deviation) across all centres and deliveries. These residuals represent the total of all sources of error, including delivery issues such as the difference between the true isocentre position and the isocentre position modelled in the TPS, as well as measurement issues such as the accuracy of positioning the film within the phantom.

Figure 2.4.6a illustrates the results of the gamma analyses for one film from each centre for the static plans. Three key observations may be made:

i. For several centres (e.g. S1, S2, S5 and S6), the measured dose outside the field was notably higher than the planned dose, as can be seen by the red regions surrounding the field in the gamma images. The result suggests that the dose calculation algorithm may underestimate the dose outside the field relative to the target by more than 7%, although further confirmation is

113

needed since low dose levels are where film dosimetry is least reliable. This would only be a concern for experiments where the dose to normal tissues in close proximity to the high dose region is important.

ii. The largest discrepancy between the planned and delivered dose distributions is the corners of the square fields, shown by the blue regions in the corner of each field in the gamma images for centres S1-S5. In the measured fields the corners have a more rounded profile and a lower dose than predicted by the TPS.

iii. At centre S6, the 10 x 10 mm square field was modelled by a 10 mm diameter circular field. This was a deliberate choice by that centre to minimise the number of apertures that had to be commissioned. As noted above, the corners of the square field measured in the film disagreed with those modelled by the TPS, therefore the use of a circular model is not as unrealistic as might be expected. In addition, if the aperture is only to be used for experiments where the dose at the centre of the field is the key factor, modelling of the field corners is likely to be unimportant.

Figure 2.4.6b illustrates the results of the gamma analyses for one film from each centre for the arc plans.
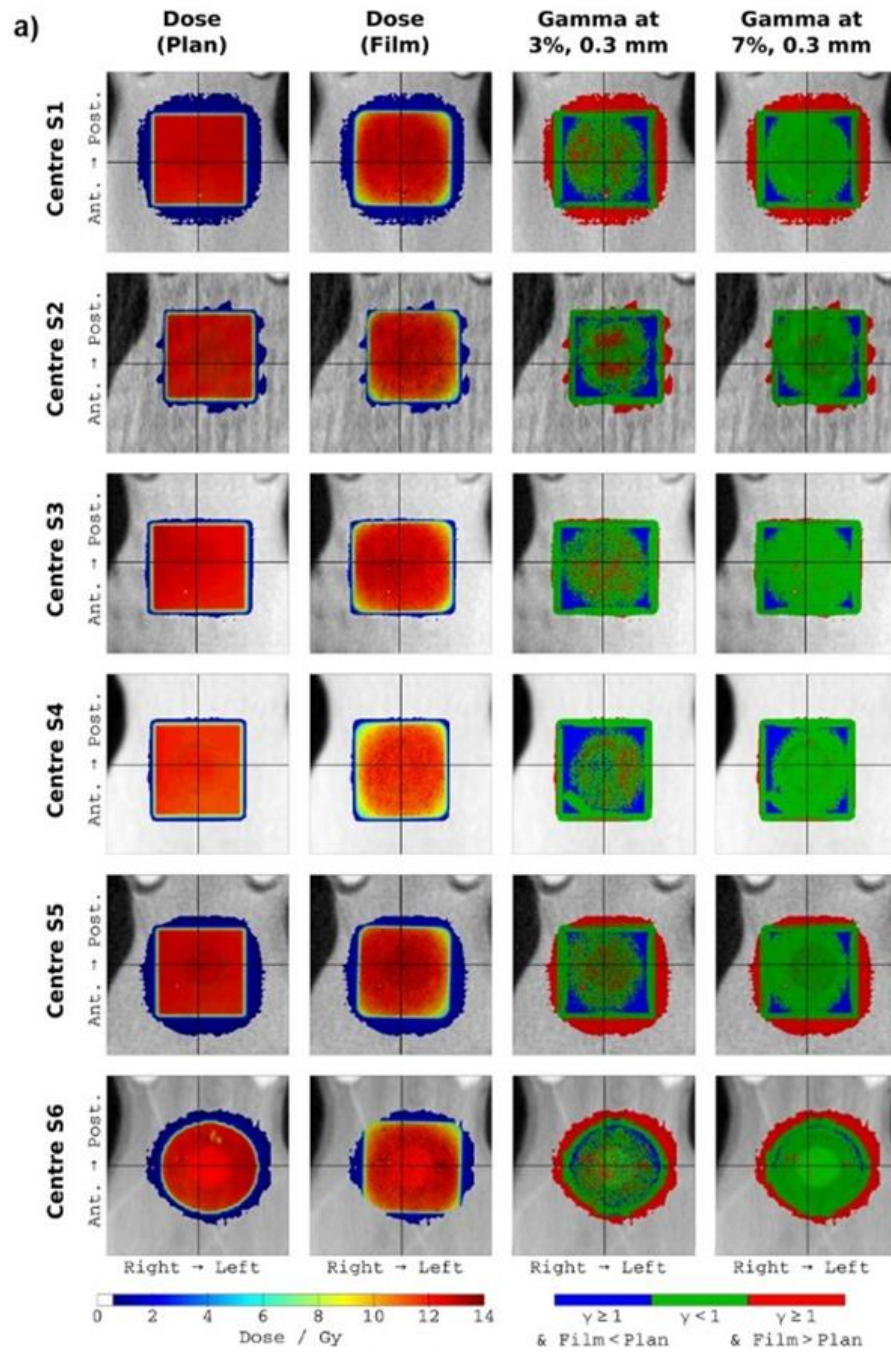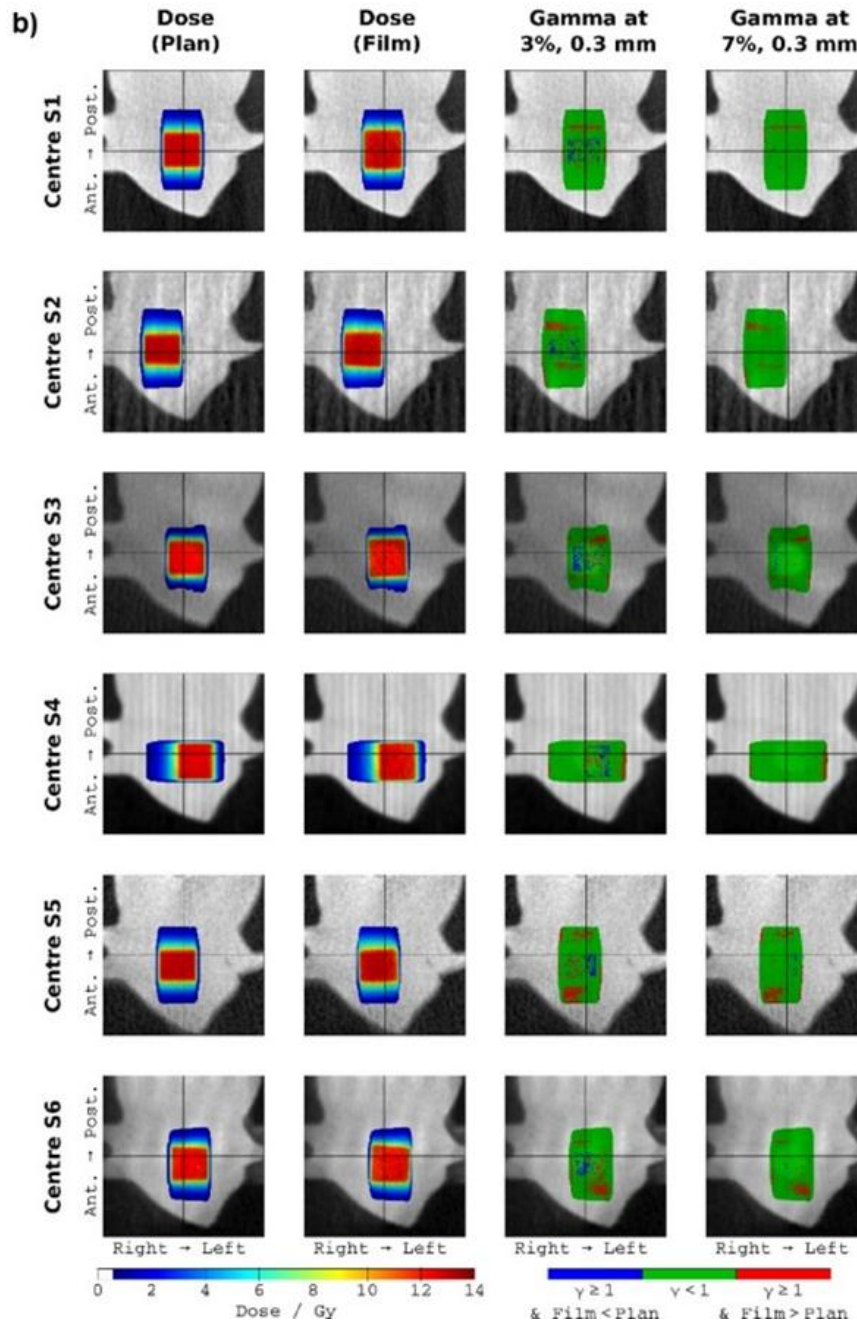
Figure 2.4.6. Results of the gamma analyses.

a) Results of the gamma analyses for one film from each centre for the static plan. Each row presents results for one centre (S1-S6). The columns present the planned dose, the film dose, and the gamma results at 3%, 0.3 mm and 7%, 0.3 mm respectively. Each image has dimensions of 20 x 20 mm. b) Results of the gamma analyses for one film from each centre for the arc plan. Each row presents results for one centre (S1-S6). The columns present the planned dose, the film dose, and the gamma results at 3%, 0.3 mm and 7%, 0.3 mm respectively. Each image has dimensions of 20 x 20 mm.

The results for all gamma analyses for the static and arc plans are summarised in Figure 2.4.7. Although the 10 x 10 mm static plans were simpler than the arc plans, the static films consistently had a smaller proportion of passing pixels ($\gamma \leq 1$). In contrast, in the arc plans the steeper out-of-plane dose gradient tended to result in a higher proportion of passing pixels. Results for all centres were broadly comparable.
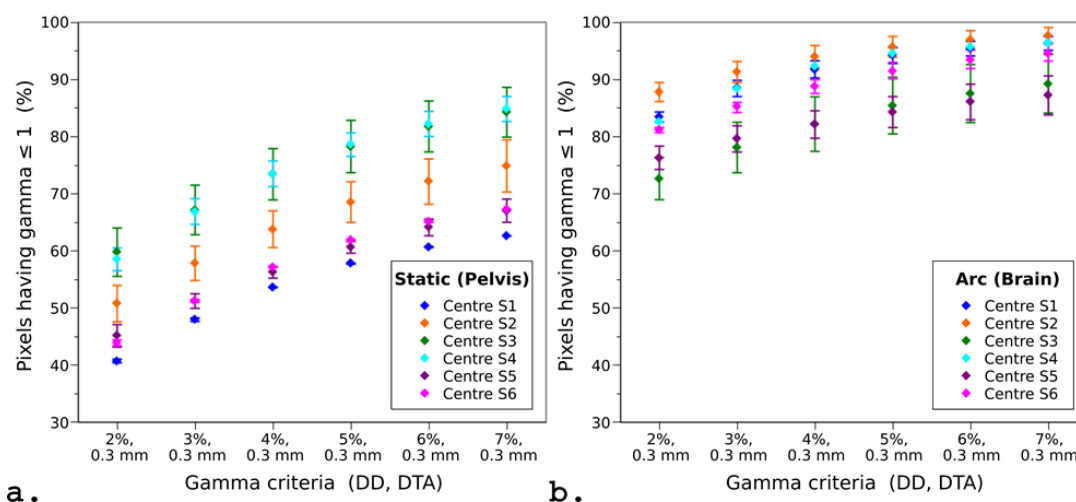
Figure 2.4.7. Gamma analyses pass rates for all measurements.

The gamma analysis pass rates for all films from each centre for the a) static beam (pelvis) and b) arc (brain) plans. The number of static and arc films analysed for each centre were 2,2,2,2,2,2 and 2,2,1,2,2,3 respectively. The points represent the mean, and the error bars represent the range of results.

2.4.3.4. Comparison of alanine and Gafchromic EBT3 film measurements of absolute dose

Figure 2.4.8 compares the absolute dose measurements obtained using Gafchromic EBT3 film and alanine pellets. Data is only shown for matched film and alanine measurements: i.e. where the film and alanine were irradiated together on a single irradiation. No matched film and alanine measurements were available for the arc plan at centre S4 due to the alanine pellets being damaged following irradiation and prior to read-out. For the static irradiations film and alanine were in good agreement, with the film being colder by 1.6% ± 2.2% (mean ± standard deviation). For the arc irradiations the agreement between film and alanine was slightly worse, which was likely due to the increased complexity of the plan, with steeper dose gradients and a high dose region no larger than the dimensions of the alanine pellet. Again the film

measurement was typically colder than the alanine, although the variation was greater than for the arc plans (2.9% ± 5.6%, mean ± standard deviation).
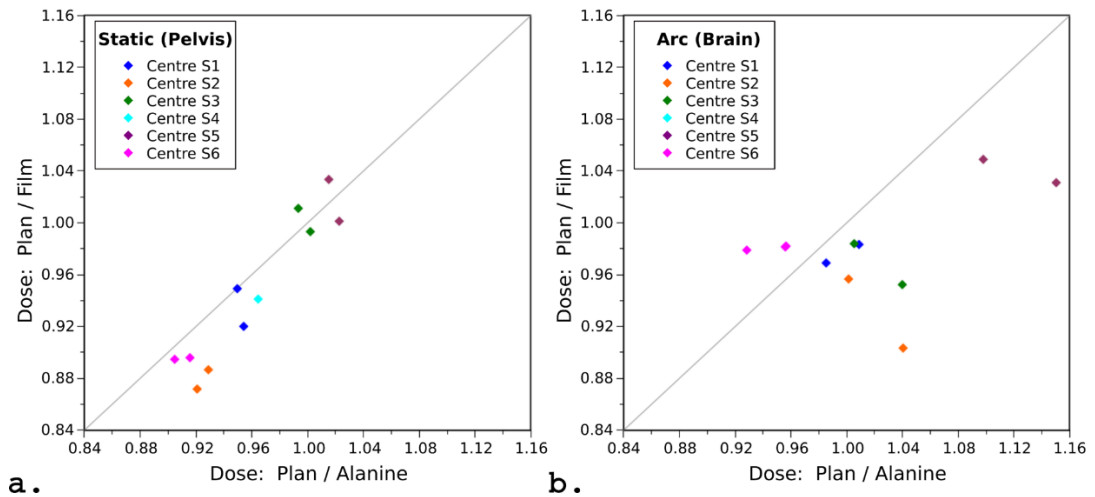
Figure 2.4.8. Comparison of the absolute dose measurements acquired using alanine pellets and Gafchromic EBT3 film.

The absolute dose measurements for (a) the static 10 x 10 mm fields and (b) the arc deliveries. Results are presented in terms of the ratio of the planned dose to the measured dose (i.e. TPS/Film and TPS/Alanine). A ratio >1 indicates that the planned dose was greater than the measured dose. The diagonal line indicates the line of agreement between the alanine and film measurements.

2.4.4. Discussion

We present results from a preclinical dosimetry audit of Xstrahl SARRP systems at 6 institutions in the UK using a realistic murine phantom. The results of the questionnaire suggest that without a routine protocol there is still some way to go before a consensus is reached across the country. One of the contributing factors to a paucity of rigorous dosimetry protocols is insufficient dosimetry knowledge or support from clinical physics colleagues (67). Some centres rely on the manufacturer to complete the dosimetry checks, which has the advantage that the checks are done in a consistent fashion by staff who are expertly trained on the system. However, it also suggests there may be a lack of support at the institutional level, and the lack of independence in the QA process increases the risk of a systemic problem going unnoticed (126). Also of importance is the wide variation in the frequency of output checks (bi-monthly to annually) and lack of calibration which

should be addressed as the output has been shown to decline by up to 4% over an 18 month period (73).

Only one of the centres reported most of the suggested requirements for accurate reporting, as outlined by Verhaegen *et al.* (72). Of the parameters suggested it is important to first specify the radiation source and include details of the manufacturer or model of the irradiator and any beam quality specifics such as energy or HVL. For experiment reproducibility it is essential to include details of the dose, dose rate and fractionation schedule, if appropriate. The field size, number and geometry, SSD, subject size and backscatter or attenuation considerations are also of note. Finally, the dosimetry equipment and protocol, medium used for calibration and measurements and the measurement geometry should be included (62). Most peer-reviewed articles fail to report basic details required to be reproduced or compared to other studies (62,68). Incomplete reporting of these easily defined parameters adds to the biological sources of error that are complex and poorly understood and is often attributed to insufficient physics expertise among users (62).

There are two main types of irradiator commissioning: commissioning based on dose rate in a standard reference geometry – equipment commissioning (73,98,109,135), or specific calibration for individual set up geometries – technique commissioning (127,138,139). General equipment commissioning is manufacturer specific and a standardised practice across different irradiators is currently not available. It is often completed upon installation but may be repeated if dosimetry checks have been neglected for some time. However, this commissioning may be irrelevant to complex experimental designs therefore the commissioning of individual techniques is vital for accurate irradiations but this is often left to the machine users and further hindered by poor reproducibility in already limited existing literature (67,88). One simple proposed standardised QA methodology is the use of the inbuilt electronic portal imaging device, which has shown to be a stable and convenient tool to assess beam quality, energy, output, profile and targeting and verify delivered doses (107,140). A thorough QA procedure would include the use of ionisation chambers for calibration (with reference to a primary dosimetry standard), film for 2D measurements and a smaller detector to validate dose at submillimetre resolution (141,142), such as MOSFETs (metal–oxide semiconductor field-effect transistors) or TLDs (thermoluminescent detectors) (67). However to implement this, first the issue of physics expertise must be addressed as the use and readout of the smaller detectors can be laborious. Currently, most centres included in this audit only use

ionisation chambers for QA. Only two centres also use film as part of their QA process.

When the SARRP was first developed over a decade ago the suggested *in vivo* dosimetry tolerance was 5-10% (125), consistent with the then 5% target used by audits of clinical low or medium energy X-ray irradiators, with action points if results exceed 10% (143). This was especially important since it is documented that a 10% dose difference can lead to mortality rates in some mice strains of up to 90% (114). All institutions in our study achieved <10% absolute dose difference, measured using alanine pellets irradiated using a static beam arrangement, with the majority being <5%. There are several uncertainties that may contribute to these discrepancies. The accuracy of the HVL measurement and the calculation of the correction factors for the alanine energy dependence (estimated to be 4.8%) or the difference in beam quality between the reference beam at NPL (^{60}Co) and the SARRPs (X-ray) used (74). Additional uncertainties in the applied correction factors may come from the difference in the spectra between the SARRPs and the NPL's reference beam (74). Using the nominal HVL thickness of 0.67 mm Cu instead of 0.847 mm Cu, which is due to additional beam gating equipment, increases the dose difference by 2.4%. Furthermore, the signal readout has been known to degrade over time, especially in humid environments (144). However, here the maximum time between irradiation and readout being < 2 months and the pellets being stored in two sealed envelopes the signal should have remained stable (144). There may also be contributing uncertainties that are related to the TPS calculations such as segmentation thresholds, commissioning or targeting, which are out of the scope of this investigation. It was assumed the CBCT dose was negligible (<0.85 cGy) in line with other studies (102,125), and did not contribute to the delivered dose difference. Apart from 1 delivery from centre S5, the arc deliveries were also all within 10% of the planned dose for the alanine measurements (see Figure 5a). That the measured doses were lower than for the static beams could be due to the width of the arc field and pellet diameter being the same. A small error in the isocentre targeting, either from user or TPS inaccuracies, would result in incomplete coverage of the alanine dosimeter and therefore the average dose measured over its volume would be reduced. There are additional uncertainties due to the rotation of the bed (during the CBCT acquisition) and gantry (during radiation delivery), which may contribute to the overall targeting uncertainty.

Film provides the ability to assess certain features of the delivered dose distribution that cannot be evaluated using point dosimeters such as alanine pellets: the shape

of the dose distribution in 2D; the position of the delivered dose; and the dose deposited outside the high dose region. Each of these types of error has the potential to lead to inaccurate conclusions being drawn from *in vivo* experiments (88). Increased focus on validating these aspects of the delivered dose distribution, rather than focussing only on the absolute dose delivered to the target region, would help to refine experiments in several ways: better agreement between planned and delivered dose distributions would increase confidence in delivered doses, consequently reducing the number of animals required, and improving control of the delivered dose away from the target may help to reduce the radiation-induced side effects experienced by the animals.

The results illustrated in Figure 2.4.6a show that agreement between the plan and EBT3 film measurements was generally poor at the field corners, where the film measurements showed a more rounded profile and lower dose than predicted by the TPS, and in the out-of-field regions, where the film measurements were notably higher than the planned dose. Dose errors in these regions could be a concern for experiments where the dose to normal tissues in close proximity to the target is important. Correcting these errors would refine the use of animals by minimising any potential toxicity and adverse effects which may impact the welfare of the animal and the experimental results. These issues were observed in all 10 x 10 cm^2 static field measurements for all centres, indicating that they are not due to a delivery error. Further investigation is warranted into the exact cause of these discrepancies. Film dosimetry is least reliable at low dose levels, and therefore the out-of-field dose discrepancy could potentially be explained by the limitations of film dosimetry. This is less likely for the discrepancies seen at the corners of the field, which are not in a low dose region and spatially are well within the resolution limits of film dosimetry. Previous studies have suggested that the superposition-convolution dose calculation algorithm used in Muriplan does not accurately model the penumbra (107,135). Implementation and evaluation of alternative dose calculation algorithms, such as using a Monte-Carlo approach, is worthy of investigation since they may have different behaviour in the out-of-field regions. Other parts of the planning and delivery process may also benefit from investigation, such as the use of bulk density overrides to segment tissue types within the CT image. It is worth noting that similar discrepancies were not observed in the arc dose distributions (Figure 6b), perhaps because of the use of a smaller field size, and because the relative motion of the beam tends to soften field edges parallel to the axis of rotation.

The density of soft tissues typically ranges from 0.95 g/cm^3 (for adipose tissue) to 1.05 g/cm^3 (for muscle)(145,146). Furthermore, the phantom used during the Muriplan TPS commissioning is kV-equivalent solid water(98). Keeping in line with published dosimetry protocols, dosimetry phantoms should be a density close to water (1 g/cm^3) such that the measurements obtained are within a few percent(117,147).The ICRU report 44 states corrections factors may be required for absorbed dose measurements obtained with phantoms that introduce uncertainties greater than 1%(146). The density of the phantoms used in the audit was 1.19 g/cm^3. This difference potentially impacts on the accuracy of the dose calculation. Within the TPS, the tissue segmentation allows voxels within an image to be assigned as one of 5 discrete materials (air, lung, fat, tissue or bone) whose densities are defined according to ICRU report 44(146,148). An underestimate in the density of the material defined as 'tissue' will lead to the TPS underestimating the attenuation of the beam within the phantom, which we estimate could lead to an error of 1-2% in the calculated dose at the film or alanine detectors. The magnitude of the dose error will be dependent on the field size, the geometry of the phantom, the depth of the dosimeter, and the SSD. This may contribute to the behaviour observed in Figure 5, where the dose differences between measurement (both alanine and film) and plan are consistently higher for the static plans than for the arc plans. In terms of the variation between institutions any dose error due to the density of the phantom would be systematic, having the same impact on all centres. For future phantom or audit work the choice and density of material used for the phantom should be carefully specified and checked to improve the accuracy of absolute dose measurements.

During the audit several problems were encountered:

1. One of the phantoms had warped during printing making the alanine cavities smaller than designed, and this was not detected during phantom quality control. This meant several pellets were damaged upon removal and were therefore unreadable (arc data for S4). The poor fit of the alanine pellet in the warped phantom also resulted in an air gap beneath the film. This resulted in an artefact in the planned dose distribution adjacent to and downstream of the film. To prevent this affecting the gamma analyses, the planned dose in the air gap was corrected using interpolation.

2. One centre mislabelled the plan information upon return so these had to be manually matched to the films during analysis.

3. One centre (S4) mis-interpreted the planning guidance and used an arc in the transverse plane rather than one in the sagittal plane. However, for the purpose of the audit the use of a transverse arc was also acceptable, since the aim was to test agreement between the planned and delivered dose.

However, this demonstrates the need for unambiguous guidance in multi-institutional studies.

4. One centre inserted the film the wrong way in the phantom, but due to the symmetrical structure of EBT3 film this had no impact on the analysis.

5. Finally, one centre sent incomplete dose information and the original plan was removed from their TPS. However, it was possible to re-create the plan within Muriplan using the data that had been exported, allowing the dose to be recalculated.

2.4.5. Conclusions

Regular end-to-end dosimetry audits complement the QA performed by the user, testing all stages of the planning and delivery process, and provide confirmation that centres' practices and results are consistent with the wider community. This audit shows the potential of using realistic phantom geometries for evaluation of dose distributions that are representative of experimental scenarios. Regular implementation of this phantom to standardise dosimetry across preclinical radiation research has the potential to reduce the sample sizes required by minimising the uncertainty associated with delivered doses. Furthermore, It will refine the use of animals by streamlining experiments thereby minimising the time the animal is required in immobilisation devices or under anaesthesia and may reduce toxicity, which would have occurred as a result of overdosing or irradiating normal tissue outside the target region. The use of two different types of dosimeter (film and alanine) allows different features of the dose distributions to be evaluated, and also provides the means to check consistency between the different dosimeters, in this case in terms of absolute dose. We recommend the phantom and detector tool proposed be adopted into routine dosimetry QA protocols.

Acknowledgements

SECTION 3: RADIOBIOLOGICAL EXPERIMENTS AND DEVELOPMENT OF 3D CELLULAR MODELS

Summary

The introduction to this section provides a literature review regarding general cancer biology, radiobiology and glioblastoma multiforme (GBM), the focus of the following experimental results chapters. This background provided possible explanations for the differences observed across the genetically heterogeneous cell lines tested, highlighting the difficulties in treating GBM using radiotherapy (RT) alone. GBM cell lines were chosen to mirror the tests being performed in the brain region of the phantom, outlined in Chapters 2.3 and 2.4, with the aim of developing a suitable 3D cellular model to be incorporated into the same location to further assess the dose delivery. These cell lines are well established in the field of radiation research, are easy to maintain in culture and are capable of producing characteristic and well-defined spheroids, important for developing appropriate 3D cellular matrices.

Chapter 3.3 outlines the results of the biological experiments investigating the response to radiation across a panel of GBM cell lines. These experiments aimed to characterise the radiosensitivity, DNA damage repair and metabolic capacity of the cells. Following the survey of the literature discussed in Chapter 3.1, it was noted that a large number of experiments focus on a limited number of cell lines so, to establish a comprehensive response, five different GBM cell lines were initially tested using the gold standard clonogenic assay, immunofluorescence microscopy using markers of DNA damage and the Seahorse mitochondrial stress assay.

The final chapter in this section describes the development of 3D cellular models in the form of spheroids and microbeads to facilitate transport between vessels for realistic irradiations within the dosimetry phantom, described in the previous section. The spheroids provided a 3D geometry of GBM cells with oxygen and nutrient gradients, representative of a tumour. The microbeads are hydrogel droplets, encapsulating the GBM cells within. Both models were easily transferred between vessels to facilitate migration and invasion assays (spheroids) and imaging (microbeads). The benefit of incorporating these 3D models into the phantom design will allow the simultaneous measurement of the biological response and a dosimetric evaluation if detectors are also included in the model. Moreover, the

inclusion of DNA damage markers throughout the 3D microbeads (~3-4 mm) could detect dose heterogeneities across the 3D volume. This combination of the phantom and a tumour model could be used as a precursor to animal experiments, potentially reducing the numbers of animals required and optimising experiments prior to animal exposure, providing preliminary supporting data in a more research-relevant orientation.

3.1. Introduction

3.1.3. Glioblastoma Multiforme

Gliomas are the most common primary tumour of the central nervous system (CNS) in adults. Based on histopathology, gliomas can be divided into astrocytomas, oligodendrogliomas, oligoastrocytomas, ependymomas, and mixed gliomas (149). Pilocytic astrocytoma have a distinguishable boundary from surrounding brain tissue and can therefore be surgically removed (grade 1). Low grade gliomas (grade 2) are slow growing in contrast to anaplastic gliomas (grade 3) which are fast growing, both are highly infiltrative making a total surgical resection difficult. The most frequent, and unfortunately most malignant, are grade 4 astrocytomas – GBM (150).

3.1.3.1. Epidemiology and diagnosis

In the UK there are approximately 12100 new cases of brain or CNS tumours diagnosed every year (6). Despite recent advances in imaging, multimodality treatments and radiotherapy delivery, prognosis still remains poor with only 12% of patients surviving 5 years or more (6).

The incidence of GBM tumours has significantly increased since 1995 (151). There has been no definitive underlying cause for malignant gliomas, although inconclusive evidence implicates head injuries, traffic-related air pollution, foods containing N-nitroso compounds, mitochondrial dysfunction, family history (<5% cases), electromagnetic field exposure and the use of mobile phones (151,152). Exposure to ionising radiation is the only recognised causal factor and could explain the gradual increase in GBM incidence as this coincides with the increased use of computed tomography (CT) imaging in recent years (151).

Dependent on location and size of the tumour, patients with GBM generally present with symptoms such as headaches, nausea, vomiting, seizures, confusion, memory loss and personality changes. Diagnosis is usually confirmed by a magnetic resonance imaging (MRI) or CT scan highlighting the tumour volume, with associated central necrosis and surrounding oedema (152).

3.1.3.2. Standard treatment for GBM

The current gold standard of treatment for GBM is a surgical resection, followed by RT and temozolomide (TMZ) chemotherapy. Although important to overall survival, surgery is rarely used as a stand-alone treatment because GBM tumours cannot be completely removed due to their invasive nature. However, surgical debulking alleviates symptoms due to mass growth and allows histologic and molecular

analysis. The implementation of intraoperative MRI or fluorescence-guided imaging, has improved safety and reduced resection margins (152).

Over the last two decades there have been an abundance of clinical trials investigating new treatment options to increase clinical benefit (153). The majority of trials investigate the addition of systemic therapy to the existing gold standard treatment rather than improvements of RT techniques. Table 3.1.1 lists the clinical trials initiated since the review by Cihoric *et al.* (153) from the ClinicalTrials.gov database.

Table 3.1.1. Glioblastoma multiforme radiotherapy clinical trials summarised from ClinicalTrials.gov database.

Trial: NCT-	Status	Phase	Study arms	Primary objectives
03514069	1	1	uMGMT: ruxolitinib + RT mMGMT: ruxolitinib + RT/TMZ	MTD (6w)
03477110	1	1	TTF + RT/TMZ	Skin toxicity (30d)
03535350	1	1	uMGMT: ibrutinib + RT mMGMT: ibrutinib + RT/TMZ	MTD (6w)
04047706	1	1	mMGMT: RT/TMZ + BMS-986205 + nivolumab uMGMT: RT + BMS-986205 + nivolumab	TEAE (30d)
04397679	2	1	RT/TMZ + chloroquine + TTF	Dermatitis
03426891	1	1	Pembrolizumab + Vorinostat + RT/TMZ	MTD (12w)
04216329	1	1	Selinexor + TMZ + RT	MTD (7w)
02871843	2	1	RRx-001 + RT/TMZ	TEAE (12w)
03423628	1	1	1: AZD1390 + IMRT (35 Gy/10 #) 2: AZD1390 + WBRT or PBRT (30 Gy/10 #) 3:AZD1390 + RT	DLTs (<10w) TEAE (1y)
03705351	1	1	RT/TMZ + TTF	TEAE (8w
03232424	1	1	TTF + RT/TMZ	TEAE (24m)
03687034	2	1	BRCX014 + RT/TMZ ± TTF	TEAE

04165941	1	1	γ-δ T cell therapy + RT/TMZ	DLT (12w)
03576612	1	1	uMGMT: AdV-tk + Valacyclovir + RT + Nivolumab mMGMT: AdV-tk + Valacyclovir + RT/TMZ + Nivolumab	TEAE (2y)
02866747	3	1/2	1: hypofract stereotactic RT (24 Gy / 3# on days 1, 3 & 5) 2: Arm 1 + Durvalumab	DLT (8m) Local progression
04019262	1	1/2	1: RT (40 Gy / 15 #) + TMZ 2: RT (25 Gy / 5 #) + TMZ	OS (9y) Lymphocyte count (5y)
04324840	2	1/2	1: CC-90010 + TMZ 2: Arm 1 + RT	TEAE (5y) MTD (14m)
04121455	1	1/2	Olaptesed (200, 400 or 600 mg) + RT	TEAE (26w)
03174197	1	1/2	1: Atezolizumab + TMZ 2: Arm 1 + RT	1. DLTs (10w) & TEAE (3y) 2. OS (3y)
04373785	2	1/2	NG101m + RT/TMZ	TEAE (1m) & OS (24m)
03596086	1	1/2	ADV/HSV-tk + Valacyclovir+ RT/TMZ	OS (5y)
04443010	2	1/2	1: RT/TMZ + L19TNF 2: RT/TMZ	DLT & TEAE OS (52w)
04119674	1	1/2	RT/TMZ + Anlotinib	PFS (18m)
02649582	1	1/2	RT/TMZ + DC vaccination	OS (24m)
04280848	1	1/2	RT/TMZ + UCPVax	Immunogenicity (60d)
04388033	1	1/2	RT/TMZ + DC/tumour cell vacc + IL-12	TEAE (3y) + PFS (6m)
04421378	1	1/2	1a: Selinexor + RT 2a: Selinexor + RT/TMZ 1b/2b: RT/TMZ 3a: Selinexor + Lomustine	MTD Recommended dose PFS & OS (24m)

			3b: Lomustine only	
03466450	1	1b/2	RT/TMZ + Glasdegib	Drug dose & OS (15m)
02928575	1	2	Sunitinib + RT/TMZ	Response rate (24w)
02968940	3	2	Avelumab + hypofract RT (30 Gy / 5 #)	TEAE (28d) & PFS (6m)
03139916	2	2	Bavituximab + RT/TMZ	OS (12m)
03212235	1	2	Hypofract RT (60 Gy/20#) + TMZ	OS (24m)
03506139	1	2	Hypofrac RT (75 Gy/30 #)	OS (12m)
03862430	2	2	1: NVX-108 + RT/TMZ 2: Placebo + RT/TMZ	PFS (22m)
02799238	3	2	1: RT/TMZ 2: ALECSAT + RT/TMZ	PFS (24m)
04157478	2	2	1: RT/TMZ + Anlotinib 2: RT/TMZ	PFS (3y)
03776071	2	2	1: RT/TMZ + ENZ 2: RT/TMZ + Placebo	OS (3y)
03367715	1	2	Nivolumab + Ipilimumab + RT (30 Gy / 5 #)	OS (1y)
03047473	2	2	Avelumab + RT/TMZ	TEAE (52w)
04195139	1	2	1: RT/TMZ + Nivolumab 2: RT/TMZ	OS (24m)
03899857	2	2	RT/TMZ + Pembrolizumab	OS (12m)
03581292	1	2	RT/TMZ + Veliparib	Response & OS (5.5y)
03197506	1	2	Pembrolizumab + RT/TMZ	DLT & TEAE (5y) OS (18m) & PFS (5y)
03650257	1	2	1: RT/TMZ + HSPPC-96 vacc 2: RT/TMZ	1 year survival rate
02758366	1	2	RT (54-60 Gy / 30 #) + TMZ + Doxorubicin + Valproic acid	Time to Doxorubicin discontinuation & TEAE

03405792	1	2	1: RT/TMZ + TTF + Pembrolizumab 2: RT/TMZ + TTF	PFS (24m)
03363659	1	2	DSF-Cu + RT/TMZ	PFS (6m) + OS (2y)
03919071	1	2	RT + Dabrafenib + Trametinib	EFS (5y)
03395587	1	2	1: RT/TMZ + DC vaccination 2: RT/TMZ	OS (34m)
04250922	1	2	1: RT/TMZ + placebo 2: RT/TMZ + 2-OHOA (3g/day) 3: RT/TMZ + 2-OHOA (12g/day)	1. PFS (124 events) 2. OS (124 events)
04218019	2	2	1: TTF + RT (SC) + TMZ 2: RT (SC) + TMZ + TTF	SCTR (1w) TEAE (31w)
03778294	1	2	PET/MRI or PET/CT planning scans + 5-10 # PBT + TMZ	OS (12m)
02655601	1	2	1: RT (59.4-60 Gy / 30 #) + TMZ 2: Arm 1 + BMX-001	OS (2y)
03388372	3	2	Nimotuzumab + RT/TMZ	PFS (2y) & OS (2y)
03018288	1	2	1: RT/TMZ + Pembrolizumab 2: Arm 1 + HSPPC-96 vaccine	OS (1y)
03055208	1	2	Gamma knife RS (15 Gy to 50% isodose) + RT/TMZ	PFS (2y)
03746080	1	2	WBRT (30 Gy / 15 #) + RT (30Gy / 15 #) + Plerixafor + TMZ	PFS (6m)
04396860	2	2/3	1: RT/TMZ 2: RT + Ipilimumab + Nivolumab	PFS (4y) OS (4y)
03008148	1	2/3	1: RT/TMZ 2: RT/TMZ + Siroquine	OS (120w)
03548571	1	2/3	1: RT/TMZ + DC vaccination 2: RT/TMZ	PFS (2y)

02685605	1	3	1: Intraop RT (20-30 Gy) + RT/TMZ 2: Standard surgery + RT/TMZ	PFS (24m)
03393000	2	3	1: TSC + RT/TMZ 2: RT/TMZ	OS (24m)
03722355	3	3	1: RT + Carmustine 2: hyperfrac RT (72 Gy / 60 #)	OS (131m)
03345095	1	3	1: RT/TMZ + Marizomib 2: RT/TMZ	OS (49m)
03243461	1	3	1: RT/TMZ + Valproic acid 2: RT/TMZ + Chloroquine	EFS (4.8y)
03181477	1	N/A	SIB-IMRT (80 Gy / 32 #) + TMZ	OS (18m)

Clinical trials searched using the keywords "Glioblastoma" and "radiation" and filtered by data first reported after December 2015, as trials prior to this were reviewed by Cihoric et al. (153). RT/TMZ indicates standard treatment regimen of 60 Gy /30 # RT followed by TMZ.

Status key: 1 = recruiting, 2 = active but not recruiting, 3 = completed.

DLT – dose limiting toxicity, EFS – event-free survival, IMRT – intensity-modulated radiotherapy, MGMT - O6-methylguanine DNA methyltransferase (m = methylated, u = unmethylated), MRI – magnetic resonance imaging, MTD – maximum tolerated dose, OS – overall survival, PBRT – partial brain RT, PBT – proton beam therapy, PET – positron emission tomography, PFS – progression free survival, RS – radiosurgery, RT – radiotherapy, SC – short course, TEAE – treatment-emergent adverse effects, TMZ – temozolomide, TTF – tumour-treating fields, WBRT – whole brain RT.

3.1.3.2.1. Radiotherapy for the treatment of Glioblastoma Multiforme

A timeline of the use of RT to treat GBM is depicted in Figure 3.1.1. RT has been used since the 1940s in the treatment of patients with GBM, initially using kilovoltage (kV) energy X-rays. It was during the 1960s that treatments began to closely resemble the RT used today, with the introduction of megavoltage (MV) X-rays delivering doses of 45-60 Gy to the whole brain (154). The 1970s saw some vast improvements to the planning and delivery of RT with very simple conformal RT being implemented, moving away from the previously used whole brain RT (WBRT)

treatment. In part, this was due to the implementation of CT imaging in treatment planning, allowing the definition of a smaller volume for boost dosing, followed by the use of MRI in the 1980s (155,156). This also coincided with the discovery of the dose-response relationship by Walker *et al.* (154) indicating doses of 60 Gy improved outcomes compared to doses below 45 Gy, without significantly increasing toxicity, at least doubling survival rates when compared to patients with GBM who received no treatment.

The current standard RT regimen for patients with GBM consists of 60 Gy delivered over 30 fractions with concomitant, then adjuvant, TMZ chemotherapy (up to 6 cycles). Elderly patients may be offered a hypofractionated RT course of 40 Gy in 15 fractions with concomitant then adjuvant TMZ chemotherapy (up to 12 cycles) (157). This multi-modality treatment regimen of RT and TMZ was deemed standard practice after a landmark phase 3 trial conducted by the European Organisation for Research and Treatment of Cancer (EORTC) and National Cancer Institute of Canada (NCIC) Clinical Trials Group which demonstrated a clinically meaningful survival benefit over RT alone (158,159). Various other chemotherapeutic agents have been trialled with adjuvant RT, summarised by Gzell *et al.* (160), but these have yet to demonstrate a significant survival advantage.

Despite these technological advances, survival rates remain poor. Attempts at dose escalation has previously involved further courses of external beam RT (EBRT) or interstitial or iodine brachytherapy which had short term beneficial effects, but caused an unacceptable level of toxicity (160). Ongoing RT research is investigating dose escalation, dose painting to target hypoxic areas of the tumour, combinations with various immunotherapeutic agents, tumour treating field therapy and nanoparticle delivery systems (19,160). The first international pooled analysis investigated the use of intraoperative RT followed by standard RT and chemotherapy treatment (161). The results suggested improved efficacy without major side effects and a phase 3 trial is now ongoing (ClincalTrials.gov ID NCT02685605).
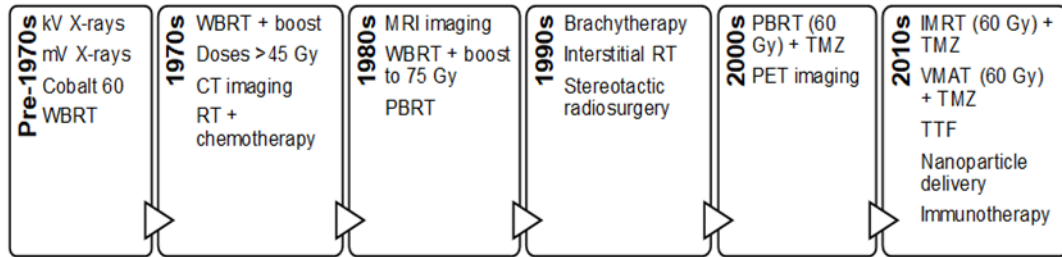
Figure 3.1.1. A timeline of radiotherapy developments in the treatment of glioblastoma multiforme (adapted from (160)).

CT – computed tomography, IMRT – intensity modulated radiotherapy, kV – kilovoltage, MRI – magnetic resonance imaging, MV – megavoltage, PBRT – partial brain RT, PET – positron emission tomography, TMZ – Temozolomide, TTF – tumour treating fields, VMAT – volumetric-modulated arc therapy, WBRT – whole brain RT.

3.1.3.3. Pathological features

As the name suggests, GBM tumours are rich with heterogeneous regions of hypoxic, necrotic, pleomorphic or pseudopalisading cells, contributing to its inherent treatment resisting nature (162,163). Histologically, there is little difference between primary and secondary tumours. Primary GBM tumours characteristically occur in older patients, whereas secondary GBM tumours initially manifest as low grade gliomas before later incurring more genetic abnormalities, transforming into GBM. Genetically the two can be distinguished with the primary tumours typically exhibiting epidermal growth factor receptor (EGFR) mutations and deletion of PTEN and p16. Secondary tumours, much less common, are characterised by a higher prevalence of the Krebs cycle enzyme isocitrate dehydrogenase 1 (IDH1) and p53 mutations, platelet-derived growth factor receptors (PDGFR) overexpression and deregulation of p16 and pRB. Regardless of these genetic differences, these tumours exhibit similar responses when treated with conventional therapies (152).

A pivotal publication from The Cancer Genome Atlas Research Network (TCGA) outlines over 60 genetic mutations in a typical GBM tumour. Characterising the genomic make-up of 206 patient samples identified the majority of GBM tumours contain mutated receptor tyrosine kinase/RAS/PI3K (RTK/RAS/PI3K) (seen in 90% of GBM tumours), p53 (85%) or pRB (79%) signalling pathways (164,165). Subsequent research identified four subtypes of tumours characterised by expression of signature genes: Classical, Neural, Proneural and Mesenchymal, discussed in detail by Verhaak *et al.* (165). The Classical subgroup is predominantly

characterised by amplification of chromosome 7, loss of chromosome 10, overexpression of EGFR and lack of p53 mutations. The Mesenchymal subtype is associated with *Neurofibromin 1* (*NF1)* and *PTEN* gene mutations, high expression of genes associated with the NF-κB (nuclear factor kappa-light-chain-enhancer of activated B cells) pathway and expression of markers Chitinase-3-like protein 1 (CHI3L1) and Hepatocyte growth factor receptor (HGFR). The Proneural class feature alterations of PDGFRA and IDH1, p53 mutations, loss of heterozygosity, high expression of oligodendrocytic development genes *NKX2*-2 and *oligodendrocyte transcription factor* (*OLIG2)* and the presence of other several proneural development genes. Finally the Neural subtype are defined by the presence of neural markers such as *NEFL, GABRA1, SYT1* and *SLC12A5 (neurofilament light, Gamma-Aminobutyric Acid Type A Receptor Subunit Alpha1, Synaptotagmin 1* and *Solute Carrier Family 12 Member 5*) (165)*.* The clinical relevance of targeting these subtypes remains unanswered, and single cell ribonucleic acid (RNA) sequencing has identified cells of all subtypes in the same tumour (166).

One of the most significant prognostic biomarkers for GBM is the methylation status of the O6-methylguanine DNA methyltransferase (MGMT) promoter. Approximately 40% of GBM tumours have a methylated MGMT promoter and are more sensitive to TMZ because of unrepaired DNA damage (164). However, in the analysis of the TCGA data, MGMT methylation status was not associated with a specific subtype, hampering efforts to identify groups patients for which TMZ would be beneficial.

Another defining characteristic of GBM tumours, and a significant cause of high reoccurrence rates, is its inherent nature to migrate and invade surrounding brain tissue. However, it rarely metastasises to other areas of the body indicating a preference for the brain microenvironment, contained by the blood-brain-barrier (167,168). Invasion through the extracellular space of the brain can be divided into two pathways, into the perivascular space mediated by laminin and collagen IV, and into the brain parenchyma (narrow space containing neuronal and glial cells) (168,169). To navigate through these different compartments imaging studies have shown invading cells undergo dramatic shape and volume changes and adhere to and then degrade the ECM (170). Improved imaging techniques, such as the use of diffusion tensor imaging, can better differentiate the gross tumour volume and infiltrative margins, which could reduce RT margins and improve normal tissue sparing (171).

3.2. Methods

All laboratory work was carried out in the Oglesby Cancer Research Building (OCRB) at The University of Manchester. Commercial suppliers and manufacturers are documented at the first mention of the product or equipment in the text. All single use plasticware was originally obtained from Corning Inc. A complete list of all stock solutions and recipes can be found in Appendix A2.1.

3.2.1. Equipment sterilisation

Reusable glassware and plasticware, pipette tips and Eppendorf tubes were sterilised prior to use by autoclaving at 121°C (2 bar) for 15 minutes. The Incucyte Woundmaker tool (Essen Bioscience) used to create uniform scratches in a 96 well plate was sterilised using 70% v/v ethanol for 5 minutes immediately before use and 0.5% w/v Alconox, sterile distilled H_2O (dH_2O) and 70% v/v ethanol for 5 minutes each. HEPES-buffered saline (HBS, pH 7.4) and $CaCl_2$ used in the hydrogel experiments were sterilised using a 0.22 μm filter and the alginate and gelatin hydrogels were filtered using a 0.45 μm filter prior to use. All other tissue culture grade solutions were sterilised by autoclaving as described above.

3.2.2. Cell culture

3.2.2.1. General

All cell culture work was undertaken in a HEPA filtered class II laminar flow biological safety cabinet using aseptic techniques. Before and after use, internal surfaces were disinfected with 10% v/v Distel (Scientific Laboratory Supplies Ltd.) followed by 70% v/v ethanol. Any waste (unwanted cells, medium or solutions) was transferred to a large bucket containing 10% v/v Distell, for a minimum of 1 hour, before being discarded.

3.2.2.2. Culture of Glioblastoma Multiforme cell lines

In between experimental use, cells were incubated at 37°C in 5% CO_2 conditions in T75 flasks containing 12 ml of Roswell Park Memorial Institute 1640 (RPMI, Sigma-Aldrich, cat. no. R0883-500ml) medium supplemented with 2 mM L-glutamine (Sigma-Aldrich, cat. no. G7513-100ml) and 10% v/v fetal bovine serum (FBS, Sigma-Aldrich, cat. no. F7524-500ml), herein referred to as complete medium. For humidification the incubators contained trays of sterile dH_2O, supplemented with Aqua Stabil (2 ml/L, Sigma-Aldrich). For routine passaging, cells were first briefly washed with sterile phosphate-buffered saline (PBS) and covered in trypsin-EDTA (Sigma-Aldrich, cat. no. T3924-100ml). The flasks were incubated (37°C in 5% CO_2)

for approximately 5 minutes until all the cells become visibly detached from the flask. Complete medium was added to the suspended cell solution to inactivate the trypsin and a volume was transferred to a new flask. When required for seeding, cells were collected, as described above, and centrifugation was performed using a benchtop centrifuge (Thermo Fisher Scientific) for 5 minutes at 400 g. Individual cell counting was performed using a Neubauer Haemocytometer with the cell suspension combined with trypan blue solution (1:1 ratio, Sigma-Aldrich, cat. no. T8154) to assess viability.

3.2.2.3. Cryopreservation and recovery

Cells were collected from T75 flasks, as detailed above for passaging, and collected as a cell pellet after centrifugation. The cell pellet was re-suspended in RPMI 1640 medium supplemented with 40% v/v FBS and 10% v/v dimethyl sulphoxide (DMSO), 2 ml for each T75 flask centrifuged. 1 ml of cell suspension was transferred into each cryovial (Thermo Fisher Scientific) and then transferred to a CoolCell (Corning Inc.) for storage in a -80°C freezer. After 24 hours at -80°C, vials were transferred to a liquid nitrogen Dewar for longer term storage.

When required, cells were thawed rapidly at 37°C before being transferred to a 15 ml tube containing 10 ml pre-warmed complete medium. Cells were centrifuged as described above, the supernatant was discarded and the cell pellet was resuspended in 5 ml of complete medium and transferred to a T25 flask. Once significant growth was seen the cells were transferred to a T75 flask using the technique for passaging as described above.

3.2.2.3. Cell line authentication and Mycoplasma testing

Cell line authentication and mycoplasma testing was performed by the Molecular Biology Core Facility, Cancer Research UK-Manchester Institute (MBCF CRUK-MI, Alderley Park). To avoid cross-contamination of cell lines, strict cell culture practice was followed and cell lines were authenticated (short tandem repeat profiling) to confirm their identity. For each cell line 50 µl samples were collected at a cell density of ~$2x10^6$ cells/ml of RPMI 1640 medium supplemented with 10% v/v FBS and 10% v/v DMSO.

All cell lines were routinely tested for mycoplasma contamination through quantitative polymerase chain reaction, by collecting 100 µl samples of medium from flasks of cells.

3.2.3. Statistics

Data is presented graphically using the programming language R and interface RStudio (v. 3.6.3). In most cases, the mean values ± the standard error of at least three independent experiments are presented, additionally the means of the individual biological replicates are included on the graphs. Method optimisation was only repeated once for most experiments. Were appropriate, statistical analyses using Wilcoxon rank sum tests were performed using R. Levels of significance are indicated in the text where the p value obtained was <0.05.

3.3. RESULTS: RADIATION RESPONSE IN GLIOBLASTOMA MULTIFORME

Summary

This chapter describes the laboratory experiments with the aim to provide a comprehensive determination of the radiation response across a panel of glioblastoma multiforme (GBM) cell lines, prior to developing 3D cellular models that could permit biologically relevant irradiations within the phantom.

The radiosensitivity of four GBM cell lines (A172, LN18, T98G and U251) were examined using the clonogenic survival assay. As GBM cell lines are inherently radioresistant, the cells were irradiated at doses ranging from 0-12 Gy. Most of the literature focuses on the use of one or two cell lines per experiment, and uses limited dose levels.

Following the results of the clonogenic survival assay, the DNA damage and repair capacity and mitochondrial metabolism profiling were performed using a dose of 4 Gy. This dose was chosen as a balance between maintaining cell viability, yet a response to radiation could be identified.

Author contributions

RADIATION RESPONSE IN GLIOBLASTOMA MULTIFORME

Emma R. Biglin[1]*, Amy L. Chadwick[1,2], Elham Santina[1,2], Kaye J. Williams[3], Adam H. Aitkenhead[1,3], Gareth J. Price[1,2], and Karen J. Kirkby[1,2]

[1]Division of Cancer Sciences, Faculty of Biology, Medicine and Health, University of Manchester, Manchester, UK. [2]The Christie NHS Foundation Trust, Manchester, UK. [3]Division of Pharmacy and Optometry, Faculty of Biology, Medicine and Health, University of Manchester, Manchester, UK, [4]Christie Medical Physics and Engineering, The Christie NHS Foundation Trust, Manchester, UK.

Abstract

Glioblastoma multiforme (GBM) is a highly aggressive brain tumour with poor survival rates, despite aggressive treatments. Although the benefit for radiotherapy (RT) is clear in increasing survival rates, only a quarter of patients survive more than a year and 5% survive for 5 years or more. Here, we investigated the clonogenic survival, DNA damage repair response and mitochondrial metabolic profile after exposure to irradiation in four distinct GBM cell lines. Variations were observed in the clonogenic survival capacity and the residual DNA damage after RT suggesting variations in the radiosensitivity of the four cell lines tested. In all but one cell line, radiation increased the oxygen consumption and extracellular acidification rates, in varying degrees, suggesting an increase in metabolic active and preference for glycolysis. Observed differences across the four cell lines confirms the cellular heterogeneity across GBM tumours, which increases the difficulty in improving clinical outcomes.

3.3.1. Introduction

Glioblastoma Multiforme (GBM) is the most malignant form of primary brain tumour in adults and accounts for 27% of all brain tumours (7,172). The current standard of care for GBM in the UK is a surgical resection then radiotherapy (RT) with concomitant temozolomide (TMZ), followed by adjuvant TMZ alone (157). There is a significant need for post-operative RT in the treatment of GBM, given the highly invasive nature limiting the success of a complete surgical resection (173). Improvements over the current standard treatment options remain limited owing to its complex and invasive nature and cellular heterogeneity, hampering efforts to develop targeted or personalised treatments based on a specific tumour genotype (152). Although there are multiple factors determining the radioresistance of GBM, the underlying molecular network has yet to be defined and it remains a significant clinical issue. Signalling pathways, microRNAs, hypoxia, the tumour microenvironment and glioma stem cells have all been implicated, and described in detail by Han *et al.* (174).

The panel of four GBM cell lines used in this study provides heterogeneity in p53 and phosphatase and tensin homolog (PTEN) function, O6-methylguanine DNA methyltransferase (MGMT) promoter methylation and cellular morphology (175–177). p53 is responsible for hundreds of genes indirectly regulating processes relating to the cell cycle, cell death, DNA damage repair and metabolism (178). Similarly, PTEN controls cell survival, proliferation and growth, predominantly as a negative regulator of the phosphatidylinositol-3-kinase, serine/threonine protein kinase B and the mammalian target of rapamycin (PI3K/AKT/mTOR) pathway (179). Genetic inactivation of PTEN and p53 tumour suppressor genes are the most frequent mutations in GBM tumours, both contributing to a heightened radioresistant phenotype and demonstrate a synergistic effect on gliomagenesis (27,28). These mutations are responsible for sustained proliferative signalling and angiogenesis, evading growth suppression and apoptosis, limitless replication, genomic instability and metabolism deregulation (181). The *MGMT* gene encodes DNA repair proteins to prevent mutation and cell death, acting as a protective mechanism from carcinogenesis (182). High levels of MGMT activity are associated with a treatment resistant phenotype via an increased DNA damage repair capacity. The methylation of the *MGMT* promoter is a significant prognostic indicator of the response to TMZ, almost doubling the median survival for patients (182).

Ionising radiation causes cell death by directly damaging the molecular structure of the DNA molecule or indirectly, through the production and subsequent action of free radicals (e.g. hydroxyl) (183). The repair of DNA double strand breaks (DSBs) occurs either via homologous recombination (HR) or non-homologous end joining (NHEJ). H2A histone family member X (H2AX) is a vital protein recruited for the repair of DNA DSBs. H2AX is phosphorylated on serine 139 (γ-H2AX), when DSBs are detected by the kinase proteins ataxia-telangiectasia mutated (ATM), DNA protein kinase catalytic subunit (DNA-PKcs) and Ataxia telangiectasia and Rad3 related protein (ATR) (184). Activation of the PI3K/AKT pathway, significantly higher in PTEN-deficient cells, accelerates the repair of DNA DSBs, contributing to the radioresistance of GBM cells (150). PTEN-null cells correlate with higher levels of ATM activation after increased levels of oxidative stress causes DNA damage. Tumour cells rely on ATM to repair this DNA damage and maintain cell viability in the presence of oxidative stress (185).

One of the more recent areas of investigation for potential anti-cancer therapeutic targets is cell metabolism. In GBM cells, significant reprogramming takes place in the metabolic machinery (177). Numerous studies have demonstrated the adaptation to glycolysis over oxidative phosphorylation even with an abundance of available oxygen, a typical hallmark of tumours (the Warburg effect), often presenting a more aggressive phenotype leading to malignant progression (186). To sustain the survival, excessive proliferation and limitless replication of malignant cells they must increase energy production by reprogramming their metabolism. Therefore many of the activated oncogenes or inactivated tumour suppressor genes, including p53 and PTEN, responsible for these phenotypes are also mediators of the metabolic pathway and promote the shift from oxidative phosphorylation to aerobic glycolysis (26,27,32). Following the loss of PTEN function, downstream signalling mediated by the PI3K/AKT pathway and augmented expression of hypoxia-inducible factor -1α (HIF-1α) enhances glycolytic enzyme activity and permits the rapid phosphorylation of glucose to adenosine triphosphate (ATP) via glycolysis (14,29). This elevated glucose uptake offers a favourable environment for the continuous growth of tumour cells, even in the presence of hypoxia (188).

The aim of this study was to profile the radiosensitivity, the extent of DNA DSBs and their repair and the health of the cells via measurement of metabolic parameters in a panel of GBM cell lines.

3.3.2. Methods

3.3.2.1. Culture of Glioblastoma Multiforme cell lines

Human GBM cells lines A172, LN18, T98G and U251 were cultured in Roswell Park Memorial Institute 1640 (RPMI, Sigma-Aldrich, cat. no. R0883-500ml) medium supplemented with 2 mM L-glutamine (Sigma-Aldrich, cat. no. G7513-100ml) and 10% v/v fetal bovine serum (FBS, Sigma-Aldrich, cat. no. F7524-500ml), referred to herein as complete medium. All cell lines were originally obtained from the American Type Culture Collection (ATCC, Middlesex, UK) and were authenticated and regularly tested for the presence of mycoplasma. In between experimental use, cells were incubated in a humidified environment at 37°C in 5% CO_2 conditions. Routine observation of cells was performed almost daily using a standard phase contrast EVOS XL (Thermo Fisher Scientific) microscope. All cell lines were passaged every 3-4 days when the cells reached >70% confluent. Use of each cell line was limited to <20 passages, with a split ratio of between 1:2 and 1:10.

3.3.2.2. Irradiation procedure

X-ray irradiation was performed using the CIX3 irradiator (Xstrahl Inc. Walsall UK) and the standard settings: 300 kV, 10 mA, source-to-surface distance of 400 mm and 0.7 mm thick Cu filter. The half value layer thickness of this irradiator is 2.3 mm Cu. The time required to irradiate samples was manually inputted based on a dose rate of 2.07 Gy/minute. Samples were placed in the centre of a rotating turntable to ensure homogenous dose delivery across the target. For each irradiation experiment control plates were included, being exposed to the same environmental conditions as the irradiated plates without exposure to X-rays, herein referred to as sham irradiated.

3.3.2.3. Clonogenic survival assay

Approximately $5x10^5$ cells were seeded into T25 flasks (Corning, Sigma-Aldrich, cat. no. CLS430639), 1 flask for each dose being tested, in 5 ml complete RPMI medium. When cells reached >70% confluent, after ~24 hours of incubation, the flasks were irradiated to doses of 2, 4, 6, 8, 10 and 12 Gy, with a sham irradiated control. Immediately after irradiating, cells were detached using trypsin-EDTA (Sigma-Aldrich, cat. no. T3924) and centrifuged. After resuspension in complete medium, cells were counted and seeded at a range of densities in 6-well tissue culture treated plates (Corning, Sigma-Aldrich, cat. no. 3516) and incubated (humidified atmosphere, 37°C and 5% CO_2) for 7-21 days. Seeding densities were

optimised based on the ability to visually count between 10-100 individual colonies for each dose, whilst maintaining the same incubation period as the sham irradiated control.

When sufficient colony formation was observed the medium was discarded, the plates were washed with sterile phosphate-buffered saline (PBS) and the colonies were fixed and stained with crystal violet solution (10% in 50% methanol in distilled H_2O (dH_2O), Appendix 2.1) for >30 minutes. Once the stain was removed, the plates were rinsed in water and left to air dry. NaOH crystals were added to the water to neutralise the crystal violet before disposal. Plates were scanned using the GelCount (Oxford Optronix) and colonies containing more than 50 cells were manually counted using ImageJ software. Surviving fraction (SF) was calculated for each dose using equation 1 and the data plotted with the curves fitted to a linear quadratic model (equation 2).

Equation 1: *Plating efficiency (PE) = (average colony count / seeding density) x 100*

SF = (average PE for each dose / average PE for 0Gy)

Equation 2: $SF = exp(-\alpha X - \beta X^2)$,

where α describes the linear and β describes the quadratic component of the curve and X is the dose. Surviving fractions at 2 and 4 Gy and the alpha/beta ratio were calculated as parameters for radiosensitivity.

3.3.2.4. Immunofluorescence for radiation-induced γH2AX foci

Cells were seeded at a density of $7.5x10^3$ cells/well in three black 96-well Nunc Optical Bottom microplates (Thermo Fisher Scientific, cat. no. 10281092) in 200 µl of complete medium. Plates were then incubated overnight to allow cell attachment prior to irradiation. Optimisation of this experiment involved seeding cells at densities of between $2.5x10^3$ and $1x10^4$ cells/well to determine the best density to isolate individual nuclei during analysis. Approximately 24 hours after seeding, two of the plates were irradiated as described above with a 4 Gy dose of photons, and one plate sham irradiated (0 Gy).

30 minutes post-irradiation cells in the 0 Gy and one of the 4 Gy plates were fixed. The medium was removed and each well washed with 100 µl of PBS. 100 µl of 10% formalin (Sigma-Aldrich, cat. no. HT501128) was added to each well for 10 minutes followed by a final PBS wash. 200 µl of PBS was added to each well and the plates

were stored at 4°C. This process was repeated with the final 4 Gy irradiated plate 24 hours post-irradiation.

To highlight the DNA double strand breaks, the PBS was removed and 200 µl of 0.1% v/v Triton-X (Sigma-Aldrich) in PBS solution was applied to each well for 15 minutes at room temperature, to permeabilise the cell membrane. Following two 100 µl PBS washes, 200 µl of 1% w/v bovine serum albumin (BSA, Sigma-Aldrich, cat. no. A9418) in PBS solution is then added for 30 minutes, to prevent non-specific binding when the antibodies are added. After the removal of the BSA, 50 µl of the diluted (1:1000 in the BSA solution described above) primary mouse monoclonal γH2AX antibody (EMD Millipore, cat. no. 05-636, lot #3153259) was added to each well and incubated at 37°C, 5% CO_2 for 1 hour. Following three PBS washes, and under reduced light, 50 µl of the diluted (1:1000 in BSA solution) conjugated secondary antibody (Alexa-488 labelled Donkey anti-mouse, Invitrogen, cat. no. A-21202, lot #1890861) was added to each well. A 45 minute incubation at 37°C 5% CO_2 was followed by two PBS washes. To highlight individual nuclei, 50 µl of Hoechst 33342 (1:2000 dilution in BSA solution, Thermo Fisher Scientific, cat. no. 10150888, lot #SF2401593) was added to each well for 10 minutes, at room temperature, then removed. Two PBS washes completed the process. 200 µl PBS is added to each well before sealing and storage of the plates at 4°C.

Cells were imaged using the Operetta CLS or Opera Phenix High-Content Analysis Systems (PerkinElmer Inc.) using a 60x 0.45 air objective and the following filters: Hoechst: excitation wavelength (ex): 360–400 nm, emission wavelength (em): 420–480 nm; Alexa488: excitation: 460–490 nm, emission: 500–550 nm. Analysis involved using the ImageJ "Analyse particles" function to highlight the nuclei and the "Find maxima" process to count individual foci (Figure 3.3.1). More than 100 cells were counted over four well technical repeats from 2 independent experiments.
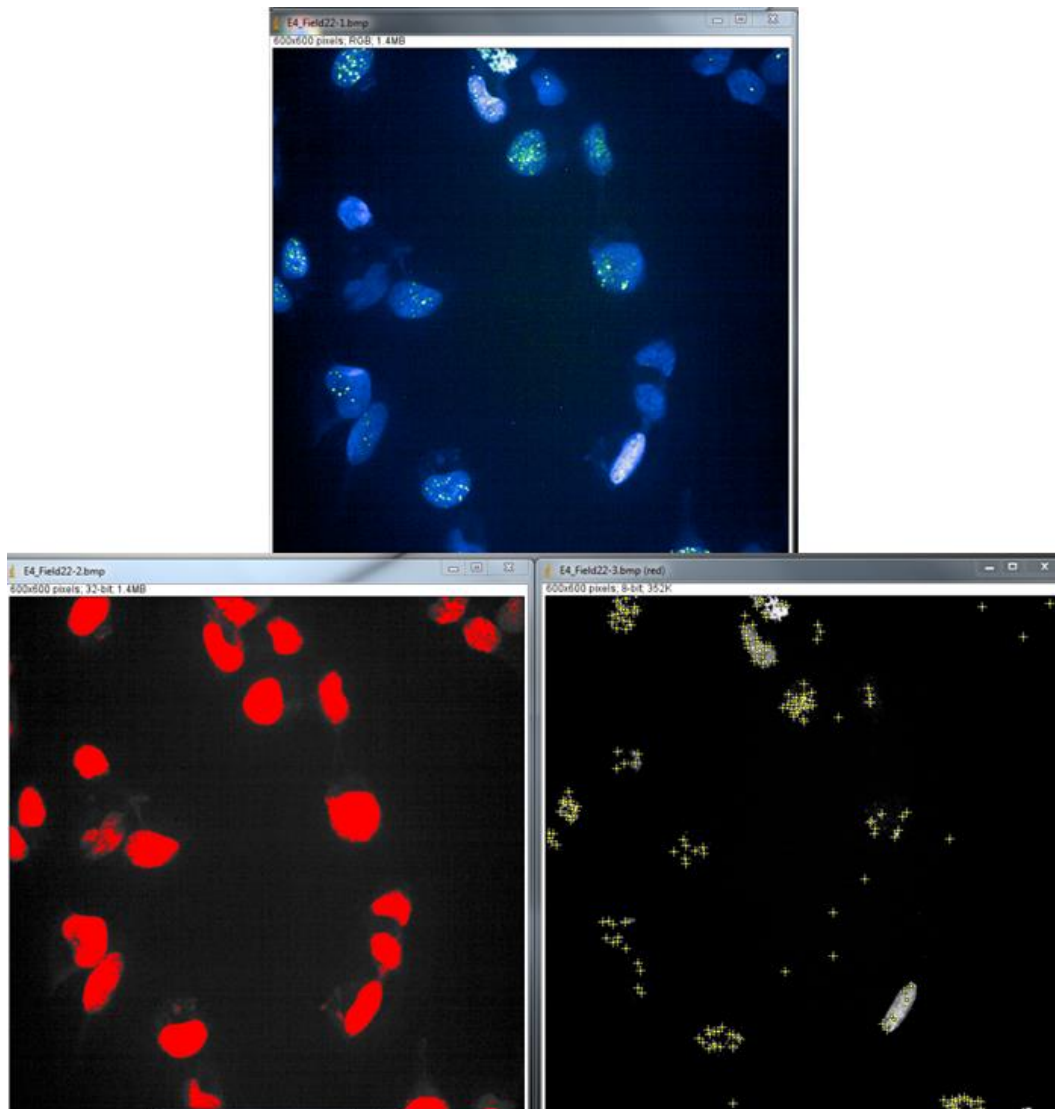
Figure 3.3.1. ImageJ analysis to quantify DNA damage

Images taken from the Operetta imaging system following γH2AX antibody labelling were opened in ImageJ. To count the individual cells the colour channels of the image were split and image thresholding was performed on the green channel image until all nuclei were highlighted (red). The "Analyse particles" analysis function was used to count the nuclei. Using the original image the "Find Maxima" process was applied and the noise tolerance adjusted until all individual foci were selected (yellow dots).

3.3.2.5. Assessment of oxygen consumption

To measure oxygen consumption and extracellular acidification rates (OCR and ECAR, respectively) the Seahorse XFe96 flux Analyser (Agilent Technologies, Inc.) was used. To avoid cell detachment as the compounds are injected, 96-well Seahorse XF Cell Culture Microplates (Agilent Technologies, Inc.) were coated with

poly-d-lysine (20 µg/ml in sterile dH_2O) by adding 25 µl for 20 minutes followed by two washes with sterile dH_2O. Once dry, $5x10^3$ cells were seeded into each well in 200 µl of complete medium and incubated overnight (37°C, 5% CO_2). The following day the one microplate was irradiated (4 Gy), as described above, and one plate was sham-irradiated.

In preparation for the assay, the Seahorse XFe96 flux Analyser was switched on and 200 µl of Seahorse XF Calibrant solution (Agilent Technologies, Inc., cat. no. 100840-000) was added to each well of the calibration plate, hydrating the sensor cartridge (Agilent Technologies, Inc.). This was left to incubate overnight (37°C, without CO_2). Immediately prior to running the assay, the complete medium was removed from each plate, followed by a wash using the pre-warmed Seahorse XF Dulbecco's Modified Eagle Medium (DMEM) medium (Agilent Technologies, Inc., cat. no. 103575-100) supplemented with 2 mM sodium pyruvate (Sigma-Aldrich, cat. no. P2256), 2 mM glutamine (Sigma-Aldrich, cat. no. G3126), and 10 mM glucose (Sigma-Aldrich, cat. no. G8644). A further 175 µl of this medium was added to each well and the plates incubated in a 0% CO_2 incubator at 37°C for 1 hour. While the plate is acclimatising to the conditions, 25 µl of each compound (in supplemented Seahorse XF DMEM medium) was added into the appropriate injection ports on the cartridge: 1 µM oligomycin (Sigma-Aldrich) added to port A, 600 nm FCCP (Carbonyl Cyanide-4-(trifluoromethoxy)phenylhydrazone, Sigma-Aldrich) added to port B and 1 µM rotenone (Sigma-Aldrich, cat. no. R8875) and antimycin A (Sigma-Aldrich) added to port C. The Seahorse flux analyser software Wave (V 2.6.0.31) was used to input the experiment details and set the injection and measurement parameters. All measurements were taken as a cycle of 3 minutes mixing and 3 minutes measuring. 5 measurements were taken prior to the first injection to indicate baseline metabolism and then each injection was followed by 3 measurements. The cartridge and calibration plate were then inserted into the analyser to equilibrate then calibrate. The plate was then inserted to the analyser when instructed.

Upon completion of the assay the cells were fixed using trichloroacetic acid (TCA). After removal of the medium and a PBS wash, 100 µl of 10% v/v TCA in dH_2O was added to each well for 1 hour at 4°C, followed by another PBS wash. The plates were left to air dry overnight. OCRs produced by the Seahorse XF Analyser were normalised against cellular protein content using a sulforhodamine B (SRB) assay. First, 100 µl of 4% v/v SRB (Sigma-Aldrich, cat. no. 230162) diluted in 1% v/v acetic acid (Sigma-Aldrich, cat. no. A6283) in dH_2O, was added to each well for 15

minutes at room temperature. Plates were then washed twice with 1% v/v acetic acid. Once dried, 100 µl of Tris buffer (adjusted to pH 8.8, Sigma-Aldrich, cat. no. T4904) was added and left on a plate shaker for 5 minutes. Absorbance was detected on the Varioscan Lux Plate reader (Thermo Fischer Scientific) at 540 nm.

3.3.2.6. Statistics

The clonogenic survival data was fitted to a linear quadratic model using RStudio (v. 3.6.3). All other data shows the overall mean ± the standard error and the means of each biological replicate from two to three independent repeat experiments. To evaluate statistical significance in the immunofluorescence microscopy and mitochondrial stress test assay, R (v. 3.6.3., (189) was used to perform Wilcoxon rank sum tests, comparing the means of the irradiated samples with the sham irradiated controls and the difference between time points to assess the extent of DNA damage and repair.

3.3.3. Results

3.3.3.1. Differences in radiosensitivity were observed between GBM cell lines

The clonogenic assay is the current gold standard for testing the cellular sensitivity to radiation and radiation/drug combinations. The assay tests the ability of cells to undergo cell division, where unlimited replicative potential is represented by the formation of colonies containing greater than 50 cells. The number of colonies for each dose provides a visual representation of cell survival compared to the number of colonies formed by non-irradiated cells (190). All cell lines exhibited proficient colony formation which gradually decreased with increasing radiation dose, regardless of increasing seeding density (Figure 3.3.2a). Only cell line U251 provided a sufficient number of colonies (>10) when irradiated with 10 Gy. The survival curves for GBM cell lines A172, LN18, T98G and U251 after irradiation with X-rays are presented in Figure 3.3.2b.
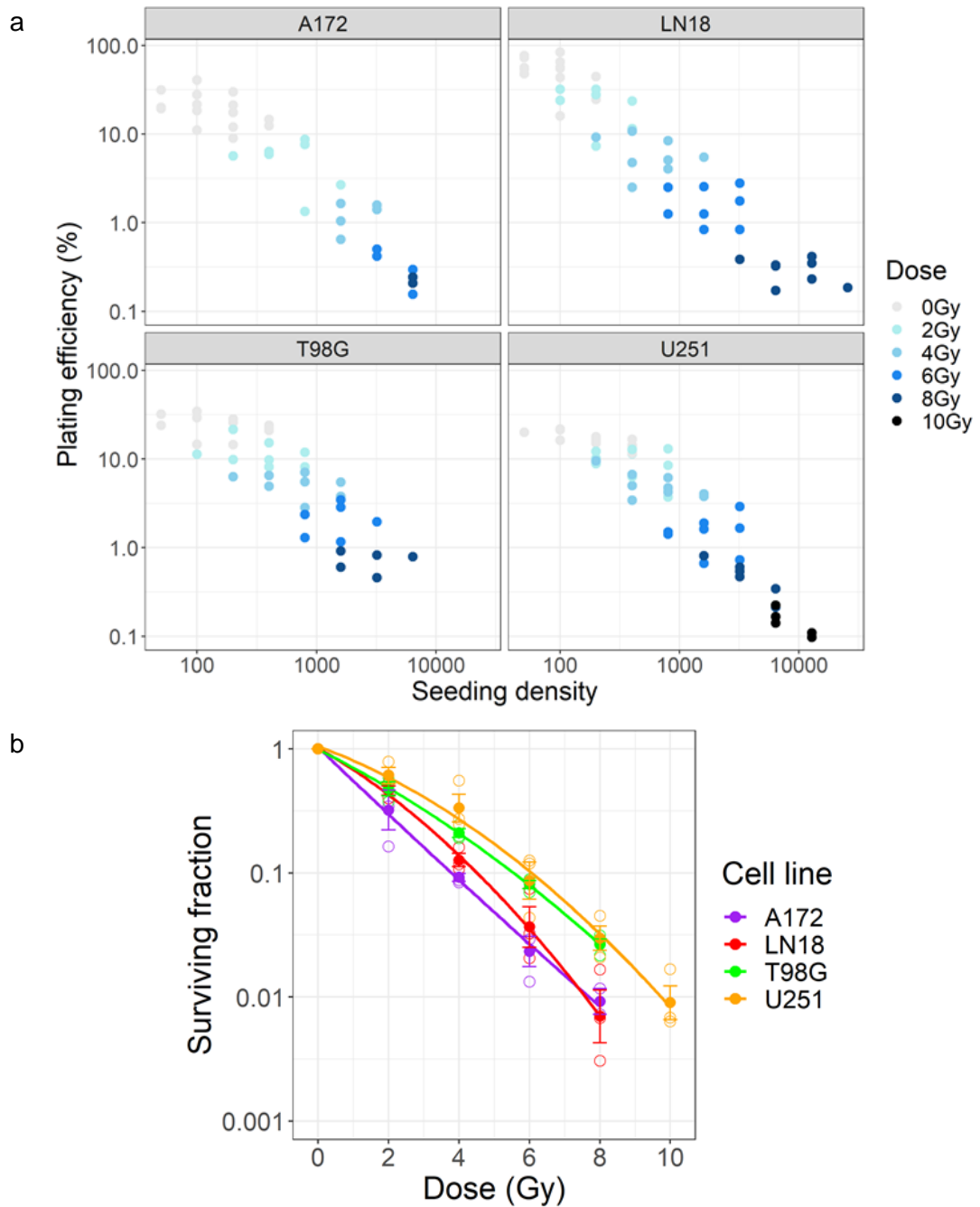
Figure 3.3.2. Human GBM cell lines have varying degrees of radiosensitivity.

a) Plating efficiencies (PE, ((average colony count / seeding density) x 100)) for all cell lines, at all doses tested. Data shown represents the mean PE for each seeding density in each of 3 individual experiments. b) Clonogenic survival curves for GBM cell lines A172, LN18, T98G and U251 after irradiation. Colonies were counted manually using ImageJ after an incubation period of between 7-11 days. Surviving fraction was calculated by calculating the PE for each dose and normalising against the 0 Gy control. Symbols represent mean (closed circles) ± standard error of 3 independent experiments (A172 8 Gy, n=2) and the mean of each independent experiment (open circle), with the curves fitted to a linear quadratic model.

By overlaying the curves for each cell line slight variations in radiosensitivity between different cell lines was observed. Overall, A172 and LN18 exhibited a higher degree of radiosensitivity than T98G and U251, supported by the α and β values (higher values indicates an increased level of radiosensitivity (160)) (Table 3.3.1). However, the SF2 (surviving fraction after exposure to 2 Gy) for LN18 and T98G were almost identical (Table 3.3.1). The sensitivity separation between cell lines becomes more apparent after exposure to 4 Gy (SF4, Table 3.3.2), the dose used in subsequent experiments.

Table 3.3.1. The surviving fraction after 2 and 4 Gy irradiation and the alpha/beta parameters for each GBM cell line.

	SF2	SF4	α/β ratio
A172	0.365 ± 0.109	0.093 ± 0.007	0.4253/0.03947 = 10.77
LN18	0.462 ± 0.039	0.129 ± 0.017	0.2795/0.0536 = 5.215
T98G	0.486 ± 0.056	0.211 ± 0.017	0.3318/0.01449 = 22.90
U251	0.643 ± 0.098	0.358 ± 0.100	0.1560/0.03178 = 4.622

3.3.3.2. Variations in the repair capacity between cell lines were observed

The extent of DSB formation and DNA repair characteristics were quantified using the presence of the DNA repair protein γH2AX as a marker of DSBs. Cells were fixed 30 minutes and 24 hours after 4 Gy irradiation (Figure 3.3.3).
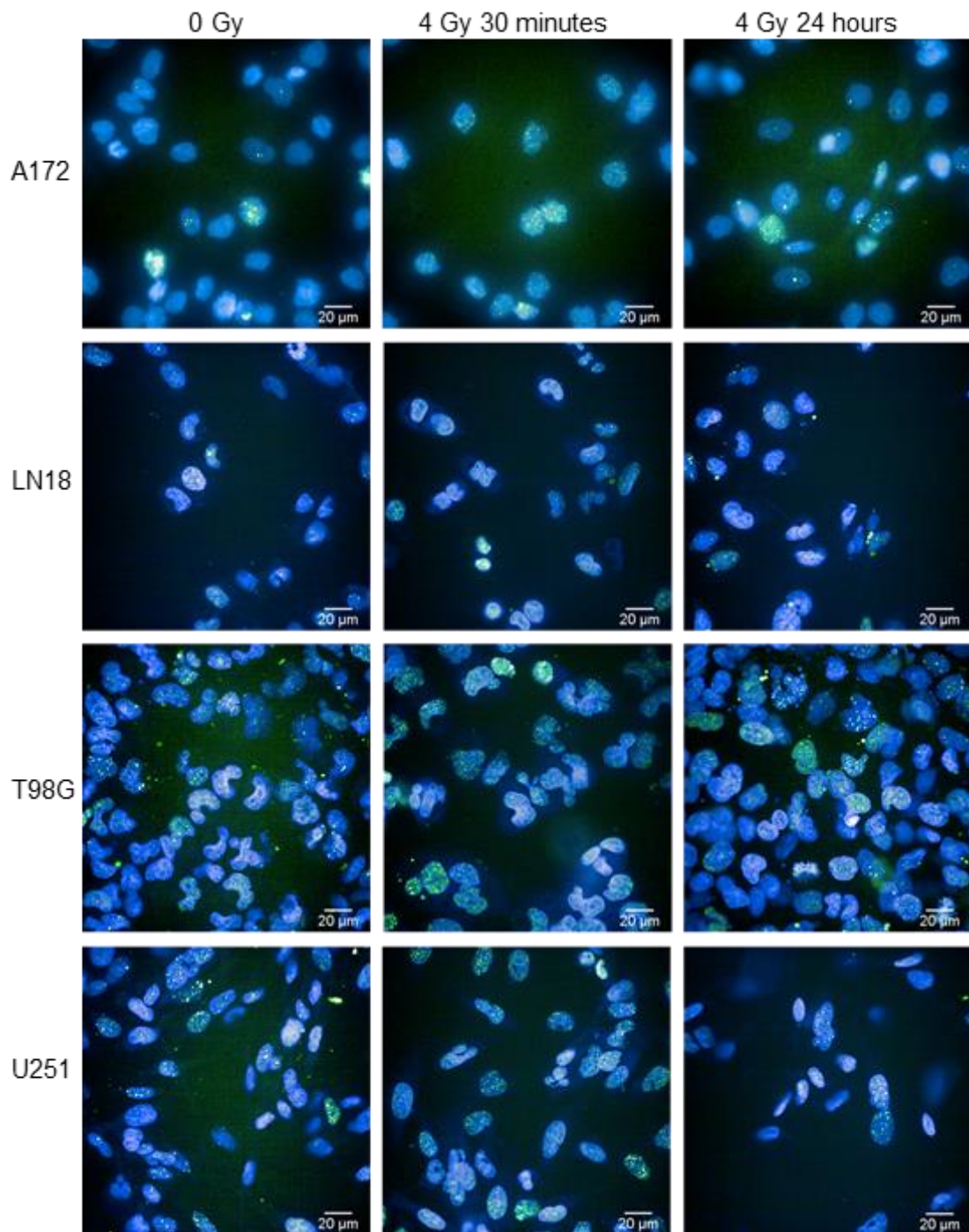
Figure 3.3.3. Immunofluorescence microscopy using γH2AX as a marker of DNA damage.

Representative images of all GBM cell lines used in this assay, stained with Hoechst and the DNA damage labelled with a fluorescent-tagged γH2AX antibody. γH2AX foci were observed in all cells lines, with background levels of DNA damage measured in the 0 Gy control, initial DNA damage quantified 30 minutes after exposure to 4 Gy and residual damage measured 24 hours post irradiation.

The mean counts of DNA damage foci in each nucleus are plotted in Figure 3.3.4 for the control (0 Gy), 30 minutes and 24 hour post-irradiation time points. 30 minutes after exposure, a significant increase in γH2AX foci is seen across all cell lines. Cell line A172 exhibited the highest degree of initial DNA DSBs after exposure to radiation, (Figure 3.3.4b) indicative of its increased radiosensitivity demonstrated in the clonogenic assay. After 24 hours, all cell lines had completed significant repair, with T98G demonstrating the fastest rate of repair (90.0% after 24 hours), and U251 the slowest (71.6%). The significant levels of residual DNA DSBs remaining 24 hours after irradiation in 3 of the 4 cell lines suggests a limited repair capacity and unlikely survival of these cells. The insignificant levels of residual γH2AX foci observed in T98G cells indicate a higher degree of radioresistance than the other cell lines, consistent with the clonogenic survival data.
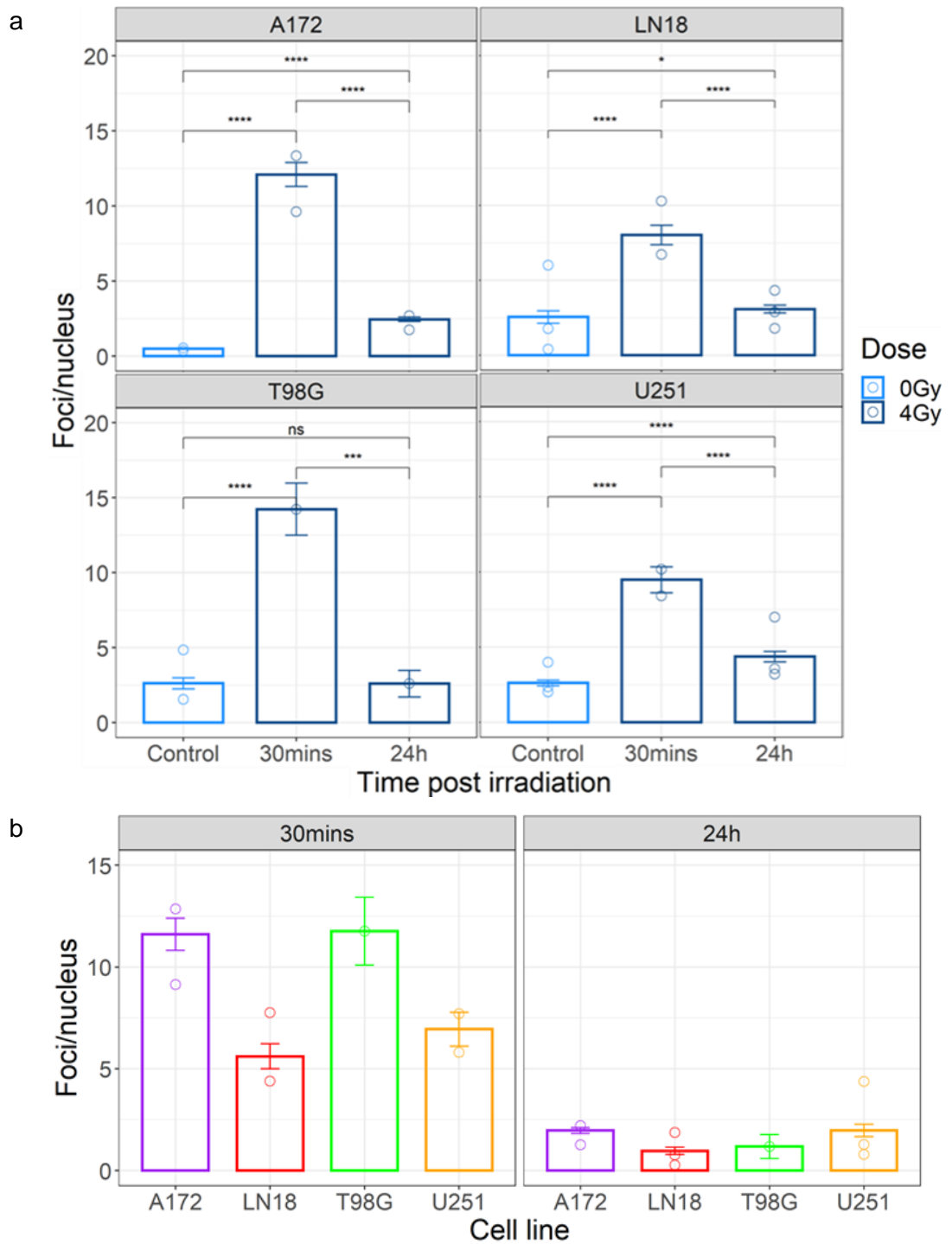
Figure 3.3.4. Levels of γH2AX foci in GBM cell lines following irradiation.

*Cells were sham irradiated or irradiated with 4 Gy and were fixed at 30 minutes and 24 hours post irradiation. The number of γH2AX foci were counted in >80 cells in at least 6 fields using ImageJ. a) The data shows the mean foci per nucleus ± standard error of at least two independent experiments. The open circles represent the mean of the biological replicates. ****: p<0.0001; ***: p<0.001; *: p<0.05; ns: p>0.05. b) The same data presented in (a) after normalising against the background levels (control) of γH2AX foci.*

3.3.3.3. Radiation increased the oxygen consumption rates in most cell lines

To investigate the impact of radiation on mitochondrial respiration, measurements of OCR, using the Seahorse XFe96 analyser, 24 hours post-irradiation were obtained. To account for any well-to-well variability and the impact of cell number on the OCR, the results were normalised against protein content, measured using an SRB assay performed upon completion of the assay. The injections of the metabolic inhibitors oligomycin, FCCP and rotenone-antimycin A permit the measurement of key parameters within mitochondrial respiration. Oligomycin inhibits ATP synthase. This inhibition hyperpolarises the mitochondrial membrane and blocks ATP-linked respiration (ALR) by preventing enzyme complexes from transporting protons across the inner mitochondrial membrane (192). The injection of FCCP as an uncoupling protonophore reverses this hyperpolarisation allowing the free flow of protons across the membrane, representing the maximum capability of the electron transport chain. Rotenone and antimycin A are inhibitors of the enzyme complexes I and III, which completely inhibits mitochondrial respiration (192).

The effects of these compounds on OCR in all four GBM cell lines are shown in Figure 3.3.5a. Following measurements of basal respiration (BR) i.e. the oxygen consumption required to maintain normal cell function by satisfying the typical ATP demand (193), the injection of oligomycin decreased the OCR by blocking ALR, with the remaining oxygen consumption a result of protons leaking across the mitochondrial membrane. A sharp increase in OCR was observed after the injection of FCCP indicating the maximum respiratory capacity (MRC), decreasing across the three measurements as the proton availability decreases. The difference in the maximum and basal respiration provides an indication of the reserve capacity (RC), reflecting the ability of the cells to respond to changing energy requirements, including those after exposure to radiation. The OCR following the injection of rotenone and antimycin A were used to normalise the previous parameters to ensure the rates calculated related only to the mitochondrial respiration. Across the four GBM cell lines, and before exposure to radiation, variations in OCR were observed (Figure 3.3.5a). LN18 demonstrated a lower BR and ALR than the similar rates seen in the other three cell lines. T98G exhibited the highest MRC, followed by U251 and A172, then LN18 with the lowest. T98G also displayed the highest RC, with similar rates seen in LN18 and U251 and almost no RC measured in A172 cells.

Variations in the OCR following exposure to X-ray radiation was observed, presented in Figure 3.3.5b. The OCR of A172 cells showed no significant change

after exposure to X-rays in any of the measured parameters. On the other hand, a significant OCR increase was measured in LN18 cells for all parameters after irradiating (Figure 3.3.5c). Radiation significantly increased the BR, ALR and MRC in T98G cells and the MRC and RC of the cell line U251.
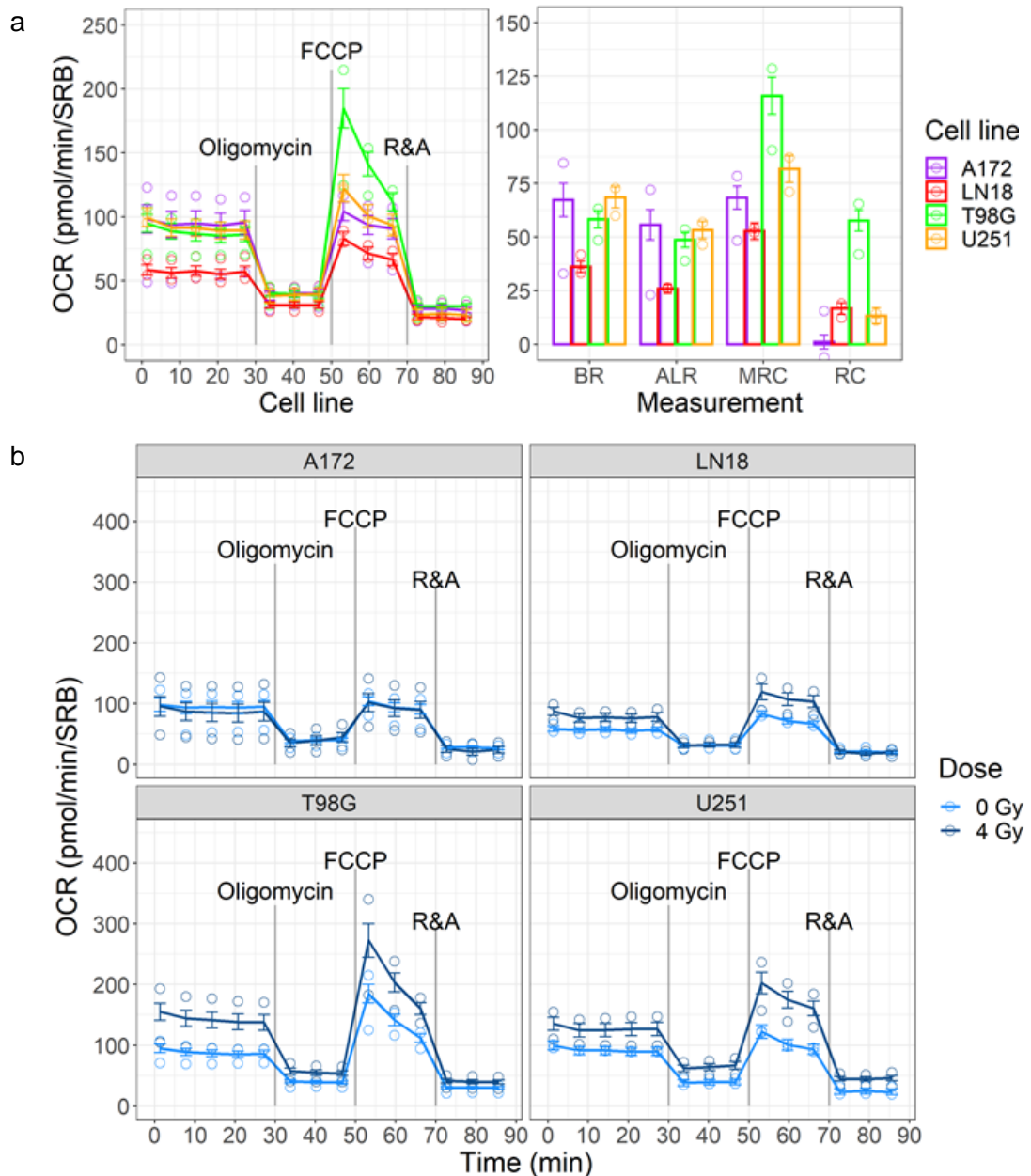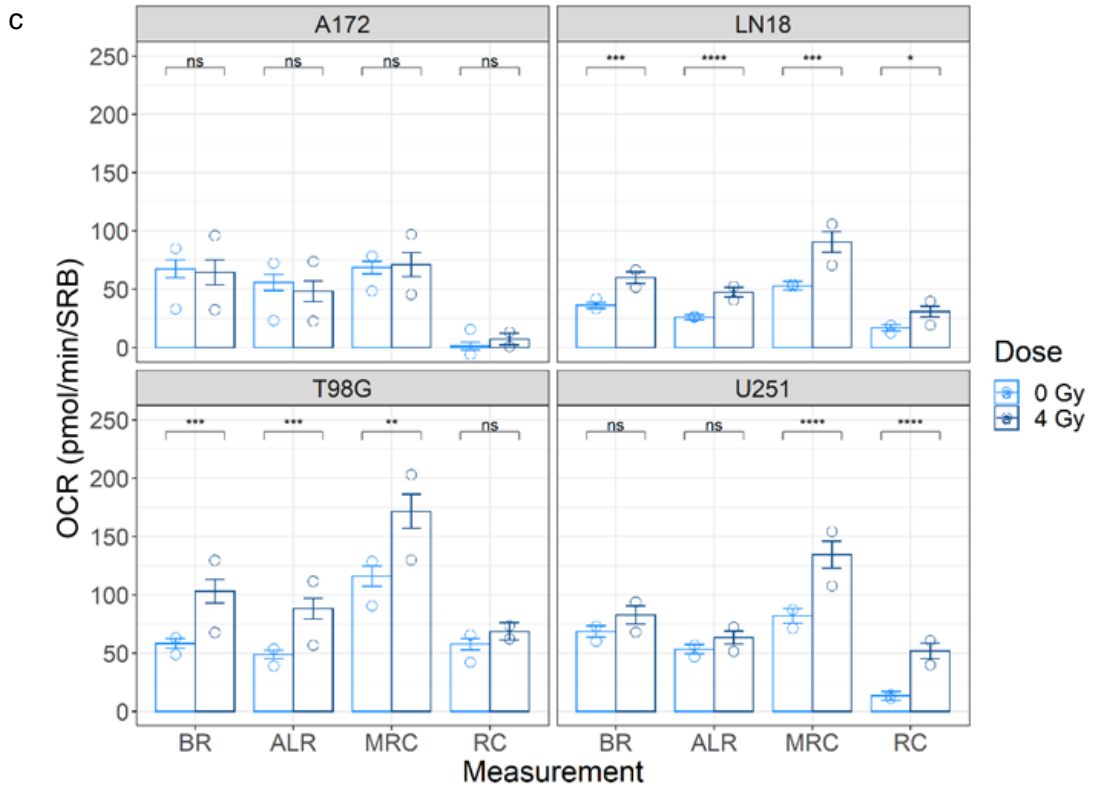
Figure 3.3.5. Radiation impacts mitochondrial respiration in GBM cell lines.

*a) Oxygen consumption rates (OCR) for GBM cell lines A172, LN18, T98G and U251 were measured using the Seahorse XF analyser. After 5 baseline respiration readings, oligomycin was injected, followed by FCCP then rotenone (R) and antimycin A (A), in 3 minute mixing/3 minute measuring cycles. Using the Seahorse traces, BR – basal respiration, ALR – ATP-linked respiration, MRC – maximum respiratory capacity and RC – reserve capacity of the mitochondria were calculated. b) The same data from the left panel of (a) compared to the OCR after exposure to 4 Gy X-ray radiation. c) The same data from the right panel of (a) compared to the OCR after exposure to 4 Gy X-ray radiation. All data presented represents the mean ± standard error of two independent experiments. The mean of each biological repeat is shown by the open circles. ****: p<0.0001; ***: p<0.001; **: p<0.01; *: p<0.05; ns: p>0.05.*

3.3.3.4. Radiation significantly increased the extracellular acidification rates of all cell lines

During the mitochondrial stress test assay, baseline ECAR was also measured, giving an indication of the levels of glycolytic capacity of each cell line (Figure 3.3.6). Baseline ECAR varied across each cell line, with A172 and U251 showing the lowest levels and T98G the highest. After exposure to radiation the ECAR increased significantly in all cell lines.
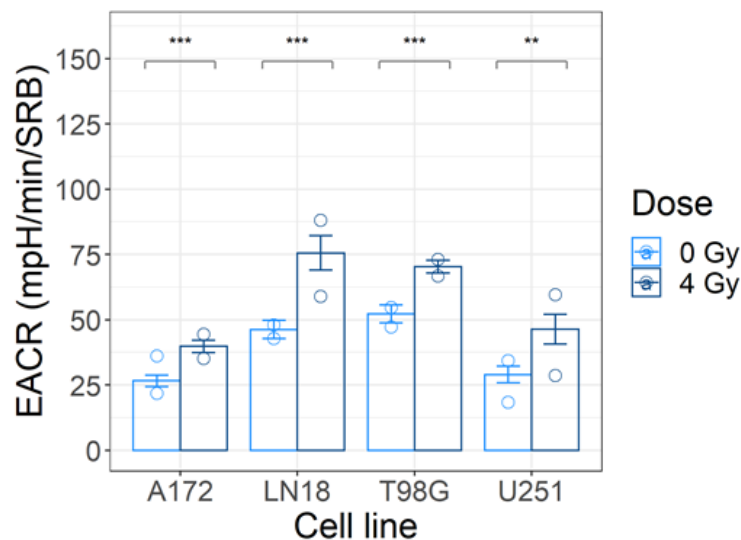
*Figure 3.3.6. Radiation increases the extracellular acidification rates in all cell lines. The mitochondrial stress test assay provides measurements of the extracellular acidification rates (ECAR), indicating the glycolytic capacity of the cells. Measured ECAR from the sham and 4 Gy irradiated samples were plotted. Data shown represents the mean ± standard error, and the mean of the two independent experiments are depicted as open circles. ***: p<0.001; **: p<0.01.*

When plotted against basal OCR, ECAR maps the preference for either oxidative phosphorylation or glycolysis. All cell lines exhibited similar levels of basal OCR/ECAR, starting in the bottom left corner of the graph, with A172 showing a slight trend towards oxidative phosphorylation and LN18 preferring glycolysis (Figure 3.3.7a). After irradiating, the metabolic profile shifted in all but the cell line A172. LN18 demonstrated a predominantly glycolytic response with an increase in ECAR. T98G and U251 became more metabolically active increasing both OCR and ECAR (Figure 3.3.7b).
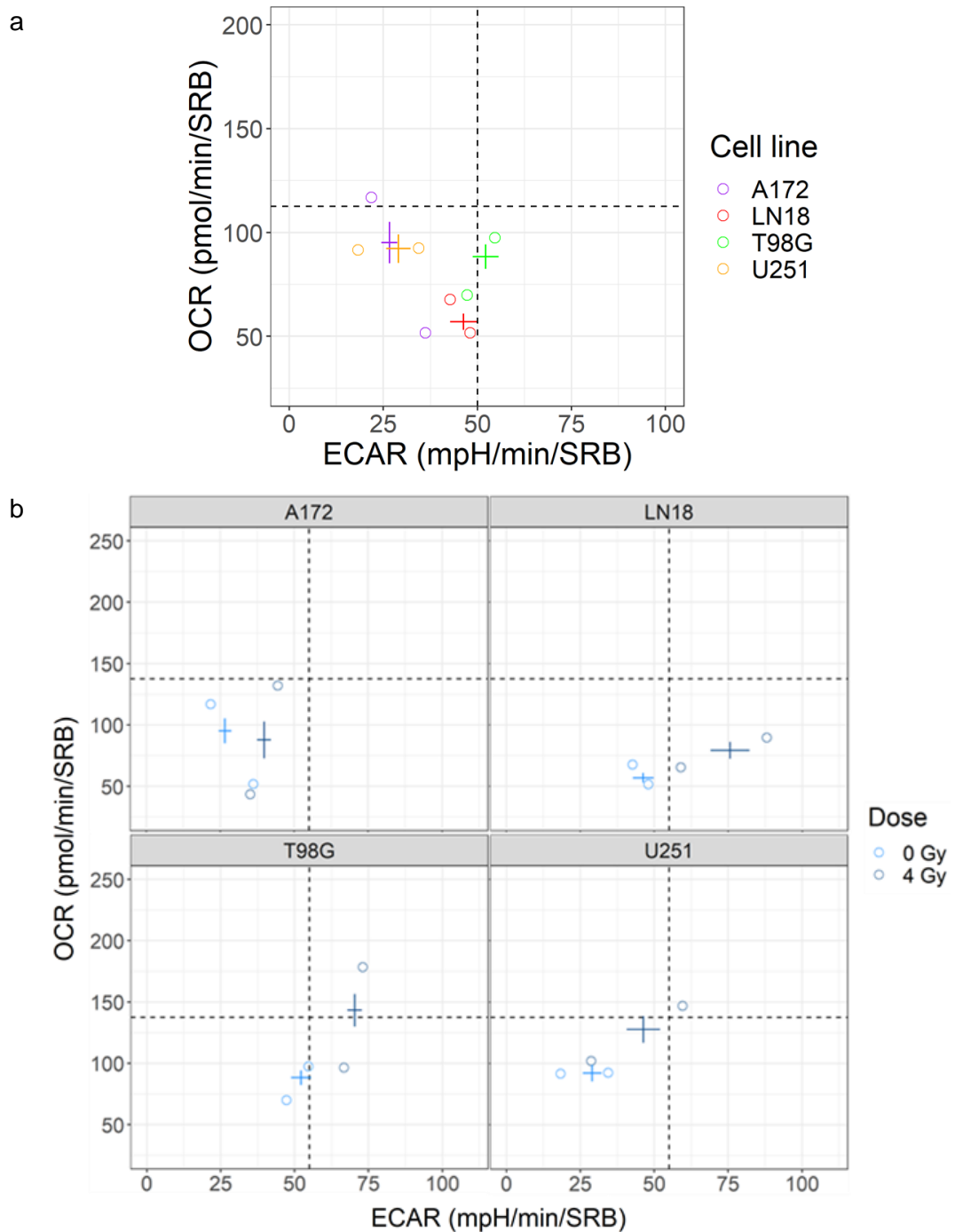
Figure 3.3.7. Radiation may shift the metabolic phenotype in some cell lines.

The mitochondrial stress test assay also provides the basal extracellular acidification rate (ECAR) which, when plotted against OCR, indicates the metabolic preference for oxidative phosphorylation (top left quadrant of the graph) or glycolysis (bottom right quadrant of the graph). a) The sham irradiated controls were plotted to compare metabolic phenotypes across the four GBM cell lines. b) OCR vs ECAR after irradiation. The data represents the mean of the biological repeats and the overall mean ± standard error of two independent experiments.

3.3.4. Discussion

Complexity is the defining feature of GBM. Aberrant genetic and epigenetic functionality, cellular plasticity, immune system evasion and metabolism changes create a diversity of phenotypes within a single tumour (165,194–196). This study demonstrated the impact of genetic heterogeneity across a panel of GBM cell lines, summarised in Table 3.3.2, following exposure to X-ray radiation. The GBM cell line A172 has an astrocytic-like morphology, with a functioning *p53* gene, deleted *PTEN* gene and has a methylated MGMT. In comparison, LN18 is an epithelial-type GBM cell line, with a functional *PTEN* gene, mutated *p53* gene and un-methylated MGMT (175). T98G and U251 cells have mutated *p53* and *PTEN* genes. Their differences lie in morphology and MGMT methylation, T98G being fibroblastic and MGMT methylated and U251 is astrocytic and MGMT un-methylated (175,176).

Table 3.3.2. Highlighted genetic heterogeneities of the cell lines examined in this study.

Cell line	Morphology	P53 status	PTEN status	MGMT status	References
A172	Astrocytic	Wild-Type	Deleted	Methylated	(177)
LN18	Epithelial	Mutated	Wild-type	Unmethylated	(175)
T98G	Fibroblast	Mutated	Mutated	Unmethylated	(176)
U251	Astrocytic	Mutated	Mutated	Methylated	(133)

PTEN - phosphatase and tensin homolog, MGMT - O6-methylguanine DNA methyltransferase.

Differences between the radiosensitivity of the four GBM cell lines were observed. The levels of radiosensitivity, measured using the clonogenic survival assay, correlate with the genomic instability of the cell lines. The cells that had functioning p53 and methylated MGMT (A172) or functional PTEN (LN18) conferred the highest levels radiosensitivity compared to PTEN and p53 deficient cell lines (T98G), further enhanced with the additional un-methylated MGMT promoter (U251, the only cell line with colony formation after exposure to 10 Gy) (175–177,197). As discussed previously, p53, PTEN and MGMT are responsible for apoptosis induction and/or regulating the DNA DSB repair response (10,198).

PTEN loss correlates with increased induction of reactive oxygen species, ATM phosphorylation and increased expression of p53, which in turn increases cell cycle

arrest and apoptosis (185,198). This could explain A172 and T98G exhibiting the highest level of initial damage after 4 Gy irradiation. After normalising against background levels of γH2AX foci, the highest residual levels of DNA damage, measured 24 hours post-irradiation, were observed in cell lines A172 and U251. Both cell lines are PTEN deficient, supporting the hypothesis proposed by McEllin *et al.* (199) that PTEN-loss disrupts the HR repair pathway due to its role in transcriptional regulation of the *Rad51* gene, although this repair pathway choice is less common than NHEJ this could still confer some sensitivity to radiation. However, the lack of a functioning p53 in U251 cells, compared to A172, could ultimately reduce the propensity for radiation-induced apoptosis, hence its increased radioresistance demonstrated in the clonogenic assay. Mansour *et al.* (200) found that although initial DNA damage levels (recorded 2 hours post-irradiation) were the same regardless of PTEN status, after 24 hours PTEN-null cells had 50% higher levels of remaining γH2AX foci. It has been reported that in some circumstances of complete PTEN function loss (A172 is PTEN deleted (177)), p53 is upregulated to activate cellular senescence, counteracting the pro-survival phenotype and increasing sensitivity to treatment (201). Functioning PTEN contributes to the repair of DNA damage, responding to the presence of DSBs and activating the repair pathways (180), which, in combination with an un-methylated MGMT promoter increasing the repair capacity (182), could explain the lower levels of γH2AX foci observed in LN18 cells 24 hours after irradiating.

The mitochondrial stress test assay provided the simultaneous measurement of the metabolic profile for all four cell lines. The assay was performed 24 hours after irradiation to allow the majority of DNA damage to repair. However, the significant quantity of remaining γH2AX foci at this time could relate to the insignificant differences in OCR noted in cell lines A172 and U251. Overall, the increase in oxygen consumption demonstrated after exposure to radiation, in cell lines LN18, T98G and U251, suggests radiation induces a stress response and consequently increases the energy demands of the cell. The little difference observed between BR and MRC in A172 (Figure 3.3.5b) suggests either an already present disruption of the mitochondrial membrane potential or p53 was counteracting the action of FCCP (202). In the other three cell lines, the reason for an increased BR, after exposure to radiation, was determined after the injection of oligomycin, inhibiting the protein ATP synthase and consequently ATP synthesis. Negligible increases in proton leak were observed in all cell lines after X-ray irradiation suggesting an increase in the activity of the enzyme complexes, transporting more protons across

the inner membrane to meet the additional energy demand. Following the injection of FCCP, and exposure to radiation, an increase in the uncoupling of oxygen consumption occurred driving the MRC. Here, the results suggest exposure to radiation further drives this disruption of the membrane potential with increases seen in the three cell lines tested with compromised p53 unable to maintain homeostatic potential (202). Complete RC depletion can be an indication of dysfunction or increased ATP demand (193), the lack of increased OCR observed suggests the former in A172 cells, possibly due to remaining DSBs present 24 hours post-irradiation. An increase in RC suggests enhanced oxidative capacity, an abundance of substrates or mitochondrial biogenesis. This spare capacity exists to allow a cell to respond to an increase in ATP demand or in preparation for stress (193).

An increase in ECAR suggests a preference for glycolysis over oxidative phosphorylation. Recent reports indicate a preference for glycolysis may be implicated in the resistance to treatment-induced cytotoxic stress, therefore using an additional treatment which inhibits glycolysis may increase the radiosensitivity of the tumour (186). In this study, the cell lines exhibiting the higher degree of radioresistance in the clonogenic assay also increased the ECAR after irradiating. A172 demonstrated the lowest increase in ECAR after irradiation, consistent with p53 function repressing glycolysis, thereby maintaining a degree of radiosensitivity (202,203). Several studies have demonstrated an upregulation of antioxidants, scavenging free radicals and pyruvate scavenging mitochondria superoxide both reduces the capacity for oxidative damage (186,188,204,205). Furthermore, the production of nicotinamide adenine dinucleotide phosphate (NADPH) from the pentose phosphate pathway, a metabolic pathway working in parallel to glycolysis, is important for antioxidant defences and preventing the release of hydroxyl free radicals (206).

3.3.5. Conclusion

To improve clinical outcomes there is an urgent need to identify biomarkers in GBM tumours to reduce the risk of recurrence, minimise long term toxicity, personalise treatments and influence clinical decision making. One such biomarker discussed within this report is the methylation status of the MGMT promoter, currently used as an indication of the potential benefit of administering TMZ (182,207). However, the inherent inter- and intratumoural genetic differences diminishes both the "one size fits all" and personalised treatment approaches to treating GBM. Collectively, the

data presented in this report demonstrates the impact of these genetic differences on the tumour cells response to radiation. Across the four GBM cell lines tested, variations in radiosensitivity, DNA damage repair capacity and mitochondrial metabolism phenotype were observed.

3.4. RESULTS: DEVELOPMENT OF 3D GLIOBLASTOMA MULTIFORME CELLULAR MODELS

Summary

This chapter documents the development and optimisation of 3D cellular models to provide a more realistic representation of a tumour volume, compared to typical 2D cell culture. To establish the migratory capacity of each cell line the simple and efficient scratch wound assay was performed. All cell lines demonstrated clear migration, even in the presence of low serum medium.

The first 3D models created were glioblastoma multiforme (GBM) cellular spheroids. Although expensive, compared to other techniques, the use of ultra-low attachment plates allows the carefully controlled and reproducible culture of individual spheroids. This technique also permits the control of the initial spheroid size, based on the seeding density, to allow some control over the levels of hypoxia and necrosis within (<250 µm diameter). Monitoring the spheroid growth after exposure to radiation provided a determination of the radiosensitivity of the cell lines in 3D culture, and also provided a mimic of tumour control.

Currently there is limited data on the effects of cellular migration in 3D culture, therefore GBM cells were cultured as spheroids and the effects of radiation on migration assessed. Once the propensity for the cells to disperse from the defined structure of the spherical spheroid was established, the addition of a hydrogel matrix to represent the surrounding brain microenvironment was added to examine the invasive nature of the GBM cells. Further use of the alginate/gelatin hydrogel was to create a protective barrier, enclosing GBM cells in the form of a microbead. These beads were developed as a potential technique to facilitate transfer between vessels, including the mouse phantom for biologically-relevant irradiations.

Following the results of the clonogenic survival and DNA damage repair assays documented in the previous chapter, X-ray doses of 2 and 8 Gy were used to irradiate the spheroids during the growth, migration and invasion assays. These doses represent sub-lethal and clinically relevant, and lethal doses of radiation, respectively. Irradiation took place 24 hours prior to the migration and invasion assessment to allow the repair of most of the DNA damage.

Author contributions

I performed all experiments with initial support and guidance from A. Chadwick, E. Santina and K. Williams. A. Aitkenhead, G. Price and K. Kirkby provided day to day supervision. All authors approved the manuscript.

DEVELOPMENT OF 3D GLIOBLASTOMA MULTIFORME CELLULAR MODELS

Emma R. Biglin[1]*, Amy L. Chadwick[1,2], Elham Santina[1,2], Kaye J. Williams[3], Adam H. Aitkenhead[1,3], Gareth J. Price[1,2], and Karen J. Kirkby[1,2]

[1]Division of Cancer Sciences, Faculty of Biology, Medicine and Health, University of Manchester, Manchester, UK. [2]The Christie NHS Foundation Trust, Manchester, UK. [3]Division of Pharmacy and Optometry, Faculty of Biology, Medicine and Health, University of Manchester, Manchester, UK, [4]Christie Medical Physics and Engineering, The Christie NHS Foundation Trust, Manchester, UK.

Abstract

3D cellular models better recapitulate the tumour environment than more commonly used 2D monolayer *in vitro* assays. This study demonstrates the use of highly reproducible 3D spheroids over long term culture to assess the effects of radiation on growth, migration and invasion in a panel of widely used glioblastoma multiforme (GBM) cell lines. 3D spheroid culture increased sensitivity to radiation compared to a 2D assay. The addition of an alginate/gelatin hydrogel, representing the extracellular matrix, further enhanced this sensitivity. In most cases, exposing spheroids to radiation elicited a dose-dependent decrease in outgrowth, migration and invasion. A second 3D model using this same alginate/gelatin hydrogel to encapsulate a GBM cell suspension was also developed to culture cells in a 3D environment and facilitate transfer between vessels for irradiation and analysis.

3.4.1. Introduction

Our collective understanding of cellular function is based on experiments in a synthetic environment, often performed on flat plastic or glass materials. The simplicity of these techniques are attractive, but the results are not always translatable due to profound phenotypical changes (208). These 2D cellular models are an inaccurate representation of the cell interactions in a tumour and fail to account for realistic external influences, such as the extracellular matrix (ECM). The ECM serves as a support for cell growth, both physically and chemically, and is unique to its location, often changing in response to stress or disease in the surrounding environment (209). Furthermore, it contains large amounts of proteoglycans, glycosaminoglycans and glycoproteins which are often upregulated in glioblastoma multiforme (GBM) tumours and play major roles in facilitating disease progression, proliferation, migration and invasion, treatment resistance and recurrence (168). In recent years there have been attempts to recreate various ECMs for different tissue types *in vitro,* but as the role of the ECM has yet to be fully determined in the development and pathology of GBM the exact composition of a brain ECM-mimicking gel has yet to be defined (210,211).

As the differences at the cellular level become more apparent between cells in 2D and 3D culture, there has now been a wider implementation of *in vitro* 3D models to better recapitulate the tumour microenvironment (163). Various novel culture systems are being adapted for use with GBM cells. Neurospheres are cells cultured in suspension to create a 3D structure (212). Organoids contain subpopulations of cells and stem cells and maintain an oxygen gradient across the model (213). Brain slices are the implantation of GBM cells into a mouse brain, allowing interactions with normal cells and observations of migration and invasion into the brain tissue (214–216). Mini-brains are either transduced, tumours generated from cerebral organoids, or implanted, cells injected into established organoids (217,218).

One of the simplest techniques to create a 3D cellular model is the formation and maintenance of a multicellular spheroid. Since the first use of spheroids in 1971 by Sutherland *et al.* (219), there have been several techniques developed to encourage cells to form a spherical structure: spontaneous aggregation, spinner flasks, poly-2-hydroxyethyl methacrylate-coated plates, liquid overlay, hydrogel/scaffold-based culture, micropatterned plates, hanging drop method, or ultra-low attachment (ULA) plates (220–222). The use of ULA plates is the most

effective technique, allowing high throughput formation of single spheroids centred within each well for easy optical analysis and high reproducibility due to controlled cell seeding density. The spheroids can then be easily harvested for further analysis (220), or a gel matrix added to the wells to promote invasion (223). Organotypic glioma spheroids are an improvement over these monoculture systems with the inclusion of multiple cell types, including immune cells (223–226). There are three critical steps to spheroid formation: individual cells form loose aggregates via the binding of ECM fibres to cell surface integrins, this upregulates cadherin expression on the membrane surface and the cells are forced together into tightly bound spherical shapes by the homophilic cadherin-cadherin binding (227). Due to the sharp nutrient and oxygen gradient along the axis of the spheroids, a structure of distinctive layers is formed: proliferative outer layer, quiescent intermediate layer and a necrotic centre. Beyond a diameter of 250 µm the diffusion of small molecules becomes impaired and the core becomes hypoxic, at around 500 µm a necrotic core develops due to the accumulation of metabolic waste (228). Treatment-related effects on the growth and disaggregation of spheroids are well-defined and reproducible endpoints. It is assumed that the cells within the structure have adapted to a 3D environment with varying availability of oxygen, glucose and nutrients, cell-cell contact, cell cycle variation and metabolic shifts, predicting a closer response to an *in vivo* model, as opposed to monolayer culture (229). The outward growth of a spheroid mimics the proliferation of tumours cells and, by providing a structure for attachment, spheroids can be used to assess migration and invasion as the cells disaggregate from the structure. However there are some key limitations to using spheroid-based assays to consider: some cell lines will form loose aggregates rather than a defined spheroid shape, there is difficulty in controlling cell density under long term maintenance and imaging the spheroid becomes progressively difficult as the density increases (230). To create more clinically relevant organotypic spheroids means compromising on throughput and additional cost (163).

Hydrogels have emerged in recent years as another promising 3D cell culture tool to provide a mimic of the ECM, with similar mechanical properties to soft tissue, and can support cell growth and sequestration for analysis. They can be formed with the cells already encapsulated within, used as an adhesive layer on a 3D scaffold or are moulded to a desired shape first before the cells are seeded onto the surface (208,231). They can also make up microfluidic systems allow circulating medium to create a dynamic microenvironment (232). The stable hydrogel is made using a

predominantly water-based polymer network with physical or chemical crosslinking required (233). When considering the use of hydrogels in experiments there are a variety of properties, both mechanical and biophysical, that require characterisation before use: swelling, mesh size, degradation, stability in culture, cell adhesion and compatibility with the cells of choice, all of which may influence cell viability and motility (208,234). Although the addition of a gel creates an enclosing structure, like surrounding brain tissue, and prevents the cells coming into contact with the plastic surface of a dish, the exact composition of the gel may be a limiting factor when understanding the cellular response to treatment (220). For example, most current GBM culture systems use Matrigel such as plugs, a 3D structure supporting the growth of tumour cells (235). This is synthesised from mouse sarcoma ECM, has higher concentrations of collagen and laminin than the brain, and there may be significant batch variation as it is extracted from mouse tumours and therefore impossible to measure the individual components (236).

The aim of this study was to develop 3D spheroid and hydrogel models, using a panel of five GBM cell lines, and investigate the effects of radiation on spheroid growth, migration and invasion. A 2D scratch wound assay was performed to determine the migratory capacity of each cell line and provide a basic comparison of a simple migration assay. The final part of this report documents the development of hydrogel microbeads with LN18 and U251 cells encapsulated in an alginate/gelatin sphere. Measurements of cell proliferation and bead diameter and roundness provided the metrics to assume cell viability and gel stability.

3.4.2. Methods

3.4.2.1. Culture of Glioblastoma Multiforme cell lines

Human GBM cells lines A172, LN18, T98G, U251 and U87MG were obtained from the American Type Culture Collection (ATCC, Middlesex, UK) and cultured in Roswell Park Memorial Institute 1640 (RPMI, Sigma-Aldrich, cat. no. R0883) medium supplemented with 2mM L-glutamine (Sigma-Aldrich, Cat. no.. G7513) and 10% v/v fetal bovine serum (FBS, Sigma-Aldrich, Cat. no.. F7524), referred to herein as complete medium. The migration and invasion experiments required a reduction in FBS concentration (1% v/v) and will be referred to as low-serum RPMI medium. This serum level was optimised, exposing cells to varying levels of FBS from 0%-10%, before determining the suitability of culturing GBM cells in 1% FBS to maintain cell function whilst minimising proliferation, as discussed later. Prior to use

all cell lines were authenticated (short tandem repeat profiling) and regularly tested for the presence of mycoplasma (quantitative polymerase chain reaction) by the Molecular Biology Core Facility (MBCF) at the Cancer Research UK Manchester Institute (CRUK MI, Alderley park, UK). In between experimental use, cells were incubated at 37°C in 5% CO_2 conditions and were passaged every 3-4 days. Use of each cell line was limited to <20 passages, with a split ratio of between 1:2 and 1:10.

3.4.2.2. Irradiation procedure

An X-ray CIX3 irradiator (Xstrahl Inc. Walsall UK) was used to irradiate all samples with the standard settings of 300 kV and 10 mA, 400 source-to-surface distance, with a 0.7 mm thick Cu filter and half value layer thickness of 2.3 mm Cu. Samples were irradiated at the 2 Gy or 8 Gy using a dose rate of 2.07 Gy/minute and to ensure the homogeneous irradiation of each 96 well plate, samples were placed in the centre of a rotating turntable. Each experiment included a sham irradiated control, with the plates exposed to the same environmental conditions as the irradiated plates, without exposure to radiation.

3.4.2.3. Observation of cell migration in a 2D assay

GBM cell migration was initially assessed by creating a scratch in a monolayer of cells using the Incucyte Woundmaker tool (Essen Bioscience). Using a 96-well tissue culture treated plate, $1x10^4$ cells/well in complete medium were seeded into each well to obtain a 100% confluent monolayer at the time of scratching, encouraging the cells to migrate into the defined void. 24 hours after seeding, 175 µl of complete medium was changed to low-serum RPMI medium and the plates were irradiated at doses of 0 Gy, 2 Gy and 8 Gy. All plates were incubated for a further 24 hours.

To create the scratch, the Incucyte Woundmaker tool was sterilised (described in Section 3.2.1) and 100 µl of medium was removed from each well before the opened 96-well plate was placed on the metal base. The pin block was then inserted over the top of the plate and the scratch made. The pin block was then removed and leftover medium removed. Finally, each well was washed with sterile phosphate-buffered saline (PBS) to remove any debris created during scratching, which may affect image analysis, and 200 µl low-serum RPMI medium added. Preliminary experiments implemented silicone inserts (Ibidi GmbH), with cells seeded on either side, to create a void in the centre (Appendix 2, Figure A2.2). Due to the low throughput and additional variability in the placement and removal of individual

inserts, use of the 96-well Incucyte Woundmaker tool was favoured in future experiments.

All scratch migration images were acquired using an Incucyte Zoom (Essen Bioscience), permitting time-lapse photographs to be taken while maintaining the cells at 37°C and 5% CO_2 for the 24 hour assay. Images were taken every hour at 4x magnification. Upon saving the images, a scale bar was added to each image by the Incucyte Zoom software, so when the images were opened in ImageJ this scale bar was used to create a reference of distance to be able to calculate the area of the gap using the ImageJ MRI Wound Healing Tool macro (https://github.com/MontpellierRessourcesImagerie/imagej_macros_and_scripts/wiki/Wound-Healing-Tool (237)), at time points 0, 5, 10, 15 and 20 hours (Figure 3.4.1). The percentage of gap closure was calculated against the area of the gap in the first image taken which was ~15 minutes after the initial gap was created due to the time taken for the Incucyte Zoom to stabilise and the images to be captured.
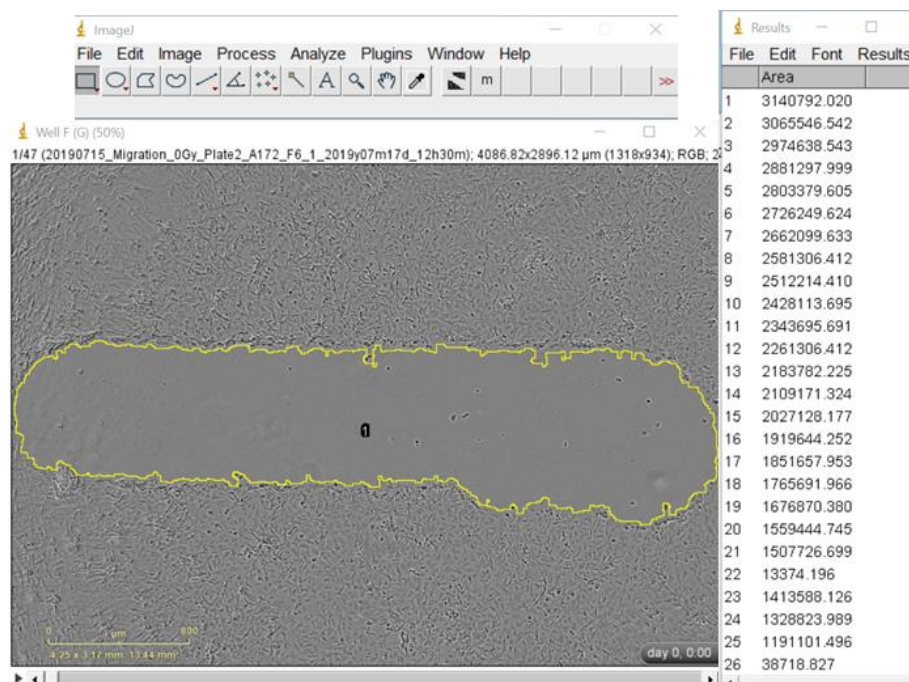
Figure 3.4.1. ImageJ analysis of the gap area.

Time lapse images taken using the Incucyte Zoom (Essen Bioscience) were opened in ImageJ. The scale bar within the image was used as an accurate reference of distance and the MRI Wound Healing Tool macro was used to measure the area of the scratch on each image. The first image taken was used as time point 0, approximately 15 minutes after the scratch was created, and the percentage of gap closure was calculated from this reference.

3.4.2.4. Spheroid growth

ULA 96-well microplates (Perkin Elmer) were used to encourage the formation of individual spheroids. By controlling the seeding density, the size of the spheroids can be optimised to control the levels of hypoxia and necrosis within. All spheroids were cultured and seeded, as described in Section 3.2, in 200 µl of complete medium. Initial optimisation involved seeding cells at a range of densities from 250-20000 cells into each well for each cell line with the aim to produce growing spheroids of approximately 400 µm diameter, after 72 hours of incubation (37°C and 5% CO_2, Table 3.4.1). Once the optimal seeding densities had been determined, spheroids were grown for 72 hours and then irradiated using the settings outlined above. One plate was sham irradiated with the other plates irradiated at doses of 2 Gy and 8 Gy.

Table 3.4.1. List of optimal seeding densities (cells/well) used in the spheroid growth and migration assays.

Cell line	Growth assay (400 µm diameter)	Migration assay (250 µm diameter)
A172	1500	500
LN18	500	400
T98G	1500	500
U251	1500	500
U87MG	500	400

Spheroids were incubated for up to 14 days at 37°C, 5% CO_2, with 150 µl of complete medium changed every 3-4 days. The ULA plates were scanned almost daily and the diameter of each spheroid measured using the GelCount (Oxford Optronix.) and accompanying software.

3.4.2.5. Spheroid-based migration assay

To move from assessing cellular migration in the 2D scratch assay, migration using spheroids was investigated. By maintaining the cells in a 3D geometry, prior to inducing migration, a more realistic environment of an *in* situ tumour was established over the 72 hours of spheroid growth. Spheroids were grown in the ULA microplates as described above however, to minimise any hypoxia or necrosis,

lower seeding densities were used to form spheroids of around 250 μm in diameter after 72 hours of incubation (Table 3.4.1). The plates were then irradiated at doses of 0, 2 and 8 Gy and 100 μl of medium was changed to low-serum RPMI medium, in each well. This reduction in serum was to decrease migration effects from cell proliferation.

24 hours after irradiating, spheroids were transferred from the ULA plates into flat bottom tissue culture treated plates using sterile P1000 pipettes, with the tips cut ~1 cm from the bottom to create a wider area to avoid damaging the spheroids. First, 150 μl of medium was removed from each well of the ULA plate. Individual spheroids were pipetted into the centre of each flat bottom well, followed by the addition of 150 μl of low-serum RPMI medium (Figure 3.4.2). The plates were then incubated for 72 hours (37°C and 5% CO_2). Images of each spheroid were obtained using an EVOS XL (10x magnification) or Incucyte Zoom (4x magnification) (Essen Bioscience). Images taken at 24, 48 and 72 hour post-transfer time points were analysed.

To track the cells migratory capacity, ImageJ software was used to measure the distance migrated from the centre of the spheroid of >20 cells, taken at regular intervals around the spheroid (Figure 3.4.2b). If the spheroid had attached near the edge of the well, only the distance of cells which had the capability to migrate freely away from the spheroid body was measured. The approximate radius of the spheroid was then deducted from these measurements to give the migration distance.
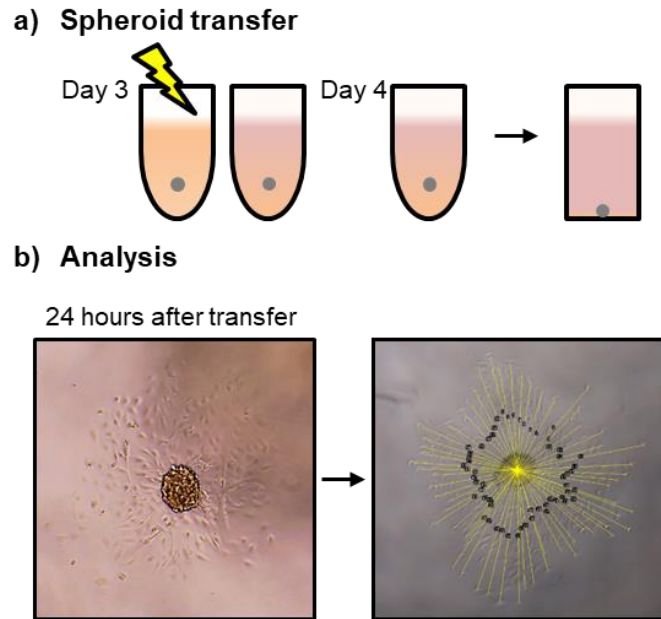
Figure 3.4.2. Spheroid migration

a) Spheroids were cultured for 72 hours and then irradiated at doses of 0, 2 and 8 Gy. At this time 100 µl of medium was changed to reduced 1% serum. 24 hours later spheroids were transferred from the ULA plate into a flat-bottomed 96-well tissue culture treated plate and left to attach and disperse. Images were taken at 24, 48 and 72 hour time points. b) ImageJ was used to measure the migration distance of >20 cells.

3.4.2.6. Spheroid invasion

As with the previous experiments, cells were seeded into three ULA microplates for 72 hours in complete medium. The same seeding densities as the migration experiments were chosen to create spheroids of ~250 µm in diameter to initially avoid the hypoxic and necrotic centre, which may have some impact on the cells ability to invade out of the spheroid structure. After this time, the plates were irradiated to doses of 0, 2 and 8 Gy. 150 µl of the complete medium was removed from each well and replaced with low-serum RPMI medium.

The combination of alginate and gelatin hydrogels creates a matrix that is durable, flexible and transparent, whilst also supporting cell adhesion and survival (238). The sodium alginate (Sigma-Aldrich, Cat. no.. W201502) and gelatin (Sigma-Aldrich, Cat. no.. G1890) powders were dissolved in HEPES-buffered saline (HBS, pH 7.4) by incubating at 37°C overnight and vortexing and, when required, were cross-linked with the addition of $CaCl_2$. It was important to keep the gels at 37°C until use

as they become too viscous to pipette. Various concentrations of gels and $CaCl_2$ were tested and, based on simulating the brain ECM stiffness of 0.1 – 1 kPa (239), concentrations of 1.5% w/v for both alginate and gelatin and 0.2 M $CaCl_2$ (in HBS) was used (~0.4 kPa). A 1:1 ratio of the alginate and gelatin gels creates a final concentration of 0.75% w/v within the hydrogel.

The gels were initially added into the wells of the ULA plate but no invasion from the spheroid was observed after 11 days of culture. Further optimisation experiments implemented 96-well flat-bottomed plates with the gels added first then the spheroids transferred on top, or vice versa. Cell lines A172, T98G and U87MG exhibited no invasion at this time so the assay was completed using cell lines LN18 and U251. The final experiments were completed with the spheroids being transferred to the flat-bottomed plates 24 hours after irradiating. Approximately 2 hours later, to allow the spheroids to settle, 100 µl alginate/gelatin hydrogel was added to each well. After 15 minutes at room temperature, 150 µl of $CaCl_2$ was pipetted down the side of each well to avoid pushing the gel to one side. After another 15 minutes at room temperature, the $CaCl_2$ was removed and three washes with HBS, 5 minutes each, were performed. Finally, 100 µl of low serum RPMI medium was added to each well and the plates were incubated in 37°C and 5% CO_2 conditions. This process is depicted in Figure 3.4.3.
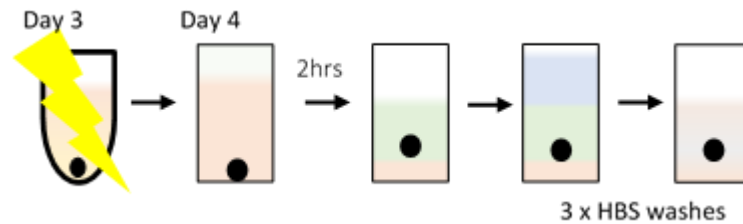
Figure 3.4.3. Spheroid invasion.

Spheroids were grown in ULA microplates, to sizes of ~250 μm diameter after 72 hours, 150 μl medium was changed to low-serum and the plates were irradiated. 24 hours later the spheroids were transferred to flat-bottomed tissue culture plates and the alginate/gelatin hydrogel was added to the well. This was followed by the addition of CaCl$_2$ and, after sufficient polymerisation, three HBS washes. The plates were then incubated for 72 hours in low-serum medium before image acquisition.

Images of each spheroid were obtained using the EVOS XL (10x magnification), initially at times points 24, 48 and 72 hours after transfer. However, little invasion was seen over this period so the final experiments obtained images at 72, 96 and 120 hours after spheroids were encapsulated in the gel. A 100 μl low serum RPMI medium change was undertaken, prior to taking the first image. Analysis was performed with ImageJ software using the same method as the spheroid migration analysis.

3.4.2.7. Microbeads

Microbeads are a 3D gel structure in which cells are encapsulated. By having an enclosed gel structure the beads can easily be transferred between tissue culture plates or elsewhere for additional experimentation or post-irradiation analysis. For the reasons mentioned above, the same composition of hydrogel (alginate and gelatin, cross-linked by CaCl$_2$) was used to create the microbeads. After optimisation, the amount of the gel powders dissolved in HBS was increased to 3% w/v (1.5% final concentration) with 0.2 M CaCl$_2$, to increase the stability of the gel over long term culture (~0.8 kPa). The alginate and gelatin gels were prepared the day before use and incubated at 37°C.

LN18 and U251 cells were cultured and counted as described in Section 3.2. The cells were centrifuged once more and resuspended in the alginate/gelatin hydrogel to create cell density of 5x10^5 cells/ml. At the same time, 200 μl CaCl$_2$ was added to each well of a 96-well round-bottomed tissue culture plate into which the beads were dropped. Using a 21 gauge needle and 1 ml syringe, the hydrogel cell

176

suspension solution was collected, the needle then switched to a 27 gauge, and the solution deposited as single droplets into each well. After 15 minutes at room temperature, the $CaCl_2$ was removed and followed by three HBS washes, 5 minutes each, at room temperature. After the final wash, the HBS was removed and replaced with complete medium and the beads were incubated at 37°C and 5% CO_2. This process is depicted in Figure 3.4.4. A 100 µl complete medium change was performed every 3-4 days.
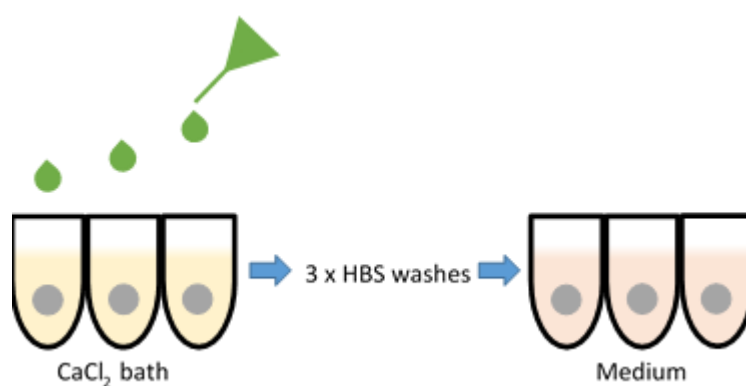
Figure 3.4.4. Formation of GBM microbeads.

Cells are suspended in the alginate/gelatin hydrogel at a density of $5x10^5$ cells/ml. Using a 27 gauge needle, droplets were deposited into each well of a 96-well round bottom plate containing $CaCl_2$. This was followed by three HBS washes and the final microbeads were incubated in complete medium 37°C and 5% CO_2 for up to 14 days.

Standard images of the microbeads were acquired using the EVOS XL microscope at 4x magnification on days 0, 3, 6, 10 and 13 after the beads were created. To measure the diameter and roundness of the microbeads, and thereby assessing any hydrogel degradation, ImageJ was used. To assess cell viability within the beads, at the same time points, a sample of beads were collected and dissolved in trisodium citrate dehydrate (TCD, pH 7.4) in a 1:4 volume ratio, respectively. This solution was centrifuged, re-suspended in complete RPMI medium and the cells counted, as described in Section 3.2.

3.4.3. Results

3.4.3.1. Limited effects of radiation on cellular migration were observed in the scratch wound assay

The scratch migration assay is an efficient and low cost technique to investigate the migratory capacity of cells (240). To encourage the cells to migrate into the scratched void, and accurately quantify the gap closure, it was important to start with a 100% confluent monolayer of cells across the plate well. It was then important to differentiate the cells migrating into the gap to those being pushed due to proliferation. One of the most common techniques to negate the effects of proliferation on closing the gap is serum starving, however the levels should be sufficient enough for the cells to continue to function normally, thereby avoiding cell detachment or apoptosis (240,241). To determine the appropriate level of FBS to include in the medium, 24 hours prior to the creation of the scratch, the medium was changed to test levels of serum between 10% (as a control) and 0% (Figure 3.4.5). Maintaining the cells in 0% and 0.2% serum medium significantly reduced the cells movements, possibly due to the cells dying or becoming detached. 1% and 2% serum medium led to similar or slight reduction in migration when compared against the 10% control, indicating the cells have retained some normal function but are more likely migrating into the gap as opposed to proliferating. Based on these results 1% serum medium was used for subsequent migration and invasion assays.
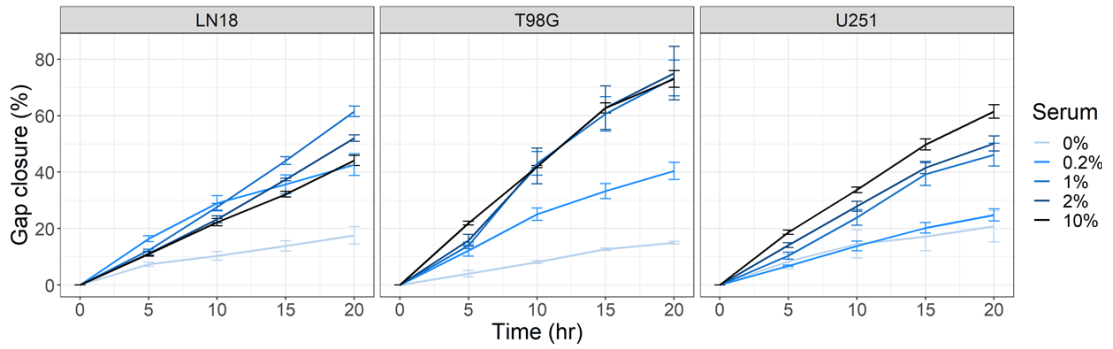
Figure 3.4.5. GBM cell migration is affected by serum starvation.

LN18, T98G and U251 cells were seeded into 96-well plates in complete RPMI medium. To account for the effects of proliferation closing the gaps, 24 hours later the medium was changed to contain serum at a concentration of between 0 and 10%. A further 24 hours later the scratches were made and the plates photographically monitored. The area of the gap was measured using the MRI Wound Healing Tool macro in ImageJ and the percentage gap closure was calculated against the first image. Data shows the mean ± standard error of one experiment (n=2-3).

Using a 96-pin device, such as the Incucyte Woundmaker tool, allowed the simultaneous creation of 96, uniform scratches (Figure 3.4.6). In addition to the high throughput advantage, this technique also reduces the impact of user variability on scratch uniformity compared to other methods, such as applying and removing silicone inserts or manually scratching with a pipette tip.
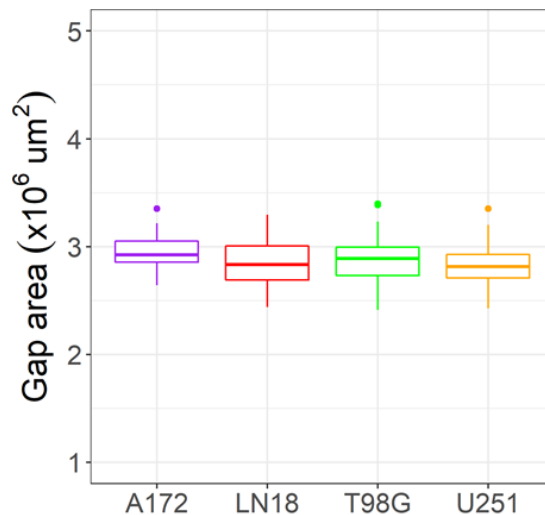
Figure 3.4.6. The Incucyte Woundmaker tool facilitates a high throughput scratch assay with highly reproducible scratch creation.

The initial gap area, imaged using the Incuycte Zoom approximately 15 minutes after the voids were created, was measured using the MRI Wound Healing Tool macro in ImageJ. Data shown is from three independent experiments (n=3-6).

The results from the 2D scratch migration assay indicate X-ray radiation had little impact on the migration of GBM cells, when compared to the sham irradiated control (Figure 3.4.7). Between cell lines the rate of migration was fairly similar, with T98G cells almost closing the gap after 20 hours. U251 cells were the slowest to close the gap, reaching 50% closure at 20 hours. Exposing A172 cells to 8 Gy of radiation decreased the migration rate slightly when compared to 0 Gy and 2 Gy, whereas irradiation of LN18 and T98G at either dose led to a slight increase in migration. U251 cells showed no difference in the rate of migration after exposure to radiation compared to the sham irradiated controls.
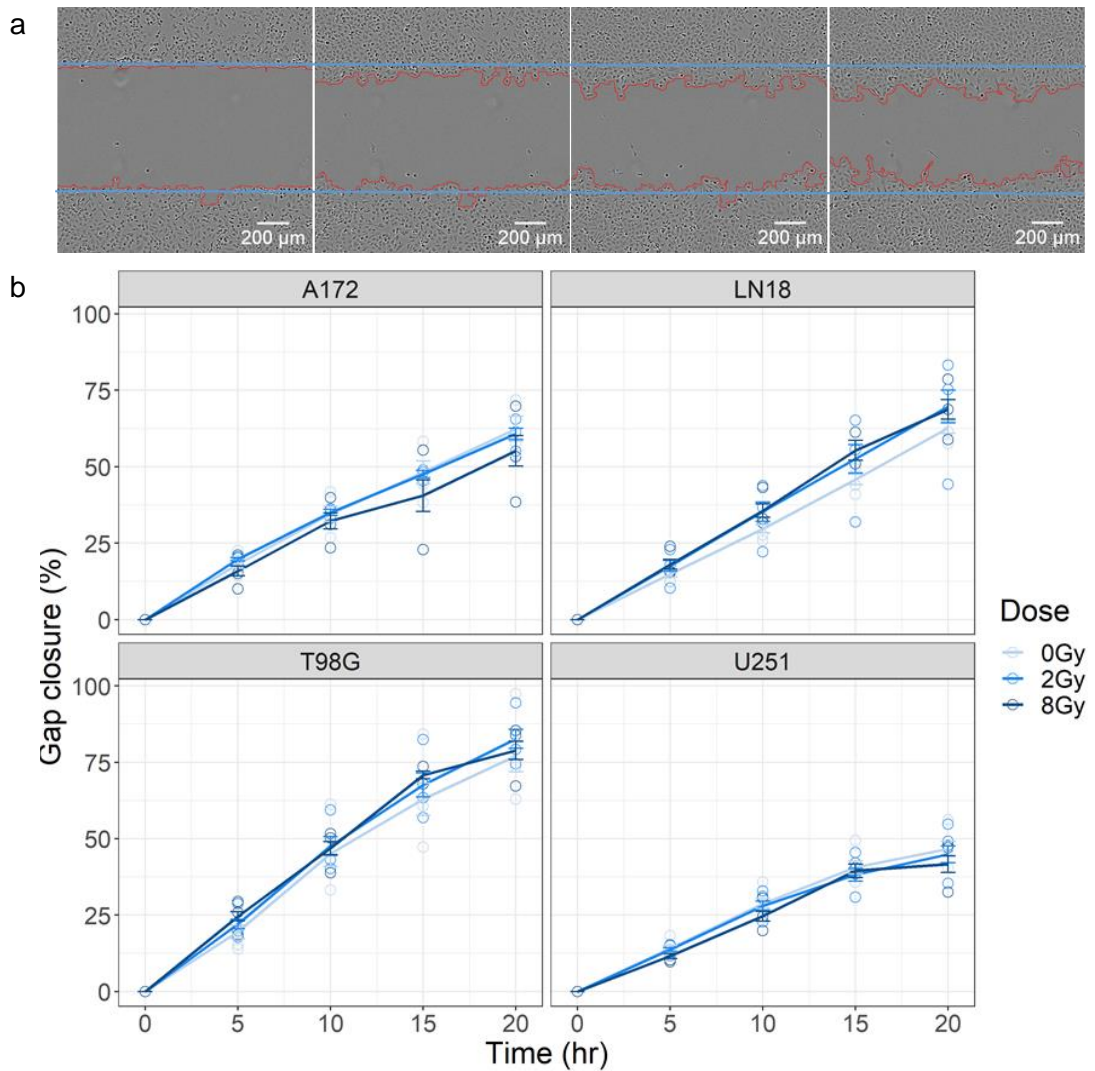
Figure 3.4.7 Response to radiation in 2D scratch migration assay.

A172, LN18, T98G and U251 GBM cell lines were seeded into three 96-well tissue culture-treated plates and the next day irradiated at doses of 0, 2 and 8 Gy. At this time 175 µl of the medium was changed to contain 1% serum. Approximately 24 hours later, a scratch was made in the centre of each well using the Incucyte Woundmaker tool. a) The plates were photographically monitored using the Incucyte Zoom for 24 hours and the area of the void measured using the MRI Wound Healing Tool macro in ImageJ, normalised against the measurement from the first image. The blue lines are a reference to the original gap width. b) Values presented are the mean ± standard error from three independent experiments (n=3-6, the mean of each biological replicate is depicted as an open circle).

3.4.3.2. Reproducible spheroids can be formed using ultra-low attachment (ULA) plates

To establish 3D spheroid models, ULA plates were chosen based on their simplicity and easily controllable environment to create individual spheroids. These plates encourage spheroid formation by preventing cellular attachment through a covalently-bound hydrogel layer (242). Optimisation was required to determine a seeding density, for each cell line, that would produce tightly bound spheroids with a diameter of ~400 µm by day 3. This size allows the formation of pathophysiological oxygen gradients across the spheroid volume (220). It was also important that the spheroid exhibited a significant growth curve to determine any effects of radiation in future experiments. Furthermore, the spheroids must produce their characteristic tightly bound shape when seeding with lower densities, with the aim of creating spheroids with a diameter of ~250 µm by day 3, for the migration and invasion assays.

All five GBM cell lines (A172, LN18, T98G, U251 and U87MG) were initially tested, however not all were suitable for each assay as demonstrated below. Cells were seeded into 96-well ULA plates at multiple seeding densities and characteristic spheroids were observed from 24-48 hours. Figure 3.4.8 shows the growth curves for each seeding density up to 10 days, sufficient time to observe the growth trend. U87MG showed significant growth over 8 days in all seeding densities and the lower seeding densities of LN18 also produced growing spheroids. The lower seeding densities of A172, T98G and U251 exhibited a slight increase in diameter, although not significant enough to be able to accurately determine any growth inhibition effects from later exposure to radiation.
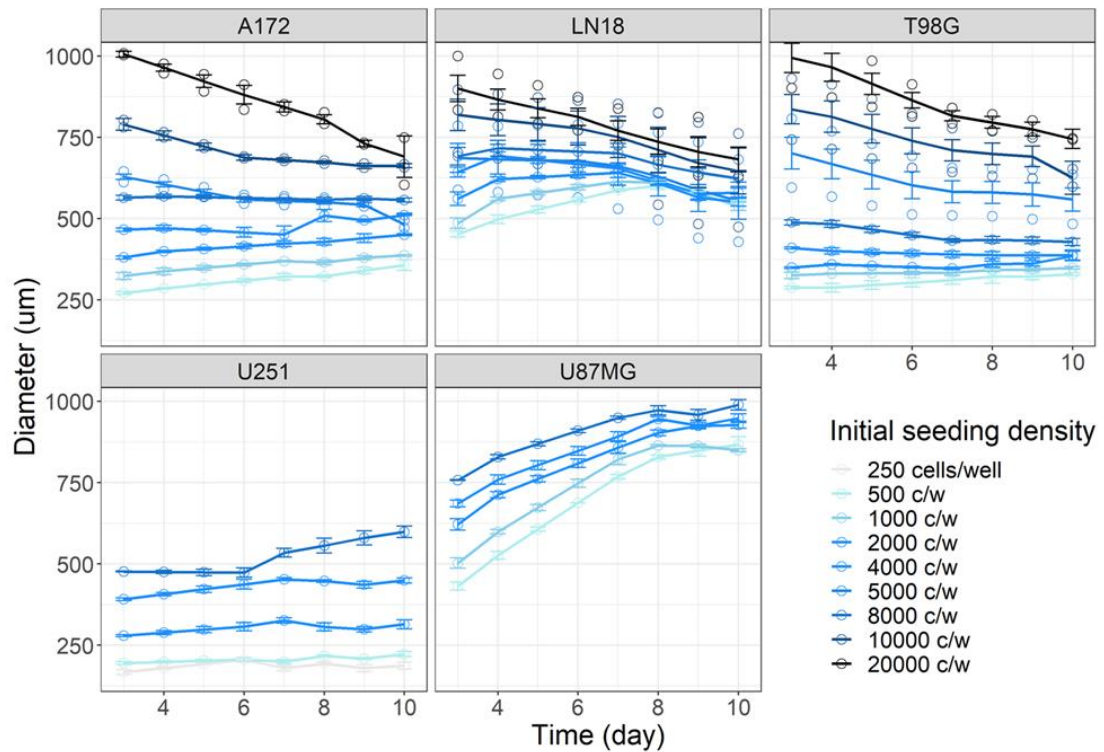
Figure 3.4.8. Growth optimisation of glioblastoma multiforme (GBM) 3D spheroids. GBM cells were seeded at densities ranging from 250 to 20000 cells/well, in 96-well ULA round-bottomed plates and incubated for up to 14 days, until the growth rate plateaued. For all cell lines, distinct spheroids formed after 24-48 hours. Diameter measurements were taken after scanning the plates using the GelCount and using the accompanying software to detect the spheroids in each well. Data represents the mean ± standard error from a minimum of one experiment (n = 3-6). The open circles represent the mean of individual experiments.

Controlling the seeding density not only allows the control of the initial (day 3) spheroid size but also produces highly reproducible spheroids. Figure 3.4.9 shows the results from 3 days after approximately 1500 A172, T98G and U251 cells and 500 LN18 and U87MG cells were seeded into individual wells in ULA plates. There were slight variations between cells lines measured, however the overall mean diameter was 390.1 ± 5.3 µm (standard error). Iversen *et al.* (243) outlined the method of using a Coefficient of Variation (CV) analysis to compare the uniformity of spheroids, suggesting that a less than 20% variation is acceptable. Across all experiments the CVs were: 13.732%, 9.676%, 7.921%, 5.302% and 6.624%, and within each experiment were: 2.692-7.693%, 4.172-6.414%, 1.598-3.080%, 2.420-5.040% and 3.903-6.513%, for cell lines A172, LN18, T98G, U251 and U87MG respectively.
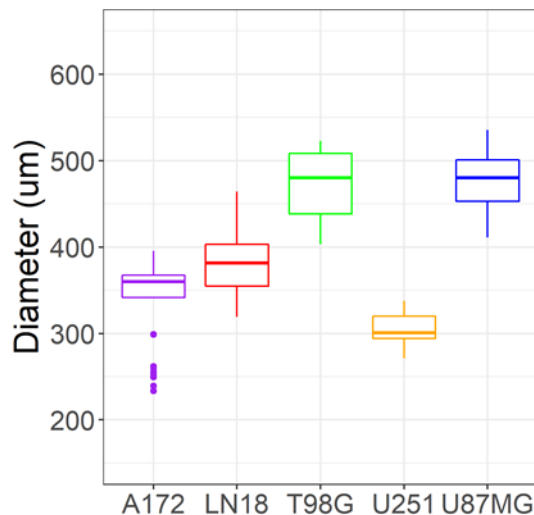
Figure 3.4.9. Ultra-low attachment (ULA) plates produce reproducible spheroids. To obtain spheroids approximately 400 µm in diameter, ~1500 A172, T98G and U251 cells and ~500 LN18 and U87MG cells were seeded into each well of an ULA plate. Box plots show little variation in the diameter of the spheroids, measured on day 3. The data represents the diameters of ≥34 spheroids per cell line across three independent experiments.

3.4.3.3. Radiation decrease 3D cellular spheroid growth

Once the optimal seeding density had been established, the effects of radiation on spheroid growth were investigated. On day 0, LN18 and U87MG cells were harvested, counted and seeded into 96-well ULA plates. Within 24-48 hours 3D spheroids were formed, with a diameter of ~400 µm achieved by 72 hours. The first spheroid-based assay aimed to characterise the growth of spheroids after exposure to X-ray radiation. One of the advantages of spheroid models is the longer term culture in which the cells are maintained compared to the 3-4 day culture 2D flasks before splitting is required. GBM spheroids were irradiated with 2 Gy and 8 Gy of X-rays, with a sham irradiated control. Representative images of the sham irradiated cell line U87MG are shown in Figure 3.4.10a. The plates were incubated and monitored daily and the resulting growth curves are presented in Figure 3.4.10b.
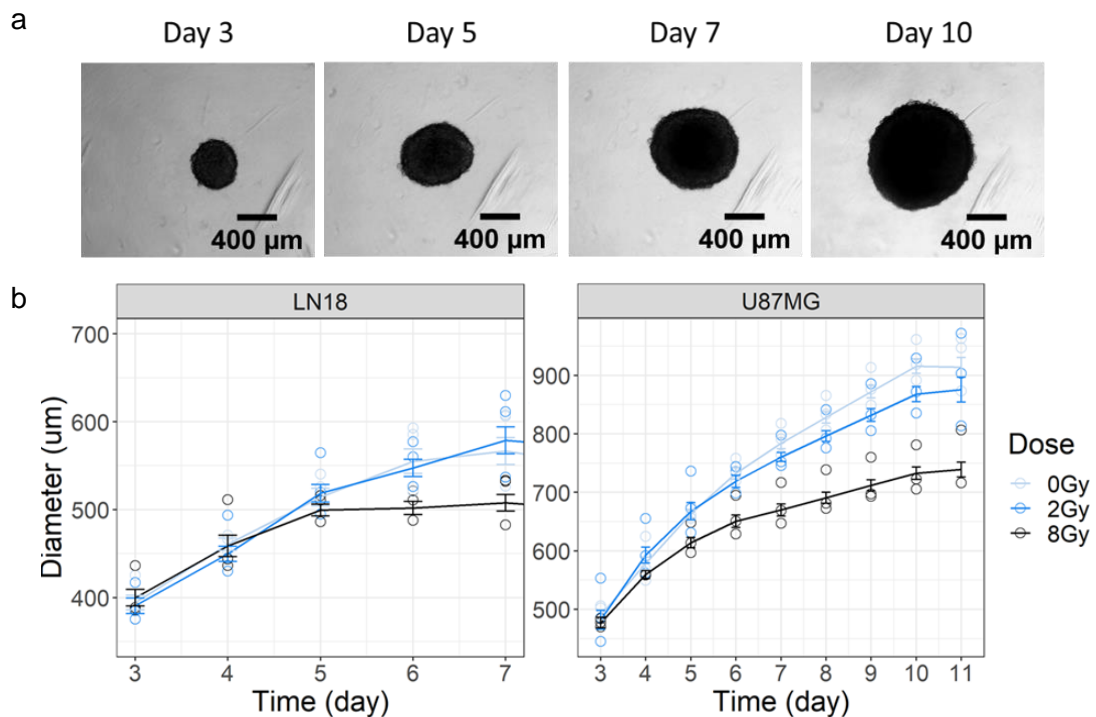
Figure 3.4.10. Radiation slows the growth of GBM spheroids.

The growth of 3D GBM spheroids was assessed after exposure to 2 and 8 Gy X-ray radiation and compared to a sham-irradiated control. The plates were incubated until no significant growth was observed and scanned almost daily using the GelCount. a) Representative images of non-irradiated U87MG cell spheroids. b) The mean ± standard error from three independent experiments (n=3-6, the mean of each biological replicate is indicated by the open circles).

The impact of the high dose irradiation on U87MG spheroids was seen within 24 hours, with the growth decreasing drastically over time. 3 days after irradiating the effects of 2 Gy also began to appear, as the rate of growth by the sham irradiated spheroids continued at a steady rate and the irradiated spheroids decreased. The impact of 8 Gy irradiation also had a dramatic effect on LN18 spheroids which exhibited minimal growth after 48 hours post-irradiation.

3.4.3.4. Radiation has some effect on cellular migration from a spheroid structure

Cellular migration was measured for irradiated and sham-irradiated spheroids (Figure 3.4.11). Smaller spheroid sizes were used to avoid any influence from potentially hypoxic or necrotic regions (220).
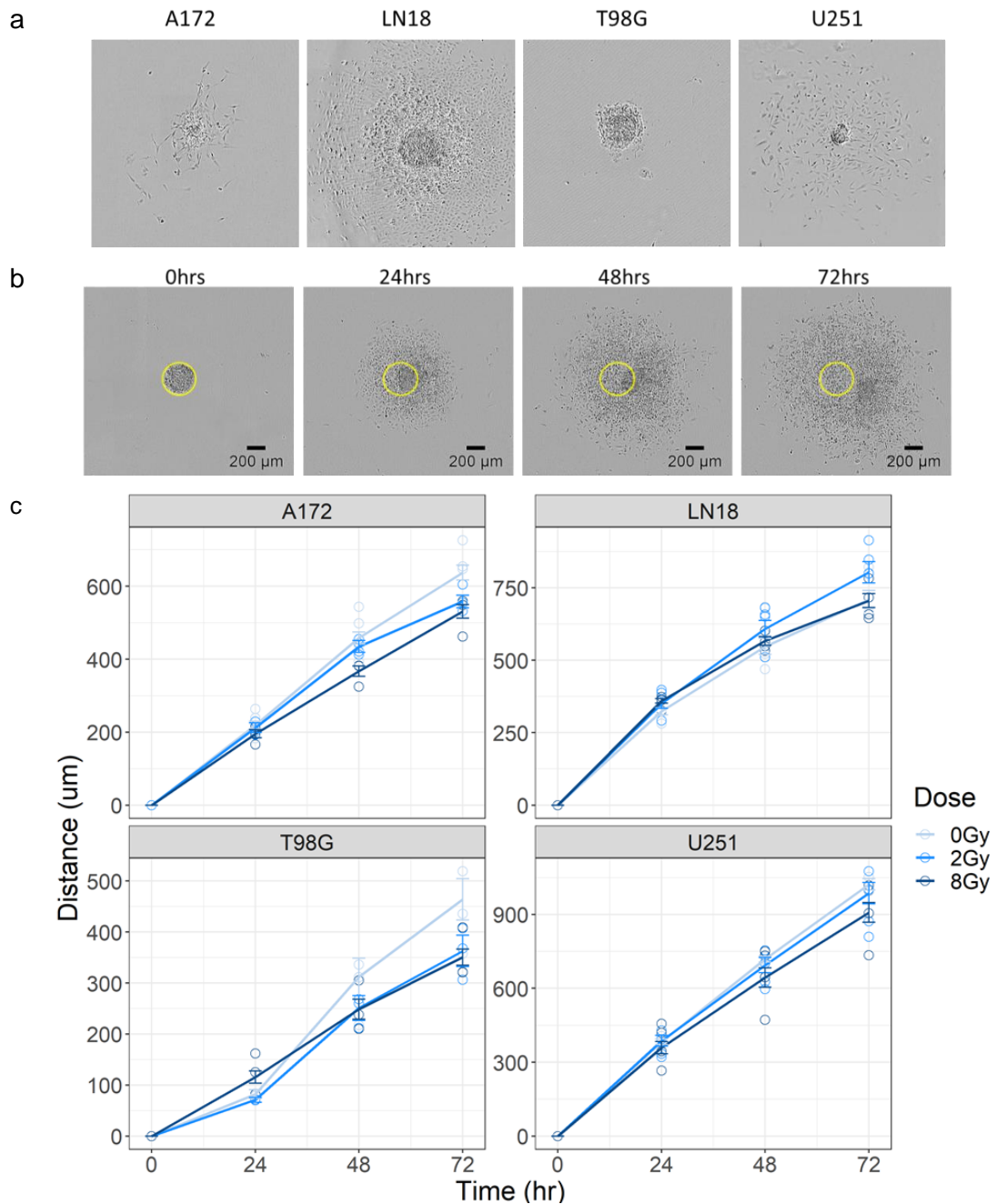
Figure 3.4.11. Exposure to radiation decreases migration from a spheroid structure.
GBM cells were seeded into ULA plates to achieve a diameter of ~250 µm diameter after
72 hours. The spheroids were then irradiated to 0, 2 and 8 Gy and the medium changed to
low serum. 24 hours later, the spheroids were transferred into flat-bottomed plates with low
serum medium. Images were captured every 24 hours and the migration of >20 cells was
measured using ImageJ. a) The migratory phenotypes exhibited by each cell line differed,
with A172 and U251 preferring individual cell migration compared to the sheet migration
exhibited by LN18. T98G cells exhibited both phenotypes. b) Representative images of
LN18 migration. The yellow circle indicates the original spheroid. c) Data represents the
mean ± standard error from three biological replicates (open circles, n=3-6).

All cell lines actively migrated from the spheroid, albeit with different characteristics (Figure 3.4.11a). A172 and U251 preferred a single cell migration approach, whilst LN18 migrated as a continuous sheet. Migration from T98G spheroids was limited but appeared to use both single cell and sheet phenotypes. Overall, a reduction in migration from this 3D structure after exposure to X-rays was seen in all cell lines 72 hours after irradiating, with the exception of LN18. The slower migration rates after 2 Gy, further inhibited after exposure to 8 Gy radiation, in A172 and U251 cells suggest this may be dose dependent. LN18 spheroids exposed to 2 Gy expressed an increased migration rate compared to the sham irradiated control.

3.4.3.5. Radiation impacts GBM invasion

Further optimisation of the spheroid migration assay involved the addition of a brain tissue-mimicking substrate. Surrounding the 3D spheroid in a hydrogel matrix provides a better recapitulation of invasion, especially important for modelling GBM due to its highly invasive nature (163). In this study, a combination of alginate and gelatin hydrogels was used, allowing the modification of viscosity to mimic the brain tissue stiffness. Following the optimisation of the gel and $CaCl_2$ concentration, LN18 and U251 were the only cell lines that demonstrated significant invasion into the hydrogel. Spheroids were generated and on day 4 were transferred into tissue culture treated, flat bottomed 96-well plates. The hydrogel was then added and, after gel polymerisation and washing, the spheroids were incubated for 72 hours. Cell invasion into the matrix was measured over the following 48 hours (Figure 3.4.12).
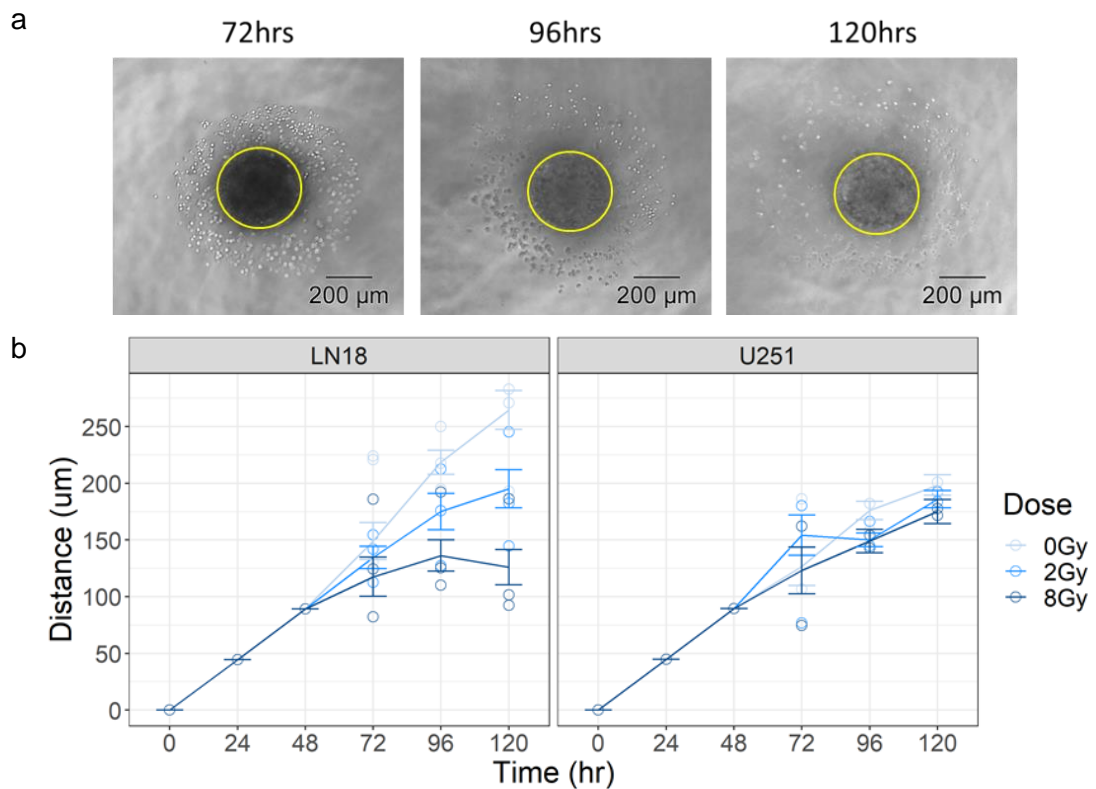
Figure 3.4.12. Radiation decreases GBM cell invasion.

As described in the spheroid migration assay, LN18 and U251 spheroids were grown in ULA plates to ~250 μm diameter, after which the plates were irradiated to 0, 2 and 8 Gy and the levels of serum in the medium was reduced to 1%. 24 hours after irradiating the spheroids were harvested from the wells using a pipette and placed into a flat-bottomed tissue culture plate in 1% serum RPMI medium. The medium was removed and alginate/gelatin hydrogel added to each well. After polymerisation by CaCl$_2$, the gels were washed and 1% serum RPMI media added. After incubation for 72 hours, each well was imaged every 24 hours using an EVOS microscope (10x zoom) and the distance travelled by >20 cells was measured using ImageJ. a) Representative images of LN18 cells taken using the EVOS microscope. The yellow circle indicates the original spheroid shape. b) The mean ± standard error from three biological replicates (open circles).

By providing a more realistic representation of the surrounding tumour environment, the addition of the hydrogel matrix reduced cellular outgrowth compared to the spheroid migration. LN18 and U251 cells invaded the hydrogel as a sheet or individual cells, respectively, consistent with the spheroid migration assay. The rate of migration gradually decreased over the course of the experiment. Radiation had a substantial reduction on the invasion of LN18 cells with 2 Gy causing a 30%

decrease after 120 hours and 8 Gy almost ceased invasion completely after 72 hours, compared to the control. Only slight effects were seen in cell line U251, initially an increase in migration was measured in cells exposed to 2 Gy but, as the assay reached 120 hours, this effect was reduced to below the rate observed in the sham irradiated control. In contrast to LN18, consistent invasion into the hydrogel by U251 cells was still observed after exposure to 8 Gy radiation across the experiment, albeit at a slower rate than the 0 Gy control.

3.4.3.6. Cell encapsulation in hydrogel microbeads

3D cell culture models enable the study of the radiation response in a physiologically-relevant environment (244). Culturing cells encapsulated in a hydrogel microbead permits the diffusion of oxygen and nutrients from surrounding medium, whilst eliminating restrictions from 2D culture. The enclosed structure also has a protective function, isolating cells from external stresses, and facilitates transport between vessels for further analyses (245). When developing a suitable hydrogel for long term culture there are many parameters that require optimisation: the concentration of the alginate and gelatin, the concentration of the polymerisation agent $CaCl_2$ and the cell density. Figure 3.4.13 presents the results of these optimisations, starting with the testing of two different gel viscosities in combination with three concentrations of $CaCl_2$. These initial tests used multiple 6-well plates, filled with $CaCl_2$, HBS and complete RPMI medium. Beads dropped into cell strainers over a $CaCl_2$ bath to polymerise the hydrogel and then transferred between plates for washing before being inverted over the wells containing complete medium for long term culture. Dropping multiple beads into the same well proved difficult to monitor individual beads and often resulted in clumps of microbeads rather than reproducible, spherical volumes (Figure3.4.13a, test 1). Using a higher viscosity gel (6% w/v) was difficult to filter so the combination of 3% w/v alginate and 3% w/v gelatin was used for further tests as this maintained gel stability, yet could still be pipetted. The optimal $CaCl_2$ concentration was determined based on the creation of a stable gel at the lowest possible concentration, due to its toxicity to cells (244). A concentration of 200 mM was chosen for the final experiments as any less than this proved unstable and the cells to leak out of the beads after 7 days in culture (Figure 3.4.13a, test 2). To facilitate monitoring of individual beads, the final experiments were performed using 96-well plates, with a single bead formed in individual wells (Figure 3.4.13a, test 3).
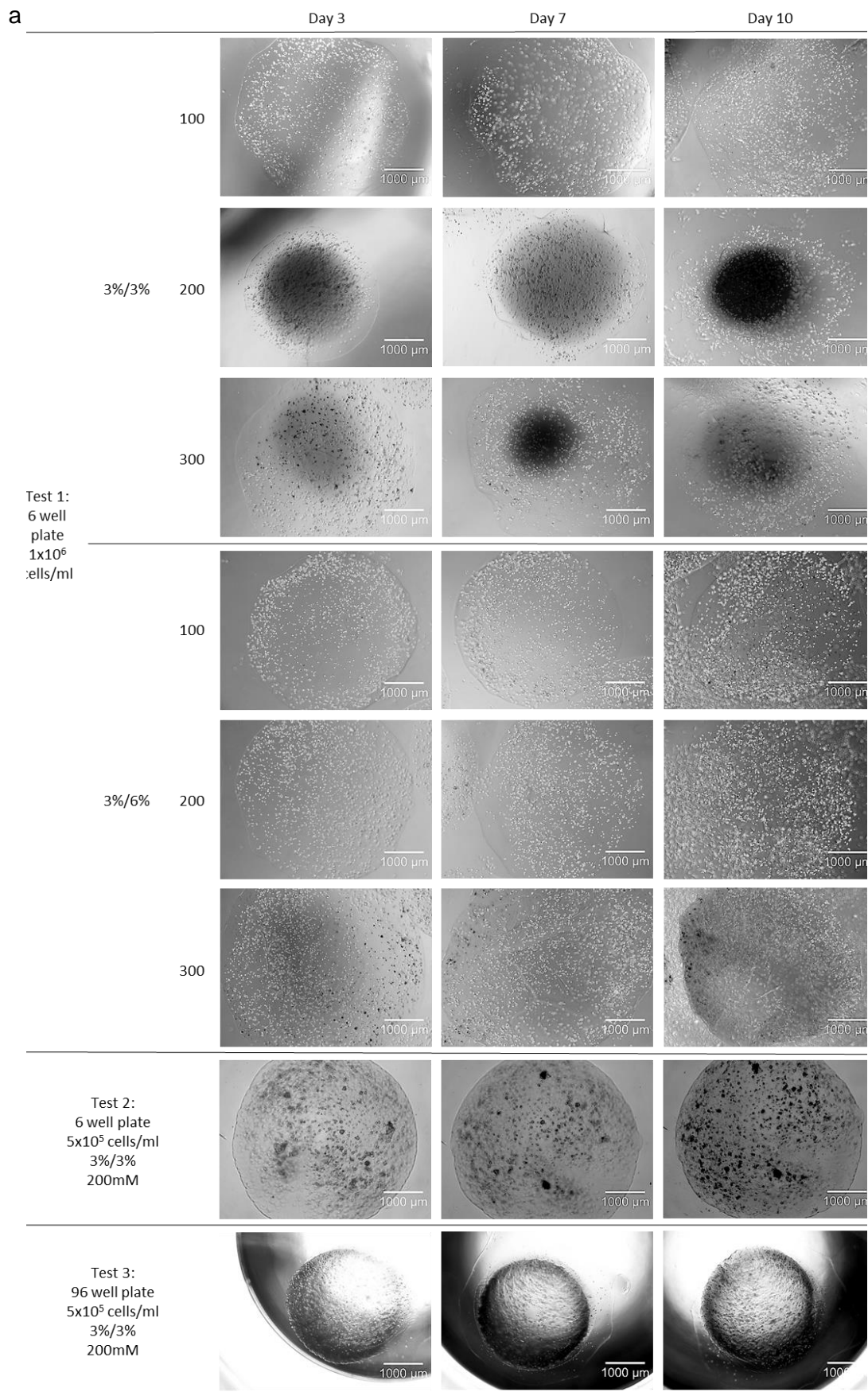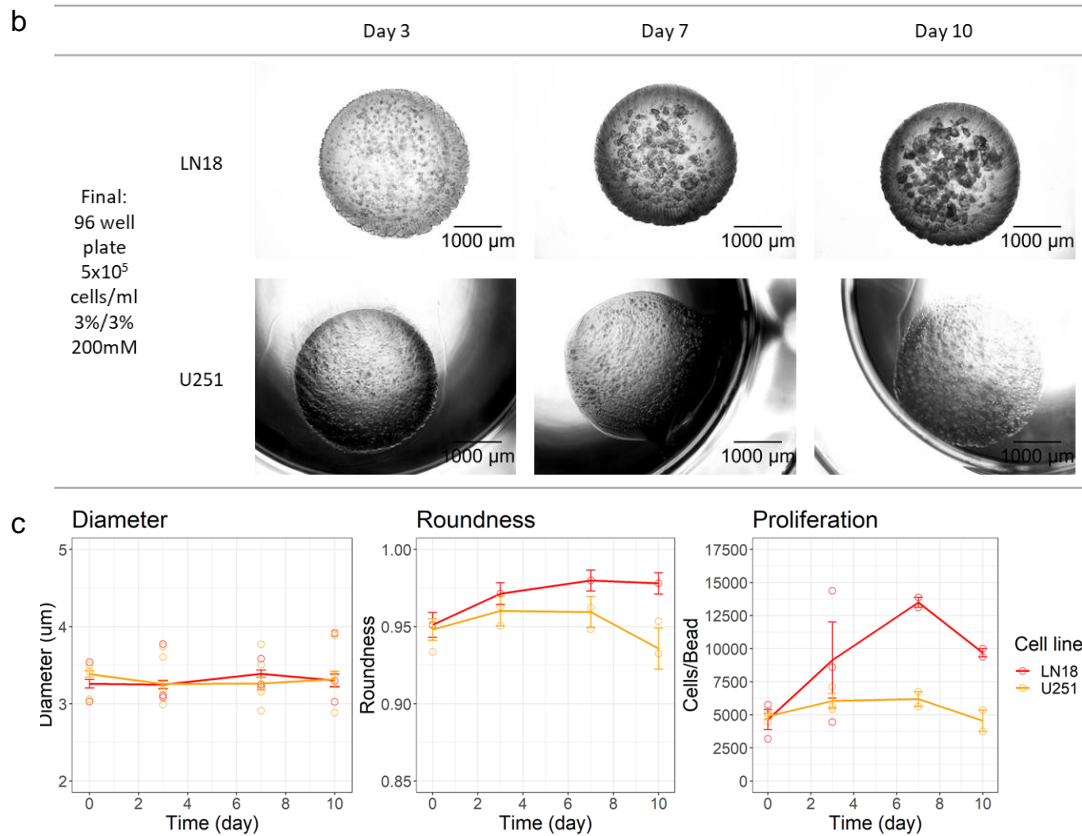
Figure 3.4.13. LN18 and U251 cells encapsulated in a hydrogel microbead.

GBM cells were suspended in an alginate/gelatin hydrogel. Using a 27 gauge needle, droplets were released into a CaCl₂ bath to polymerise the gels. a) Images show the microbeads formed during the optimisation of culturing, seeding density, gel density and CaCl₂ concentration. b) Following the optimisation, a density of 5x10⁵ cells/ml, 1.5% w/v final concentration of the hydrogel and 96-well round-bottomed plates were used for optimal stability, handling and efficient monitoring over the 10 days. c) Images of several microbeads were obtained (n=1-19), using an EVOS microscope, on days 0, 3, 7 and 10. Using ImageJ, the diameter was measured and a roundness value calculated (4*(Area/(Pi*(Major axis)^2))). To calculate the cells/bead at each time point, the beads were dissolved using trisodium citrate dehydrate (TCD) and the cells were collected and counted using a haemocytometer. Data represents the mean ± standard error from a minimum of two independent experiments. The means of these biological replicates are depicted as open circles.

Figure 3.4.13b shows the final gel construction of GBM hydrogel microbeads. As presented in Figure 3.4.13c, the beads retain their spherical structure over the 10-day experiment, and the increase in proliferation suggests the cells are well-maintained within the beads. A slight decrease in roundness at day 10, coupled with the decrease in proliferation, is indicative of the cells becoming over confluent within the beads, causing them to expel from the hydrogel structure.

3.4.4. Discussion

The importance of 3D cell culture has been widely discussed in recent years (163). These cellular models provide a more clinically-relevant representation of the spatial conformation of an *in situ* tumour than conventional 2D techniques. The aim of this study was to develop suitable 3D spheroid models to be utilised in various radiation response studies. In addition, the use of hydrogels as cell scaffolds in the form of microbeads demonstrated promising results as a 3D cellular model, here and elsewhere (239,244,245), acting as a protective barrier, facilitating easy transfer between vessels for further analysis and allowing the diffusion of required oxygen and nutrients. A panel of five widely-used GBM cell lines were tested, however not all were suitable for all assays. U87MG was excluded from the 2D scratch migration assay due to the preference for forming spheroids in a confluent environment. LN18 and U87MG were the only spheroids to exhibit significant spheroid growth over the 10-day optimisation test. U87MG was excluded from the spheroid migration and invasion assays as the outer edges of the spheroids were easily damaged during transfer between plates, consequently depositing cells which could not be distinguished from migrating or invading cells. Furthermore, no invasion into the hydrogel was observed in cell lines A172 and T98G after 7 days in culture.

Prior to investigating the effects of radiation on 3D models of migration and invasion, the migratory characteristics of each cell line were first defined in a 2D orientation using the scratch assay to determine the influence of cellular structure and the architecture of the environment. This migration involves a combination of mechanical forces, cellular interactions and biochemical cascades to encourage to cells to move into the cell free area (241). Forgetting the lack of spatial similarities, this technique mimics the migration of cells *in situ* where cells migrate in order to maintain cell-cell contact (240). The simplest way to create the gap is using a pipette tip or other sharp tool to scratch away a line of cells in the middle of the cell monolayer. Although this is an inexpensive and easy to implement technique, it can damage the cells on the edges of the gap which may impact motility and is difficult

to reproduce and time consuming if scratching the individual wells separately (241). One improvement implemented in recent years is the use of a multi-well device which uses a set of pins specifically designed to create reproducible gaps in each well in a multi-well plate (246). Mechanically scratching the monolayer will leave behind cellular debris, which may create an artefact within the image difficult to distinguish from migrating cells, so it is important that each well is washed to remove this before the cell culture medium is replaced. Addition of fresh medium also removes any growth factors released from the damaged cells (241). Alternatively, a way to create the gap without causing any damage is by seeding the cells around a silicon insert adhered to the surface of a well or dish such that upon removal a gap remains. In theory, this should produce reproducible gaps but upon removal cell layers can also be disturbed and if the adhesive layer is compromised the cells may travel into the empty areas.

Differences between the 2D and 3D migration assays were observed, with radiation having a negative effect on the migration from the 3D spheroids, further enhanced with the addition of the hydrogel. During the scratch assay LN18 and T98G cells demonstrated evidence of radiation-induced migration, consistent with existing literature (176,247–251). Spheroid migration showed almost the opposite effect in cell lines A172, T98G and U251, reducing migration after irradiation, in a dose dependent manner. This reduction in migration from U251 cells was further enhanced in the invasion assay, which also induced a reduction in the migratory capacity of LN18 cells, not seen in the previous assays. These conflicting results are of concern and may be due to the profound phenotypical changes observed in response to the surrounding environment (163). It is also important to note the slight radiation-induced migration seen with some of the 2 Gy results when considering individual RT fractions administer similar sub-lethal doses (252). Although higher doses have been shown to inhibit the migration of tumour cells, dose escalation studies are required to investigate the risk on surrounding tissues before changing these treatment regimens (253). Other studies have demonstrated an increase to the migration rate of the GBM cell line U87MG after irradiating with 2 Gy of photons, which then decreased when exposed to doses of 5 Gy and above (58,60,61). Similar results were seen in cell line A172 which showed a decrease in overall migration when exposed to 5 Gy (256). Increased expression of the epidermal growth factor receptor (EGFR) and the loss of the phosphatase and tensin homolog (PTEN) protein inhibiting the phosphatidylinositol 3-kinase (PI3K) pathway are correlated with a poor prognosis and play an important role in tumour cell functions,

including migratory capacity (247). Other studies report that gain-of-function mutations of the p53 gene promote migration, invasion and metabolic changes (197). This is consistent with the findings from the scratch migration assay, in which the PTEN and p53 mutated and EGFR overexpressing T98G demonstrated the fastest migration rate (176,257). Pickhard *et al.* (247) propose that the phosphorylation of the EGFR in LN18 cells, following irradiation, activates downstream signalling pathways which induce migration, supporting the LN18 results from the scratch wound and spheroid migration assays presented here.

The migratory phenotypes of each cell also behaved differently between the 2D and 3D models, most likely due to the set up of the experiment. Starting in a confluent monolayer, the cells in the scratch wound assay travelled as a continuous sheet until the cells established cell-to-cell contact as the gap was closed. In the spheroid migration assay, differences between the cells migratory phenotypes was observed, with both sheet and single cell migration approaches relating to the morphology of the GBM cells. Astrocytic A172 and U251 cells (175,177) preferred single cell migration, in contrast to the epithelial-like LN18 cells (175), favouring a sheet-like approach. The fibroblast-like cell line T98G (176) elicited both phenotypes, sending out single cells in front of a sheet.

Other techniques to address the problem of culturing GBM cells in a static, 2D environment include microfluidic systems, brain slices, mini-brains and tumour organoids, reviewed extensively by Caragher *et al.* (163). In short, microfluidic systems allow the culture of cells in tubes surrounded by circulating medium which allows the exposure to relevant ECM molecules and control of the microenvironment. Brain slices are a culture technique in which tumour cells are implanted into mouse brains, allowing an accurate depiction of invasion. Mini-brains are genetically modified cerebral organoids that develop tumours, accurately depicting the morphology and function of all brain cell types. Finally, tumour organoids are developed from tumour cells seeded onto a Matrigel pellet, allowing the formation of oxygen gradients and cell subpopulations (163). The main pitfalls of these techniques are the cost, complexity, time and, in most cases, mono-culture. The alginate/gelatin hydrogel microbeads provide a simple and cost effective, 3D structure to maintain long term culture of GBM cells. Assuming the structures were completely spherical, the beads developed here were approximately 200 mm^3 in volume, representative of a typical tumour model (258). However, this size is determined by the gauge of the needle used to form the hydrogel droplets so could be adapted to develop microbeads of various sizes dependent on the end point of

the experiment. Microbeads containing different cell lines, including normal cells such as astrocytes, neurons and endothelial cells, could be created as a form of co-culture model, modulating the surrounding microenvironment and as such creating a more representative brain milieu (163). As the cells proliferate within the gel, oxygen levels may fluctuate across the gel volume and ECM components can be added to the gel to create a better representation of the surrounding environment. The optimisation experiments highlighted the difficulties in handling the gels whilst maintaining an appropriate viscosity to ensure the beads could be maintained in long term culture, the gels became increasingly viscous as the temperature dropped after removing the vials from the 37°C water bath. Several attempts at pipetting the microbeads were made before spherical geometries were formed, often the pipetting left peaks or dropping into the $CaCl_2$ created a flat edge. The final limitation with this experiment was not irradiating in the murine phantom as planned. Irradiation of these microbeads was to be performed within a realistic murine phantom, as described in Section 2, alongside the use of radiation dosimeters to validate the dose delivery. Moreover, the phantom provides a realistic vessel to carry the biological material to take advantage of the image guidance and precision delivery techniques of small animal radiation units such as the Small Animal Radiation Research Platform (SARRP). However, this study demonstrates the capability to transport the microbeads between plates and other vessels so it is probable that future irradiations in the phantom could be performed.

3.4.5. Conclusion

The results from this study suggest differences in the migration of GBM cells, dependant on the surrounding environment. With the exception of U251, all other cell lines exhibited different migration rates between the 2D scratch wound assay and the 3D spheroid migration and invasion assays. The use of spheroids and microbeads as 3D models of GBM cell lines have been established here and demonstrate suitability for further downstream assays. Improvements to current *in vitro* assays, that better represent the tumour structure and surrounding microenvironment, will ultimately lead to better translational research.

SECTION 4: FINAL DISCUSSION AND CONCLUSIONS

The first part of this thesis describes the development and application of a 3D printed tissue-equivalent murine phantom to capture realistic dosimetry measurements. The purpose of this phantom is to be implemented into quality assurance (QA) procedures for precision small animal radiation units, to increase the occurrence and sophistication of the currently lacking tests. In recent years, many publications have described the development of preclinical dosimetry phantoms. The advantage of the model described here is in its construction, using 3D printing, to allow the efficient and cost effective production of unique designs to incorporate various detectors. Once the use on the Small Animal Radiation Research Platform (SARRP) had been established, the implementation of the phantom in dosimetry QA measurements by end users was validated by the completion of a multicentre audit.

The second part of the thesis documents the development of 3D cellular models to provide a realistic representation of a tumour model. These constructions could then be placed in specifically designed pockets within the phantom to facilitate biologically-relevant irradiations. Until recently, most of the literature documents the cellular response to radiation using 2D-based assays, in glass or plastic vessels, not relevant to the composition of an *in situ* tumour. Prior to developing these novel models, the response to radiation was characterised using a panel of glioblastoma multiforme (GBM) cell lines. The clonogenic survival, DNA damage and repair capacity and the mitochondrial metabolism were investigated to give an indication of the radiosensitivity and metabolic phenotype of each cell line. Cells cultured in a hydrogel to model the surrounding tumour environment for a given cell line circumvents any potential response due to the unrealistic 2D environment or geometry when culturing on flat cell culture dishes. Development of a stable hydrogel also allowed the transfer of the cells between vessels and, in theory, the phantom.

Together, the tissue-equivalent phantom and 3D cellular models create a potential model suitable to replace, refine and reduce animal use in preclinical radiation research. The tissue-equivalent plastics and realistic geometry of the phantom, in combination with appropriate detectors, make the model a suitable replacement for

animals purely used to test new equipment or techniques or to obtain internal dosimetry measurements measured within the animal, often performed using euthanized animals. This murine geometry means the phantom can be used to optimise experiment set up prior to animal use, thereby reducing the final experiment time and subsequent duration the animal is immobilised or under anaesthesia. Use of the phantom with radiation detectors prior to any experiment, could also be used to validate the dose delivered and the dose distribution across the target, identifying any areas of heterogeneous dose distribution that may affect the response. Regular use of the phantom for dosimetry QA, as either an additional tool to the standard dosimetry tests or as part of a multi-institute audit, permits robust assessment of the dose delivery, refining animal use by minimising the risk of unnecessary toxicity either due to over- or under-dosing the tumour or geographically missing the target and irradiating surrounding normal tissue. By minimising the uncertainties in the amount of radiation dose delivered, the numbers of animals required statistically robust data will be reduced.

The serious lack of rigorous QA procedures implemented in preclinical radiation research can impact scientific quality and put into question the ethical production of such research if the results are not fit for purpose or able to progress into clinical outcomes. The heterogeneous density phantom described in this thesis would be a suitable tool to assess the individual steps of the workflow in small animal irradiators and, through the results of the dosimetry audit, can be easily adopted into standardised practice by the preclinical radiotherapy community, potentially at the international scale. Designing and 3D printing the models allows the possibility of incorporating the latest developments in detector technology to rigorously test the image acquisition, treatment plan development, image guidance and treatment delivery. Furthermore, the irradiation of 3D cellular models within the phantom could provide preliminary data prior to the use of animals as to the radiation response in a more clinically-relevant environment.

Here, the results demonstrate an improvement to preclinical dosimetry QA and an increasing recognition of the importance it has to producing translatable radiation research. Also highlighted is the difficulty in treating GBM using current modalities, given the contrasting results from a panel of GBM cell lines. Finally, differences were observed in the response to radiation between assays of 2D and 3D culture, important to consider in the future of research. This thesis is presented in the alternative format with each results chapter presented as a series of potential standalone publications. Each publication contains its own discussion relevant to the

results presented, therefore the following section highlights the overall discussion in the wider context of the thesis objectives.

4.1. Meeting the aims

The main aims of this thesis were:

- To incorporate the phantom developed by Price *et al.* (1) into routine QA procedures and
- To better integrate *in-vitro* experimentation with pre-clinical radiobiology to understand the contribution of real world dose distributions on tumour response.

In addressing the first main aim, the testing of 3D printing was performed to create custom designs to incorporate appropriate detectors. Phantoms to hold Gafchromic film, a commonly used detector in dosimetry QA, an array of TLDs, to show the capability of including smaller detectors in an array design, and a hollow model for dosimetry gel, for more sophisticated dosimetry tests. Once the design to hold Gafchromic EBT3 film had been optimised it was then important to test the use of the phantom on the SARRP, and assess all aspects of the treatment pathway from image guidance, treatment planning and dose delivery. To determine whether the phantom could be used as a tool to standardise SARRP QA and adopted into routine dosimetry checks the phantom was sent to 6 UK-based radiation research institutions to perform measurements as part of an audit. The postal audit format allowed regular end users of the SARRPs hands on experience with the phantom, holding film and alanine pellets, proving the ease of use and potential adoption of the phantom in regular and nationwide practice.

To address the second main aim, first the radiosensitivity, DNA damage and repair response and oxygen consumption rates were characterised across a panel of GBM cell lines to determine if there were any potential differences between these cell lines originating from the same tumour type. The next step was to develop appropriate 3D models to further close the gap between *in vitro* and *in vivo* studies. There was also the aim to create a suitable model that could be transferred into the phantom for a realistic irradiation of a tumour within a mouse, but this was not logistically possible. However, it was demonstrated that the hydrogel model developed could be transferred between 96 well tissue culture plates and other vessels.

4.2. Chapter 2.3. SARRP commissioning and phantom validation

The aim of Chapter 2.3 was to establish a set of reference standards for the robust dosimetry QA for the SARRP at the University of Manchester. This would ensure accurate and traceable dosimetry in all future measurements for this project and experiments within this laboratory. Measurements were also performed to optimise the use of the phantom on the SARRP and prepare for a national multicentre dosimetry audit. In advance of any phantom measurements, the SARRP was recommissioned to ensure accurate dosimetry, minimising any uncertainties relating to the dose delivered in subsequent phantom tests. Following the commissioning, QA procedures were regularly implemented with output and alignment checks performed prior to any measurements (Appendix A1.1). Regular robust dosimetry checks increase confidence in the dose delivered to both the phantom and real animals. By minimising uncertainties there is the potential to reduce the sample sizes required and the use of animals is refined by minimising toxicity. The use of a murine geometry phantom allows a realistic simulation of an experiment prior to the involvement of a mouse, allowing a test of the experiment set up and validation of the dosimetry. This further refines the use of mice by potentially reducing the experiment time and the time the animal is required in restrictive immobilisation or under anaesthesia, especially when using more sophisticated or new techniques.

This chapter details the first use of the phantom. In the advent of precision small animal irradiation units there is the requirement for regular and sophisticated QA procedures to ensure accurate dose delivery and use these clinical RT-mimicking units to their full potential. Within the literature, several preclinical dosimetry phantoms have been proposed for such purpose (71,76,86,116). However, these lack the realistic murine geometry, tissue-equivalence or are not 3D printed so lack the ability to create bespoke designs. In order to test the phantom as a tool to accurately quantify the dose delivery, and determine any attenuation effects from the higher density bone material contained within, Gafchromic EBT3 film was employed. The use of Gafchromic EBT3 and gamma analysis process is well documented and characterised in clinical practice (111,112). Several film measurements were undertaken in regions containing significant volumes of the skeleton, such as the spine, pelvis and skull. It was concluded that the bone-mimicking material had little effect on the overall dose delivered but in fact the biggest difference observed across the dose distribution was at the field edges, when using a static beam delivery. This work did not investigate the exact cause for this sharp dose gradient in the plan vs the blurred field edges in the measurement,

although it is assumed to be due to the treatment planning system (TPS) modelling and could be investigated using the recent software update incorporating Monte Carlo modelling into the current superposition convolution model. These results determined the phantom and Gafchromic EBT3 film to be a suitable tool to assess differences between planned and delivered doses. However, future use of the phantom, including in the dosimetry audit described in Chapter 2.4, would utilise a homogeneous density model, with air gaps in the place of lungs, due to the negligible attenuation observed from the skeleton and to avoid any tissue segmentation issues during the treatment planning process.

As described in Section 2.3, there are several limitations with 3D printing these murine phantoms. Unless a high resolution 3D printer is used it may be difficult to create the finer details within the phantom such as the lung spaces that may contain supporting material, which is difficult to remove from such a small volume. As discussed previously, when creating unique designs to hold detectors it is important to consider the best orientation on the printing plate to ensure all aspects of the murine geometry (ears and feet) or the detector holders (alanine cavities or slots) are able to print.

As the SARRP had previously been commissioned upon its installation in 2014, a validation of the existing beam model was not performed. If necessary, this would have involved developing a treatment plan for the commissioning dose depth film stack to match the delivered beam geometry and the dose calculated for comparison. The phantom does not include any soft tissue subtypes such as adipose or muscle, due to their similar composition to the more generalised soft tissue and the limitations in 3D printing technology, in the resolution of the printing and the ability to simultaneously print with a limited number of filaments. This work did not investigate the use of the phantom with other detector types, although several models were printed to demonstrate the capability of 3D printing to incorporate 1D thermoluminescent detectors or 3D polymer gels. These early models also relied on the use of tape to secure the film, in the absence of pegs, which led to a slight air gap between the film and phantom, hampering the analysis and requiring additional interpolation to compensate for the resulting artefact. Other issues observed, which would be considered in future irradiations, was the phantom rotation and the need for film markings to match the measurement to the plan data.

4.3. Chapter 2.4. Preclinical dosimetry audit:

Chapter 2.4 of this thesis documents the results from a national multicentre preclinical dosimetry audit of SARRPs, using the murine phantom and the irradiation procedures optimised in the latter stages of Chapter 2.3. This audit demonstrates the dissemination of the developed phantom across sites and the suitability of incorporating it into QA procedures by regular users of the SARRPs. The completion of this audit, and the acceptable results measured, provides comparable data across these sites to aid in collaborative studies. These audited irradiation units have accurate and traceable dosimetry, refining the use of any animals subsequently used on these machines, as described above, and may reduce the sample sizes required in line with the reduced uncertainties in delivered dose. The phantom split down the coronal plane, described in Chapter 2.3.2, was designed with additional cavities to place alanine pellet detectors to be used in combination with Gafchromic EBT3 film, capturing measurements of both the absolute dose delivered and the distribution across the irradiation field.

Much of the literature surrounding preclinical radiation dosimetry discusses the lack of standardised practice and so, prior to performing any measurements, a questionnaire was sent to participating institutes to gauge the current QA practices adopted by 7 UK centres. A mixture of open and closed questions concluded there is currently no consensus in the types and frequency of QA tests performed between centres.

There have been a number of preclinical dosimetry audits undertaken in recent years, either comparing planned and delivered doses (68) or as an end-to-end test of the complete irradiation procedure (74). The audit presented was an improvement over these previous tests in the use of a 3D printed, realistic geometry phantom to assess the dose delivery in both 1 and 2 dimensions and using both simple static and complex arc beam arrangements. Two irradiation scenarios were measured, a static beam plan with the aim to measure the absolute dose and an arc to test the positional accuracy. The 12 Gy dose was chosen based on the uncertainties in low doses when using alanine pellets, whist still being suitable for film dosimetry, and in keeping with a radiobiologically-relevant dose level. The measured dose was compared to the planned dose and analysed by calculating the percentage dose difference and using a local gamma analysis. The conclusion was reached that, although the performance of QA tests vary between the institutions involved in the

audit, the SARRPs tested were within the tolerances currently regarded as acceptable.

Limitations of this study come from the uncertainties within the use of alanine and the associated correction factors required when using alanine at medium energy X-rays. These uncertainties are an accumulation of those from the measurement of the HVL and the difference in energy spectra and beam quality between the SARRPs (X-ray) and the National Physical Laboratory's (NPL's) reference beam (^{60}Co). There may also be contributing uncertainties that are related to the treatment planning system (TPS) calculations such as segmentation thresholds, commissioning or targeting, which are out of the scope of this investigation. As discussed in Section 2.4, a homogeneous density phantom was used in the audit to avoid uncertainties in the segmentation process during the treatment plan development. The overall density of the phantom was 1.19 g/cm^3 which is slightly higher than the typical range for the density of soft tissue (0.95 - 1.05 g/cm^3) (145,146). This difference potentially impacts on the accuracy of the dose calculation. Within the TPS, the tissue segmentation allows voxels within an image to be assigned as one of 5 discrete materials (air, lung, fat, tissue or bone) whose densities are defined according to ICRU report 44 (146,148). An underestimate in the density of the material defined as 'tissue' will lead to the TPS underestimating the attenuation of the beam within the phantom, which we estimate could lead to an error of 1-2% in the calculated dose at the film or alanine detectors. Unambiguous guidance would be provided to ensure the detectors are used correctly and the treatment plan is designed as required, especially if the aim of the measurement is more stringent that dose differences, for example targeting a specific area within the phantom. Many of the practical issues encountered during the audit arose due to the logistics of it being a postal audit as opposed to having being undertaken by the authors. However, a benefit of a postal audit is that it provides information regarding the real use of the machines by the end users.

Future investigations would repeat those measurements missed due to damaged alanine pellets and to reassess those plans that included large air gaps between the film and phantom surface. New phantoms would be assessed prior to distribution to ensure the correct fit of the alanine pellets, or other detectors if required. The inclusion of more relevant treatment plans such as parallel-opposed pairs could be performed to fully assess the dose delivery for all beam arrangements used, and arc deliveries using larger field sizes would provide measurements of the absolute dose delivered during a more spread out dose distribution. Including more institutions or

other types of small animal radiation units, such as cabinet irradiators (see Appendix, Figure A1.2), would further provide a standardised dosimetry reference for collaborative studies and demonstrate the use of the phantom across the country.

4.4. Chapter 3.3. Radiation response

Chapter 3.3 describes the characterisation of the radiation response across four GBM cell lines. The response to radiation in 2D culture was established prior to investigating the effects of radiation in 3D cellular models, outlined in Chapter 3.4.

The first objective, within Chapter 3.3, was to assess the radiosensitivity using the gold standard clonogenic survival assay, to identify differences between each of the four GBM cell lines. The clonogenic survival results were then compared to the residual DNA damage foci, measured 24 hours post-irradiation using γH2AX as a marker of DNA double strand breaks (DSBs), indicating irreparable damage. Finally the health of the cells, based on the mitochondrial oxygen consumption, was examined using the Seahorse Mitochondrial Stress Test.

Based on the knowledge of the inherent radioresistance of GBM cells, the clonogenic assay was performed over a range of doses, initially up to 12 Gy. All cell lines exhibited sufficient colony formation up to 8 Gy, with U251 maintaining limitless replicative potential at 10 Gy. The surviving fraction at 2 Gy (SF2) is commonly used as a measure of radiosensitivity to establish differences between cell lines. The aim of future assays was to accurately quantify a response to radiation, whilst the cells still retained a level of "normal" function after irradiation, therefore a dose of 4 Gy was used to induce DNA damage and a mitochondrial stress response. Differences in radiosensitivity were observed between the four cell lines tested in both the clonogenic survival and DSB repair. However, differences in the results between the two assays were observed, with U251 cells surviving exposure to 10 Gy radiation yet had almost the highest levels of unrepaired DNA damage 24 hours after irradiation at 4 Gy, which indicates a radiosensitive response. The use of an additional DNA repair marker p53-binding protein 1 (53BP1) could provide information regarding the function of the p53 protein (mutated in cell line U251) and could provide some explanation as to this discrepancy. This could also determine whether any mutagenic effects are impacting the DSB repair response regarding the repair pathway choice, as 53BP1 demonstrates a preference for non-homologous end joining over homologous recombination. It would also be useful to have included

further time points during the DNA damage repair assay to establish the repair kinetics of each cell line.

To illicit a mitochondrial stress response, a 4 Gy dose of X-rays was used. The Seahorse mitochondrial stress test was performed 24 hours after the cells were irradiated to allow for most of the DNA damage to repair, as observed in the immunofluorescence microscopy assay. Radiation induced a stress response in the mitochondria, increasing the oxygen consumption rate (OCR) of every cell line, except A172. This assay also provides the baseline extracellular acidification rate (ECAR), indicating the preference for glycolysis over oxidative phosphorylation – a common occurrence in cancer cells.

On the whole, the data obtained from the three assays performed in this study demonstrate that although the cell lines originated from the same tumour type, differences were observed in the response to radiation. This emphasises the difficulty in developing a targeted therapy to treat GBM.

4.5. Chapter 3.4. Development of 3D cellular models

Chapter 3.4 details the development of 3D cellular models to provide a better representation of an *in situ* tumour. Within the literature, many cell culture experiments rely on 2D assays due to the simple and efficient production of results. However, the relevance of such data to translate into clinical outcomes are far from conclusive due to the lack of relevant cellular geometry and environment. The combination of biologically-relevant tumour models and the zoomorphic phantom could provide accurate preliminary tumour control data prior to the irradiation of small animals and test the initial experiment set up and design. This has the potential to be a refinement of the use of animals by testing hypotheses and obtaining relevant radiobiological data in a realistic geometry to support in vivo experimentation. Irradiating samples within the phantom provides a realistic external environment (murine geometry and tissue-equivalent density) and allows the advantage of using the sophisticated irradiation techniques of the precision small animal radiation units, further closing the gap between the laboratory bench and the clinic. The use of DNA damage markers within the 3D geometry could provide an indication of the biological dose heterogeneity across the tumour model at micrometre scale resolution. Radiation detectors could also be incorporated in such models to validate the dose delivery.

The main purpose of Chapter 3.4 was to develop a 3D cellular model that could be incorporated into the phantom design to facilitate these biologically-relevant irradiations, without the need for animals. As such, models of spheroids and microbeads were developed due to their popularity in the literature, simple generation and handling and the protective nature of a hydrogel. When constructing a 3D model, considerations of size, to control the levels of hypoxia and necrosis within, and culture technique, to allow high throughput experiments and easy maintenance, must be accounted for to generate useable results. Ultra low attachment (ULA) plates provide a simple, yet effective, way of developing cellular spheroids, providing a platform to perform growth, migration and invasion assays, after irradiating. Encapsulating cells in a hydrogel structure permits a realistic cell geometry, can be designed to represent the relevant extracellular matrix (ECM) environment and is structurally stable to facilitate transfer whilst maintaining a sufficient diffusion of oxygen and nutrients and the removal of waste products. Further development of the hydrogel could have included the addition of brain ECM-relevant components such as hyaluronic acid or collagen.

Spheroid models were then developed to provide a 3D environment to determine differences between the 2D scratch assay and 3D culture. Once the spheroid growth characteristics had been established, smaller spheroids were cultured and transferred to a tissue culture treated plate to assess migration after the cells had spent some time in a 3D environment. The next assay was completed using the same protocol as the spheroid migration assay, with the addition of a hydrogel to mimic the surrounding brain tissue and provide an imitation of GBM invasion. This same composition of hydrogel was used to develop microbeads to contain GBM cells in a protective and stable 3D structure to facilitate long term culture in a realistic cell geometry.

The use of spheroids and the hydrogel as an invasion model was a simple way of mimicking the migratory and invasive properties of GBM *in situ.* However as the spheroids had to be transferred to flat bottomed tissue culture treated plates and then the gel added on top it was difficult to detect the positioning of the spheroid within the gel structure and it may be likely that some spheroids may have attached to the bottom of the plate, giving them a structure to migrate across more easily than through the gel. The size and shape of the hydrogel mucrobeads was dependent on the pipetting technique, in some cases the beads developed a peak or a flat edge which impact reproducibility and may restrict movement within the gel.

With the introduction of radiation, it was found that sub-lethal doses of X-rays (2 Gy) had little impact on spheroid growth or migration in either the 2D or 3D assays. It was only upon the addition of the hydrogel in the invasion assay that a decrease in invasion was detected. The use of a lethal dose (8 Gy, as determined from the clonogenic survival data) significantly impacted spheroid growth and invasion into the hydrogel structure but had little impact on 2D or 3D migration, compared to the control or 2 Gy irradiated samples. It may have been appropriate to extend the assays beyond the 24 or 72 hour time points to examine potential delayed effects, but once the cells have migrated to almost fill the empty void this may decrease the rate of migration, independent of any irradiation effects, and long term culture over 72 hours may require medium changes which may disturb the migrating cells.

Future work would involve fixing the spheroids after irradiating, sectioning and staining for hypoxic and necrotic areas, to validate the sizes chosen based on the development of oxygen and nutrient gradients. Further development of the microbeads would involve irradiating the beads in both tissue culture plates and the murine dosimetry phantom, and then fixing and performing immunofluorescence microscopy, using an adapted protocol described in Chapter 3.3, to determine the extent of DNA damage throughout the microbead. It would also be useful to use a marker of hypoxia to determine the oxygen and nutrient availability within the gel.

4.6. Overall conclusions and future directions

The work presented in this thesis documents the development, optimisation and validation of a 3D printed zoomorphic phantom, capable of capturing accurate dosimetry measurements suitable for QA purposes. In parallel with the development of this phantom, biological experiments were performed to characterise the radiation response in a panel of glioblastoma multiforme (GBM) cell lines and develop suitable 3D cell structures to facilitate biologically-relevant irradiations in the dosimetry phantom.

Variations of the model, with Gafchromic EBT3 film, were tested on a newly commissioned SARRP to ensure accurate and precise dosimetry. After which, phantoms split in the central coronal plane, containing the film and alanine pellet detectors, were sent to several UK institutions as part of a SARRP dosimetry audit. The use of the phantom as a tool for dosimetry received positive feedback from the participants in the audit. It is hoped that this initial use will stimulate more researchers to develop their own version of this 3D printed model and implement

this into regular practice. Collectively, a standard tool such as this will increase the accuracy, reproducibility and comparability of research.

GBM cells were irradiated with X-rays to examine the radiosensitivity, indicated using clonogenic survival, DNA damage repair and spheroid growth. Further models of GBM cells investigated the migration and invasion after irradiation. Spheroid and microbead 3D cellular matrices provided suitable models for simple generation, efficient culture and easy analysis. This kind of approach to developing a 3D model allows for the desirable harvesting of samples to transfer to other vessels, including the murine phantom.

In the context of the four GBM cell lines tested, A172 was identified as the most radiosensitive when exposed to X-ray doses up to 8 Gy. This was confirmed in the immunofluorescence microscopy assay, in which A172 had the highest levels of residual, and assumed, irreparable damage 24 hours after irradiating. No change was detected in the oxygen consumption rate, or the metabolic phenotype, after irradiating most likely due to the effects of the limited DNA DSB repair at the time of the assay. The rates of migration also decreased after exposure to 2 and 8 Gy X-rays, consistent with these findings. The cell line LN18 demonstrated the second lowest clonogenic survival curve and the second highest levels of residual DNA damage, concluding that this is the second most radiosensitive cell line tested. Little change was detected in the spheroids growth after 2 Gy, but after exposure to 8 Gy the spheroid growth rate began to plateau. The invasion of LN18 cells into the alginate/gelatin hydrogel matrix also declined after exposure to irradiation. However, radiation increased migration in the 2D scratch wound assay for both doses, and 2 Gy increased migration from the spheroid structure. Small, but significant, changes were observed across all oxygen consumption rates measured. T98G GBM cells showed the second highest clonogenic survival and had the lowest levels of residual DNA damage remaining, indicating elevated DNA repair and radioresistance. A heightened mitochondrial stress response was observed in this cell line, with the largest significant difference observed across all oxygen consumption measurements and metabolic phenotype, demonstrating a preference for glycolysis, compared to the other cell lines. Contrasting results were observed between the 2D and 3D migration assays, with radiation increasing the migration rate in the scratch wound assay but decreasing the migration from the spheroid. The cell line U251 demonstrated the highest clonogenic survival, exhibiting cell survival after exposure to 10 Gy. However, the levels of remaining residual DNA DSBs were among the highest across the four cell lines and only slight changes were observed in the

mitochondrial stress. U251 cells exhibited the slowest migration rate to close the scratched void, with radiation decreasing migration and invasion across all assays.

To incorporate detectors or biological material the following parameters should be considered:

1. The positioning of the cavity should be in a location which allows the best printing orientation i.e. using the least amount of supporting material that can be removed easily.
2. With a high resolution 3 printer, the cavity for detectors should be made approximately 0.5mm wider than the detector but this should be tested prior to any measurements and adjustments made when necessary.
   a. For biological material the size and shape of the cavity is less important but should be made large enough to hold the sample but may be filled with medium or hydrogel material to avoid air gaps.
3. For biological irradiations the ABS-based phantom is best suited as it can be sterilised by soaking in 70% ethanol for 10 minutes. PLA may dissolve or warp in ethanol so this would not be suitable for these irradiations. The biological samples can be inserted into the phantom by pipetting in a HEPA filtered class II laminar flow biological safety cabinet as described in Section 3.4.2.7. The phantom may then be placed in a sealed sterile falcon tube for irradiation and the beads returned to the 96 well plate, when this is complete, for further analysis.

The benefit of creating a zoomorphic phantom with biological inserts, even in the absence of high quality dosimetry, is the increased relevance of the 3D cellular construct and tissue equivalent densities in the surrounding vessel, compared to irradiating cells in 2D, plastic plates. Including detectors to be irradiated at the same time captures dose measurements so that in the event of inaccurate or imprecise dose delivery the collected data is still useable as even though the dose may not be what was planned it is still known and conclusions can be drawn. With accurate dosimetry and high-precision delivery systems in use, the phantom and biological material will provide preliminary data for *in vivo* experiments by mimicking the irradiation of a tumour within a mouse.

The zoomorphic phantom with radiation detectors, and potential combination of the 3D cellular models, creates a model suitable to replace, refine and reduce animal use in research. The tissue-equivalent materials and murine geometry of the dosimetry phantom make the model a suitable replacement for animals purely used

for dosimetry purposes in the testing of new shielding or collimation equipment or precision targeting techniques or in those animals used purely to obtain dosimetry measurements within an animal, an often invasive procedure. Regular use of the phantom in robust and standardised dosimetry QA practice allows accurate and comparable dose delivery, refining research by minimising the risk of unnecessary toxicity in the case of overdosing normal tissue, improving the reliability of results, and can be used to optimise many aspects of the experimental procedure prior to animal use, thereby reducing the duration the animal is required in restrictive immobilisation devices or under anaesthesia. A reduction in the sample sizes required for statistically significant data will also be achievable with regular implementation of the phantom by minimising the uncertainties with delivered dose thereby increasing the signal to noise ratio.

This thesis lays the foundations for a combination of dosimetric and biological validations of preclinical radiation delivery. Establishing the dosimetry phantom in standard QA practice across UK institutions, and further afield, would provide a reference for collaborative studies and work towards ensuring every animal used contributes to robust and translatable radiation research. Future development of the 3D printed phantom could involve the inclusion of more sophisticated detector technology capable of determining delivered dose at micron scale resolution such as diamond detectors. This could detect the delivered dose with sufficient spatial resolution to predict the impact of physical dose on the biological response in the tumour vs normal cells. This could be further validated with the inclusion of the microbead cellular models and markers of DNA damage to assess the impact of the dose delivered. The use of a holder such as the tissue-equivalent phantom provides a vessel for realistic irradiation and allows the implementation of more sophisticated irradiation techniques, such as the SARRP, compared to cabinet irradiators. This becomes a step closer to more relevant *in vivo* experimentation, increasing the likelihood for translational results.

References

1. Price GJ, Biglin ER, Collins S, Aitkenhead AH, Subiel A, Chadwick AL, et al. An open source heterogeneous 3D printed mouse phantom utilising a novel bone representative thermoplastic. Phys Med Biol. 2020;13.

2. Ciecior W, Ebert N, Borgeaud N, Thames HD, Baumann M, Krause M, et al. Sample-size calculation for preclinical dose–response experiments using heterogeneous tumour models. Radiother Oncol. 2021;158:262–7.

3. Cancer Research UK. Cancer Statistics for the UK [Internet]. 2017 [cited 2021 Jul 22]. Available from: https://www.cancerresearchuk.org/health-professional/cancer-statistics-for-the-uk

4. Ahmad AS, Ormiston-Smith N, Sasieni PD. Trends in the lifetime risk of developing cancer in Great Britain: comparison of risk for those born from 1930 to 1960. Br J Cancer. 2015;112(5):943–7.

5. Baumann M, Ebert N, Kurth I, Bacchus C, Overgaard J. What will radiation oncology look like in 2050? A look at a changing professional landscape in Europe and beyond. Mol Oncol. 2020;14(7):1577–85.

6. Cancer Research UK. Brain, other CNS and intracranial tumours statistics [Internet]. 2017 [cited 2020 Jun 16]. Available from: https://www.cancerresearchuk.org/health-professional/cancer-statistics/statistics-by-cancer-type/brain-other-cns-and-intracranial-tumours/incidence#heading-Seven

7. Cancer Research UK. Astrocytoma and glioblastoma (GBM) [Internet]. 2019 [cited 2020 Jun 16]. Available from: https://www.cancerresearchuk.org/about-cancer/brain-tumours/types/astrocytoma-glioblastoma-multiforme

8. Hanahan D, Weinberg RA. The Hallmarks of Cancer. Cell. 2000;100(1):57–70.

9. Shibata A, Jeggo PA. DNA Double-strand Break Repair in a Cellular Context. Clin Oncol. 2014;26(5):243–9.

10. Hanahan D, Weinberg RA. Hallmarks of cancer: The next generation. Cell. 2011;144(5):646–74.

11. Boss M-K, Bristow R, Dewhirst MW. Linking the History of Radiation Biology to the Hallmarks of Cancer. Radiat Res. 2014;181(6):561–77.

12. Phadngam S, Castiglioni A, Ferraresi A, Morani F, Follo C, Isidoro C. PTEN dephosphorylates AKT to prevent the expression of GLUT1 on plasmamembrane and to limit glucose consumption in cancer cells. Oncotarget. 2016;7.

13. Crellin AM, Burnet NG. Proton Beam Therapy: The Context, Future Direction and Challenges Become Clearer. Clin Oncol. 2014;26:736–8.

14. Durante M, Paganetti H. Nuclear physics in particle therapy: A review. Reports Prog Phys. 2016;79(9).

15. Scaife JE, Barnett GC, Noble DJ, Jena R, Thomas SJ, West CML, et al. Exploiting biological and physical determinants of radiotherapy toxicity to individualize treatment. Br J Radiol. 2015;88(1051).

16. Emami B, Lyman J, Brown A, Coia L, Goitein M, Munzenrider JE, et al. Tolerance of normal tissue to therapeutic irradiation. Int J Radiat Oncol Biol Phys. 1991;21(1):109–22.

17. International Atomic Energy Agency. The Role of PET/CT in Radiation Treatment Planning for Cancer Patient Treatment. 2008.

18. Niyazi M, Brada M, Chalmers AJ, Combs SE, Erridge SC, Fiorentino A, et al. ESTRO-ACROP guideline "target delineation of glioblastomas." Radiother Oncol. 2016;118(1):35–42.

19. Burnet NG, Jena R, Burton KE, Tudor GSJ, Scaife JE, Harris F, et al. Clinical and Practical Considerations for the Use of Intensity-modulated Radiotherapy and Image Guidance in Neuro-oncology. Clin Oncol. 2014;26(7):395–406.

20. O'Shea T, Bamber J, Fontanarosa D, Meer S van der, Verhaegen F, Harris E. Review of ultrasound image guidance in external beam radiotherapy part II: intra-fraction motion management and novel applications. Phys Med Biol. 2016;61(8).

21. Ishikura S. Quality Assurance of Radiotherapy in Cancer Treatment: Toward Improvement of Patient Safety and Quality of Care. Jpn J Clin Oncol. 2008;38(11):723–9.

22. Boustani J, Grapin M, Laurent P-A, Apetoh L, Mirjolet C. The 6th R of Radiobiology: Reactivation of Anti-Tumor Immune Response. Cancers (Basel). 2019;11(6).

23. Withers HR. The Four R's of radiotherapy. Adv Radiat Biol. 1975;5:241–7.

24. Steel GG, McMillan TJ, Peacock JH. The 5Rs of Radiobiology. Int J Radiat Biol. 1989;56:1045–8.

25. Withers HR, Taylor JMG, Maciejewski B. The hazard of accelerated tumor clonogen repopulation during radiotherapy. Acta Oncol (Madr). 1988;27(2):131–46.

26. Ang KK, Berkey BA, Tu X, Zhang HZ, Katz R, Hammond EH, et al. Impact of epidermal growth factor receptor expression on survival and pattern of relapse in patients with advanced head and neck carcinoma. Cancer Res. 2002;62(24):7350–6.

27. Yamada M -a., Puck TT. Action of Radiation on Mammalian Cells, Iv. Reversible Mitotic Lag in the S3 Hela Cell Produced By Low Doses of X-Rays. Proc Natl Acad Sci. 1961;47(8):1181–91.

28. Little JB. Delayed initiation of DNA synthesis in irradiated human diploid cells. Nature. 1968;218(5146):1064–5.

29. Kuerbitz SJ, Plunkett BS, Walsh W V., Kastan MB. Wild-type p53 is a cell cycle checkpoint determinant following irradiation. Proc Natl Acad Sci U S A. 1992;89(16):7491–5.

30. Trowell O. The sensitivity of lymphocytes to ionising radiation. J Pathol Bacteriol. 1952;64(4):687–704.

31. Hallahan D, Kuchibhotla J, Wyble C. Cell adhesion molecules mediate radiation-induced leukocyte adhesion to the vascular endothelium. Cancer Res. 1996;56(22):5150–5.

32. Drake CG. Molecular Determinants of Radiation Response. DeWeese TL, Laiho M, editors. New York: Springer; 2011. 251–263 p.

33. Puck TT, Morkovin D, Marcus PI, Cieciura SJ. Action of x-rays on mammalian cells. II. Survival curves of cells from normal human tissues. J Exp Med. 1957;106(4):485–500.

34. Sugarman BJ, Aggarwal BB, Hass PE, Shepard HM. Recombinant Human Tumor Necrosis Factor-a: Effects on Proliferation of Normal and Transformed Cells in Vitro. Science (80-). 1985;230(4728):943–5.

35. Gallin E, Green S. Exposure to Gamma-Irradiation Increases Phorbol

Myristate Acetate-Induced H2O2 Production in Human Macrophages. Blood. 1987;70(3):694–701.

36. Lehnert BE, Goodwin EH. Extracellular factor(s) following exposure to α particles can cause sister chromatid exchanges in normal human cells. Cancer Res. 1997;57(11):2164–71.

37. Strong MS, Vaughan CW, Kayne HL, Aral IM, Ucmakli A, Feldman M, et al. A randomized trial of preoperative radiotherapy in cancer of the oropharynx and hypopharynx. Am J Surg. 1978;136(4):494–500.

38. Anderson P, Dische S. Local tumor control and the subsequent incidence of distant metastatic disease. Int J Radiat Oncol Biol Phys. 1981;7(12):1645–8.

39. Brizel DM, Sibley GS, Prosnitz LR, Scher RL, Dewhirst MW. Tumor hypoxia adversely affects the prognosis of carcinoma of the head and neck. Int J Radiat Oncol Biol Phys. 1997;38(2):285–9.

40. Moeller BJ, Cao Y, Li CY, Dewhirst MW. Radiation activates HIF-1 to regulate vascular radiosensitivity in tumors: Role of reoxygenation, free radicals, and stress granules. Cancer Cell. 2004;5(5):429–41.

41. Sullivan R, Graham CH. Hypoxia-driven selection of the metastatic phenotype. Cancer Metastasis Rev. 2007;26(2):319–31.

42. Semenza GL. Defining the Role of Hypoxia-Inducible Factor 1 in Cancer Biology and Therapeutics. Oncogene. 2010;29(5):625–34.

43. Thomlinson RH, Gray LH. The histological structure of some human lung cancers and the possible implications for radiotherapy. Br J Cancer. 1955;9(4):539–49.

44. Eriksson D, Stigbrand T. Radiation-induced cell death mechanisms. Tumor Biol. 2010;31(4):363–72.

45. Griffiths JR, McSheehy PMJ, Robinson SP, Troy H, Chung YL, Stubbs M, et al. Metabolic changes detected by in vivo magnetic resonance studies of HEPA-1 wild-type tumors and tumors deficient in hypoxia-inducible factor-1β (HIF-1β): Evidence of an anabolic role for the HIF-1 pathway. Cancer Res. 2002;62(3):688–95.

46. Gordan JD, Thompson CB, Simon MC. HIF and c-Myc: Sibling Rivals for Control of Cancer Cell Metabolism and Proliferation. Cancer Cell.

2007;12(2):108–13.

47. Huang R, Zhou P-K. DNA damage repair: historical perspectives, mechanistic pathways and clinical translation for targeted cancer therapy. Signal Transduct Target Ther. 2021;6.

48. Mah LJ, El-Osta A, Karagiannis TC. γh2AX: A sensitive molecular marker of DNA damage and repair. Leukemia. 2010;24(4):679–86.

49. Chatterjee N, Walker GC. Mechanisms of DNA damage, repair and mutagenesis. Environ Mol Mutagen. 2017;58(5):235–63.

50. Grimes DR, Partridge M. A mechanistic investigation of the oxygen fixation hypothesis and oxygen enhancement ratio. Biomed Phys Eng Express. 2015;1(4).

51. Hammond EM, Asselin MC, Forster D, O'Connor JPB, Senra JM, Williams KJ. The Meaning, Measurement and Modification of Hypoxia in the Laboratory and the Clinic. Clin Oncol. 2014;26:277–88.

52. Biau J, Chautard E, Berthault N, De Koning L, Court F, Pereira B, et al. Combining the DNA repair inhibitor DBAIT with radiotherapy for the treatment of high grade glioma: Efficacy and protein biomarkers of resistance in preclinical models. Front Oncol. 2019;9(JUN):1–10.

53. Kakarougkas A, Jeggo PA. DNA DSB repair pathway choice: An orchestrated handover mechanism. Br J Radiol. 2014;87(1035).

54. Paliwal B, Tewatia D. Advances in radiation therapy dosimetry. J Med Phys. 2009;34(3):108–16.

55. Thwaites D. Accuracy required and achievable in radiotherapy dosimetry: have modern technology and techniques changed our views? J Phys Conf Ser. 2013;444.

56. Palmer A, Kearton J, Hayman O. A survey of the practice and management of radiotherapy linear accelerator quality control in the UK. Br J Radiol. 2012;85(1019):1067–73.

57. Mayles W, Lake R, McKenzie A, Macauley E, Morgan H, Jordan T, et al. Physics aspects of quality control in radiotherapy. Report no. 81. York, UK; 1999.

58. Clark CH, Aird EG, Bolton S, Miles EA, Nisbet A, Snaith JA, et al.

Radiotherapy dosimetry audit: three decades of improving standards and accuracy in UK clinical practice and trials. Br J Radiol. 2015;88(1055):20150251.

59. Ricoul M, Gnana-Sekaran T, Piqueret-Stephan L, Sabatier L. Cytogenetics for Biological Dosimetry. In: Wan T (eds) Cancer Cytogenetics Methods in Molecular Biology, vol 1541. New York, NY: Humana Press; 2017.

60. Tillner F, Thute P, Bütof R, Krause M, Enghardt W. Pre-clinical research in small animals using radiotherapy technology - a bidirectional translational approach. Z Med Phys. 2014;24(4):335–51.

61. Medina L-A, Herrera-Penilla B-I, Castro-Morales M-A, García-López P, Jurado R, Pérez-Cárdenas E, et al. Use of an orthovoltage X-ray treatment unit as a radiation research system in a small-animal cancer model. J Exp Clin Cancer Res. 2008;27.

62. Draeger E, Sawant A, Johnstone C, Koger B, Becker S, Vujaskovic Z, et al. A Dose of Reality: How 20 Years of Incomplete Physics and Dosimetry Reporting in Radiobiology Studies May Have Contributed to the Reproducibility Crisis. Int J Radiat Oncol Biol Phys. 2020;106(2):243–52.

63. Desrosiers M, Dewerd L, Deye J, Lindsay P, Murphy MK, Mitch M, et al. The Importance of Dosimetry Standardization in Radiobiology. J Res Natl Inst Stand Technol. 2013;118.

64. Verhaegen F, Granton P, Tryggestad E. Small animal radiotherapy research platforms. Phys Med Biol. 2011;56:R55–83.

65. Stojadinovic S, Low D a, Vicic M, Mutic S, Deasy JO, Hope AJ, et al. Progress toward a microradiation therapy small animal conformal irradiator. Med Phys. 2006;33(10):3834–45.

66. Deng H, Kennedy CW, Armour E, Tryggestad E, Ford E, Mcnutt T, et al. The small-animal radiation research platform (SARRP): dosimetry of a focused lens system. Phys Med Biol. 2007;52:2729–40.

67. Yoshizumi T, Brady SL, Robbins ME, Bourland JD. Specific issues in small animal dosimetry and irradiator calibration. Int J Radiat Biol. 2011;87(10):1001–10.

68. Pedersen KH, Kunugi KA, Hammer CG, Culberson WS, DeWerd LA.

Radiation Biology Irradiator Dose Verification Survey. Radiat Res. 2016;185(2):163–8.

69.   Graves EE, Zhou H, Chatterjee R, Keall PJ, Gambhir SS, Contag CH, et al. Design and evaluation of a variable aperture collimator for conformal radiotherapy of small animals using a microCT scanner. Med Phys. 2007;34(11):4359–67.

70.   Sibtain A, Morgan A, Macdougall N. Physics for Clinical Oncology. 1st ed. Oxford: Oxford University Press; 2012. 83–85 p.

71.   Subiel A, Silvestre Patallo I, Palmans H, Barry M, Tulk A, Soultanidis G, et al. The influence of lack of reference conditions on dosimetry in pre-clinical radiotherapy with medium energy x-ray beams. Phys Med Biol. 2020;65(8).

72.   Verhaegen F, Dubois L, Gianolini S, Hill MA, Karger CP, Lauber K, et al. ESTRO ACROP: Technology for precision small animal radiotherapy research: Optimal use and challenges. Radiother Oncol. 2017;

73.   Feddersen T V., Rowshanfarzad P, Abel TN, Ebert MA. Commissioning and performance characteristics of a pre-clinical image-guided radiotherapy system. Australas Phys Eng Sci Med. 2019;42(2):541–51.

74.   Silvestre Patallo I, Subiel A, Westhorpe A, Gouldstone C, Tulk A, Sharma RA, et al. Development and Implementation of an End-To-End Test for Absolute Dose Verification of Small Animal Preclinical Irradiation Research Platforms. Int J Radiat Oncol Biol Phys. 2020;107(3):587–96.

75.   Welch D, Turner L, Speiser M, Randers-Pehrson G, Brenner DJ. Scattered Dose Calculations and Measurements in a Life-Like Mouse Phantom. Radiat Res. 2017;187(4):433–42.

76.   Welch D, Harken AD, Randers-Pehrson G, Brenner DJ. Construction of mouse phantoms from segmented CT scan data for radiation dosimetry studies. Phys Med Biol. 2015;60(9):3589–98.

77.   Belley MD, Wang C, Nguyen G, Gunasingha R, Chao NJ, Chen BJ, et al. Toward an organ based dose prescription method for the improved accuracy of murine dose in orthovoltage x-ray irradiators. Med Phys. 2014;41(3).

78.   Noblet C, Delpon G, Supiot S, Potiron V, Paris F, Chiavassa S. A new tissue segmentation method to calculate 3D dose in small animal radiation therapy.

Radiat Oncol. 2018;13(1):1–8.

79. O'Toole M, editor. Mosby's Dictionary of Medicine, Nursing & Health Professions. 10th ed. Elsevier; 2016. 1333 p.

80. Rossomme S, Marinelli M, Verona-Rinati G, Romano F, Cirrone GAP, Kacperek A, et al. Response of synthetic diamond detectors in proton, carbon and oxygen ion beams. Am Assoc Phys Med. 2017;44(10):5445–9.

81. H. H. Rossi, J. L. Bateman, V. P. Bond LJG and EES. Patterns of Dynamical Behaviour in Single-Species Populations Author (s): M . P . Hassell , J . H . Lawton and R . M . May Published by : British Ecological Society Stable URL : http://www.jstor.org/stable/3886. Radiat Res Soc. 1960;13(4):503–20.

82. Broerse JJ, Zoetelief J, Puite KJ. Dosimetry Intercomparisons for Evaluation of Late Effects of Ionizing Radiation. Acta Radiol Oncol Radiat Phys Biol. 1978;17(3):225–34.

83. Wu L, Zhang G, Luo Q, Liu Q. An image-based rat model for Monte Carlo organ dose calculations. Am Assoc Phys Med. 2008;35(8):3759–64.

84. Zhang H, Hou K, Chen J, Dyer BA, Chen JC, Liu X, et al. Fabrication of an anthropomorphic heterogeneous mouse phantom for multimodality medical imaging. Phys Med Biol. 2018;63(19).

85. Dancewicz OL, Sylvander SR, Markwell TS, Crowe SB, Trapp J V. Radiological properties of 3D printed materials in kilovoltage and megavoltage photon beams. Phys Medica. 2017;38:111–8.

86. Esplen N, Alyaqoub E, Bazalova-Carter M. Technical Note: Manufacturing of a realistic mouse phantom for dosimetry of radiobiology experiments. Med Phys. 2019;

87. Soultanidis G, Subiel A, Renard I, Reinhart AM, Green VL, Oelfke U, et al. Development of an anatomically correct mouse phantom for dosimetry measurement in small animal radiotherapy research. Phys Med Biol. 2019;64(12).

88. McGurk R, Hadley C, Jackson IL, Vujaskovic Z. Development and Dosimetry of a Small Animal Lung Irradiation Platform. Health Phys. 2012;103(4):454–62.

89. Perks JR, Lucero S, Monjazeb AM, Li JJ. Anthropomorphic Phantoms for

Confirmation of Linear Accelerator-Based Small Animal Irradiation. Cureus. 2015;7(3).

90. Kamomae T, Shimizu H, Nakaya T, Okudaira K, Aoyama T, Oguchi H, et al. Three-dimensional printer-generated patient-specific phantom for artificial in vivo dosimetry in radiotherapy quality assurance. Phys Medica. 2017;44:205–11.

91. Cherry P, Duxbury A, editors. Practical radiotherapy: physics and equipment. Third. Wiley Blackwell; 2020. 58 p.

92. Winslow JF, Hyer DE, Fisher RF, Tien CJ, Hintenlang DE. Construction of anthropomorphic phantoms for use in dosimetry studies. J Appl Clin Med Phys. 2009;10(3):195–204.

93. Parsons D, Church C, Syme A. Toward a pre-clinical irradiator using clinical infrastructure. Phys Medica. 2019;58(January):21–31.

94. Koutsouvelis N, Rouzaud M, Dubouloz A, Nouet P, Jaccard M, Garibotto V, et al. 3D printing for dosimetric optimization and quality assurance in small animal irradiations using megavoltage X-rays. Z Med Phys. 2020;1–9.

95. Baumann BC, Benci JL, Santoiemma PP, Chandrasekaran S, Hollander AB, Kao GD, et al. An integrated method for reproducible and accurate image-guided stereotacti cranial irradiation of brain tumors using the small animal radiation research platform. Transl Oncol. 2012;5(4):230–7.

96. Cho NB, Wong J, Kazanzides P. Dose Painting with a Variable Collimator for the Small Animal Radiation Research Platform (SARRP). Midas. 2014;1–8.

97. Kiehl EL, Stojadinovic S, Malinowski KT, Limbrick D, Jost SC, Garbow JR, et al. Feasibility of small animal cranial irradiation with the microRT system. Med Phys. 2008;35(10):4735–43.

98. Tryggestad E, Armour M, Iordachita I, Verhaegen F, Wong JW. A comprehensive system for dosimetric commissioning and Monte Carlo validation for the small animal radiation research platform. Phys Med Biol. 2009;54(17):5341–57.

99. Verhaegen F, van Hoof S, Granton P V., Trani D. A review of treatment planning for precision image-guided photon beam pre-clinical animal radiation studies. Z Med Phys. 2014;24(4):323–34.

100. McCarroll RE, Rubinstein AE, Kingsley C V, Yang J, Yang P, Court LE. 3D-Printed Small-Animal Immobilizer for Use in Preclinical Radiotherapy. J Am Assoc Lab Anim Sci. 2015;54(5).

101. Schneider U, Pedroni E, Lomax A. The calibration of CT Hounsfield units for radiotherapy treatment planning. Phys Med Biol. 1996;41:111–24.

102. Rutherford A, Stevenson K, Tulk A, Chalmers AJ. Evaluation of four different small animal radiation plans on tumour and normal tissue dosimetry in a glioblastoma mouse model. Br J Radiol. 2019;92(1095).

103. Vanstalle M, Constanzo J, Karakaya Y, Finck C, Rousseau M, Brasse D. Analytical dose modeling for preclinical proton irradiation of millimetric targets. Med Phys. 2017;45(1):470–8.

104. Ngwa W, Tsiamas P, Zygmanski P, Makrigiorgos GM, Berbeco RI. A multipurpose quality assurance phantom for the small animal radiation research platform (SARRP). Phys Med Biol. 2012;57:2575–86.

105. Le Deroff C, Pérès EA, Ledoux X, Toutain J, Frelin-Labalme AM. In vivo surface dosimetry with a scintillating fiber dosimeter in preclinical image-guided radiotherapy. Med Phys. 2020;47(1):234–41.

106. Kuess P, Bozsaky E, Hopfgartner J, Seifritz G, Dörr W, Georg D. Dosimetric challenges of small animal irradiation with a commercial X-ray unit. Z Med Phys. 2014;24:363–72.

107. Anvari A, Modiri A, Pandita R, Mahmood J, Sawant A. Online dose delivery verification in small animal image-guided radiotherapy. Med Phys. 2020;47(4):1871–9.

108. Jermoumi M, Korideck H, Bhagwat M, Zygmanski P, Makrigiogos GM, Berbeco RI, et al. Comprehensive quality assurance phantom for the small animal radiation research platform (SARRP). Phys Medica. 2015;31(5):529–35.

109. Lindsay PE, Granton P V., Gasparini A, Jelveh S, Clarkson R, Van Hoof S, et al. Multi-institutional Dosimetric and geometric commissioning of image-guided small animal irradiators. Med Phys. 2014;41(3).

110. Butterworth KT, Prise KM, Verhaegen F. Small animal image-guided radiotherapy: Status, considerations and potential for translational impact. Br

J Radiol. 2015;88(1045).

111. Dreindl R, Georg D, Stock M. Radiochromic film dosimetry: Considerations on precision and accuracy for EBT2 and EBT3 type films. Z Med Phys. 2014;24(2).

112. Devic S, Tomic N, Lewis D. Reference radiochromic film dosimetry: Review of technical aspects. Phys Medica. 2016;32(4):541–56.

113. Baldock C, Deene Y De, Doran S, Ibbott G, Jirasek A, Lepage M, et al. Polymer gel dosimetry. Phys Med Biol. 2010;7(55).

114. Plett PA, Sampson CH, Chua HL, Joshi M, Booth C, Gough A, et al. Establishing a Murine Model of the Hematopoietic Syndrome of the Acute Radiation Syndrome. Health Phys. 2012;103(4):343–55.

115. Gould SE, Junttila MR, De Sauvage FJ. Translational value of mouse models in oncology drug development. Nat Med. 2015;21(5):431–9.

116. Bache ST, Juang T, Belley MD, Koontz BF, Adamovics J, Yoshizumi TT, et al. Investigating the accuracy of microstereotactic-body-radiotherapy utilizing anatomically accurate 3D printed rodent-morphic dosimeters. Am Assoc Phys Med. 2015;42(2):846–55.

117. Ma CM, Coffey CW, DeWerd LA, Liu C, Nath R, Seltzer SM, et al. AAPM protocol for 40-300 kV x-ray beam dosimetry in radiotherapy and radiobiology. Med Phys. 2001;28(6):868–93.

118. Tagiling N, Ab Rashid R, Azhan S, Dollah N, Geso M, Rahman WN. Effect of scanning parameters on dose-response of radiochromic films irradiated with photon and electron beams. Heliyon. 2018;4(10).

119. Aitkenhead AH, Rowbottom CG, Mackay RI. Marvin: An anatomical phantom for dosimetric evaluation of complex radiotherapy of the head and neck. Phys Med Biol. 2013;58(19):6915–29.

120. Hussein M, Clark CH, Nisbet A. Challenges in calculation of the gamma index in radiotherapy – Towards good practice. Phys Medica. 2017;36:1–11.

121. Low DA, Harms WB, Mutic S, Purdy JA. A technique for the quantitative evaluation of dose distributions. Med Phys. 1998;25(5):656–61.

122. Chaikh A, Ojala J, Khamphan C, Garcia R, Giraud JY, Thariat J, et al. Dosimetrical and radiobiological approach to manage the dosimetric shift in

the transition of dose calculation algorithm in radiation oncology: how to improve high quality treatment and avoid unexpected outcomes? Radiat Oncol. 2018;13(60).

123. Eaton J, Bateman D, Hauberg S, Wehbring R. GNU Octave version 5.1.0 manual: a high level interactive language for numerical computations. 2019.

124. Low DA, Dempsey JF. Evaluation of the gamma dose distribution comparison method. Med Phys. 2003;30(9):2455–64.

125. Wong J, Armour E, Kazanzides P, Iordachita I, Tryggestad E, Deng H, et al. A High-Resolution Small Animal Radiation Research Platform (SARRP) With X-Ray Tomographic Guidance Capabilities. Int J Radiat Oncol Biol Phys. 2008;71(5):1591–9.

126. Chen Q, Carlton D, Howard TJ, Izumi T, Rong Y. Technical Note: Vendor miscalibration of preclinical orthovoltage irradiator identified through independent output check. Med Phys. 2021;48(2):881–9.

127. Ghita M, McMahon SJ, Thompson HF, McGarry CK, King R, Osman SOS, et al. Small field dosimetry for the small animal radiotherapy research platform (SARRP). Radiat Oncol. 2017;12(1):1–10.

128. Stojadinovic S, Low DA, Hope AJ, Vicic M, Deasy JO, Cui J, et al. MicroRT-Small animal conformal irradiator. Med Phys. 2007;34(12):4706–16.

129. Hussein M, Tsang Y, Thomas RAS, Gouldstone C, Maughan D, Snaith JAD, et al. A methodology for dosimetry audit of rotational radiotherapy using a commercial detector array. Radiother Oncol. 2013;108(1):78–85.

130. Percie du Sert N, Hurst V, Ahluwalia A, Alam S, Avey M, Baker M et al. The ARRIVE guidelines 2.0: Updated guidelines for reporting animal research. PLoS Biol [Internet]. 2020;18(7). Available from: https://doi.org/10.1371/journal.pbio.3000410

131. Ableitinger A, Vatnitsky S, Herrmann R, Bassler N, Palmans H, Sharpe P, et al. Dosimetry auditing procedure with alanine dosimeters for light ion beam therapy. Radiother Oncol. 2013;108(1):99–106.

132. Ultimaker BV. Ultimaker Cura [Internet]. [cited 2021 Apr 8]. Available from: https://ultimaker.com/en/products/ultimaker-cura-software

133. NPL. Alanine dosimeter reference service [Internet]. 2021. Available from:

https://www.npl.co.uk/products-services/radiotherapy-diagnostic/alanine-reference-dosimetry

134. Bandalo V, Greiter MB, Brönner J, Hoedlmoser H. Validation of Radiation Qualities By Means of Half-Value Layer and Hp(10) Dosimetry. Radiat Prot Dosimetry. 2019;187(4):438–50.

135. Wang YF, Lin SC, Na YH, Black PJ, Wuu CS. Dosimetric verification and commissioning for a small animal image-guided irradiator. Phys Med Biol. 2018;63(14).

136. Boylan CJ, Aitkenhead AH, Rowbottom CG, Mackay RI. Simulation of realistic linac motion improves the accuracy of a Monte Carlo based VMAT plan QA system. Radiother Oncol [Internet]. 2013;109(3):377–83. Available from: http://dx.doi.org/10.1016/j.radonc.2013.08.046

137. Aitkenhead AH, Sitch P, Richardson JC, Winterhalter C, Patel I, Mackay RI. Automated Monte-Carlo re-calculation of proton therapy plans using Geant4/Gate: implementation and comparison to plan-specific quality assurance measurements. Br J Radiol. 2020;93(1114):20200228.

138. Hill MA, Thompson JM, Kavanagh A, Tullis IDC, Newman RG, Prentice J, et al. The development of technology for effective respiratory-gated irradiation using an image-guided small animal irradiator. Radiat Res. 2017;188(3):247–63.

139. Frelin AM, Beaudouin V, Le Deroff C, Roger T. Implementation and evaluation of respiratory gating in small animal radiotherapy. Phys Med Biol. 2018;63(21).

140. Anvari A, Poirier Y, Sawant A. Kilovoltage transit and exit dosimetry for a small animal image-guided radiotherapy system using built-in EPID. Med Phys. 2018;45(10):4642–51.

141. Kampfer S, Cho N, Combs SE, Wilkens JJ. Dosimetric characterization of a single crystal diamond detector in X-ray beams for preclinical research. Z Med Phys. 2018;28(4):303–9.

142. Munoz Arango E, Peixoto JG, De Almeida CE. Small-field dosimetry with a high-resolution 3D scanning water phantom system for the small animal radiation research platform SARRP: a geometrical and quantitative study. Phys Med Biol. 2020;65(1).

143. Eaton DJ, Earner B, Faulkner P, Dancer N. A national dosimetry audit of intraoperative radiotherapy. Br J Radiol. 2013;86(1032):1–5.

144. Desrosiers M. Post-Irradiation Study of the Alanine Dosimeter. J Res Natl Inst Stand Technol. 2014;119.

145. ICRP. Adult reference computational phantoms. ICRP Publication 110. Ann ICRP. 2009;39(2).

146. ICRU. ICRU Report 44: Tissue Substitutes in Radiation Dosimetry and Measurement. J ICRU. 1989;23(1):1–189.

147. Hill R, Kuncic Z, Baldock C. The water equivalence of solid phantoms for low energy photon beams. Med Phys. 2010;37(8).

148. Reinhart AM, Fast MF, Ziegenhein P, Nill S, Oelfke U. A kernel-based dose calculation algorithm for kV photon beams with explicit handling of energy and material dependencies. Br J Radiol. 2017;90.

149. Chen R, Smith-Cohn M, Cohen AL, Colman H. Glioma Subclassifications and Their Clinical Significance. Neurotherapeutics. 2017;14(2):284–97.

150. Chautard E, Guy Z, Ouédraogo JB, Verrelle P. Role of Akt in human malignant glioma: from oncogenesis to tumor aggressiveness. J Neurooncol. 2014;117:205–15.

151. Philips A, Henshaw DL, Lamburn G, O'Carroll MJ. Brain Tumours: Rise in Glioblastoma Multiforme Incidence in England 1995-2015 Suggests an Adverse Environmental or Lifestyle Factor. J Environ Public Health. 2018;

152. Wen PY, Kesari S. Malignant gliomas in adults. N Engl J Med. 2008;359:492–507.

153. Cihoric N, Tsikkinis A, Minniti G, Lagerwaard FJ, Herrlinger U, Mathier E, et al. Current status and perspectives of interventional clinical trials for glioblastoma - analysis of ClinicalTrials.gov. Radiat Oncol. 2017;12(1):1–12.

154. Walker MD, Strike TA, Sheline GE. An analysis of dose-effect relationship in the radiotherapy of malignant gliomas. Int J Radiat Oncol. 1979;5(10):1725–31.

155. Marsa GW, Goffinet DR, Rubinstein LJ, Bagshaw MA. Megavoltage irradiation in the treatment of gliomas of the brain and spinal cord. Cancer. 1975;36(5):1681–9.

156. Ten Haken R, Thornton A, Sandler H, LaVigne M, Quint D, Fraass B, et al. A quantitative assessment of the addition of MRI to CTbased, 3-D treatment planning of brain tumors. Radiother Oncol. 1992;25(2):121–33.

157. National Institute for Health and Care Exellence. Brain tumours (primary) and brain metastases in adults [Internet]. 2018. Available from: https://www.nice.org.uk/guidance/ng99/chapter/Recommendations#management-of-glioma

158. Stupp R, Mason W, van den Bent M, Weller M, Fisher B, Taphoorn M, et al. Radiotherapy plus concomitant and adjuvant temozolomide for glioblastoma. N Engl J Med. 2005;352(10):987–96.

159. Stupp R, Hegi ME, Mason WP, van den Bent MJ, Taphoorn MJ, Janzer RC, et al. Effects of radiotherapy with concomitant and adjuvant temozolomide versus radiotherapy alone on survival in glioblastoma in a randomised phase III study: 5-year analysis of the EORTC-NCIC trial. Lancet Oncol. 2009;10(5):459–66.

160. Gzell C, Back M, Wheeler H, Bailey D, Foote M. Radiotherapy in Glioblastoma: the Past, the Present and the Future. Clin Oncol. 2017;29(1):15–25.

161. Sarria GR, Sperk E, Han X, Sarria GJ, Wenz F, Brehmer S, et al. Intraoperative radiotherapy for glioblastoma: an international pooled analysis. Radiother Oncol. 2020;142:162–7.

162. Holland EC. Glioblastoma multiforme: The terminator. Proc Natl Acad Sci. 2000;97(12):6242–4.

163. Caragher S, Chalmers AJ, Gomez-Roman N. Glioblastoma's next top model: Novel culture systems for brain cancer radiotherapy research. Cancers (Basel). 2019;11(1).

164. The Cancer Genome Atlas Research Network. Comprehensive genomic characterization defines human glioblastoma genes and core pathways. Nature. 2008;455(7216):1061–8.

165. Verhaak RGW, Hoadley KA, Purdom E, Wang V, Qi Y, Wilkerson MD, et al. Integrated Genomic Analysis Identifies Clinically Relevant Subtypes of Glioblastoma Characterized by Abnormalities in PDGFRA, IDH1, EGFR, and NF1. Cancer Cell. 2010;17(1):98–110.

166. Patel AP, Tirosh I, Trombetta JJ, Shalek AK, Gillespie SM, Wakimoto H, et al. Single-cell RNA-seq highlights intratumoral heterogeneity in primary glioblastoma. Science (80-). 2014;344(6190):1396–401.

167. Beauchesne P. Extra-neural metastases of malignant gliomas: Myth or reality? Cancers (Basel). 2011;3(1):461–77.

168. Xiao W, Sohrabi A, Seidlits SK. Integrating the glioblastoma microenvironment into engineered experimental models Glioblastoma. Futur Sci. 2017;3(3).

169. Cuddapah VA, Robel S, Watkins S, Sontheimer H. A neurocentric perspective on glioma invasion. Nat Rev Neurosci. 2014;15(7):455–65.

170. Watkins S, Sontheimer H. Hydrodynamic cellular volume changes enable glioma cell invasion. J Neurosci. 2011;31(47):17250–9.

171. Price SJ, Jena R, Burnet NG, Hutchinson PJ, Dean AF, Peña A, et al. Improved delineation of glioma margins and regions of infiltration with the use of diffusion tensor imaging: An image-guided biopsy study. Am J Neuroradiol. 2006;27(9):1969–74.

172. Shen H, Hau E, Joshi S, Dilda PJ, McDonald KL. Sensitization of glioblastoma cells to irradiation by modulating the glucose metabolism. Mol Cancer Ther. 2015;14(8):1794–804.

173. Barani I., Larson DA. Radiation Therapy of Glioblastoma. In: Raizer J, Parsa A, editors. Cancer Treatment and Research. Springer, Cham; 2015. p. 49–73.

174. Han X, Xue X, Zhou H, Zhang G. A molecular view of the radioresistance of gliomas. Oncotarget. 2017;8(59):100931–41.

175. Sesen J, Dahan P, Scotland SJ, Saland E, Dang VT, Lemarié A, et al. Metformin inhibits growth of human glioblastoma cells and enhances therapeutic response. PLoS One. 2015;10(4):1–24.

176. Xiong Y, Ji W, Fei Y, Zhao Y, Wang L, Wang W, et al. Cathepsin L is involved in X-ray-induced invasion and migration of human glioma U251 cells. Cell Signal. 2017;29:181–91.

177. Comelli M, Pretis I, Buso A, Mavelli I. Mitochondrial energy metabolism and signalling in human glioblastoma cell lines with different PTEN gene status. J

Bioenerg Biomembr. 2018;50(1):33–52.

178. Bergeaud M, Mathieu L, Guillaume A, Moll U, Mignotte B, Floch N Le, et al. Mitochondrial p53 mediates a transcriptionindependent regulation of cell respiration and interacts with the mitochondrial F_1F_0-ATP synthase. Cell Cycle. 2013;12(17):2781–93.

179. Snietura M, Jaworska M, Mlynarczyk-Liszka J, Goraj-Zajac A, Piglowski W, Lange D, et al. PTEN as a Prognostic and Predictive Marker in Postoperative Radiotherapy for Squamous Cell Cancer of the Head and Neck. PLoS One. 2012;7(3).

180. Kang Y-J, Balter B, Csizmadia E, Haas B, Sharma H, Bronson R, et al. Contribution of classical end-joining to PTEN inactivation in p53-mediated glioblastoma formation and drug-resistant survival. Nat Commun. 2017;8.

181. Chen C-Y, Chen J, He L, Stiles BL. PTEN: Tumor Suppressor and Metabolic Regulator. Front Endocrinol (Lausanne). 2018;9.

182. Hegi ME, Diserens A-C, Gorlia T, Hamou M-F, Tribolet N de, Weller M, et al. MGMT Gene Silencing and Benefit from Temozolomide in Glioblastoma. N Engl J Med. 2005;352:997–1003.

183. Desouky O, Ding N, Zhou G. Targeted and non-targeted effects of ionizing radiation. J Radiat Res Appl Sci. 2015;8(2):247–54.

184. Burma S, Chen BP, Murphy M, Kurimasa A, Chen DJ. ATM Phosphorylates Histone H2AX in Response to DNA Double-strand Breaks. J Biol Chem. 2001;276(45):42462–7.

185. McCabe N, Hanna C, Walker SM, Gonda D, Li J, Wikstrom K, et al. Mechanistic Rationale to Target PTEN-Deficient Tumor Cells with Inhibitors of the DNA Damage Response Kinase ATM. Cancer Res. 2015;75:2159–65.

186. Sattler UGA, Meyer SS, Quennet V, Hoerner C, Knoerzer H, Fabian C, et al. Glycolytic metabolism and tumour response to fractionated irradiation. Radiother Oncol. 2010;94(1):102–9.

187. Maroon J, Seyfried T, Donohue J, Bost J. The role of metabolic therapy in treating glioblastoma multiforme. Surg Neurol Int. 2015;6(1).

188. Chen F, Zhuang M, Zhong C, Peng J, Wang X, Li J, et al. Baicalein reverses hypoxia-induced 5-FU resistance in gastric cancer AGS cells through

suppression of glycolysis and the PTEN/Akt/HIF-1α signaling pathway. Oncol Rep. 2015;33:457–63.

189. R Core Team. R: A language and environment for statistical computing [Internet]. Vienna, Austria: R Foundation for Statistical Computing; 2020. Available from: https://www.r-project.org/

190. Franken NAP, Rodermond HM, Stap J, Haveman J, van Bree C. Clonogenic assay of cells in vitro. Nat Protoc. 2006;1(5):2315–9.

191. van Leeuwen CM, Oei AL, Crezee J, Bel A, Franken NAP, Stalpers LJA, et al. The alfa and beta of tumours: a review of parameters of the linear-quadratic model, derived from clinical radiotherapy studies. Radiat Oncol. 2018;13(96).

192. Gu X, Ma Y, Liu Y, Wan Q. Measurement of mitochondrial respiration in adherent cells by Seahorse XF96 Cell Mito Stress Test. STAR Protoc. 2021;2(1).

193. Divakaruni AS, Paradyse A, Ferrick DA, Murphy AN, Jastroch M. Analysis and interpretation of microplate-based oxygen consumption and pH data [Internet]. 1st ed. Vol. 547, Methods in Enzymology. Elsevier Inc.; 2014. 309–354 p. Available from: http://dx.doi.org/10.1016/B978-0-12-801415-8.00016-3

194. Safa AR, Saadatzadeh MR, Cohen-Gadol AA, Pollok KE, Bijangi-Vishehsaraei K. Glioblastoma stem cells (GSCs) epigenetic plasticity and interconversion between differentiated non-GSCs and GSCs. Genes Dis. 2015;2(2):152–63.

195. Nduom EK, Weller M, Heimberger AB. Immunosuppressive mechanisms in glioblastoma. Neuro Oncol. 2015;17(July):vii9–14.

196. Miranda-Gonçalves V, Cardoso-Carneiro D, Valbom I, Cury FP, Silva VA, Granja S, et al. Metabolic alterations underlying Bevacizumab therapy in glioblastoma cells. Oncotarget. 2017;8(61):103657–70.

197. Djuzenova CS, Fiedler V, Memmel S, Katzer A, Hartmann S, Krohne G, et al. Actin cytoskeleton organization, cell surface modification and invasion rate of 5 glioblastoma cell lines differing in PTEN and p53 status. Exp Cell Res. 2015;330(2):346–57.

198. Li H-L, Wang C-Y, Fu J, Yang X-J, Sun Y, Shao Y-H, et al. PTEN expression

in U251 glioma cells enhances their sensitivity to ionizing radiation by suppressing DNA repair capacity. Eur Rev Med Pharmacol Sci. 2019;23(23):10453–8.

199. McEllin B, Camacho C V., Mukherjee B, Hahm B, Tomimatsu N, Bachoo RM, et al. PTEN loss compromises homologous recombination repair in astrocytes: implications for GBM therapy with temozolomide or PARP inhibitors. Cancer Res. 2011;70(13):5457–64.

200. Mansour WY, Tennstedt P, Volquardsen J, Oing C, Kluth M, Hube-Magg C, et al. Loss of PTEN-assisted G2/M checkpoint impedes homologous recombination repair and enhances radio-curability and PARP inhibitor treatment response in prostate cancer. Sci Rep. 2018;8.

201. Chen Z, Trotman L., Shaffer D, Lin H., Dotan Z., Niki M, et al. Crucial role of p53-dependent cellular senescence in suppression of PTEN-deficient tumorigenesis. Nature. 2005;436:725–30.

202. Lonetto G, Koifman G, Silberman A, Attery A, Solomon H, Levin-Zaidman S, et al. Mutant p53-dependent mitochondrial metabolic alterations in a mesenchymal stem cell-based model of progressive malignancy. Cell Death Differ. 2018;26:1566–81.

203. Zhang C, Liu J, Liang Y, Wu R, Zhao Y, Hong X, et al. Tumour-associated mutant p53 drives the Warburg effect. Nat Commun. 2013;4:2935.

204. Sattler UGA, Mueller-Klieser W. The anti-oxidant capacity of tumour glycolysis. Int J Radiat Biol. 2009;85(11):963–71.

205. Meijer TWH, Kaanders JHAM, Span PN, Bussink J. Targeting hypoxia, HIF-1, and tumor glucose metabolism to improve radiotherapy efficacy. Clin Cancer Res. 2012;18(20):5585–94.

206. Ge T, Yang J, Zhou S, Wang Y, Li Y, Tong X. The Role of the Pentose Phosphate Pathway in Diabetes and Cancer. Front Endocrinol (Lausanne). 2020;11(365).

207. Thon N, Kreth S, Kreth F-W. Personalized treatment strategies in glioblastoma: MGMT promoter methylation status. Onco Targets Ther. 2013;6:1363–72.

208. Caliari SR, Burdick JA. A Practical Guide to Hydrogels for Cell Culture. Nat

Methods. 2016;13(5):405–14.

209.   Rauti R, Renous N, Maoz BM. Mimicking the Brain Extracellular Matrix in Vitro: A Review of Current Methodologies and Challenges. Isr J Chem. 2019;1–12.

210.   Abdeen AA, Lee J, Kilian KA. Capturing extracellular matrix properties in vitro: Microengineering materials to decipher cell and tissue level processes. Exp Biol Med. 2016;241(9):930–8.

211.   Burnside ER, Bradbury EJ. Review: Manipulating the extracellular matrix and its role in brain and spinal cord plasticity and repair. Neuropathol Appl Neurobiol. 2014;40(1):26–59.

212.   Tunici P, Bissola L, Lualdi E, Pollo B, Cajola L, Broggi G, et al. Genetic alterations and in vivo tumorigenicity of neurospheres derived from an adult glioblastoma. Mol Cancer. 2004;3(25).

213.   Hubert CG, Rivera M, Spangler LC, Wu Q, Mack SC, Prager BC, et al. A Three-Dimensional Organoid Culture System Derived from Human Glioblastomas Recapitulates the Hypoxic Gradients and Cancer Stem Cell Heterogeneity of Tumors Found In Vivo. Cancer Res. 2016;76:2465–77.

214.   Sliwa M, Markovic D, Gabrusiewicz K, Synowitz M, Glass R, Zawadzka M, et al. The invasion promoting effect of microglia on glioblastoma cells is inhibited by cyclosporin A. Brain. 2007;130:476–89.

215.   Eisemann T, Costa B, Strelau J, Mittelbronn M, Angel P, Peterziel H. An advanced glioma cell invasion assay based on organotypic brain slice cultures. BMC Cancer. 2018;18(103).

216.   Marques-Torrejon MA, Gangoso E, Pollard SM. Modelling glioblastoma tumour-host cell interactions using adult brain organotypic slice co-culture. Dis Model Mech. 2018;11(2).

217.   Lancaster MA, Renner M, Martin CA, Wenzel D, Bicknell LS, Hurles ME, et al. Cerebral organoids model human brain development and microcephaly. Nature. 2013;501:373–9.

218.   Ogawa J, Pao GM, Shokhirev MN, Verma I. Glioblastoma Model Using Human Cerebral Organoids. Cell Rep. 2018;23:1220–9.

219.   Sutherland RM, McCredie JA, Inch WR. Growth of Multicell Spheroids in

Tissue Culture as a Model of Nodular Carcinomas. J Natl Cancer Inst. 1971;46(1):113–20.

220. Vinci M, Gowan S, Boxall F, Patterson L, Zimmermann M, Court W, et al. Advances in establishment and analysis of three-dimensional tumor spheroid-based functional assays for target validation and drug evaluation. BMC Biol. 2012;10(March).

221. Foty R. A Simple Hanging Drop Cell Culture Protocol for Generation of 3D Spheroids. J Vis Exp. 2011;20(51):4–7.

222. Jong BK, Stein R, O'Hare MJ. Three-dimensional in vitro tissue culture models of breast cancer - A review. Breast Cancer Res Treat. 2004;85(3):281–91.

223. Narayan RS, Fedrigo CA, Brands E, Dik R, Stalpers LJA, Baumert BG, et al. The allosteric AKT inhibitor MK2206 shows a synergistic interaction with chemotherapy and radiotherapy in glioblastoma spheroid cultures. BMC Cancer. 2017;17(1):1–8.

224. Bjerkvig R, Tonnesen A, Laerum OD, Backlund EO. Multicellular tumor spheroids from human gliomas maintained in organ culture. J Neurosurg. 1990;72:463–75.

225. De Witt Hamer PC, Van Tilborg AA, Eijk PP, Sminia P, Troost D, Van Noorden CJ, et al. The genomic profile of human malignant glioma is altered early in primary cell culture and preserved in spheroids. Oncogene. 2008;27:2091–6.

226. Jensen SS, Aaberg-Jessen C, Andersen C, Schroder HD, Kristensen BW. Glioma spheroids obtained via ultrasonic aspiration are viable and express stem cell markers: A new tissue resource for glioma research. Neurosurgery. 2013;73:868–86.

227. Cui X, Hartanto Y, Zhang H. Advances in multicellular spheroids formation. J R Soc Interface. 2017;14(127).

228. Curcio E, Salerno S, Barbieri G, De Bartolo L, Drioli E, Bader A. Mass transfer and metabolic reactions in hepatocyte spheroids cultured in rotating wall gas-permeable membrane system. Biomaterials. 2007;28(36):5487–97.

229. Schughart LAK. Multicellular tumor spheroids: intermediates between

monolayer culture and in vivo tumor. Cell Biol Int. 1999;23(3):157–61.

230. Ayuso JM, Virumbrales-Muñoz M, Lacueva A, Lanuza PM, Checa-Chavarria E, Botella P, et al. Development and characterization of a microfluidic model of the tumour microenvironment. Sci Rep. 2016;6(October):1–16.

231. Gomez-Roman N, Stevenson K, Gilmour L, Hamilton G, Chalmers AJ. A novel 3D human glioblastoma cell culture system for modeling drug and radiation responses. Neuro Oncol. 2017;19:229–41.

232. Li Q, Lin H, Rauch J, Deleyrolle LP, Reynolds BA, Viljoen HJ, et al. Scalable Culturing of Primary Human Glioblastoma Tumor-Initiating Cells with a Cell-Friendly Culture System. Sci Rep. 2018;8:3531.

233. Tibbit MW, Anseth KS. Hydrogels as Extracellular Matrix Mimics for 3D Cell Culture. Biotechnol Bioeng. 2009;104(4):655–63.

234. Koh I, Cha J, Park J, Choi J, Kang SG, Kim P. The mode and dynamics of glioblastoma cell invasion into a decellularized tissue-derived extracellular matrix-based three-dimensional tumor model. Sci Rep. 2018;8(1):1–12.

235. Storch K, Eke I, Borgmann K, Krause M, Richter C, Becker K, et al. Three-dimensional cell growth confers radioresistance by chromatin density modification. Cancer Res. 2010;70:3925–34.

236. Pedron S, Becka E, Harley BA. Spatially gradated hydrogel platform as a 3D engineered tumor microenvironment. Adv Mater. 2015;27(9):1567–72.

237. Bäcker V. ImageJ Macro Tool Sets for Biological Image Analysis ImageJ Macro Tool Sets for Biological Image Analysis. 2015;(March).

238. Sarker B, Papageorgiou DG, Silva R, Zehnder T, Gul-E-Noor F, Bertmer M, et al. Fabrication of alginate-gelatin crosslinked hydrogel microcapsules and evaluation of the microstructure and physico-chemical properties. J Mater Chem B. 2014;2(11):1470–82.

239. Kumachev A, Greener J, Tumarkin E, Eiser E, Zandstra PW, Kumacheva E. High-throughput generation of hydrogel microbeads with varying elasticity for cell encapsulation. Biomaterials. 2011;32(6):1477–83.

240. Liang C-C, Park AY, Guan J-L. In vitro scratch assay: a convenient and inexpensive method for analysis of cell migration in vitro. Nat Protoc. 2007;2(2):329–33.

241. Jonkman JEN, Cathcart JA, Xu F, Bartolini ME, Amon JE, Stevens KM, et al. Cell Adhesion & Migration An introduction to the wound healing assay using livecell microscopy An introduction to the wound healing assay using livecell microscopy. Cell Adhes Migr. 2014;8(5):440–51.

242. Roper SJ, Linke F, Scotting PJ, Coyle B. 3D spheroid models of paediatric SHH medulloblastoma mimic tumour biology, drug response and metastatic dissemination. Sci Rep [Internet]. 2021;11(1):1–17. Available from: https://doi.org/10.1038/s41598-021-83809-6

243. Iversen PW, Beck B, Chen Y, Dere W, Devanarayan V, Eastwood BJ, et al. HTS Assay Validation 2 . Stability and Process Studies. Assay Guid Man. 2012;(Md):1–26.

244. Tirella A, La Marca M, Brace LA, Mattei G, Aylott JW, Ahluwalia A. Nano-in-micro self-reporting hydrogel constructs. J Biomed Nanotechnol. 2014;11(8):1401–17.

245. Almari B, Brough D, Harte M, Tirella A. Fabrication of amyloid-β-secreting alginate microbeads for use in modelling alzheimer's disease. J Vis Exp. 2019;2019(149):1–9.

246. Essen BioScience. Scratch Wound Migration and Invasion Assays for Live-Cell Analysis [Internet]. [cited 2020 Jun 10]. Available from: https://www.essenbioscience.com/en/applications/live-cell-assays/scratch-wound-cell-migration-invasion/#2

247. Pickhard A, Margraf J, Piontek G, Knopf A, Reiter R, Boulesteix A-L, et al. The Radiation Induced Migration of Human Malignant Glioma Cells can be Blocked by Inhibition of the EGFR Downstream Pathways. J Nucl Med Radiat Ther. 2012;03(04).

248. Palumbo S, Tini P, Toscano M, Allavena G, Angeletti F, Manai F, et al. Combined EGFR and Autophagy Modulation Impairs Cell Migration and Enhances Radiosensitivity in Human Glioblastoma Cells. J Cell Physiol. 2014;229(11):1863–73.

249. Steinle M, Palme D, Misovic M, Rudner J, Dittmann K, Lukowski R, et al. Ionizing radiation induces migration of glioblastoma cells by activating BK K + channels. Radiother Oncol. 2011;101(1):122–6.

250. Vanan I, Dong Z, Tosti E, Warshaw G, Symons M, Ruggieri R. Role of a DNA

damage checkpoint pathway in ionizing radiation-induced glioblastoma cell migration and invasion. Cell Mol Neurobiol. 2012;32(7):1199–208.

251. Choi EJ, Cho BJ, Lee DJ, Hwang YH, Chun SH, Kim HH, et al. Enhanced cytotoxic effect of radiation and temozolomide in malignant glioma cells: Targeting PI3K-AKT-mTOR signaling, HSP90 and histone deacetylases. BMC Cancer. 2014;14(1):1–12.

252. Rieken S, Habermehl D, Wuerth L, Brons S, Mohr A, Lindel K, et al. Carbon ion irradiation inhibits glioma cell migration through downregulation of integrin expression. Int J Radiat Oncol Biol Phys. 2012;83(1):394–9.

253. Rieken S, Habermehl D, Mohr A, Wuerth L, Lindel K, Weber K, et al. Targeting avb3 and avb5 inhibits photon-induced hypermigration of malignant glioma cells. Radiat Oncol. 2011;6(132).

254. Fehlauer F, Muench M, Richter E, Rades D. The inhibition of proliferation and migration of glioma spheroids exposed to temozolomide is less than additive if combined with irradiation. Oncol Rep. 2007;17(4):941–5.

255. Goetze K, Scholz M, Taucher-Scholz G, Mueller-Klieser W. The impact of conventional and heavy ion irradiation on tumor cell migration in vitro. Int J Radiat Biol. 2007;83(11–12):889–96.

256. Zhen L, Li J, Zhang M, Yang K. MiR-10b decreases sensitivity of glioblastoma cells to radiation by targeting AKT. J Biol Res. 2016;23(1):1–10.

257. Arriagada C, Cavieres VA, Luchsinger C, González AE, Muñoz VC, Cancino J, et al. GOLPH3 Regulates EGFR in T98G Glioblastoma Cells by Modulating Its Glycosylation and Ubiquitylation. Int J Mol Sci. 2020;21(22):8880.

258. Demidenko E. Three endpoints of in vivo tumour radiobiology and their statistical estimation. Int J Radiat Biol. 2010;86(2):164–73.

Appendix 1

A1.1. SARRP commissioning data

The following Table describes the conversion of the ionisation chamber and electrometer readings, measured regularly during the commissioning process, into a dose output following the calculation denoted in the American Association of Physicists in Medicine Task Group 61 (AAPM TG-61) protocol. Figure A1.1 plots these output measurements.

Table A1.1. SARRP commissioning radiation dose output data.

Chamber	SN: 000882	SN: 000882	SN: 000882	SN: 000882	SN: 000882	SN: 000882	SN: 000882
Electrometer	SN: 081008	SN: 081008	SN: 081008	SN: 081008	SN: 081008	SN: 081008	SN: 081008
User	AA / EB	AA / EB	AA / EB	AA / EB	AA / EB	AA / EB	AA / EB
Date	19/12/17	21/12/17	04/01/18	04/01/18	04/01/18	05/01/18	05/01/18
Temp start (°C)	20.0	21.9	20.0	22.0	19.8	20.8	20.3
Pressure (inches Hg)	30.386	30.379	28.942	28.931	29.026	29.097	29.184
Pressure (torr)	771.80	771.63	735.13	734.85	737.26	739.06	741.27
P_{tp}	0.9780	0.9859	1.0268	1.0342	1.0232	1.0241	1.0194
Tube peak voltage (kVp)	220.0	220.0	220.0	220.0	220.0	220.0	220.0
Tube current (mA)	13.0	13.0	13.0	13.0	13.0	13.0	13.0
Focus	Broad	Broad	Broad	Broad	Broad	Broad	Broad
Filter material	Cu	Cu	Cu	Cu	Cu	Cu	Cu
Filter thickness (mm)	0.15	0.15	0.15	0.15	0.15	0.15	0.15
Exposure time (s)	60.0	60.0	60.0	60.0	60.0	60.0	60.0
Step 1: Phantom set up: 33 cm SSD; 2 cm depth; open 17x17cm field							
Step 2: Output is measured over a 1 minute exposure.							
Bias voltage (V)	-300						
Exposure time	60 seconds						
Trial no.	Reading (nC)						
1	68.84	69.09	-65.78	-65.68	-65.59	-65.96	-66.38
2	68.83	69.06	-65.81	-65.68	-65.59	-65.97	-66.41

3		69.09					
Mean	68.835	69.080	-65.795	-65.680	-65.590	-65.965	-66.395
Pelect	1.0000	1.0000	1.0000	1.0000	1.0000	1.0000	1.0000

Step 3: Ion Recombination correction

Bias voltage (V)	-150						
Exposure time	60 seconds						
Trial no.	Reading (nC)						
1	68.72	68.91	-65.65				
2	68.71	68.93	-65.63				
Mean	68.715	68.920	-65.640				
Pion recombination	1.0006	1.0008	1.0008	1.0007	1.0007	1.0007	1.0007

Step 4: Polarity Correction

Bias voltage (V)	300						
Exposure time	60 seconds						
Trial no.	Reading (nC)						
1	68.61	68.85	-65.59				
2	68.58	68.84	-65.59				
Mean	68.595	68.845	-65.590				
Ppolarity	0.9983	0.9983	0.9984	0.9983	0.9983	0.9983	0.9983

Step 5: End effect (ramp-up characterization)

Bias voltage (V)	-300						
Exposure time	18 seconds						
Trial no.	Reading (nC)						
1	20.68	20.67	-19.78				
2	20.70	20.67	-19.78				
Mean	20.690	20.670	-19.780				
Plinearity	0.9992	1.0011	0.9991	0.9998	0.9998	0.9998	0.9998

Step 6: Compute correction factor for steps 2-5.

Total correction factor	0.9761	0.9861	1.0251	1.0330	1.0220	1.0230	1.0182
Corrected reading (C)	6.7190 E-08	6.8121 E-08	-6.7447 E-08	-6.7850 E-08	-6.7032 E-08	-6.7480 E-08	-6.7602 E-08

Step 7: Compute dose to water

Refer to TG-61 worksheet C.2 (page 24)							
PQ, chamb	1.0250	1.0250	1.0250	1.0250	1.0250	1.0250	1.0250
Psheath	1	1	1	1	1	1	1

Chamber correction factor	1.0250	1.0250	1.0250	1.0250	1.0250	1.0250	1.0250
Conversion factor	1.0518	1.0518	1.0518	1.0518	1.0518	1.0518	1.0518
Nk (Gy/C)	4.7619 E+07	4.7619 E+07	4.7619 E+07	4.7619 E+07	4.7619 E+07	4.7619 E+07	4.7619 E+07
Dose to water (Gy) at 2 cm depth	3.4494	3.4972	3.4626	3.4833	3.4413	3.4643	3.4706
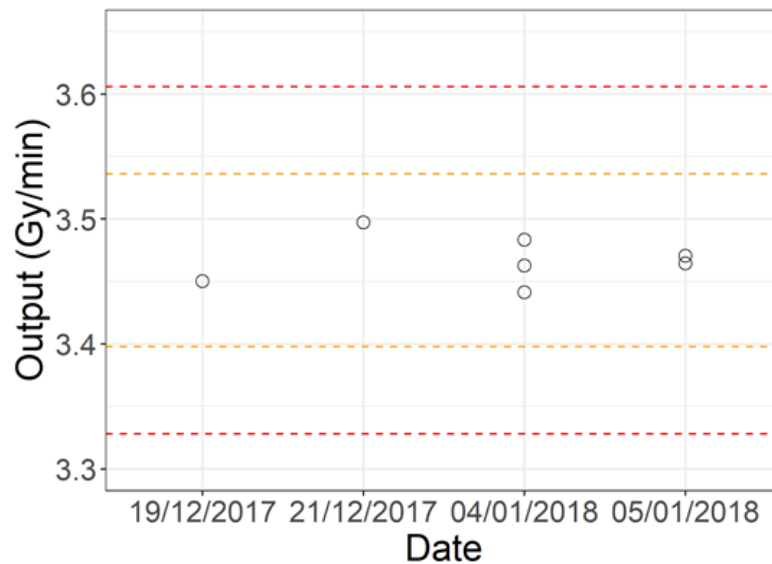
Figure A1.1. Radiation dose outputs measured during the SARRP commissioning process.

A Farmer-type ionisation chamber model TM300 10-10 (PTW Freiburg) was used to measure the dose output. Regular measurements were taken using an open field, with the chamber positioned at a depth of 2 cm within a solid water phantom, located 33 cm from the source. Readings from the connected electrometer were converted to a dose output as documented by the American Association of Physicists in Medicine Task Group 61 (AAPM TG-61) protocol, as described in Table A1.1, and plotted.

Table A1.2 documents the Gafchromic EBT3 film calibration as described in Section 2.3.2.1.1. The exact dose rate was calculated on the day of the measurements using a Farmer-type ionisation chamber model TM300 10-10 (PTW Freiburg), calbirated against the national primary standard, set at 2 cm depth, 33 cm source to surface distance and irradiated using the standard SARRP irradiation settings (220 kV, 13 mA, 0.15 mm Cu filter) for 60 seconds. The AAPM TG-61 converts this reading into a dose rate used to irradiate samples to the required dose, as shown in Table A1.1.

Table A1.2. Gafchromic EBT3 calibration for the commissioning of the SARRP.

Film number	Requested dose (cGy)	Requested time (s)	Actual time (s)	Actual dose (cGy)	Actual dose (cGy)	Actual dose (cGy)
Cal1-01	0	0.0	0	0.0	0.0	0.0
Cal1-02	40	6.9	7	40.6	40.4	40.5
Cal1-03	80	13.8	14	81.3	80.8	81.0
Cal1-04	120	20.7	21	121.9	121.2	121.5
Cal1-05	160	27.6	28	162.6	161.6	161.9
Cal1-06	200	34.4	34	197.4	196.2	196.6
Cal1-07	250	43.1	43	249.7	248.1	248.7
Cal1-08	300	51.7	52	302.0	300.1	300.8
Cal1-09	350	60.3	60	348.4	346.2	347.0
Cal1-10	400	68.9	69	400.7	398.2	399.1
Cal1-11	450	77.5	77	447.1	444.3	445.3
Cal1-12	500	86.1	86	499.4	496.3	497.4
Cal1-13	550	94.7	95	551.7	548.2	549.4
Cal1-14	600	103.3	103	598.1	594.4	595.7
Cal1-15	650	111.9	112	650.4	646.3	647.8
Cal1-16	700	120.5	121	702.6	698.3	699.8
Cal1-17	800	137.8	138	801.4	796.4	798.1
Cal1-18	900	155.0	155	900.1	894.5	896.5

The right three columns (actual dose) represent three independent measurements and were based on dose rates on each day of the commissioning measurements (3.4842, 3.4624 and 3.4702 Gy/min, respectively)

A1.2. Supplementary data from the preclinical dosimetry audit

Table A1.3. The preclinical radiation dosimetry audit protocol.

Audit aims	Investigate the current status of pre-clinical dosimetry of SARRPs in the UK.
Equipment provided	Two mice phantoms. Gafchromic EBT3 film - please handle by the edges. Alanine pellets - please handle carefully with gloves and avoid contact with water. USB stick - please save the dose information (.nrrd file), treatment plan (CurrentRecon.nrrd) and SARRP CBCT.
Pre-irradiation checks	Prior to irradiating please perform any standard QA checks and record the current room temperature and the date/time of irradiations.
Irradiation: Static beam - Pelvis	Insert an alanine pellet in the pelvis cavity and place the film labelled "A1" on top and clip the two halves of the phantom together. Place the phantom on the bed in the prone position, head to gantry. Use the lasers to ensure the film is parallel to the floor and not rotated. CBCT scan the phantom using the standard imaging settings. Define segmentation thresholds for air & soft tissue. Set the isocentre as the centre of the alanine pellet Irradiate using the standard SARRP irradiation settings with the: 10 mm x 10 mm collimator - Gantry at 0° - Bed rotation at 0° 12 Gy Place the alanine pellet back in the pre-labelled plastic envelope and record this as measurement A1. Place the film in the white envelope provided. Repeat this measurement using another alanine pellet and the film marked "A2".
Irradiation: Arc beam - Brain	Insert an alanine pellet in the brain cavity and place the film labelled "B1" on top and clip the two halves of the phantom together. Place the phantom on the bed in the prone position, head to gantry. Use the lasers to ensure the film is parallel to the floor and not rotated. CBCT scan the phantom using the standard SARRP imaging settings. Defined threshold for air & soft tissue.

Set the isocentre as the centre of the alanine pellet.

Irradiate using the standard irradiation settings with the:

- 5 mm x 5 mm collimator
- Gantry to rotate from -45° to 45°
- Bed rotation at 90°
- 12 Gy

Place the alanine pellet back in the pre-labelled plastic envelope and record this as measurement B1. Place the film in the white envelope provided.

Repeat this measurement using another alanine pellet and the film marked "B2".

Table A1.4. Summary of the questionnaire results from each institution.

Centre	What should the dose tolerance be?	Use of irradiator and techniques used	Who performs QA checks? How often? What equipment is used?	Is the equipment calibrated against a primary standard?	How often is the output checked?	How often is the output calibrated? When was this last?	What irradiation parameters should be reported?	What dosimetry parameters should be reported?
S1	5%	Cell culture & animals Static & arc	Physicists. Farmer chamber type 30010 and film	Y	Yearly			
S2	5%	Cell culture & animals Static	Dedicated user & physicists. Every two months or after service. PTW Unidose & Farmer chamber type 30012	Y	Bi-monthly	2018	Device used, gating, dose delivered, dose rate, fractionation, image guidance, irradiation technique, field size, SSD, backscatter, couch, D95	HVL, voltage, filtration, dosimetry protocol (air or water), output measurements, SSD, depth, backscatter, medium, calibration conditions.

S3		Animals Static	Dedicated user. Before every use. Unidose	Calibrated by PTW				
S4	5%	Animals Arc	Manufacturer & dedicated user. Every 6 months		Every 6 months	Every 6 months. 2019	Correct dose and isocentre	Isolines dosages giving less or avoiding oral cavity
S5		Cell culture Arc	Manufacturer. Every 6 months. Isocentre and machine colorimetric system				If the area that has to be irradiated is receiving the correct dose	Consistency of dosing
S6	10-15%	Animals Static	Dedicated user. Daily/weekly geometry checks. Farmer chamber & film	Y	Yearly	Every 2 years. 2016	Dose, dose rate, irradiation protocol & geometry and collimation	Commissioning, tube current and filtration, D90

| S7 | 5% | Cell culture & animals Static | All users. Daily (alignment)/ monthly (shielding & dosimetry). PTW, semiflex, farmer | Calibrated by PTW | Monthly | When necessary. 2019 | Filters, setup, energy, mAs | Chamber, field size, beam quality |

Table A1.5. Full data set for all alanine measurements and percentage difference compared to the treatment planning system (TPS) calculated dose

Centre	Measurement	TPS dose	Alanine result	HVL (mm Cu)	RQ, Q_0	Alanine result (corrected)	% difference
S1	Static	12.10	10.07			12.70	5.2
	Static	12.06	9.98	0.67	0.79	12.57	4.6
	Arc	12.04	9.61			12.11	1.4
	Arc	11.99	9.38			11.82	-0.9
S2	Static	12.07	10.58			13.01	8.2
	Static	12.07	10.52	0.85	0.81	12.94	7.3
	Arc	12.09	9.75			11.99	-0.2
	Arc	12.14	9.40			11.57	-4.
S3	Static	12.08	9.52			12.00	-0.2
	Static	12.12	9.51	0.67	0.79	11.99	-0.6
	Arc	12.11	9.16			11.55	-4
	Arc	12.05	9.46			11.92	-0.6
S4	Static	12.12	9.88	0.67	0.79	12.46	3
	Static	12.17	9.97			12.57	3.6
S5	Arc	11.95	8.60			10.80	-9.4
	Arc	12.04	8.29	0.7	0.80	10.40	-14
	Static	11.86	9.28			11.65	-1.5
	Static	11.95	9.24			11.59	-2.3
S6	Static	12.09	10.41			13.17	8.8
	Static	11.93	10.39			13.14	10
	Arc	11.99	10.09	0.65	0.79	12.76	7.4
	Arc	12.07	9.88			12.49	4.4
	Arc	11.99	9.84			12.44	4.5

Three local cabinet radiation units were also included in the initial audit measurements. The murine phantom, containing alanine pellets and Gafchromic EBT3 film, was irradiated using the standard operating procedure for each machine, to a dose of 12 Gy. For the Xstrahl CIX3 systems (institutions (a) and (c)) the stage is a rotating turntable at a SSD of 40 cm and irradiated at 300 kV and 10 mA. Institution (b) irradiated the phantom using the settings 250 kV and 6 mA and 0.32 mm Cu and 1 mm Al filtration. The alanine pellet results are presented in Figure A1.2.
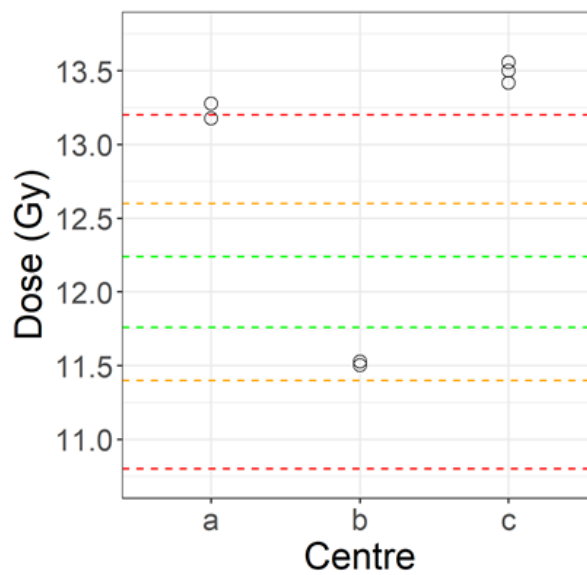

Figure A1.2. Alanine pellet dose measurements from the cabinet irradiators. The graph presents the measured doses from three cabinet irradiators when 12 Gy was prescribed. The dashed green, orange and red lines represent 2%, 5% and 10% differences respectively.

Appendix 2

A2.1. Stock solutions

Hydrogels

HEPES-buffered saline (HBS)	20 mM HEPES (H4034, Sigma-Aldrich) + 150 mM NaCl (S/3160/60, Thermo Fisher Scientific) in dH2O. pH adjusted to 7.4 using NaOH.
$CaCl_2$	200 mM $CaCl_2$ (C/1400/53, Thermo Fisher Scientific) in HBS.
Alginate	3% (microbeads) 1.5% (invasion assay) w/v sodium alginate (W201502, Sigma-Aldrich) in HBS.
Gelatin	3% (microbeads) & 1.5% (invasion assay) w/v gelatin powder (G1890, Sigma-Aldrich) in HBS.
Trisodium citrate dehydrate (TCD)	100 mM HEPES + 500 mM TCD (W302600, Sigma-Aldrich) in PBS. pH adjusted to 7.4 using NaOH.

Immunofluorescence microscopy

|	
Formalin	10% formalin (Sigma-Aldrich, Cat. no.. HT501128)
Triton X	0.1% v/v Triton X (Sigma-Aldrich) in PBS
Bovine serum albumin (BSA)	1% w/v BSA (Sigma-Aldrich, Cat. no.. A9418) in PBS
γH2AX	1:1000 γH2AX (EMD Millipore, Cat. no.. 3043548) dilution in 1% BSA
AlexaFluor 488	1:1000 AlexaFluor (Invitrogen, Cat. no.. 1890861) dilution in 1% BSA
Hoechst 33342	1:2000 Hoechst (Thermo Fisher Scientific, Cat. no.. 62249) dilution in 1% BSA

Seahorse

|	
Mito XF basal medium	DMEM medium pH 7.4 + 2 mM sodium pyruvate + 2 mM glutamine + 10 mM glucose.
Oligomycin	1 µM in mito XF basal medium
Carbonyl Cyanide-4-(trifluoromethoxy)phenylhydrazone (FCCP)	600 nM in mito XF basal medium
Rotenone & Antimycin	1 µm in mito XF basal medium
Trichloroacetic acid (TCA)	10% v/v TCA in dH$_2$O
Sulforhodamine B (SRB)	4% v/v SRB (230162, Sigma-Aldrich) in 1% acetic acid

Clonogenics

Crystal violet/methanol	10% v/v in dH20 + methanol. i.e. 50 ml crystal violet + 250 ml dH2O + 250 ml methanol

A2.2. Mitochondrial stress test data after exposure to proton radiation

One mitochondrial stress test assay was performed after cells were irradiated with protons. The irradiation was performed by Dr Elham Santina and due to beam-time constraints the assay was performed 36 hours post-irradiation, as described in Section 3.3.2.5. Compared to the X-ray data presented in Figure 3.3.5, the oxygen consumption rates (OCR), across all measurements, increased in cell lines A172, LN18 and T98G. U251 exhibited similar levels of oxygen consumption after exposure to either X-rays or protons. Exposure to protons had similar effects to X-ray irradiation on the extracellular acidification rate.
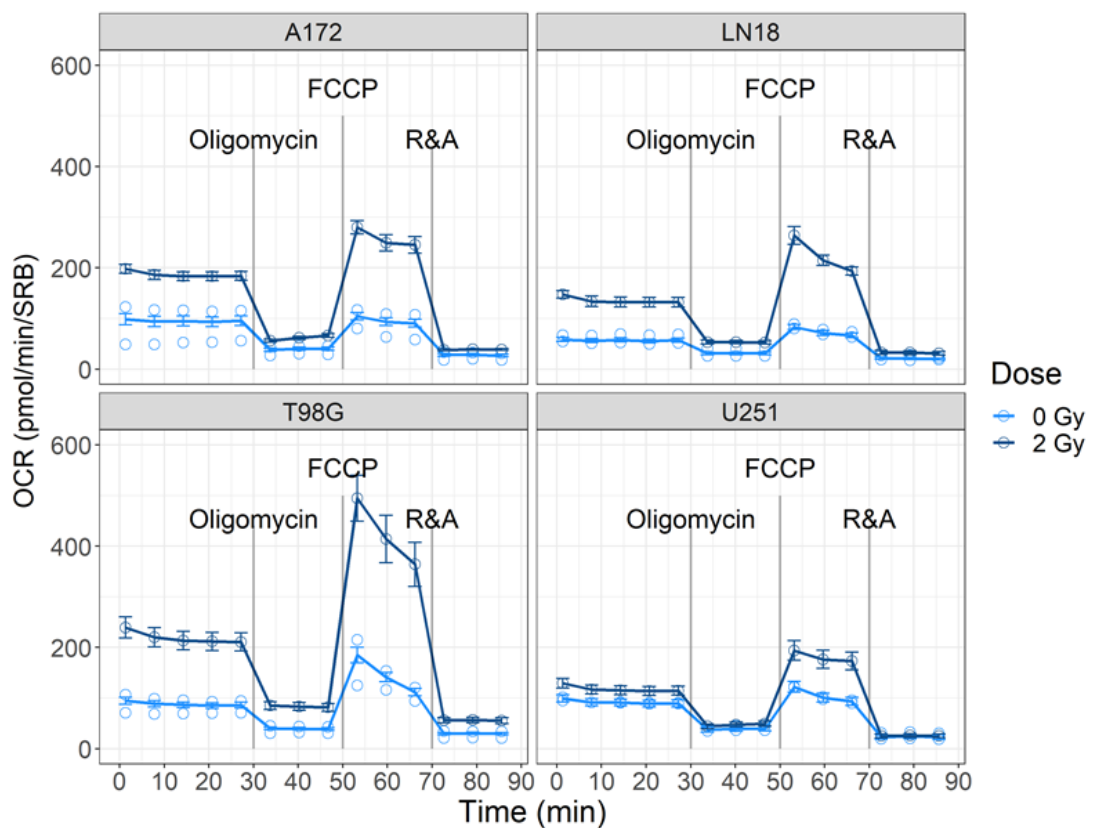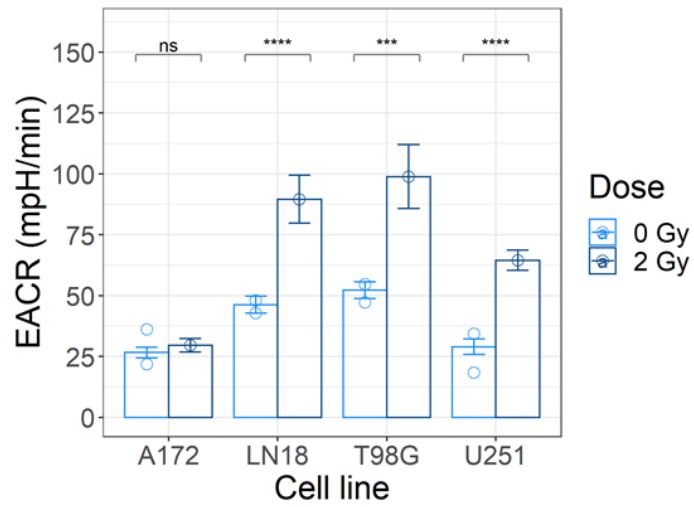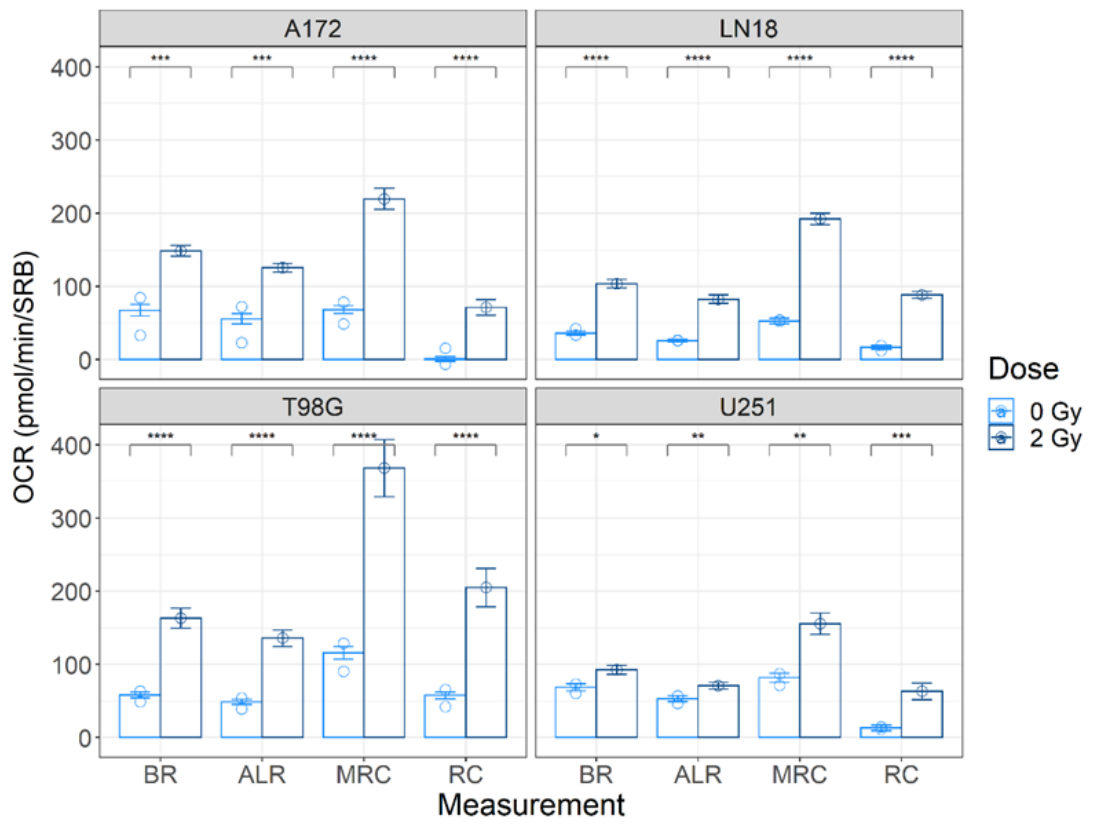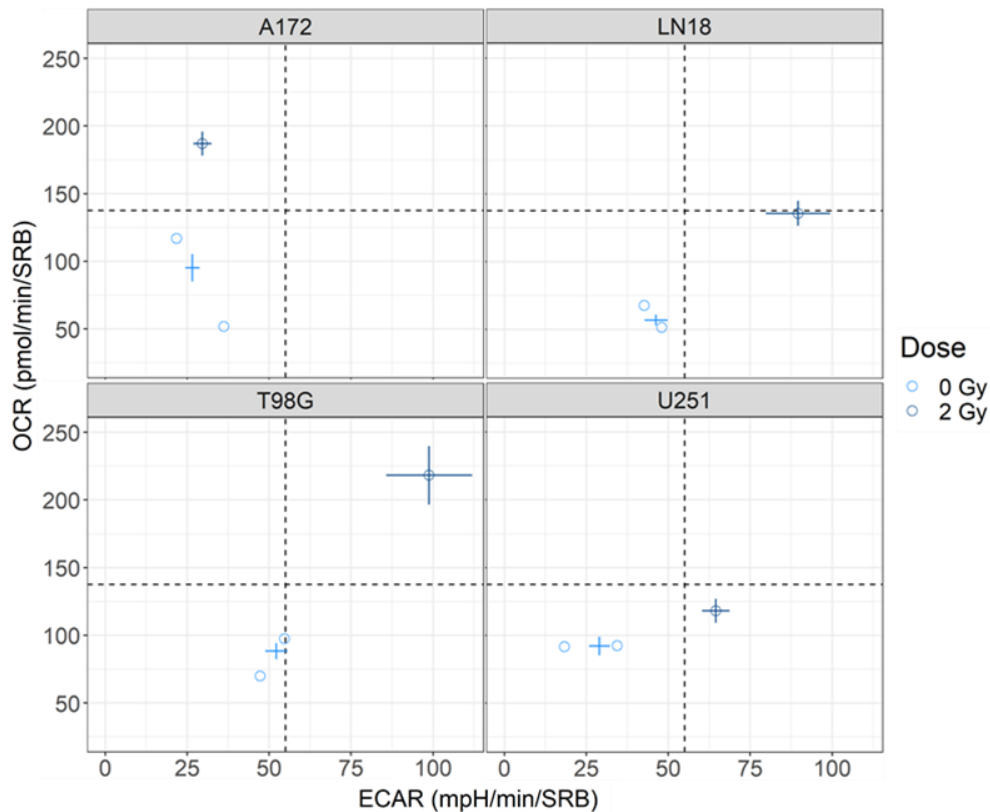
Figure A2.1. Glioblastoma multiforme cell lines exposed to proton radiation increased oxygen consumption and extracellular acidification rates.

The 0 Gy control data presented in Figures 3.3.5, 3.3.6 and 3.3.7 compared to the oxygen consumption and extracellular acidification rates measured from 1 experiment in which cells were irradiated with approximately 2 Gy protons. Due to time constraints, the assay was performed 36 hours post-irradiation. Data presented represents the mean ± standard error.

A2.2. Gap creation using inserts to assess migration

To create two confluent areas of cells 70 µl cell suspension at a concentration of 6×10^5 cells/ml was deposited into either side of an insert (Ibidi GmbH), positioned in the centre of each well of a 12 well cell culture plate. Plates were incubated (37°C, 5% CO_2) overnight to allow cell attachment. After careful removal of the insert, leaving behind two confluent monolayers of cells divided by a 500 µm width gap, 1 ml of complete RPMI media or 1% serum RPMI media was added to each well. Irradiation took place immediately after the inserts were removed, at doses ranging from 0 to 10 Gy. The migration of cells into the wounded area was photographically monitored at regular intervals and ImageJ was used to quantify the gap closure, described in detail in Section 3.4.2.3.

A comparison of the effect of using low serum media to reduce the effects of proliferation on cellular migration was performed with cell line LN18, to minimise the effects of proliferation. As shown for cell line A172, irradiating the cells with 4 Gy increases migration whereas 2 Gy decreases migration, compared to the sham irradiated control. For LN18 seeding the cells in 1% serum increased the migration for all doses compared to the 10% serum cultured cells. This could be a consequence of reduced proliferation and avoiding an over confluent cellular environment. Cell line T98G exhibited reduced migration when irradiated with 2 Gy and similar migration with 4 Gy of irradiation when compared to 0 Gy.
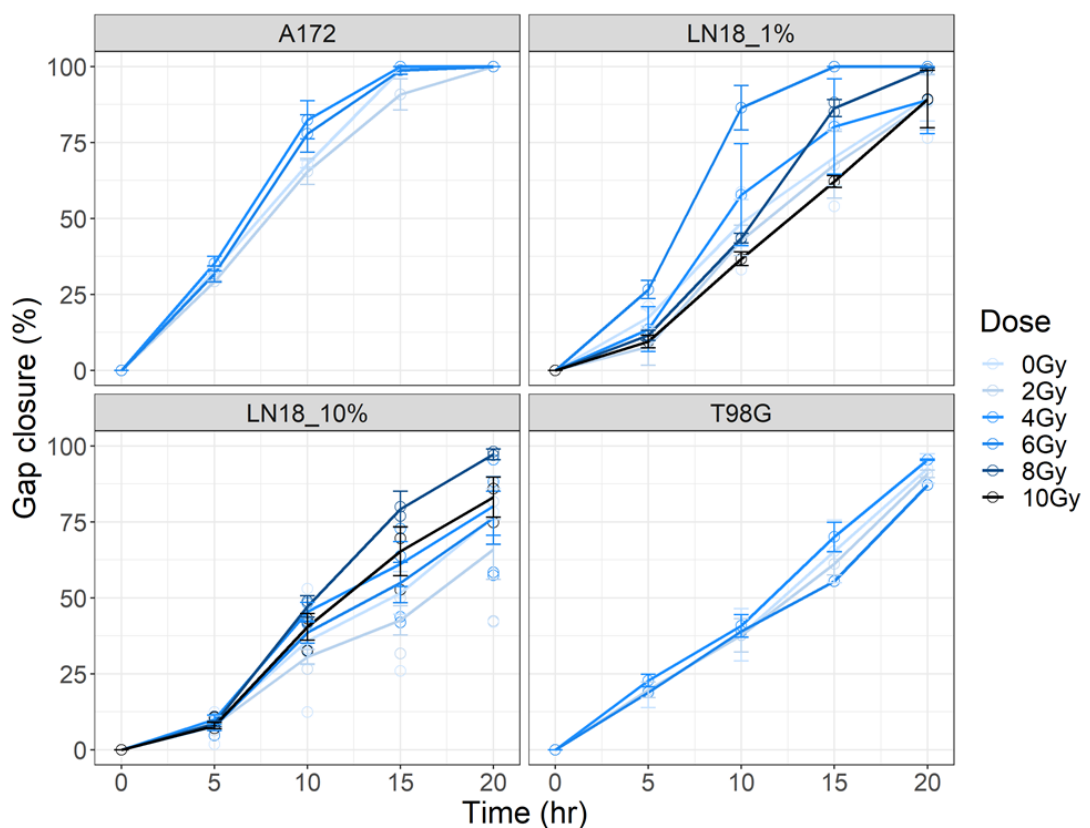

Figure A2.2. GBM cell migration using an insert (Ibidi) to create the gap.

Using an insert (Ibidi GmbH) gaps were created in the centre of a monolayer of cells. 1ml of RPMI media either supplemented with 1% or 10% FBS was added to each well before irradiating at doses of between 0Gy – 10Gy. Images were taken using an Incucyte Zoom (Essen Bioscience) at hourly intervals for 25 hours. Percentage gap closure was calculated using the area of the gap measured using ImageJ. Data shown represents the mean ± standard error (n = 2-3). The open circles represent the mean of the individual biological repeats (n = 1-4)